Sheffield Hallam University

A Sheffield Hallam University thesis

Fines are charged at 50p per hour

25 OCT 2006 6·40pm

31 JAN 2007 8m

30 MAR 07
5·55pm

-3 APR 2007
5pr

-4 APR 2007
5·00pm

23 APR 2007
9pm

DYE SENSITISATION OF SOL-GEL DERIVED TITANIUM DIOXIDE FILMS

Sandra Michelle Tracey BSc(Hons.)

A thesis submitted in partial fulfilment of the requirements of
Sheffield Hallam University
for the degree of Doctor of Philosophy

School of Engineering
Physical Electronics and Fibre Optics Research Laboratories
Sheffield Hallam University
UK

August 1997

Declaration

I hereby declare that whilst registered as a candidate for the degree of Doctor of Philosophy at Sheffield Hallam University, I have not been registered a candidate or enrolled student for any other award of the University, CNAA or other academic or professional organisation.

Signed

Sandra Michelle Tracey

This thesis is dedicated to my parents

Alan Tracey
&
Brenda Christine Tracey

Abstract

This thesis describes the development and characterisation of dye sensitised Inorganic:Organic, (IO) heterojunction photovoltaic (PV) cells of the form Au/MPc/TiO$_2$/InSnO$_2$ or F-SnO$_2$ (where MPc= copper phthalocyanine, chloroaluminium phthalocyanine or lead phthalocyanine).

The transparent TiO$_2$ films were prepared by Sol-Gel techniques and characterised optically, structurally and electrically. The effects of and interactions between Sol-Gel process parameters have shown that the parameters undergo significant interaction with particular effects on the TiO$_2$ film thickness and thickness related properties obtained during dip coating. The film refractive index n was in the range 2.73-1.81 and wavelength dependent. The conductivity of the films derived from Au/TiO$_2$/InSnO$_2$ structure was 4.26×10^{-6}S/cm. E$_o$ varied from 3.4-3.35eV where $\delta=2$ indicting an indirect allowed transition in 1 layer thick films to E$_o$ ~3.2eV where $\delta=3$ indicating indirect forbidden transition as the number of coating layers increased.

The spectral response, dark and illuminated J(V) and dark C(V) characteristics of the dye sensitised IO PV cells have been determined. Spectral response indicates that all of the organic dyes studied can be used to sensitise Sol-Gel derived TiO$_2$ into the visible region Corresponding photovoltaic and junction parameters were derived. Photovoltaic effects were observed in all devices studied, however cell efficiencies were poor, in the range (η~0.0001-0.046%). The low quantum efficiencies were anticipated to be a consequence of the presence of recombination centres at the TiO$_2$/MPc heterointerfaces and the high observed series resistance due to the low conductivity of the MPc films.

The MPc/TiO$_2$ junction formed a rectifying contact. C(V) analysis indicated that the junction was electrically abrupt. The dark J(V) characteristics were divided into three regimes. (i) A reverse bias regime in which the device acts as a p-n heterojunction, (ii) an intermediate forward voltage regime, where the derived values of m>2 indicating the presence of a high density of interface states (iii) High forward regime. All devices deviate from the standard diode equation as a consequence of space charge effects in the organic layer, the ideality factors m>>2. Temperature dependence measurements of PbPc/TiO$_2$ heterojunctions show that the junction currents are a composite of tunnelling and recombination.

PV cell parameters were influenced by changes in ambient conditions, the thickness of organic layers and variations in incident intensity. The J$_{sc}$ and V$_{oc}$ were proportionally and logarithmically dependent on the incident intensity respectively. The high R$_s$ is believed to be responsible for the poor cell efficiencies reducing FF, J$_{sc}$ and η. A 30 fold increase in η was observed when the organic film thickness was reduced from 500nm to 100nm. Exposure to atmosphere reduced η and is likely to be a consequence of O$_2$ trapping centres.

The work has demonstrated the feasibility of a low cost solid state IO heterojunction photovolatic cell. However improvements in efficiency are required to produce a commercially viable device.

Acknowledgements

List of Symbols

Symbol	Quantity	Units
α	Absorption co-efficient	m^{-1}
E	Activation energy	eV
E_g	Fundamental energy band gap	"
E_o	Optical band gap	"
n	Film refractive index	-
n_s	Substrate refractive index	-
σ	Conductivity	$\Omega^{-1}m^{-1}$
σ_o	Metallic conductivity	"
υ_g	Frequency of electromagnetic radiation	Hz, s^{-1}
υ_{ph}	Phonon frequency	"
δ	Nature of electronic transition	-
ε	Permittivity	Fm^{-1}
ω	Angular frequency	rad s^{-1}
ΔE_c	Discontinuity in conduction band	eV
ΔE_v	Discontinuity in valence band	"
A	Absorbance	-
a	Device active area	m^2
C	Capacitance	F
c	Speed of light	$m.s^{-1}$
d	Electrode spacing	m
e	Elementary charge	C
E_c	Energy of conduction band	eV
E_d	Dispersion energy	"
E_f	Energy of Fermi level	"
E_s	Single effective oscillator energy	"
E_v	Energy of valence band	"
E_{vac}	Vacuum level	"
FF	Fill factor	-
h	Planck's constant	J.s
J	Current density	A/m^2
J_L	Photocurrent density	"
J_s	Saturation current density	"
J_{sc}	Short circuit current density	"
k	Boltzmann constant	$J.K^{-1}$
K_{et}	Electron transfer rate	s^{-1}
N(E)	Density of states	m^{-3}
N_a	Acceptor concentration	"
N_d	Donor concentration	"
n_i	Intrinsic carrier concentration	"
p	Hole concentration	"

Symbol	Quantity	Units
ϕ	Transmitted radiation intensity	W/m^2
λ	Wavelength of electromagnetic radiation	m
ϕ	Work Function	eV
η	Conversion efficiency	%
χ	Electron affinity	eV
ϕ_{bp}	Built in potential	"
σ_{DC}	DC conductivity	$\Omega^{-1}m^{-1}$
μ_e	Electron mobility	$cm^2.V.s^{-1}$
μ_h	Hole mobility	$cm^2.V^{-1}.s^{-1}$
ϕ_o	Incident radiation intensity	W/m^2
λ_o	Average oscillator position	nm
m	Diode ideality factor	-
n	Electron concentration	m^{-3}
n_c	Complex refractive index	-
P	Electrode perimeter	m
R	Device responsivity	$Am^{-2}W^{-1}$
R_s	Series resistance	Ωcm^{-2}
R_{sh}	Shunt resistance	"
R_{ST}	Sheet resistance	$\Omega/$
S	Conductance	Ω^{-1}
t	Film thickness	m
T	Temperature	K
T_s	Transmission	-
V_{oc}	Open circuit voltage	V
W	Depletion layer width	m
x	Depletion layer penetration distance	"
Z	Quantum efficiency	%

CONTENTS OF THESIS

CHAPTER 4 : Sol-Gel Processing

CHAPTER 5 : Experimental Methodology

CHAPTER 6 : TiO$_2$ Characterisation: Results

CHAPTER 7 : Dye Sensitised IO Heterojunction : Results

CHAPTER 8 : Discussion of Experimental Results

CHAPTER 9 : Conclusions and Suggestions for Further Work

Appendix A: Swanepoel Procedure

Appendix B: Anovas and Tables Derived From Yates Analysis

Appendix C: IO Heterojunction Parameters

Appendix D: Publications and Conferences Attended

Chapter

Introduction

Conventionally, optoelectronic devices such as the photovoltaic cell, photodiodes and phototransistors have been fabricated from inorganic materials such as silicon, gallium arsenide, cadmium selenide and the more recent CdTe and Cu-In-diselenide alloys. However, during the last 20 years, there has been increasing interest in organic alternatives. In the case of photovoltaic devices, this is primarily due to the realisation that there is not necessarily a single optimum material and/or fabrication solution and that a range of devices are required, engineered for specific applications and suited to a variety of environmental factors.

Organic dyes such as the merocyanines, perylenes and phthalocyanines have been intensively investigated for photovoltaic applications[1-3]. However the single layer Schottky barrier type organic cells have not been able to compete with their inorganic counterparts due to problems such as low fill factors and quantum efficiencies. Notwithstanding this, there are a number of potential benefits of using organic dye materials which include low cost and ease of fabrication and consequently there remains considerable interest in their use. One area of particular promise for the use of these materials is dye sensitisation[4-6].

Phthalocyanines are a particularly interesting class of organic dyes of this type. Whilst these compounds have inherently low charge carrier mobilities[3,7], (typically 10^{-4}-$1cm^2/Vs$ compared with monocrystalline silicon which is in the order of $1350cm^2/Vs$) they exhibit considerable absorption within various parts of the visible spectrum. These materials can therefore be exploited for their excellent photocarrier generation capabilities. To overcome the problem of low mobility, recent work[6,8] has aimed at the development of composite devices exploiting materials with higher carrier mobilities to carry out the function of carrier transportation, in conjunction with the organic phthalocyanine photocarrier generator. This leads to the fabrication of a n-type (inorganic)/p-type (organic) or (IO) heterojunction photovoltaic cell.

It is postulated that the operation of such devices involves the photo-induced creation of electron-hole pairs within the phthalocyanine, the electrons transfer to the conduction band of the metal oxide layer due to its higher electron affinity. From here they are transported in-plane, the holes remaining within the phthalocyanine layer and subsequently transported therein[6].

The ultimate aim of this work is to present the results of investigations on three such dye sensitised photovoltaic devices incorporating the organic dyes, lead phthalocyanine (PbPc), chloroaluminium phthalocyanine (ClAlPc) and copper phthalocyanine (CuPc) respectively as the organic component. The material chosen to form the inorganic n-type layer was titanium dioxide (TiO_2). This material exhibits characteristics (outlined in section 2.5) that make it a most suitable choice. In order to fully understand and consequently optimise these devices it is necessary to appreciate the characteristics of the various materials from which they are constructed.

This thesis is presented in nine chapters. Chapters two to four comprise a critical review of the literature and relevant theories. The second chapter describes the development of the dye sensitised solar cell, addresses some of the more notable historical advances that have led to an interest in devices of this type. The third chapter reviews the necessary theoretical information required for an understanding of the optical, electrical and photoelectrical characterisations performed on both materials and devices during these studies. The concepts of photogeneration in specifically metal substituted phthalocyanines are reported and the current thinking on the mechanisms of dye sensitisation is introduced. A brief review of the Sol-Gel processing technique of the type used in this research is contained within chapter four. Chapter five describes the experimental methods and procedures. Chapters six and seven describe the experimental results obtained in the work, for the TiO_2 Sol-Gel films, and the dye sensitised (IO) heterojunction devices respectively. Additional work was carried out on PbPc, investigating both the steady state and spectroscopic characteristics, the results are presented in the form of a paper given in appendix D.

Discussion of the results is contained within chapter eight, while chapter nine outlines the conclusions and possibilities for future work stemming from this research.

REFERENCES

1. Ghosh, A.K., Morel, D. L., Feng., T., Shaw., R.F., and Rowe, C. A. *J. Appl. Phys.* **45**(1) (1974) 230-235.

2. Verzimacha, Y. I., Kovalchuk, A. V., Kurik, M. V., Hamann, C., and Mrwa, A. *Phys. Stat. Sol. (a)* **82** (1984) K111.

3. Simon, J. and Andre, J.J. *Molecular Semiconductors*, Springer, 1984.

4. Sakata, T., Hashimoto, K., and Hiramoto, M. *J. Phys. Chem.* **94** (1990) 3040-3045.

5. Borsenberger, P.M. J. *Appl. Phys.* **62**(7) (1987) 2942-2945.

6. Shen, Y., Wang, L., Lu, Z., Wei, Y., Zhou, Q., Mao, H., and Xu, H. *Thin Solid Films.* **257** (1995) 144-146.

7. Shafai, T. S., and Gould, R. D. *Int. J. Elec.* **69**(1) (1990) 3-9.

8. Antohe, S. *Rev. Roum. Phys.* **37**(3) (1992) 309-313.

Chapter 2

The Development of the Dye Sensitised Photovoltaic Device

2.1 Introduction

Becquerel's discovery[1] in 1839 that a silver halide coated metal electrode would produce a small voltage and current when placed in an electrolyte solution and exposed to sunlight sparked the beginning of what has now become an immense interest amongst scientists and engineers to develop cheaper, more efficient and reliable devices for converting light into electricity.

By 1876, 37 years after Bequerel's first photovoltaic (PV) cell (or battery cell), progress had been made towards understanding the concepts of the PV phenomenon. Materials[1] such as selenium and cuprous oxide had been shown to produce significant light dependent voltage and semiconducting materials were isolated as the most suitable for light to electric conversion. Major advancements in PV technology occurred with the developments of the first p-n junction, constructed from diffused silicon by RCA and Bell Laboratories in 1954[2] and the first cuprous sulphide/cadmium sulphide heterojunctions[3] which were responsible for the subsequent investigations into thin film photovoltaics.[4]

The major application of the PV cell is for commercial electricity generation. Due to the limited supply of fossil fuels the pollution problems associated with present day power stations and the general environmental concern over nuclear fuels, solar energy is a popular alternative. But for solar energy to become a realistic possibility a number of conditions need to be satisfied. Firstly, the energy generation costs using PVs has to be competitive with other ways of producing energy. Furthermore, the total amount of energy obtained during the lifetime of the PV must be larger than the energy required to manufacture and operate it, and there must be an abundance of the raw materials required for production of the cell.

The major drawback of today's single crystal cells are the high material and processing costs, primarily due to the purity of the materials required. Research into polycrystalline and amorphous silicon succeeded in lowering the production costs of the cells but both alternatives are not without problems. The oxide thickness required by the polycrystalline-Si (MIS) structures would be difficult to mass produce, and a-Si cells have limitations on efficiency and long term stability[5]. For cadmium based devices such thin film n-CdS/p-CdTe heterojunction cells[6], there could be limitations on the availability of cadmium, as well as the potential toxicity hazards[7].

There subsequently remains a demand for research into novel PV materials and device structures. In particular, research into stable materials which are sensitive to wide ranges of the solar spectrum. The future widescale use of solar energy could depend on the successful development of cost efficient, large area devices, that are constructed by manufacturing processes which are environmentally acceptable.

In recent years particular attention has been given to organic materials for PV applications[5,8], especially those organics based on chlorophyll, as this is a highly abundant material. One such group of organics are a class of commercial dyes known as the phthalocyanines. The phthalocyanines contain highly absorbing chromophores within the solar spectrum. This significant property has stimulated the recent interest in their use as a sensitising material for the development of dye-sensitised PV devices[9,10], in which a wide band gap inorganic semiconductor with high charge carrier mobility can be made sensitive to wavelengths outside its intrinsic sensitivity. Such a concept offers inherently less complex manufacturing techniques and substantially lower costs, together with the potential for reaching conversion efficiencies that are comparable with commercial Si cells[11]. This combination of properties would be highly attractive to potential manufacturers and end users of PV devices.

2.2 The Metallo-Phthalocyanines

The phthalocyanine molecule was discovered in 1907, when a study was conducted on 1,2-cyanobenzamide. When the benzamide was heated in an alcoholic solution precipitation of a highly insoluble blue product was observed[12]. Linstead and co-workers[13] were the first to carry out an in-depth study on phthalocyanine compounds and determine their basic structure, though the structure was later confirmed using X-ray analysis techniques[14]. The similarity of chlorophyll to the Phthalocyanine ring is shown in Figure 2.1. A wide variety of metallo-phthalocyanines (MPcs) can now be prepared, in fact almost all metal atoms can be substituted into the phthalocyanine ring, hence allowing a range of different energy levels[12].

7

The central metallic ion in the macro-ring alters the electronic state density of the molecule, and can have significant effects on the optical and electrical properties of the resulting compound. The MPcs have become extensively investigated due to their large number of inherent properties. In particular, they are tinctorially strong, abundant, chemically and thermally stable, cheap and easy to fabricate, easily crystallised and sublimed, so that the material may be obtained in a highly pure form and suitable for a number of deposition techniques which include Langmuir-Blodgett (LB)[15] and vacuum sublimation[16]. In addition, they often exhibit semiconducting properties, which were first observed by Vartanyan[17]. Later work by Sussman[18] identified as-evaporated films exhibited semiconductivity that was inherently p-type, due to the large number of acceptor states which inject holes into the valence band.

2.2.1 Lead, Chloroaluminium and Copper Phthalocyanine

Although a wide variety of MPcs are available the studies were restricted to three, namely lead (PbPc), chloroaluminium (ClAlPc) and copper (CuPc) phthalocyanine. These were chosen as they are easily acquired, purified and vacuum sublimed. They are also complementary, in that each is sensitive to different regions of the solar spectrum, structurally distinct and each has been researched to varying degrees, while the CuPc has been intensively investigated PbPc and especially ClAlPc are less well documented.

2.2.1.1 Structural Properties

The molecular structures of PbPc, ClAlPc and CuPc have been studied[5,12,19]. The CuPc molecule is similar in structure to most metallo-phthalocyanine molecules. It comprises of a large macrocylic ring with the copper atom comfortably fitting in the space between the four nitrogen atoms. The planarity is reported to be within 0.3Å[9]. In contrast, both PbPc and ClAlPc comprise of a non-planar molecular structure possessing a 'cone' arrangement. In the case of PbPc the lead atom deviates from the plane of the free molecule by 0.37-0.40Å due to the steric repulsion of the relatively large radius lead atom[20].

CuPc can exist in a variety of polymorphic forms (or phases), α and β are among the most common. Both forms possess the 'herringbone' stacking arrangement, however the angle between the stacking axis and the normal to the molecular plane is 25° for the α phase and 45° for the β phase[21]. The β phase is also considered to be more stable than the α phase. Indeed, it has been reported that β-CuPc is more stable than α-CuPc by 10.3 kJ/mol[21].

(a)   (b)
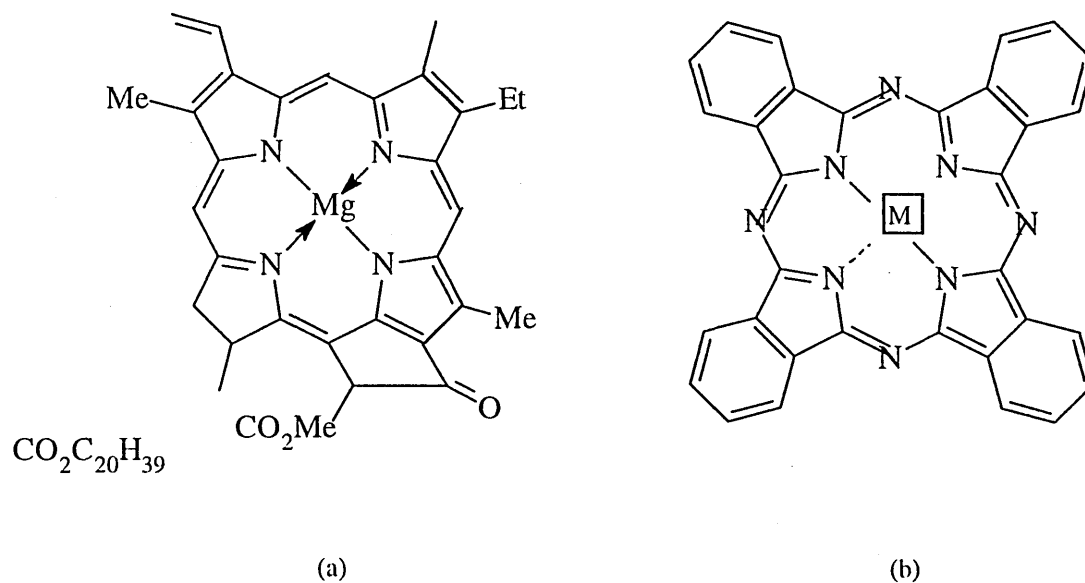
Figure.2.1. Chemical structure of (a) chlorophyll and (b) metal-substituted phthalocyanine. For metallophthalocyanines the metal atom is substituted into the phthalocyanine ring, between the nitrogen atoms (denoted 'M'). M=Cu; Al-Cl or Pb for copper phthalocyanine, chloroaluminium phthalocyanine or lead phthalocyanine respectively.

(a)   (b)
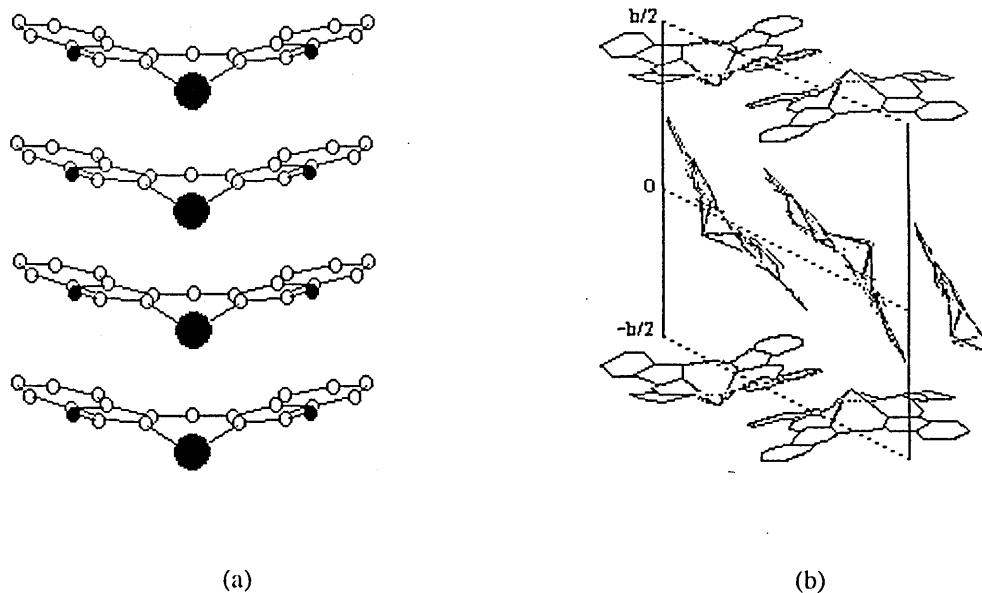
Figure 2.2. Structures of (a) monoclinic and (b) triclinic lead phthalocyanine[12].

The non-planar PbPc and ClAlPc also have distinct polymorphs. Those formed by PbPc are regarded as being analogous to the α and β phases formed by the planar metallo-phthalocyanine molecules. These are known as triclinic and monoclinic and are shown in Figure 2.2. The molecules in the monoclinic phase stack linearly to form a molecular column parallel to the c-axis. In the triclinic structure the molecules stack along the a-axis[22]. The crystalline structure of ClAlPc is believed to possess a similar structural arrangement to the monoclinic PbPc[21]. Chloro related MPcs are reported to possess a 'slipped disc' arrangement where the molecules are bound in a linear polymeric chain[23].

The crystallographic structure of PbPc, CuPc and ClAlPc vacuum sublimed film have been shown to be dependent upon deposition conditions such as the substrate type and temperature, the evaporation rate and any subsequent heat treatment of the films [21,24-28]. Predominantly monoclinic PbPc films have been prepared when glass substrate temperatures are 50-100°C, above 150°C, triclinic single phase films have been produced[25]. At room temperature, PbPc films are primarily amorphous[25]. However, it has been observed that when substrates are held at room temperature films produced at a low deposition rate (1-2Å/s) contain a mixture of monoclinic and triclinic phases, with the monoclinic phase predominating[26]. The fraction of triclinic phase can be decreased by increasing the evaporation rate. At a rate of 10Å/s, films of monoclinic with an amorphous phase have been reported[26].

Predominantly amorphous ClAlPc films have been produced when deposited onto glass substrates held at room temperature, using an evaporation rate of 5nm/min[24]. Gradually increasing the substrate temperature to a maximum of 200°C resulted in a corresponding decrease in film discontinuity, however the predominantly amorphous phase of the films

remained. This is in contrast to ClAlPc films prepared on n-Si and InSnO$_2$ electrodes, where an increase in substrate temperature resulted in crystal growth of ClAlPc[10,28].

Studies on films of CuPc show that room temperature deposition onto Corning 7059 substrates results in films which are predominantly of the α polymorph and subsequent heat treatment results in a transformation to the more stable β-form[27]. A deposition rate of 0.1 to 2.5nm/sec was used. This is in agreement with results obtained for many MPcs sublimed under vacuum pressures of < 50torr, onto substrates which are held at room temperature[12].

2.2.1.2 Optical Properties

Due to the weak Van der Waals forces between molecules of the phthalocyanine lattice[12], optical absorption results in a discrete transition between ground and excited electronic states. In phthalocyanines this refers to the so-called π-π^* transition, and is considered to be the cause of the strong bands observed in MPc absorption spectra.

MPcs have high absorption coefficients[29] ($\sim 10^5 cm^{-1}$), a substantial amount of work has therefore been devoted to investigations of the optical properties of these materials as thin sublimed films[20,29-31], vapours[30], single crystals[30,32] and in solvent solutions[31]. The effects of the substituted metal atoms on absorption properties of phthalocyanines have been extensively investigated by Davidson[33].

Many phthalocyanines are known to form molecular aggregates which cause a broadening and splitting of the long wavelength band of the spectrum into two bands one red the other blue.[34]

The bands are referred to as the Soret band (300-400nm) and the Q-band (650-700nm)[12]. Such bands have been observed in ClAlPc[31], CuPc[33], and PbPc[20]. The absorption spectra of CuPc as observed by Yoneyama[35] is shown in Figure 2.3.

Zhang[31] and co-workers studied the absorption properties of ClAlPc in CH_2Cl_2 solution as well as in the solid state. In solution a strong band at 684nm was observed. In thin film form the band split into two, located at 415nm and 912nm. Monoclinic PbPc films[20] have shown two absorption bands at photon energies ≥ 2.6eV and at ≤ 2.1eV.

The early work of Chadderton[30] on CuPc identified similarities in the absorption spectra of CuPc in vapour, evaporated films and single crystal form. The results were interpreted in terms of a simple band model, in which the sharp energy levels of the free molecule become broad quasi-continuous bands when the material is crystallised.

For MPcs in solution, the Q-band is observed as a narrow peak which is transformed into a broad peak when the material is in solid state form. A splitting of this peak is observed and commonly referred to as Davydov splitting[12]. The amount of splitting is dependent on the interaction energy between molecules. A correlation between the magnitude of Davydov splitting and the amount of out of plane bonding of the central metal ion has been observed by Day and Williams[32].
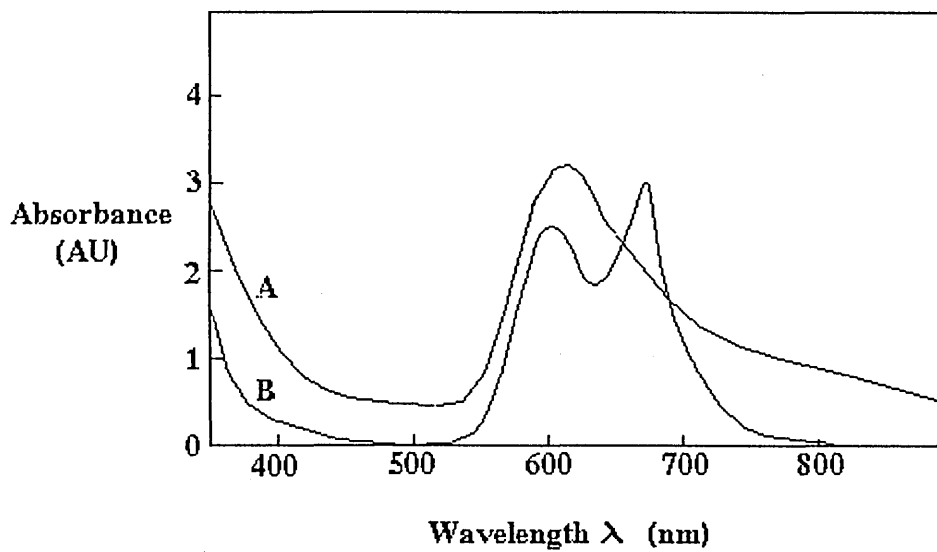
Figure 2.3. Typical absorption spectra of CuPc film, after Yoneyama[35].
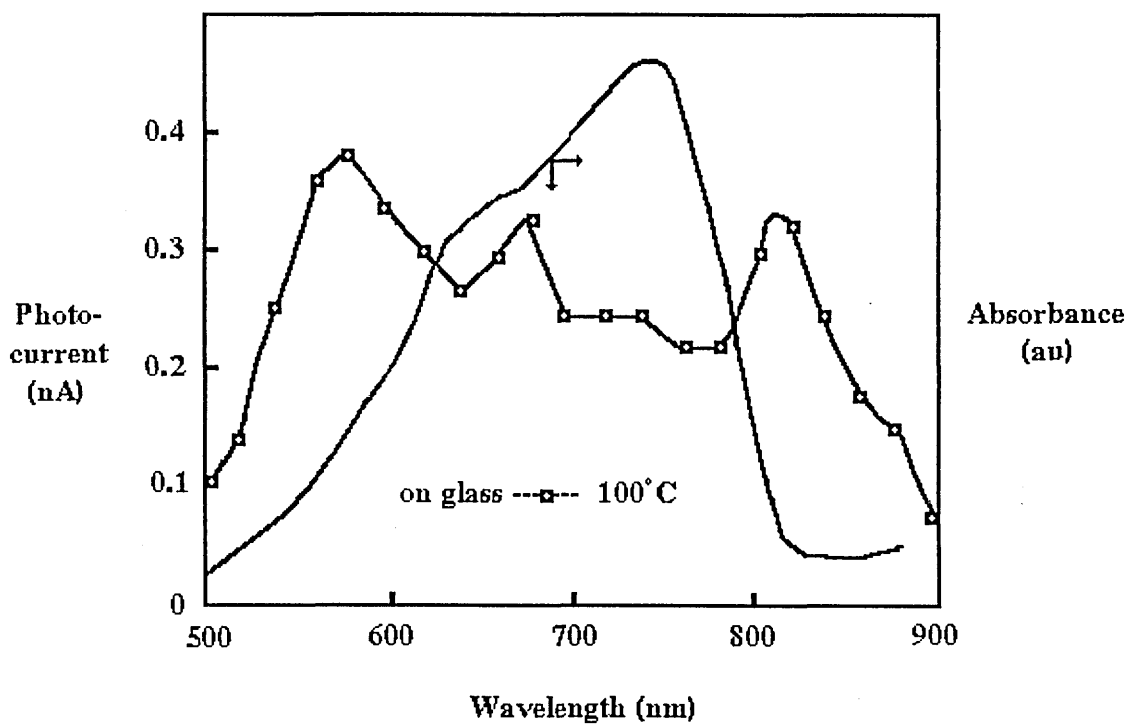
Figure 2.4. Action and absorption spectra of sublimed ClAlPc films after Yanagi.[37]

14

2.2.1.3 Photovoltaic Properties

Due to the materials' excellent ability to photogenerate free charge carriers[12], the potential application of MPc compounds in photovoltaic devices has been investigated by a number of workers[5,35-37]. Photovoltaic cells constructed from these materials have usually consisted of a sandwich structure where the absorbing dye layer is placed between two metals each having different work functions, forming a Schottky barrier cell[5].

The photoelectrical properties of CuPc have been investigated in both single crystal[38] and thin film form[35]. Asymmetrically substituted CuPc[35] in the form Al/15asy-CuPc/Ag, and prepared using the LB technique[15], exhibited J/V photoelectric behaviour typical of a p-type schottky solar cell where J_{sc} was negative and flowed from Ag to Al electrode. A close match was observed between J_{sc} action spectra and the absorption spectra. The maximum $J_{sc} \sim 10^{-8} Acm^{-2}$ for $100 \mu Wcm^{-2}$ of monochromatic light.

PbPc solar cells of the form M/PbPc/Au where M=Pb, Ni or Sn, were investigated by Verzimacha[36]. V_{oc}, J_{sc} and m were higher when illumination was through the bottom electrode i.e. Pb, Sn or Ni. The spectral response of V_{oc} and J_{sc} correlated well with the spectral dependence of the absorption coefficient, α. Though there was an anticorrelation when $\alpha > 10^4 cm^{-1}$. The diode quality factor m was between 1 and 2, and found to be dependent on the incident light intensity.

Photocurrent as a function of wavelength has been measured for ClAlPc films evaporated onto glass substrates by Yanagi[37] and co-workers.

15

The action spectra of the films did not match the absorption spectrum of a ClAlPc film, as shown in Figure 2.4. This spectral mismatch was attributed to a morphology dependent recombination of charge carriers. The magnitude of the photocurrent was found to be highly dependent on the amount of absorbed O_2 in the amorphous films.

A variety of factors are believed to contribute to the low conversion efficiencies obtained for cells of the type described. Often aluminium is used as the blocking contact and gold as an ohmic contact, illumination of the cell is through one of these contacts, causing a reduction in the incident light directly available to the dye layer. There has also been the suggestion that the quantum yields from this type of cell may have a fundamental limit due to Forster radiationless transfer of excitons from the dye to the metal contacts where heat is produced rather than carrier pairs.[5]

The low charge carrier mobility of these materials, (for CuPc values of approximately $5 \times 10^{-7} m^2 V^{-1} s^{-1}$ are reported[39]), the insulating nature of the organic layer (therefore causing a large series resistance) especially if the dye layer is thick and the low absorption coefficient if the dye layer is very thin may also contribute.

Recent attempts to increase power conversion efficiency include a surface plasmon polariton enhancement technique (SPP) as applied to a Au/CuPc/Al organic solar cell[40]. The power conversion efficiency was increased by a factor of 7, this was thought to be a consequence of enhanced light absorption under SPP excitation causing an increase in photocarrier generation in the CuPc layer. Nevertheless, the current single layer organic solar cell seems unlikely to compete with present inorganic technology.

2.3 The Evolution of Dye Sensitisation

In 1873 Hermann Wilhelm Vogel noticed that commercially available photographic plates had an unexpected spectral sensitivity beyond 540nm. It was discovered from the British manufacturer Stuart Worthly, that the plates contained organic dyes. A range of dyes were tested including coralline and methyl green and all could sensitise photographic silver halide plates optically for wavelengths > 540nm, outside the normal sensitivity of the Ag-Halide used. It was concluded that the mechanism responsible could either be electron or energy transfer. For the following 50 years most of the work in the field was carried out by Eastman Kodak mainly on silver halide plates for photographic applications[41].

Spectral sensitisation of semiconductors is a concept that is now approximately 20 years old. One of the earliest attempts came from Regansburger and Petruzzella[42] in 1971, where photoinduced injection of charge carriers from metal free phthalocyanine (H_2Pc) into selenium was achieved. The H_2Pc proved to be an efficient sensitiser for amorphous selenium and a gain of 0.6 electrons/incident photon was measured.

Light in the 570-700nm region did not lead to a photoconductive response in Se and so the observed response of the device to red light was ascribed to light absorption in the H_2Pc layer.

Unfortunately the mechanisms of spectral sensitisation are still not well understood. Gurney and Mott[43] in 1938 suggested a mechanism of electron transfer which is the currently accepted theory. However, an alternative mechanism involving energy transfer

was believed to be the most important until the 1967 symposium on spectral sensitisation. In 1969, West and Gilman[44] produced an extensive review in which the theory of spectral sensitisation energies and mechanisms were discussed. It was concluded that spectral sensitisation must involve either (i) direct transfer of an electron from the optically excited dye to the semiconductor, (ii) energy transfer from the excited dye so as to bring about an electron liberating process in the surface of the semiconductor, or (iii) both of these mechanisms may be present simultaneously. Recently, T.Sakata[45] and co-workers outlined an alternative mechanism suggesting that electron transfer from the excited dye to the surface states and from the surface states to the continuum of the semiconductor may occur. However, from a comparison of theoretical with experimental investigations the direct electron transfer mechanism is the most favoured.

2.4 Heterojunction Photovoltaic Devices Incorporating Organic Materials

The principle of dye sensitisation has been applied to the development of PV heterojunction devices[11,19,46-54]. The overwhelming advantage of PV devices which incorporate organic materials such as those which will be described, is their use of low to medium purity materials which are widely available and have low processing costs in comparison to silicon. It has recently been demonstrated by O'Regan and Grätzel[11] that it is possible to produce an organic/inorganic device with a power conversion efficiency comparable with that of some silicon devices. The cell reached an overall light to electrical energy conversion efficiency, (η) of 12% in diffuse daylight. When compared

18

with the recently reported efficiency of 12.7% for an amorphous Silicon[55] terrestrial cell measured under the global AM1.5 spectrum the results are encouraging.

In the literature there exists a variety of PV cell structures that utilise organic materials. These have been of the form, organic/organic[46,47] and organic/inorganic[19,48-50]. Even multilayer structures of alternating layers of organic and inorganic materials[9] have been investigated. The heteromultilayer cell, developed by Takada et al[9] consists of alternating layers of CuPc and TiO$_2$. A 50-fold increase in photoconduction compared with a single layer CuPc device was observed, although the dominant photoconductivity mechanism was not fully recognised. Whether such multilayer systems would be cost effective for large scale production is debatable due to the fabrication technologies employed for their manufacture. The multilayer structure was also inhibited by charge separation difficulties from the dye to the transporting layer, as a consequence of recombination effects in the CuPc films.

Work by Harima[46] and co-workers, reported an energy conversion efficiency of 2% for an organic/organic PV cell of the form Au / ZnPc (zinc phthalocyanine) / TPyP (5,10,15,20-tetra(3-pyridyl)porphyrin) /Al. This was achieved under monochromatic light at 430nm corresponding to a maximum in the absorption spectra of the TPyP film. In this device a good spectral match to the solar spectrum was achieved and a strong spectral sensitisation of the ZnPc by the TPyP, as a consequence photocurrent generation was substantially enhanced across the visible region. Charge separation induced by light absorption was thought to occur at the interface between the two materials. The ZnPc was shown to be responsible for hole transport while the TPyP responsible for electron transport.

It is more desirable however to obtain conversion efficiencies for cells illuminated under the entire solar spectrum rather than at wavelengths of maximum absorption. This is especially true if the cell is being designed for terrestrial PV applications. Nevertheless, this efficiency represents one of the highest achieved for a purely organic PV device, though the reasons why these particular organics in combination should display such relatively high conversion efficiencies are unclear. An organic/organic device of the form CuPc/ PTV(a perylene tetrocarboxylic derivative) prepared by Tang[47] achieved a power conversion efficiency of ~ 0.95% and a fill factor, (FF) of 0.65 under simulated AM2 illumination. According to Tang[47], a similar situation as that described for the Hirama[46] cell occurs in which both organic materials contribute to the generation of charge carriers. Dissociation of excitons created by absorption of light in both the CuPc and the PTV layers occurs at the interface between the two organic materials, holes are transported within the CuPc and the electrons within the PTV. This is in contrast to single layer devices in which the electrode/material interface is responsible for photogeneration[47]. Organic/organic designs of this type are still limited by the low carrier mobilities associated with organic dyes, their high resisitivity and in some cases can be limited by instability due to light fatigue of the dyes[51].

The organic/inorganic device structures have the advantage that inorganic materials are often associated with higher carrier mobilities and are thus able to transport charge carriers more effectively than the dye layers. In addition, depending on the fabrication technique employed, the inorganic layer can be structurally engineered to enhance light harvesting efficiency (LHE). This has been successfully demonstrated by O'Regan and Gratzel[11] and Knödler[52] in the TiO_2/dye photoelectrochemical (PE) cells.

The cell developed by O'Regan and Gratzel[11] at the Swiss Federal Institute of Technology, comprises of a specially engineered porous TiO_2 film, hence possessing a high surface area. It is coated with a monolayer of an antenna dye complex. Photovoltaic measurements revealed an overall conversion efficiency of 7.1-7.9% under simulated solar light, the fill factor remained above 0.7 even under low light conditions. The LHE of the incident solar energy flux was 46%, and attributed to the increased TiO_2/dye interfacial area due to the porous nature of the TiO_2 layer. This represents a vast improvement over previous PE cells. MPc/(n-TiO_2 or n-WO_3) single crystal electrodes in aqueous solution[53] have shown low quantum efficiencies. The cause was considered to be the inefficient production or the rapid recombination of charge carriers. However, the low light harvesting efficiency, due to the smooth surface of the inorganic films could contribute. Among the PE cells fabricated by Korsunovskii[54] those which consisted of a TiO_2 film deposited onto a titanium substrate, and sensitised by Rhodamine B only reached a quantum efficiency (Z) of 5×10^{-5} electrons/photon. The efficiency was presumed to be strongly dependent on the technique of fabrication, porosity and conductivity of the electrode, and the dye treatment.

There is still debate as to the cost and practicality of the large scale production of PE cells[56]. The cells in the past have been prone to corrosion, electrolyte evaporation and dye degradation through electrochemical reactions with the electrolyte, caused by photogenerated minority carriers[52]. Although the Knödler[52], O'Regan and Gratzel[11] cells have recently demonstrated high efficiency and improved stability, there is nevertheless continuing interest in the development of alternative, low cost solid state PV devices.

As previously mentioned one of the first attempts to produce a solid state dye sensitised inorganic/organic PV device came from Regansburger and Petruzzella[42] in 1971. They also demonstrated that sensitisation was strongly field dependent. At high fields, in the order of $4 \times 10^5 Vcm^{-1}$, a gain of 0.6 was observed and a quantum efficiency of 0.8 electron injected per absorbed photon. The efficiency of sensitisation decreased as the applied field decreased. The field dependence of the generation and/or injection efficiency was dominant and transport was not found to limit the performance of the device. The low field electron injection from H_2Pc to Se was accounted for by examination of the respective energy levels of the materials. The valence band of H_2Pc lies at 5-5.3eV while that of Se is reported to lie at 6eV. Absorption of 1.7eV radiation in H_2Pc is believed to form excitons which dissociate forming mobile electrons. The electrons are then easily injected across the H_2Pc interface then move through the Se in the applied field. This model accounted for the lower hole injection from H_2Pc into Se which was also observed at low applied fields. A similar model was applied to a ZnO/merocyanine cell fabricated by Kudo and Moriizumi[50]. The photovoltaic effects observed were attributed to light absorption in the dye layer and separation of photoexcited carriers at the ZnO/Merocyanine interface, a relatively low efficiency of 0.5% was observed and attributed to the high resistivities of the ZnO and the merocyanine dye. However a good spectral match between the short circuit current, I_{sc} action spectra and the dye absorption spectra was observed as shown in Figure 2.5, indicating that the I_{sc} was due to the sensitising effects of the dye.

Few MPcs have been explored as potential sensitisers for inorganic semiconductors, specifically for use as solid state photovoltaic devices. In 1987 Borsenburger[49] attempted spectral sensitisation of a-Si by bromoindium phthalocyanine.
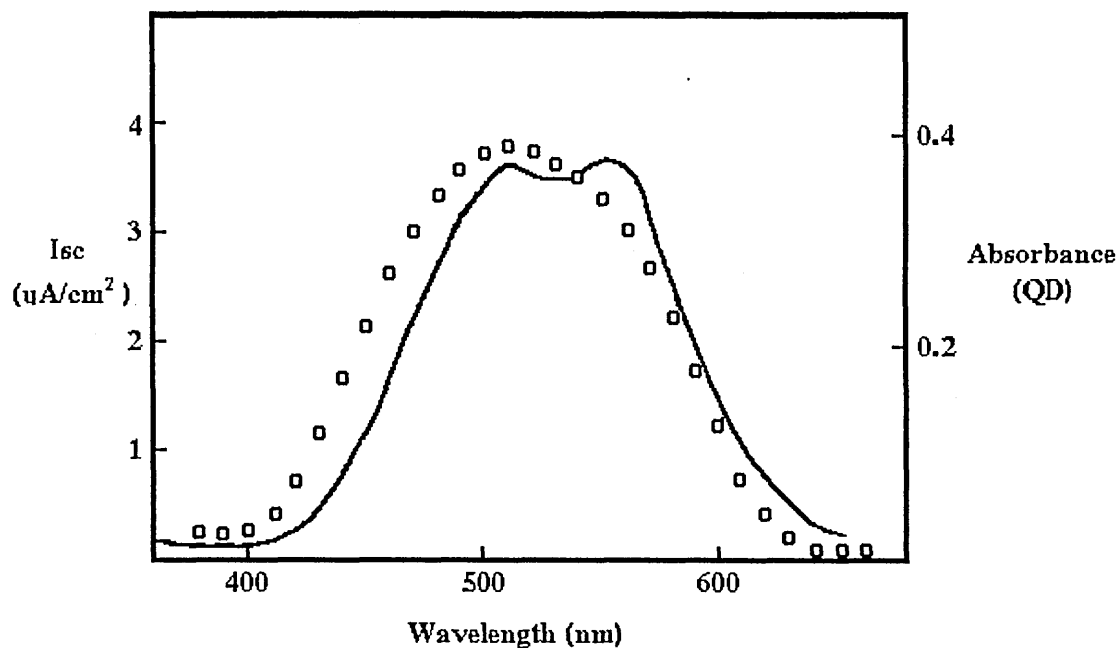
Figure 2.5. Action spectra of ZnO/Merocyanine cell according to Kudo and Moriizumi.[50]
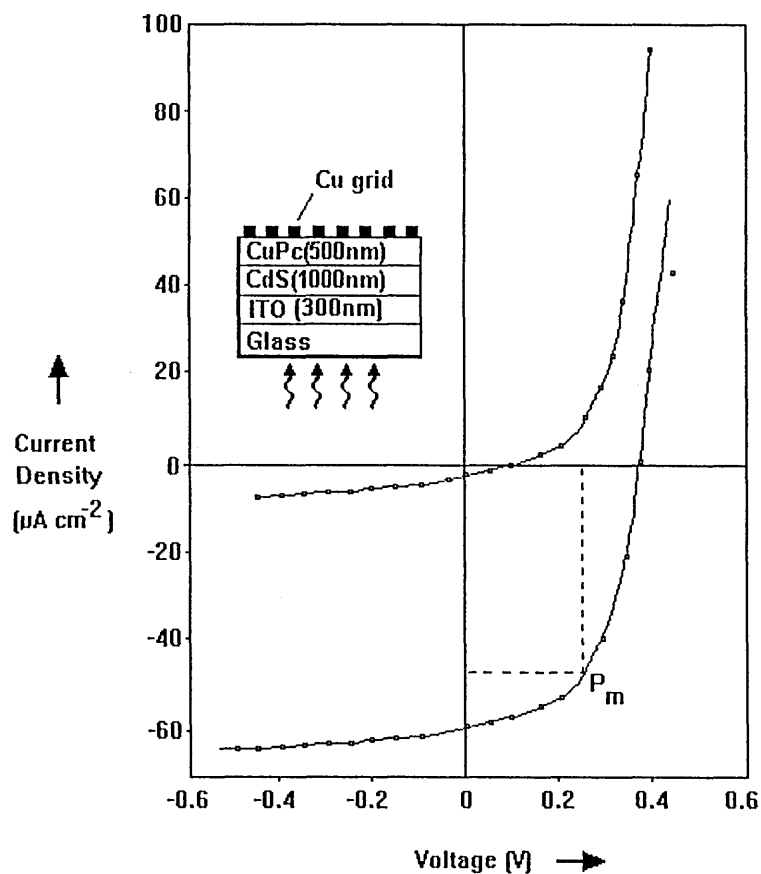
Figure 2.6. Current -voltage characteristics of InSnO$_2$/CdS/CuPc/Cu cell under darkness and under white light. From Anthoe[19]

Sensitisation of a-Si into the wavelength range of 730-780nm was achieved, a quantum efficiency of 0.3 was measured. CuPc[19] has been successfully used to sensitise cadmium sulphide (CdS).

The current/voltage characteristics of the $InSnO_2$(300nm) /CdS(1000nm) /CuPc(500nm) /Cu cell are shown in Figure 2.6, under darkness and white light illumination with an incident intensity (I_o) of 10mW/cm^2. The cell exhibited both rectifying and photovoltaic properties. The diode quality factor (m) and reverse saturation current density (J_s) were estimated to be 2.54 and 1.36×10^{-7}A/cm^2 respectively.

These results indicated that a large number of defects were present at the CdS/CuPc interface thus facilitating electron/hole recombination. At higher forward voltages space charge limited conduction (SCLC) was observed, typical of an organic molecular semiconductor containing an exponential trapping distribution within the band gap. Various PV parameters were calculated for the device, the highest conversion efficiency obtained was 0.115%, the fill factor, FF ~0.53± 0.01, open circuit voltage, V_{oc} ~375 ±10mV, and the short circuit current density, J_{sc} ~58.12± 0.01 A/cm^2.

The thickness and morphological dependent photovoltaic properties of a Au/ClAlPc/n-Si cell have recently been assessed by Yanagi[10] and co-workers. Both the J_{sc} and η% were found to be dependent on the thickness of the ClAlPc layer, where η~6.4×10^{-3}% for a 150nm ClAlPc film, and η~5.7×10^{-1}% for a 10nm film. It was anticipated that the thicker ClAlPc films resulted in the formation of a higher series resistance. The action spectra of the devices were analysed in terms of the morphology of the dye layer.

A significant difference between the spectra of devices consisting of homogenous layers of ClAlPc and those in which discontinuous islands of ClAlPc were formed onto the n-Si electrode (when held at temperatures of 200°C) was detected. Discontinuous ClAlPc islands had no sensitising effect on the n-Si electrode, and the observed photoactivity was attributed to the Au/n-Si junction. For devices comprising of homogenous layers of ClAlPc the action spectra was primarily due to photocarrier generation within the ClAlPc layer and the subsequent sensitisation of the n-Si electrode.

These investigations have identified the future potential of a dye sensitised PV cell, indicating the requirements for further research into areas such as the development of materials, fabrication technologies and device behaviour. In particular there are requirements for ;

(i) identification of the most appropriate sensitising dyes. Factors such as the conductive behaviour, ambient effects, film morphology and structure need to be considered. In principle, the selected dye must have an excited state level that is above the conduction band edge of the semiconductor, and its ground state must lie within the band gap, thus allowing dissociation of charge carriers at the dye/semiconductor interface. The MPcs previously discussed fulfil this condition and in keeping with the aim to produce low cost devices offer the use of relatively low cost manufacturing technologies.

(ii) determination of the energy band structure of the devices and subsequently apply the most appropriate charge separation and transport mechanisms to explain the observed device behaviour.

(iii) obtaining satisfactory spectral sensitisation of the transporting layer by ensuring there is a good spectral match between the photocurrent action spectrum and the absorption spectrum of the dye (indicating that the observed photocurrent is due to charge carrier injection from dye into the transporting material).

(iv) identification of the most appropriate transporting material and associated fabrication technology. The transporting material must have higher electron affinity (χ) than the dye, in order for charge carrier transfer to occur.

Sol-Gel derived TiO_2 has been chosen to act as the transporting layer for these studies, the following sections review this material and offer justification for the choice of fabrication technology.

2.5 Titanium Dioxide

Titanium dioxide (TiO_2) is an inorganic material which exists at moderate temperatures in three stable crystalline phases, brookite[57], anatase[57] and rutile[57,58], though the material may be prepared in amorphous form[59]. It has found applications in a wide variety of areas. TiO_2 films have been examined for their suitability as NO_x gas sensors[60], as electrochromic materials for display devices[61] and planar waveguides[62]. The material is also commercially available as ceramic membranes for use in food processing, gas separations and biomedical processes[63], and is used as an infra-red reflecting coating on commercial energy saving glass products, (e.g. IROX glass)[64]. It is suitable for

fabrication by a number of techniques including sputtering[63], plasma enhanced chemical vapour deposition[58] and Sol-Gel[59] ,(as used in the present studies).

It exhibits good transmittance within the visible region[59,65], chemical stability[66], and a high dielectric constant ε (the highest amongst the metal oxides)[66,67] . The large ε makes it suitable to sustain high fields, hence its suitability for microelectronic device fabrication[67]. The ε has been found to vary with annealing temperature. The work of Vorotilov[66] identified an increase in dielectric constant from 20 to 150 as the annealing temperature was raised from 400 to 800°C. TiO_2 films heated to 850°C had a dielectric constant of between 130 and 150.

The material has also been shown to possess a relatively high refractive index, n. This also was found to vary depending on annealing temperature which in turn induces structural changes[65,66]. Vorotilov[66] determined an index of 2 for anatase and 2.2 for rutile films, and identified that amorphous TiO_2 possesses a lower n than the crystalline phases. The n of TiO_2 films has also been found to be wavelength dependent. Takahashi[65] measured the n of Sol-gel derived TiO_2 films in both anatase and rutile forms. The films were manufactured by dipcoating onto glass substrates. The n was observed to decrease exponentially with increasing wavelength. The absorption coefficient (α) of reduced TiO_2 films has been measured by Ardakani[68]. At 514nm α was in the range 0.68-1.52 $\times 10^7 m^{-1}$ depending on the substrate temperature and hydrogen pressure.

For determination of an energy band diagram for the dye sensitised (IO) PV cell, knowledge of the band structure of the TiO_2 films is essential. The optical band gap energy (E_0) of TiO_2 films prepared by a variety of methods has been determined for

both rutile and anatase forms. In a fashion similar to the n, the E_o has been found to vary, depending on fabrication procedures. Leinen[69] and co-workers have recently reported a band gap in the range 3.42eV to 3.36eV for TiO_2 films prepared by ion induced chemical vapour deposition. The films displayed peaks in the X-ray diffraction spectra indicative of the anatase form. The E_o was found to decrease with increasing thickness, similar to that observed in CdS thin films by Chun[70]. This observation is thought to be a consequence of the quantum size effect[70] whereby the physical properties of a solid became dependent on its characteristic geometric dimensions when the dimensions become comparable to the de Broglie wavelength of the charge carriers. In contrast pure anatase single crystals have a reported band gap of 3.28eV[71].

The nature of interband transitions are not as clear. Yoko[72] and co-workers determined the band gap of both anatase and rutile forms prepared by Sol-Gel methods. TiO_2 anatase was reported to have only an indirect bandgap at 3.03eV while TiO_2 rutile an indirect bandgap at 2.92eV and a direct bandgap at 3.13eV.

From Hall voltage measurements Forro[71] concluded that anatase TiO_2 is an n-type semiconductor, with a high mobility of charge carriers ($\gg$1 $cm^2V^{-1}s^{-1}$ for temperatures >50K), which are produced by thermal excitation. Ardakani[68] investigated the electrical properties of 'hydrogen reduced' titanium dioxide films deposited by pulsed excimer laser ablation. Activation energies at room temperature were in the range 8meV to 160meV. The low average activation energy indicated that at normal temperature nearly all of the electrons were free to contribute to conduction. The activation energy of 0.16eV was attributed to hopping of an electron from singly ionised centres to free oxygen vacancies. In comparison, Könenkamp and Henninger[73] also measured a room

temperature activation energy of 0.16eV and a typical room temperature conductivity of $10^{-9}(\Omega cm)^{-1}$ under a vacuum environment. Conduction was attributed to transport in extended states, with the Fermi-level near mid-gap.

In the design of the proposed dye sensitised (IO) solid state PV device, the transporting layer must have a higher carrier mobility to ease carrier transport, a higher electron affinity to allow charge transfer, a high n to reduce reflection losses and be readily formed at low cost. A review of literature on TiO_2 has revealed that these characteristics are intrinsic, there is consequently sufficient potential to justify its use. The properties required for the successful fabrication of a dye sensitised TiO_2 PE cell could be applied to the PV cell.

According to Knödler[52], for a successful dye sensitised TiO_2 PE cell, the transporting TiO_2 layer must fulfil the following requirements: (i) a high specific surface area to increase the LHE of the cells, (ii) a predominantly anatase phase structure. It has been reported that rutile forms have lower transmittance than anatase. Largely due to the optically anisotropic rutile crystals[65] (iii) A homogenous and crack free surface structure. These characteristics are capable of being engineered using Sol-Gel technology[64].

2.6 Sol-Gel Technology

Sol-Gel processing[64] is a low temperature chemical route for the production of inorganic oxide materials. The process can be used to produce a wide range of single and multi-component oxides in crystalline or amorphous (glass) form. The process can be used to produce bulk materials but is particularly suitable for the production of thin film coatings.

Some of the earliest literature relating to the Sol-Gel method appears in 1943 in the form of a patent by Gefficken and Berger[74] on oxide coatings, particularly silica. The first major industrial use of Sol-Gel appeared in 1959 for the volume production of coated rear view mirrors for the automotive industry, the system being TiO_2-SiO_2-TiO_2[74]. An important review appeared in 1969 by Schroeder[75] which explains oxide layers deposited from organic solutions. Schroeder also reviews the deposition techniques available to the Sol-Gel technologist, and the production of both single and multioxide coatings. By 1970, dip-coating had been applied by Schroeder[64] to glasses in order to modify their optical properties. From this time Sol-Gel was fully recognised as a viable way of producing inorganic materials, and in particular metal oxides. The last decade has seen intensive interest in Sol-Gel technology, due to possibilities for engineering the properties of glassy and ceramic materials.

Sol-Gel offers many attractive advantages over conventional ways of producing oxide materials. These include the possibility of varying the film properties extensively by changing the composition of the solution (to produce change in film microstructure) and a relatively low process cost. In addition Sol-Gel overcomes the difficulties of producing a high quality dielectric-semiconductor interface, and obtaining a stoichiometric ratio of elements and molecular homogeneity in multicomponent oxide films[76]. There are many forms in which the oxide gel product can be produced. These include powders, coatings, monoliths and fibres[63,64,76] which often require very low processing temperatures. The possibility of the use of high purity starting materials and the ease with which large and complex shaped substrates can be coated has meant that this technique is becoming increasingly attractive to optoelectronic specialists. The need for low-cost thin film

production processes has increased the interest in Sol-Gel (and other non-vacuum deposition techniques) capable of deposition at high rates and over larger areas.

2.7 Summary

Solar power has not become the major alternative energy source it was once anticipated to be. This is mainly due to the high material and processing costs associated with conventional PV cells. While there is considerable research effort into the development of amorphous silicon (a-Si), and cadmium technologies, there is an interest to develop PV cells constructed using less traditional materials and methods that may offer a cost effective alternative.

MPcs are organic dyes that are sensitive to various regions of the visible spectrum and have therefore been intensively investigated for PV applications. Added to this they are chemically and thermally stable, abundant, cheap and easy to fabricate. But as PV cells they have not reached the required high conversion efficiencies. This limitation is due to the materials' poor ability to collect and transport charge carriers.

Recent research has emphasised the potential of using organic dyes to spectrally sensitise wide band gap semiconductors for use in PV applications, an approach which offers relatively low cost materials and fabrication methods. It is anticipated that with the addition of the MPc sensitising dyes; ClAlPc, CuPc, and PbPc the absorption of light in the PV cell is modified to the dyes spectral sensitive region resulting in a much broader range of the solar spectrum being utilised therefore in contrast to traditional PV cells the

photoeffect (or production of photogenerated carriers) does not take place inside the semiconductor but in the sensitising dye on its surface.

MPcs are organic based macromolecules which have potential as the dye species, they are inherently p-type semiconductors with an energy gap of ~2eV. It is expected that the photoinduced electrons created in the MPc layer are transferred to the conduction band of the inorganic semiconductor (TiO_2), which has a higher mobility, a larger energy gap and exhibits no photoconduction sensitivity over most of the visible region.

Although it is the principal intention of the author to investigate the feasibility of spectrally sensitising Sol-Gel derived TiO_2, the constituent materials from which the devices are constructed are optically, structurally and electrically characterised. This will assist in reproducibility and future optimisation. It is recognised that Sol-Gel process parameters have a major influence on factors such as refractive index and structure of Sol-Gel products. The full extent to which Sol-Gel processing parameters interact to affect the properties of TiO_2 films are not known, and could have serious implications for the PV cell performance.

It is hoped that this work will help in the identification of the most appropriate dyes and demonstrate the versatility and advantages of using Sol-Gel technology in the manufacture of the TiO_2 transporting layer.

REFERENCES

1. Möller, H. J. *Semiconductors for Solar Cells*, Artech House, 1993.

2. Chapin, D. M., Fuller, C. S., and Pearson, G. L. *J. App. Phys.* **25** (1954) 676.

3. Raynolds, D. C. *Phys. Rev.* **96** (1954)

4. Coutts, T. J. *Thin Solid Films.* **50** (1978) 99-117.

5. Whitlock, J. B., Panayotatos P., Sharma, G. D., Cox, M. D., Sauers, R. R., and Bird,

   G. R. *Opt. Eng.* **32**(8) (1993) 1921-1933.

6. Das, S. K., and Morris, G. C. *J. Appl. Phys.* **72**(10) (1992) 4940.

7. Green, M. A. *Prog. Photovoltaics: Res. appl.* **2** (1994) 87-94.

8. Al-Mohammad, A., and Soulieh, M. *Thin Solid Films.* **271** (1995) 132-137.

9. Takada, J., Awaji, H., Koshioka, M., Nevin, W. A., Imanishi, M., and Fukada, N. *J. Appl. Phys.* **75**(8) (1994) 4055.

10. Yanagi, H., Kataura, H., and Yasukiyo, U. *J. Appl. Phys.* **75**(1) (1994) 568.

11. O'Regan, B., and Grätzel, M. *Nature.* **353** (1991) 737-740.

12. Simon, J., and Andre, J.J. *Molecular Semiconductors*, Springer, 1984.

13. Linstead, R. P. *J. Chem. Soc.* (1934) 1016, 1031.

14. Robertson, J. M. *J. Chem. Soc.* (1935) 613.

15. Petty, M. C. *Polymer Surfaces and Interfaces.* John Wiley & Sons, 1987, p.173.

16. Vincett, P. S., Popovic, Z. D., and McIntyre, L. *Thin Solid Films* **82** (1981) 357.

17. Vartanyan, A. T. *Zh. Fiz. Khim.*, **22** (1948) 769.

18. Sussman, A. *J. Appl. Phys.* **38** (1967) 2738-2752.

19. Antohe, S. *Rev. Roum. Phys.* **37**(3) (1992) 309-313.

20. Krier, A., Abass, A. K., and Collins, R. A. *Adv. Mat. Opt. Elec.* **2** (1993) 289-293.

21 Wright, J. D. *Prog. Sur. Sci.* **31**(1-2) (1989) 1-60.

22. Frauenheim, T. H., Hamann, C., and Müller, M. *Phys. Stat. Sol. (a)* **86** (1984) 735.

23. Wynne, K. A. *Inorg. Chem.* **23** (1984) 4658.

24. Yanagi, H., Imamura, M., and Ashida, M. *J. Appl. Phys.* **75**(4) (1994) 2061.

25. Hamann, C. and Mrwa, A. *Int. J. Elec.* **73**(5) (1992) 1039-1040.

26. Machida, Y., Saito, Y., Taomoto, A., Nichogi, K., Waragai, K., and Asakawa, S. *Jpn. J. Appl. Phys.* **28**(2) (1989) 297-298.

27. Hassan, A. K., and Gould, R. D. *Phys. Stat. Sol. (a)* **132** (1992) 91-101.

28. Yanagi, H. *J. Appl. Phys.* **96** (1992) 1366.

29. Schechtman, B. H., and Spicer, W. E. *J. Mole. Spec.* **33** (1970) 28-48.

30. Chadderton, L. T. *J. Phys. Chem. Solids.* **24** (1963) 751-757.

31. Zhang, H., Pan, D., and Fang, J. *Proc. 3rd. Int. Conf. Properties and Applications of Dielectric Materials.* July 8-12 (1991) 647.

32. Day, P., and Williams, J. P. *J. Chem. Phys.* **37**(3) (1962) 567.

33. Davidson, A. T. *J. Chem. Phys.* **77**(1) (1982) 168

34. Loutfy, R. O., Hor, A. M., and Rucklldge, A. *J. Imag. Sci.* **31** (1987) 31-37.

35. Yoneyama, M., Sugi, M., Saito, M., Ikegami, K., Kuroda, S., and Iizima, S. *Jap. J. Appl. Phys.* **25**(7) (1986) 961-965.

36. Verzimacha, Y. I., Kovalchuk, A. V., Kurik, M. V., Hamann, C., and Mrwa, A. *Phys. Stat. Sol. (a)* **82** (1984) K111.

37. Yanagi, H., Imamura, M., and Ashida, M. *J. Appl. Phys.* **75**(4) (1994) 2061-2068.

38. Hamann, C. *Phys. Stat. Sol. (a)* **10** (1972) 83-90.

39. Gould, R. D. *Thin Solid Films.* **125** (1985) 63-69.

40. Hayashi, S., Kozaru, K, and Yamamoto, K. *Sol. Stat. Comms.* **79**(9) (1991) 763-767.

41. Dähne, S. *J. Imag. Sci. Tech.* **38**(2) (1994) 101-117.

42. Regansburger, P. J., and Petruzzella, N. L. *J. Non-Cryst. Solids.* **6** (1971) 13-26.

43. Gurney, R. W. and Mott, N. F. *Proc. Roy. Soc.* **A164** (1938) 151-167.

44. West, W., and Gilman, P. B. *Photo. Sci. Eng.* **13**(5) (1969) 221-230.

45. Sakata, T., Hashimoto, K., and Hiramoto, M. *J. Phys. Chem.* **94** (1990) 3040-3045.

46. Harima, Y., Yamashita, K., and Suzuki, H. *Appl. Phys. Letts.* **45**(10) (1984) 1144-1145.

47. Tang, C. W. *Appl. Phys. Letts.* **48**(2) (1986) 183-185.

48. Shen, Y., Wang, L., Lu, Z., Wei, Y., Zhou, Q., Mao, H., and Xu, H. *Thin Solid Films.* **257** (1995) 144-146.

49. Borenberger, P. M. *J. Appl. Phys.* **62**(7) (1987) 2942-2945

50. Kudo, K., and Moriizumi, T. *Jap. J. Appl. Phys.* **19**(11) (1980) L683-L685.

51. Hiramoto, M., Fujiwara, H., and Yokoyama, M. J. Appl. Phys. 72(8) (1992) 3781-3787.

52. Knödler, R., Sopka, J., Harbach, F., and Grünling, H. W. *Solar Energy Materials and Solar Cells.* **30** (1993) 277-281.

53. Giraudeau, A. *J. Am. Chem. Soc.* **102**(16) (1980) 5137.

54. Korsunovskii, G. A. *Translated from: Élektrokhimiya,* **19**(5) (1983) 615-620.

55. Green, M. A., and Emery, K. *Progress in Photovoltaics: Research. and Applications.***2** (1994) 27-34.

56. Komp, R. J. *Practical Photovoltaics: Electricity from Solar Cells.*2nd edition, Actec, (1989).

57. Calderon, W. *IEEE Potentials.* Feb/Mar (1995) 13-16.

58. Cronemeyer, D. C. *Phy. Rev.* **87**(5) (1952) 876-886.

59. Lee, W. G., Woo, S. I., Kim, J. C., Choi, S. H., and Oh, K. H. *Thin Solid Films.* **237** (1994) 105-111.

60. Huusko, J., Lantto, V., and Torvela, H. *Sensors and Actuators. B.* **15-16** (1993) 245-248.

61. Cantâo, M. P., Cisneros, J. I., and Torresi, R. M. Thin Solid Films 259 (1995) 70-74.

62. Sorek, Y., Reisfeld, R., Finkelstein, I., and Ruschin, S. *Appl. Phys. Letts.* **63**(24) (1993) 3256-3258.

63. Anderson, M. A., Gieselmann, M. J. and Xu, Q. *J. Memb. Sci.* **39** (1988) 243-258.

64. Brinker, C. J., and Scherer, G. W. *Sol-Gel Science*, Academic Press, New York (1990).

65. Takahashi, Y., and Matsuoka, Y. *J. Mat. Sci.* **23** (1988) 2259-2266.

66. Vorotilov, K. A. *Thin Solid Films.* **207** (1992) 180-184.

67. Feuersanger, A. E. *Proc. IEEE.* Dec (1964) 1463-1465.

68. Ardakani, H. K. *Thin Solid Films.* **248** (1994) 234-239.

69. Leinen, D., Espinós, J. P., and Gonzàlez-Elipe, A. R. *J. Vac. Sci. Technol. A.* **12**(5) (1994) 2728-2732.

70. Chuu, D. S., and Dai, C. M. *Phys. Rev. B.* **45**(20) (1992) 805.

71. Forro. L., Chauvet, O., Emin, D., Zuppiroli, L., Berger, H., and Lévy, F. *J. Appl. Phys.* **75**(1) (1994) 633-635.

72. Yoko, T., Yuasa, A., Kamiya, K., and Sakka, S. *J. Electrochem. Soc.* **138**(8) (1991) 2279-2285.

73. Könenkamp, R., and Henninger, R. *Appl. Phys. A* **58** (1994) 87-90.

74. Dislich, H., and Hinz, P. J. *J. Non-Cryst-Solids.* **48** (1982) 11-16.

75. Shroeder, H., *Physics of Thin Films.* 5 Academic Press New-York (1969) 87.

76. Jones, R. W. *Fundamental Principles of Sol-Gel technology* Institute of Metals (1989)

Chapter 3

Theoretical Background

3.1 Introduction

In this work attempts have been made to give physical interpretation of experimental results. This chapter is devoted to the theories that are used for this purpose. Optical absorption and DC conduction in semiconducting materials are reviewed. Attention is drawn to current thinking on the dye sensitised (IO) heterojunction photovoltaic cell function. Current transport and the processes of photocarrier generation and charge transfer are described as well as the assessment methods used to evaluate the cells performance.

3.2 Optical Absorption

The process of optical absorption in semiconductors can be interpreted using band theory[1,2]. If light is incident on a crystalline semiconductor, optical absorption will take place when an electron is promoted from the valence band to the conduction band of the semiconductor.

The minimum amount of energy required for the transition is given by the expression;

$$E_g = h\upsilon_g = \frac{hc}{\lambda_g} = E_c - E_v \qquad\qquad 3.1$$

where E_g is the fundamental energy band gap, E_c, E_v the conduction and valence band respectively, υ_g and λ_g are the frequency and wavelength of the incident electromagnetic radiation respectively and h is Planck's constant. Therefore, for absorption to occur the energy of the incident photon must be greater than or equal to the energy of the band gap i.e. $h\upsilon_g \geq E_g$. In an absorption spectrum this transition is observed as a sudden increase in absorption at a particular frequency and is commonly termed the 'fundamental absorption edge'. Figure 3.1 is a plot of optical density as a function of wavelength in microns for clear rutile titanium dioxide[3], where the absorption edge at $0.41\mu m$ is clearly visible.

In crystalline semiconductors there are two types of optical transition processes that can occur at this edge, direct and indirect. In a direct transition the interaction of a photon leads to the vertical transition of an electron from the maximum of the valence band to the minimum of the conduction band, as shown in Figure 3.2 (a). If the formation of excitons (electron-hole interaction) is disregarded then a theoretical calculation of the probability for direct transitions gives the well known power law dependence of the absorption coefficient as a function of photon energy [4,5] ;

$$\alpha(\omega) = \frac{B(\hbar\omega - E_o)^\delta}{\hbar\omega} \qquad\qquad 3.2$$

where $\alpha(\omega)$ is the absorption coefficient as a function of optical angular frequency ω, B is assumed to be constant in the optical frequency range, E_o is the optical band gap, ($\hbar = h / 2\pi$), and δ is the power index which describes the nature of electronic transitions. The value of δ can take on two values depending on whether the transition is a direct allowed transition or a direct forbidden transition, in which case $\delta = 1/2$ or $3/2$ respectively.

Conversely an indirect transition occurs when the photon interacts with phonons in order to conserve momentum i.e. the wavevector k. The main role of the phonon is therefore to transfer momentum. As the photon is absorbed, one or more phonons are simultaneously absorbed or emitted. In a semiconductor exhibiting this type of behaviour, the maximum in the valence band and minimum in the conduction band occur at different values of k, with the absorbed/emitted phonons providing the necessary change in momentum (Figure 3.2(b)).

Calculations of transition probabilities therefore reveal[5] that the absorption coefficient for an indirect transition is the sum of both these absorption and emission processes, the first and second term respectively in the formula;

$$\alpha n \hbar \omega = \frac{\left(\hbar \omega - E_o + h \upsilon_{ph} \right)^{\delta}}{\exp\left(h \upsilon_{ph} / kT \right) - 1} + \frac{\left(\hbar \omega - E_o - h \upsilon_{ph} \right)^{\delta}}{1 - \exp\left(-h \upsilon_{ph} / kT \right)} \qquad 3.3$$

where n is the refractive index. k is the Boltzmann constant and υ_{ph} the phonon frequency, all other terms being defined previously.
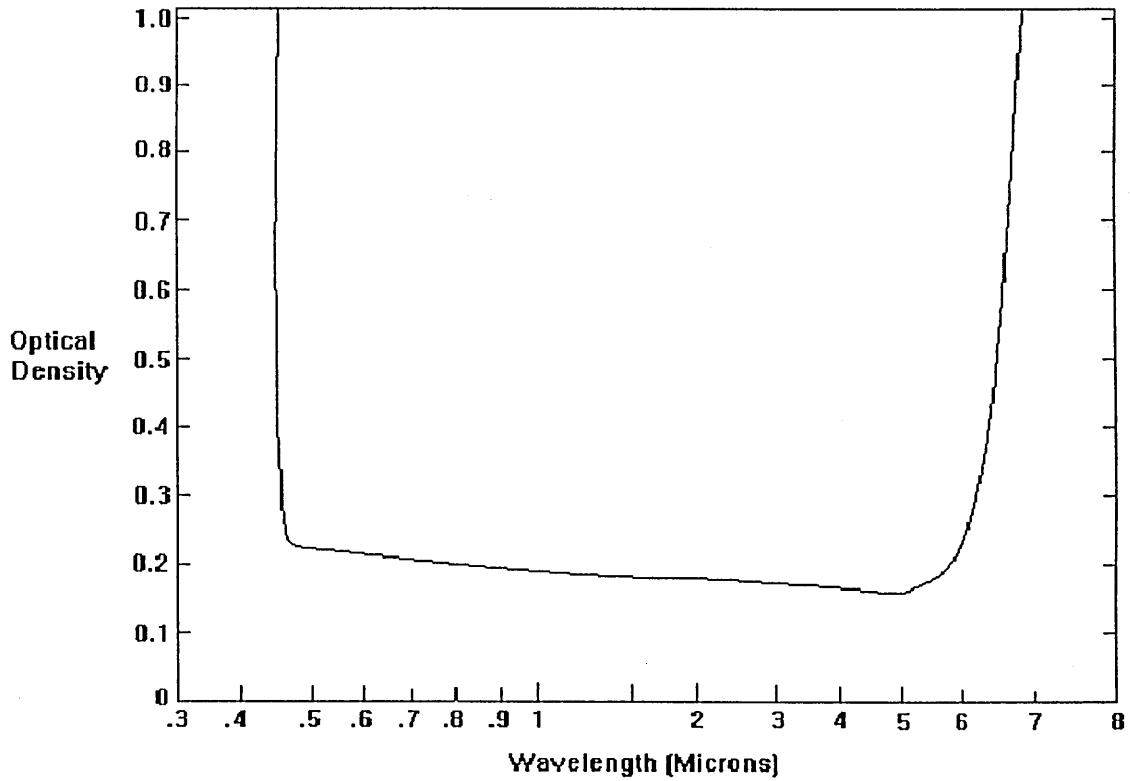
Figure 3.1. Optical density of pure clear rutile titanium dioxide at 4°K. The fundamental absorption edge is seen clearly at ~0.41μm. After Grant (1959)[3]

(a)   (b)
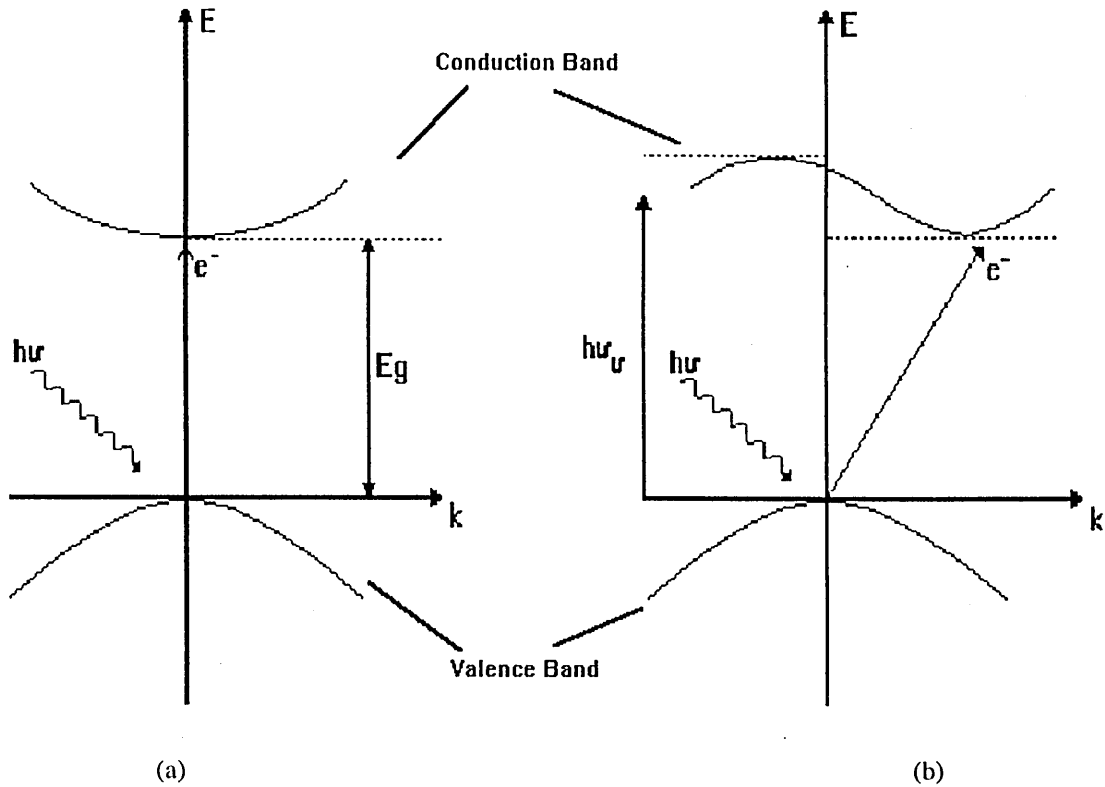
Figure 3.2. Photon absorption by (a) a direct gap semiconductor; where the conduction band minimum and valence band maximum are at the same value of k. (b) an indirect gap semiconductor; where the valence band maximum occurs at different values of k to the conduction band minimum.

40

Again values of δ denote whether the transitions are allowed or forbidden, (2 and 3 respectively).

In amorphous materials the fundamental edge is often observed as a gradual increase in absorption sometimes extending over several eVs[5]. This edge is described as an Urbach edge after Urbach(1953)[6]. A dependence of this type has been observed in both crystalline and non-crystalline materials for example, anatase TiO_2[7] and amorphous $GaAs$[8]. Within the Urbach region the absorption coefficient has an exponential dependence on photon energy given by[6];

$$\alpha(\omega) = \alpha_0 \exp\left\{-\frac{\gamma(E_o - \hbar\omega)}{kT}\right\}$$ 3.4

where γ is a temperature dependent parameter and T the absolute temperature. Although this exponential behaviour has been observed in many materials, its origin remains controversial The equation predicts that $\ln(\alpha)$ is proportional to $\hbar\omega$, Figure 3.3 is an example of this dependence observed in amorphous vanadium tellurite (V_2O_5-TeO_2) blown films[9].

For photon energies above the exponential tail[10] (or Urbach tail) amorphous semiconductors have been observed to obey equation (3.2) for $\alpha(\omega) > 10^4 m^{-1}$. Assuming a parabolic density of states ($N(E) \propto E^{1/2}$) the exponent δ is predicted to be equal to 2. Mott and Davis[11] have assumed a linear function of density of states N(E) as depicted in Figure 3.4.

41
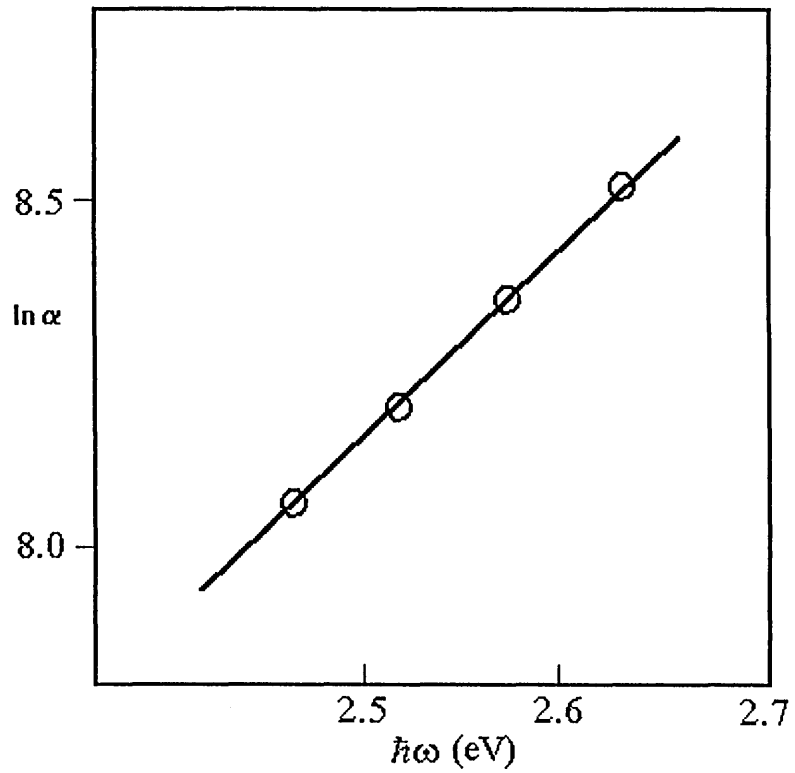
Figure 3.3. A plot of ln α Vs $\hbar\omega$ for V_2O_5-TeO_2 amorphous blown films. V_2O_5 content (10mol%) TeO_2 content (90mol%). (After Chopra[9] 1990)
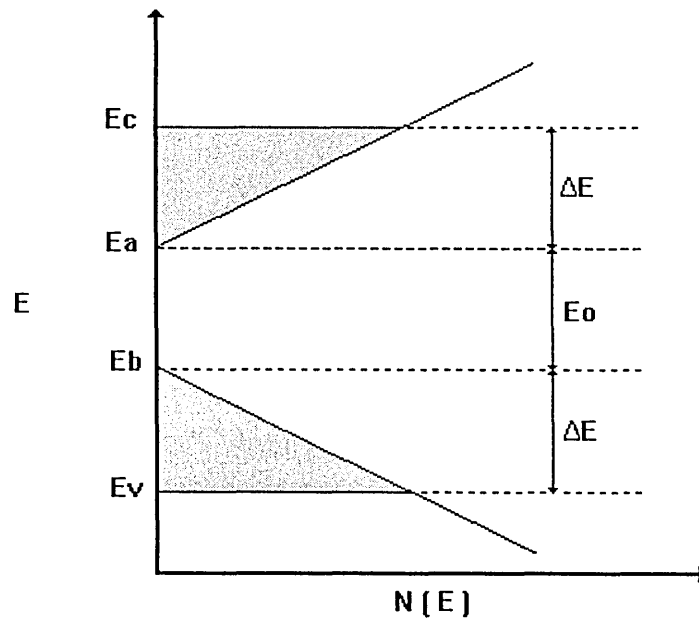
Figure 3.4. The density of states N(E) as a function of energy E in amorphous semiconductors (according to Mott and Davis[11] 1979). ΔE is the range of localised states, E_o the optical band gap.

In this case an equation similar to (3.2) was derived where a quadratic dependence of $\alpha(\omega)\hbar\omega$ on $\hbar\omega$ may be obtained, the assumption is that all transitions where both the initial and final states are localised are neglected. Assuming that the probability of transitions between localised states is the same as other transitions then a cubic relation can be observed,

$$\alpha(\omega) = \frac{C(\hbar\omega - E_o)^3}{\hbar\omega}$$ 3.5

Where $C = (4\pi\sigma_o / 3nc) / (\Delta E)^2$ 3.6

c is the speed of light, σ_o the metallic conductivity and ΔE the range of localised states. For some materials such as binary vanadate glasses[12] this relation has been found to provide a better fit to experimental data.

3.2.1 Organic Semiconductors

At this point careful consideration must be given to the case of optical absorption in organic semiconductors such as the metallophthalocyanines. The models already discussed can be used to interpret the absorption properties of inorganic semiconductors yet caution must be taken when applying such models to organic semiconductors.

It has been noted that in inorganic semiconductors the absorption of light involves the transition of an electron from the valence band to the conduction band . The strong ionic or covalent bonds between atoms of the lattice forming the energy bands. A distinct

optical energy gap is observed, as depicted in Figure 3.5. This model first proposed by Mott-Wannier[13] may be applied to semiconductors whose dielectric constant is large. For organic semiconductors this is often not the case and the model proposed by Frenkal[14] is adopted.

In the Frenkal model light absorption is considered to be a molecular process due to the weak Van der Waals forces that bond the molecules together. Photon absorption results in discrete transitions between the ground state and the excited electronic states of the free molecule. The result is the formation of an 'excition', (or tightly bound electron-hole pair) as shown in Figure 3.6. The energy gap of a transition is therefore a molecular property and is characteristic of molecular structure. The band gap energy of the organic semiconductor refers to the energetic gap between the HOMO (highest occupied molecular orbital) and the LUMO (lowest unoccupied molecular orbital). Heavy doping of organic semiconductors may increase their dielectric constant and consequently the Mott-Wannier model can become applicable.[13]

3.2.2 Computation of Optical Band Gap, E_o

Calculation of the optical band gap can be determined using equation (3.2). The slope of a linear plot of $(\alpha\hbar\omega)^{1/\delta}$ against $\hbar\omega$ will give the optical band gap E_o, the value of the absorption coefficient is calculated from a knowledge of the sample absorbance and thickness, the value of δ however must be assumed. This assumption of δ has resulted in conflicting values of E_o for similar materials[15].

Empty Conduction Bands

←—● Electron

Eg=hν

Hole ○ —→
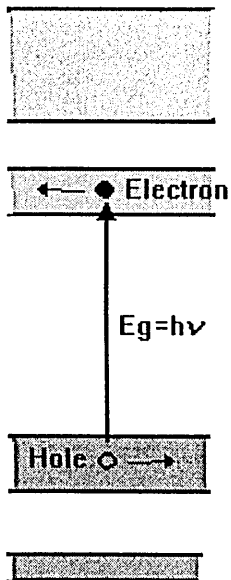
Filled Valence Bands

Figure 3.5. Distinct energy levels of an inorganic semiconductor.

2

Excited Electronic
States

ΔE=hν

1

} Vibrational States

0
Ground Electronic State
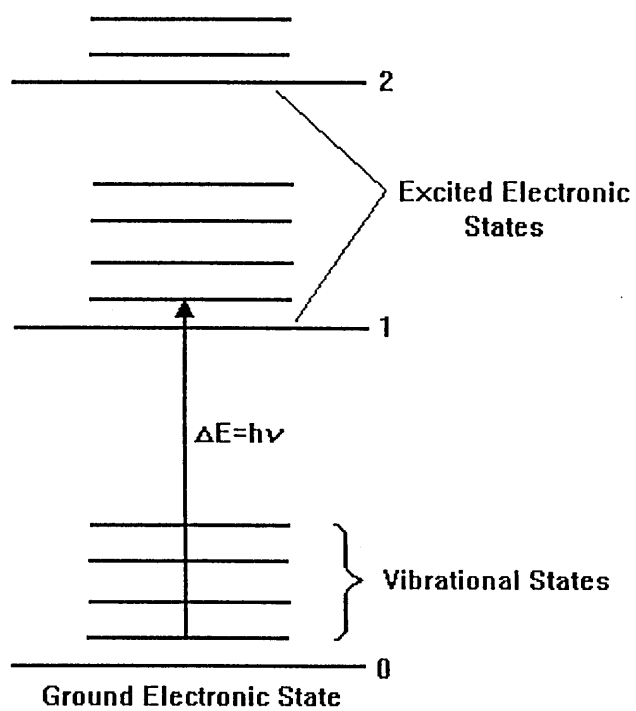
Figure 3.6. Electronics states of an organic (molecular) semiconductor.

45

An alternative technique was developed by Ray and Hogarth[15] to allow the determination of E_o and δ simultaneously from the absorption data, obviating the need for an assumption of the optical transition processes occurring in the material. This alternative method, described in more detail below is particularly useful as the thickness of the film is not required to deduce these optical parameters.

The absorption coefficient $\alpha(\omega) = \ln(\phi_o/\phi)/t$, where t is the material thickness and ϕ_o and ϕ are the intensities of incident and transmitted light respectively. If the substitution $Y=Ln(\phi_o/\phi)\hbar\omega$ for absorption coefficient is made into the power law (equation (3.2)), then a modified version of the power law is obtained given as;

$$Y = C(\hbar\omega - E_o)^{\delta} \qquad\qquad 3.7$$

C is a constant coefficient for a given material thickness yet it is dimensionally different from B in equation (3.2). Taking the derivative of Y with respect to ω, then Y/Y' becomes;

$$\frac{Y}{Y'} = \frac{C(\hbar\omega - E_o)^{\delta}}{\delta C(\hbar\omega - E_o)^{\delta-1}} = \frac{(\hbar\omega - E_o)}{\delta} \qquad\qquad 3.8$$

From this equation it can be observed that a plot of Y'/Y against $\hbar\omega$ will be linear and reveal δ and E_o/δ as the gradient and intercept respectively. Y' can be calculated using the midpoint difference rule.

46

3.2.3 Computation of t, α and n.

In the case of a thin film on a non-absorbing substrate, if the film thickness is homogeneous and of the same order of magnitude of the wavelength of the incident visible light, it is possible to observe oscillating curves in the transmission spectra caused by interference effects due to multiple reflections. In 1976, Manifacier[16] and co-workers proposed a method of calculating the optical constants and thicknesses of thin weakly absorbing dielectric films surrounded by non-absorbing media from these transmission interference patterns. Later, work by Swanepoel[17] developed the method further showing that an accuracy in the order of 1% for thickness t, absorption coefficient $\alpha(\lambda)$ and refractive index $n(\lambda)$ could be achieved.

This technique presents a number of advantages over the conventional method that requires detailed computer iteration procedures using both the transmission and reflection spectra. A particular advantage is that an assumption of the film refractive index n is not required to determine the film thickness, t and vice versa. In fact a variety of optical constants as well as the film thickness are derived directly from the same transmission spectra. The following is a brief review of this technique in relation to these studies, for a more detailed theoretical interpretation the reader is referred to Manifacier[16] (1976) and Swanepoel[17] (1983).

The theory is designed for use on a system in which a thin film is coated onto a transparent substrate as shown in Figure 3.7.
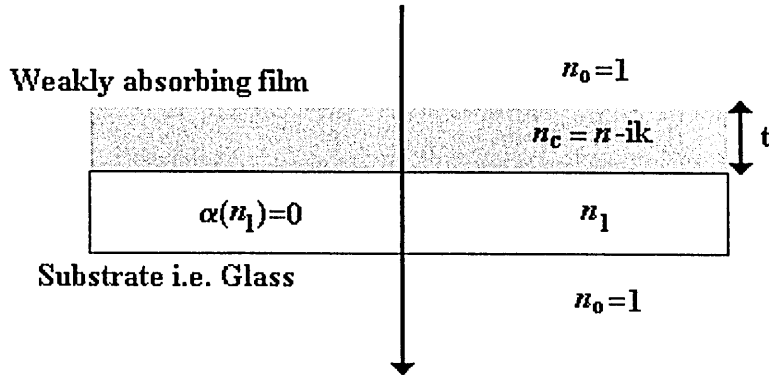
Figure 3.7. System of a thin film on a thick finite transparent substrate. Placed at normal incidence to a beam. t is the film thickness, k the extinction coefficient. n_0, n_c, n, n_1 are the refractive indices of air=1, film (complex), film(real) and glass respectively. $\alpha(n_s)=0$ is the absorption coefficient of the glass.
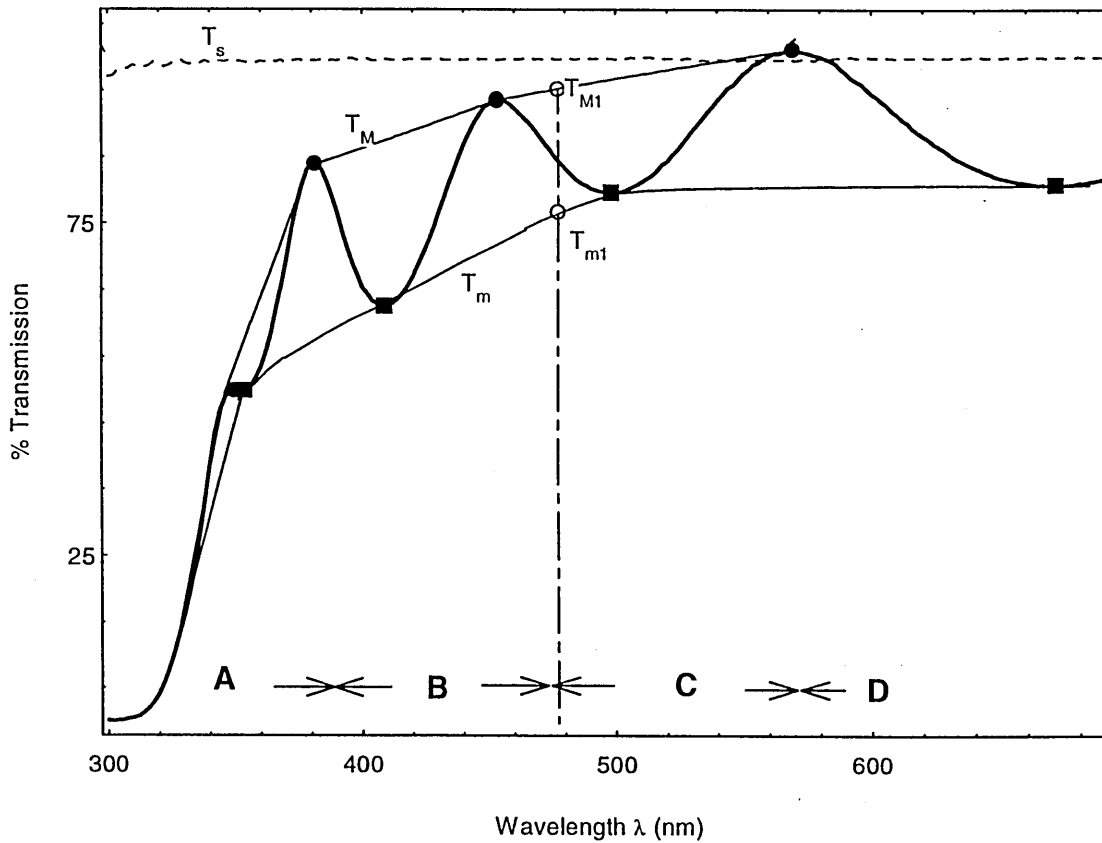
Figure 3.8. Typical Transmission interference fringe observed for the TiO_2 Sol-Gel films on a glass substrates showing T_m. T_M T_s . T_{m1}, and T_{M1}. For regions A-D refer to Table 3.1.

48

Assuming the film, glass and surrounding air are homogenous and optically isotropic, the complex refractive index of the film $n_c(\lambda)$ is given by;

$$n_c(\lambda) = n(\lambda) - ik(\lambda)$$ 3.9

where $n(\lambda)$ is the film refractive index and $k(\lambda)$ is the extinction coefficient given by;

$$k = \frac{\alpha\lambda}{4\pi}$$ 3.10

Consideration of the effects of multiple interactions and transmissions that occur at all three interfaces leads to a complex function for the transmission, (T) which in the case of this optical system is given by Heavens[18];

$$T = T(\lambda, n_s, n, t, \alpha)$$ 3.11

where n_s is the substrate refractive index and all other symbols have been previously defined. For the substrate alone the well known[10] expression for an interference free transmission spectrum, (T_s) is given by;

$$T_s = \frac{(1-R)^2}{1-R^2}$$ 3.12

R is the reflection coefficient and is equal to ;

$$R = \left[\frac{(n_s - 1)}{(n_s + 1)} \right]^2$$ 3.13

Substitution of R into T_s gives;

$$T_s = \frac{2n_s}{n_s^2 + 1}$$
3.14

$$\text{or } n_s = \frac{1}{T_s} + \left(\frac{1}{T_s^2} - 1\right)^{\frac{1}{2}}$$
3.15

The refractive index of the substrate $n_s(\lambda)$ can therefore be determined from experimentally determined values of the interference free $T_s(\lambda)$.

If n_s is known, the complex function in equation (3.11) may be rewritten in terms of $n(\lambda)$ and the absorbance $A(\lambda)$;

$$T = T(n,A)$$
3.16

where $A(\lambda)$ is the absorbance. Making the assumption that k=0 over the visible spectrum, equations were derived to represent T_M and T_m, the maximum and minimum extremes of the interference fringes[16]. These are shown as two curves representing the continuous functions T_m and T_M in Figure 3.8. For a particular wavelength λ_1, T_{m1} has a corresponding value T_{M1}.

Swanepoel[17] divided the spectrum into 4 regions outlined in Table 3.1. In the region of strong absorption the refractive index, n must be determined by extrapolation of previous calculated values of n in other parts of the spectrum as in this region fringes do not occur.

For the transparent region the transmission at the maxima of the interference fringes T_M coincides with T_s the substrate transmission. From Swanepoel[17] the refractive index, n may then be calculated according to the formula;

$$n = \left[M + \left(M^2 - n_s^2 \right)^{\frac{1}{2}} \right]^{\frac{1}{2}}$$

3.17

where M is defined as;

$$M = \frac{2n_s}{T_m} - \frac{n_s^2 + 1}{2}$$

3.18

When the maxima T_M begins to fall away from T_s, (i.e. as the wavelength decreases), absorption begins to take place. It is this region (the weak to medium absorption region) that is usually of most interest. For the calculation of refractive index $n(\lambda)$, values of T_m and the corresponding values of T_M must be obtained for a variety of wavelengths.

It is usual to determine values of T_m and T_M between experimentally determined points, with interpolation between 3 nearest points being used to allow the determination of these intermediate values. As n_o (the refractive index of air) and n_s are known, the refractive index of the film n_1 can be calculated according to the formulae;

$$n_1 = \left[N + \left(N^2 - n_o^2 n_s^2 \right)^{1/2} \right]^{1/2}$$

3.19

$$\text{where} : N = \frac{n_o^2 + n_s^2}{2} + 2n_o n_s \frac{T_M - T_m}{T_M T_m}$$

3.20

n_1 is a first approximation to the refractive index. This accuracy may be improved after determination of the film thickness, t.

If n_{c1} and n_{c2} are the refractive indices at two adjacent maxima or minima located at λ_1 and λ_2 respectively. Considering the basic equation for interference fringes

$$2nt = m\lambda \qquad\qquad 3.21$$

where m is an integer for a maxima and a half integer for minima, the thickness t can be determined from the equation;

$$t_1 = \frac{\lambda_1 \lambda_2}{2(\lambda_1 n_{c2} - \lambda_2 n_{c1})} \qquad\qquad 3.22$$

Equation (3.22) is very sensitive to errors in the refractive index and therefore results in an inaccurate estimation of t. However this initial estimate t_1 can be used with the initial estimate of n_1 (determined from equation (3.19)) in equation (3.21) to obtain a value m_o. Taking the nearest integer or half integer of m_o and using n_1 in equation (3.21) a new value of the thickness t_2 can be calculated. The more accurate determination of n can then be found by again using equation (3.21) and the new values of m_1 and t_2 to estimate n_2.

n_2 can be determined accurately for a variety of wavelengths. The new value of n_2 can be plotted against $1/\lambda^2$, fitted to a linear function using the method of least squares and extrapolated to shorter wavelengths in the region where the transmission fringes disappear. The result is an accurate knowledge of the refractive index for a wide range of

wavelengths. The absorption coefficient may then be calculated according to the equation

$$A \propto \exp(-\alpha t)$$
3.23

where from Swanepoel[17], A(λ) can be determined in a variety of ways with the suggested method being to use values of T_M according to;

$$A = \frac{E_M - \left[E_M^2 - \left(n^2 - 1\right)^3 \left(n^2 - n_s^4\right)\right]^{\frac{1}{2}}}{\left(n-1\right)^3 \left(n - n_s^2\right)}$$
3.24

$$\text{where}: E_M = \frac{8n^2 n_s}{T_M} + \left(n^2 - 1\right)\left(n^2 - n_s\right)$$
3.25

Finally once $\alpha(\lambda)$ is known if required k(λ) can be determined using equation (3.10).

53

Region	α	Absorption	Cause of Transmission effects
A	Very strong	Strong	Almost entirely due to α of the film
B	Large	Medium	Mainly due to α
C	Small	Weak	α has limited effect on T
D	=0	Transparent	Determined by n and n_s through multiple reflections

Table 3.1. Division of transmission spectrum according to Swanepoel[17] (1983). A-D refer to regions as depicted in Figure 3.8.

3.3 DC Conduction

3.3.1 Density of States

The models used in interpreting electrical data depend on whether the semiconductor is amorphous, polycrystalline or crystalline. The material structure also determines the form of the density of states (or energy levels) at the band edges which in turn determines the electrical transport properties It is therefore worth reviewing the major differences in the variation of density of states N(E) (or the number of states per unit volume) with electron energy (E), that have been proposed for both amorphous and crystalline semiconducting materials.

Crystalline semiconductors have a well defined forbidden gap due to the sharp band edges at the valence and conduction bands. This is a direct result of the inherent lattice periodicity and the short and long range atomic order[19]. The density of states N(E) is proportional to $E^{1/2}$ as shown in Figure 3.17 (a). Amorphous materials have been observed to have some short range order although long range order is lost[19]. Nevertheless, some of the features of the electronic band structure that apply to crystalline materials may be applied to both polycrystalline and amorphous materials. In non-crystalline materials the $N(E) \propto E^{1/2}$ relationship is not expected. Mott and Davis[5] assume a $N(E) \propto E^{s}$ relationship where s can be determined experimentally.

A number of models have been proposed for the density of states in amorphous materials. All are based on the concept of localised states in the band tails.

Of the most widely recognised are the Davis-Mott[11] model in which a distinct energy gap is identified and the Cohen-Fritzsche-Ovshinsky (CFO)[20] model, in which an overlapping of valence and conduction band tails is proposed. In the CFO model the Fermi level is pinned in the centre of the overlap, the tail overlap being a consequence of the large disorder in the semiconductor as shown in Figure 3.17 (b). This leads to a relatively high density of states in the middle of the gap. However sharp absorption edges have been observed in truly non-crystalline materials e.g. in V_2O_5 amorphous thin films.[21] This suggests that an overlapping of conduction and valence band tails does not occur. Nevertheless, the concept of a mobility gap rather than a well defined 'forbidden gap' which evolved from this model is now widely accepted for amorphous semiconductors. The mobility gap (depicted in Figure 3.17 (b)) was derived from the concept of a mobility edge introduced by Mott[22].

The Davis-Mott model[11] is one of the most widely used models for amorphous semiconductors[23]. One of the most significant differences to the CFO model being the introduction of a defect level in the middle of the gap and localised tail states which extend less into the mobility gap as shown in Figure 3.17 (c). From this model at least three conduction processes have been proposed, which are dependent on the temperature regime. At low temperatures thermally assisted tunnelling between states at the Fermi level is responsible for conduction. At intermediate temperatures, charge carriers are excited into the localised states of the band tails and the carriers in these localised states are transported by hopping. At high temperatures carriers are excited across the mobility gap into the extended states.

3.3.2 Metal-Semiconductor Contacts

The type of contact made to a semiconducting and/or insulating material is of extreme importance in determining whether the observed conduction process is barrier or bulk limited[24] It is therefore worth mentioning at this point the various types of metal-semiconductor contacts.

The type of contact made to a semiconducting material is dependent on the relative workfunctions of both the metal (ϕ_m) and the semiconductor (ϕ_s) under investigation[1-2]. The work function (ϕ) is simply the energy required to remove an electron from the Fermi level to the vacuum outside the material. In general two types of contact can be formed, the rectifying (otherwise known as the blocking or Schottky barrier) and the ohmic contact. Table 3.2 summarises the conditions required for both ohmic and rectifying contacts depending on the type of semiconductor.

If $\phi_m = \phi_s$ a third type of contact is formed called a neutral contact. In this case the vacuum and Fermi levels align without charge transfer. No space charge exists and in the energy band diagram no band bending is present. Simmons[24] described this type of contact as effectively a transitional stage between ohmic and rectifying.

(a)

(b)

(c)
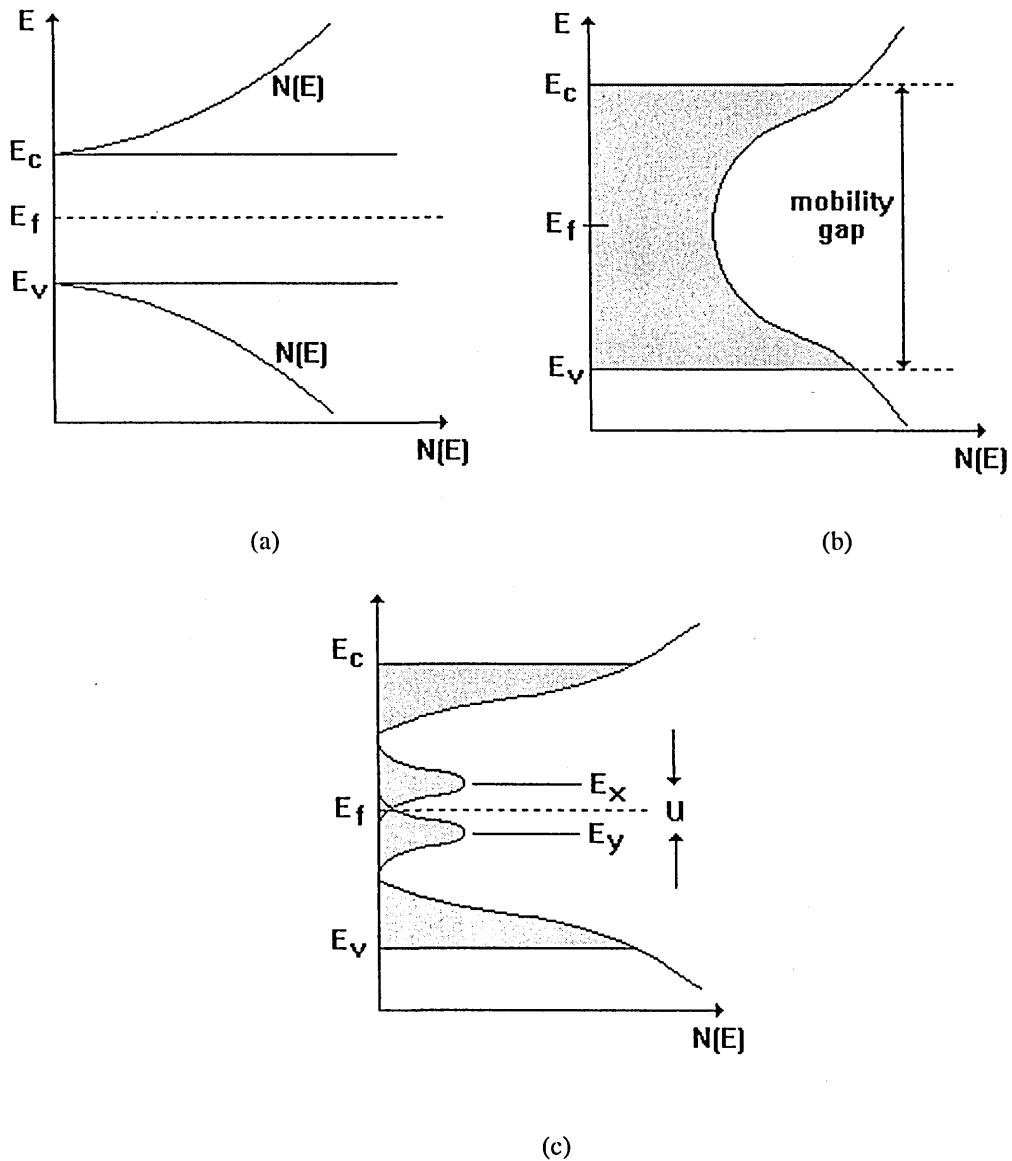
Figure 3.17. (a) Density of states N(E) in a crystalline semiconductor (n-type) at room temperature.

(b) The CFO model of overlapping valence band and conduction band tails.

(c) Proposed Davis-Mott[11] model for the density of states of an ideal amorphous semiconductor showing a real gap and overlapping bands of donor and acceptor levels $(U=E_x-E_y.)$ Where E_f, E_c, and E_v, represent the energy (E) of the Fermi level, conduction band, valence band respectively.

Type of Contact → Type of Semiconductor ↓	Rectifying	Ohmic
n-type	$\phi_m > \phi_s$	$\phi_m < \phi_s$
p-type	$\phi_m < \phi_s$	$\phi_m > \phi_s$

Table 3.2. Conditions of the respective work functions of metal(ϕ_m) and semiconductor(ϕ_s) for the formation of either rectifying or ohmic contacts.

3.3.3 Temperature Dependent DC Conductivity

Electrical conduction suggests that on application of an external electrical field there will be a net transport of charge carriers within the material. In crystalline extrinsic semiconducting materials this transport is assumed to be due to free carriers and conductivity is simply the sum of the number of available carriers n, p, the corresponding charges e, and mobilities μ;

$$\sigma = n|e|\mu_e + p|e|\mu_h \qquad\qquad 3.26$$

where σ is the conductivity ($\Omega^{-1}cm^{-1}$). For an intrinsic semiconductor $n=p=n_i$ (where n_i is the intrinsic carrier concentration) and the equation becomes;

$$\sigma = e(\mu_e + \mu_h)n_i \qquad\qquad 3.27$$

The variation of n, p, μ_e and μ_h with temperature therefore determines the temperature dependence of the conductivity. From a knowledge of the temperature dependence of carrier mobility and carrier concentrations, the total conductivity (σ_{total}) for an extrinsic semiconductor is given as the sum of both the extrinsic and intrinsic contributions[25];

$$\sigma_{total} = \sigma_{oi}\exp\left(-\frac{E_g}{2kT}\right) + \sigma_{oe}\exp\left(-\frac{E_i}{kT}\right) \qquad\qquad 3.28$$

σ_{oi}, σ_{oe} are constants, E_g the energy band gap and E_i is the impurity level excitation energy.

Thus, if the temperature dependence of conductivity is measured, a plot of $\ln\sigma$ against $1/T$ (an ideal case is shown in Figure 3.18) will reveal E_i and E_g from the slope. Where E_i dominates at low temperatures and E_g at higher temperatures.

An analysis of the temperature dependence of the conductivity of organic semiconducting materials is required in order to make an adequate identification of the energy distribution of traps.

The following phenomenological Arrhenius equation is often reported for organic materials[13,26] when the temperature dependence is studied.

$$\sigma = \sigma_o \exp\left[\frac{-E}{kT}\right] \qquad\qquad 3.29$$

where E = activation energy, σ_o = pre-exponential factor. In organic materials the activation energy represents the energy required for thermally-activated hopping of carriers in states near the Fermi level, rather than E_g, which is the energy difference between the occupied valence band and the empty conduction band.
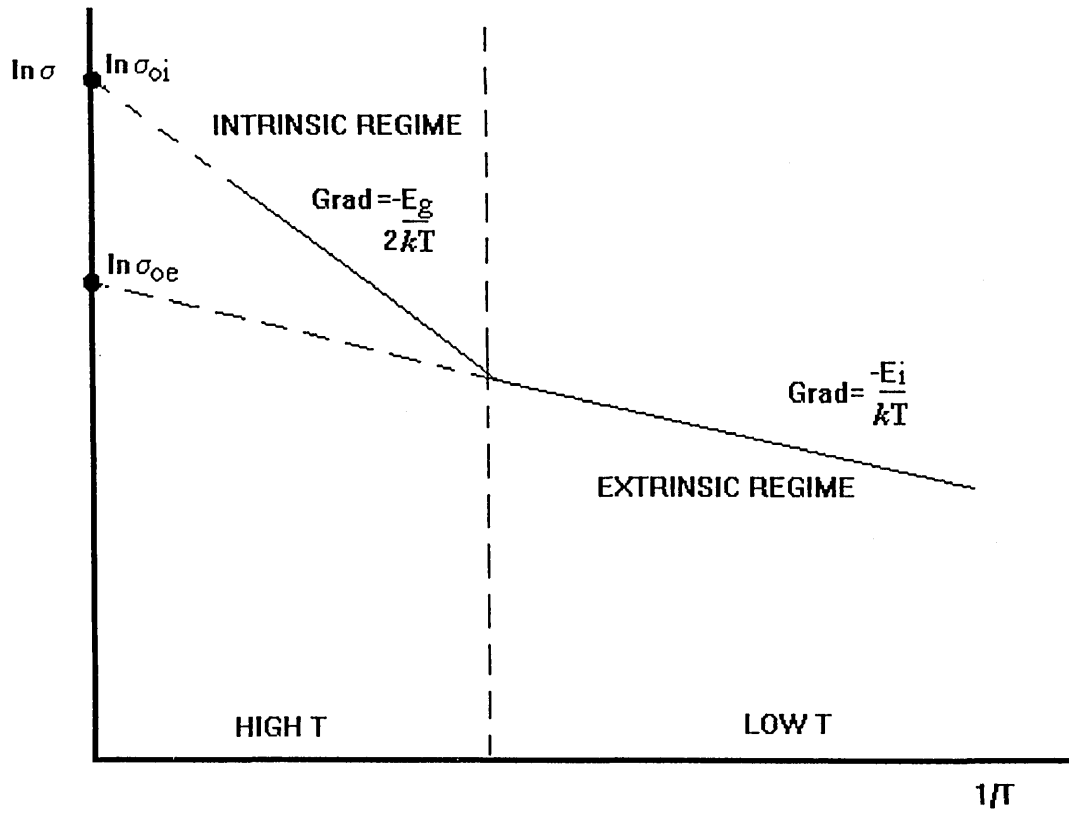
Figure 3.18. Ideal variation of conductivity with reciprocal temperature for an extrinsic semiconductor.

3.4 The N-p (Inorganic:Organic) Heterojunction

The metallo-phthalocyanines (MPcs) and the TiO_2 used in these investigations are regarded as p-type[13,27] and n-type[28] semiconductors respectively. For the purposes of these investigations it is therefore hypothesised that the resulting dye sensitised photovoltaic cells form what could be regarded as an anisotype or N-p heterojunction. (Where the N (TiO_2) material has the wider bandgap.). Analysis of the measured cell characteristics are primarily carried out under the assumption of the formation of such a junction.

Extensive literature exists regarding the theoretical concepts of a wide variety of purely inorganic heterojunctions such as n-CdO/p-CdTe[29], and particularly Si and GaAs based devices[1,2,30]. However, little information exists on the theoretical aspects of junction formation and behaviour as well as charge transport and transfer mechanisms associated with N-p (Inorganic:Organic) or 'IO' heterojunctions. Forrest and So[31] have presented a transport theory, that results in an expression for diffusion-limited current in (IO) heterojunction diodes, from which the barrier energy ϕ_{bp} and ΔE_v may be determined. The IO heterojunction J(V) behaviour was predicted to be more complex than that of its inorganic counterpart, and identified the existence of three working regimes which were dependent on the applied biases (see section 3.4.4). Antohe[32] has confirmed this behaviour in a study of In/PTCDI/p-Si and Ag/CuPc/p-Si diodes. However, generally relatively little experimental evidence exists in support of this model.

The following is a brief review of heterojunction physics and analysis in relation to photovoltaic applications. Current thinking on the mechanisms responsible for charge

generation, transport and transfer in IO heterojunctions for the purposes of these investigations are also reviewed. For more detailed interpretation the reader is referred to the texts of Wang[1], Tyagi[2], Forrest and So[31], Sakata[33], Antohe[34,35] and Hovel[36].

3.4.1 Photocarrier Generation and Charge Transfer

The processes of photocarrier generation particularly in MPcs has been reviewed by Simon and Andre[13]. The mechanisms available to describe photogeneration of carriers in molecular semiconductors, can be classified into two basic groups, those which involve the dissociation of excitons and those which do not as summarised in Table 3.3. In phthalocyanines the photogeneration of free electron hole pairs is usually described by an exciton-dissociation process. Direct photogeneration is rarely observed[37]. The absorption of a photon creates a loosely bound exciton which then dissociates at either a free surface or at some internal dissociation centre e.g. an impurity.

Dye sensitisation is usually described as the process by which absorbed dyes are photoexcited and then inject electrons or holes into the semiconductor onto which they are absorbed[38-40]. (i.e. the process of photocarrier generation and charge transfer).

Although several models[40] have been proposed to explain the processes of charge separation and transfer the detailed mechanisms of dye sensitisation are still not well established. Dye-sensitisation systems have been investigated by Sakata[40]. Experimental observations of Rhodamine/ZnO systems strongly suggest the direct electron transfer from the excited dye to the conduction band of the oxide semiconductor as the most likely sensitisation process, depicted in Figure 3.19.

A model for the electron transfer rate from the excited dyes to the conduction band of the semiconductor was proposed, in which the electron transfer rate is dependent on the electron exchange energy υ, the normalised state density ρ_o and the energy difference between the energy level of the excited dye and the bottom of the conduction band of the oxide semiconductor ΔE. The electron transfer rate K_{et} is then expressed as;

$$K_{et} = \frac{2\pi}{\hbar}\upsilon^2\rho_o(\Delta E - \lambda) \qquad\qquad 3.30$$

where

$$\rho_o(E) = \rho(E)/N \qquad\qquad 3.31$$

$\rho(E)$ is the state density and is proportional to N the number of atoms or molecules of the oxide semiconductor.

The mechanism was further reviewed by Takada[41] in which the complete charge generation and separation of carriers for IO heterojunction was considered. The photoinduced exciton in the organic semiconductor diffuses to the heterointerface due to the built in electric field and donates its excited electron directly into the conduction leaving a free hole in the valence band of the organic semiconductor.

Further mechanisms include energy transfer from the excited dye to the surface states followed by electron (or hole) injection from the excited states and electron transfer from the excited dye to the surface states and from surface states to the continuum of the semiconductor.[40]

Dissociation processes	1. Exciton dissociation at electrode/semiconductor interface
	2. Exciton dissociation due to interaction of excitons and trapped carriers
	3. Exciton dissociation due to interaction of excitons and impurities
Non-dissociation processes	1. Direct excitation of trapped carriers into CB or VB
	2. Direct band to band transitions

Table 3.3. Processes of photocarrier generation in molecular solids after Nespurek (1993)[37]
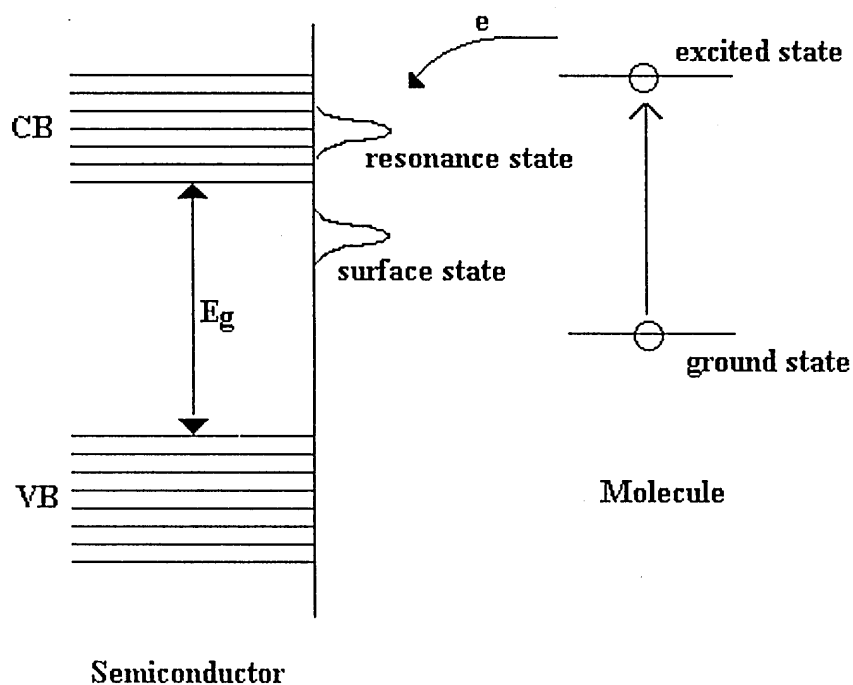
Figure 3.19 Dye sensitised electron transfer. Dyes are photoexcited under illumination to create excitons which dissociate at the IO heterointerface. Electrons transfer from the excited dye to the conduction band. According to Sacata's model of electron transfer (1990).[40]

3.4.2 Energy Band Diagram

From the Anderson model[42] which assumes no interfacial layer between the two materials and no interface states, it is possible to construct an energy band diagram for an ideal N-p heterojunction. It is the work function ϕ_1, ϕ_2, (difference between the vacuum level E_{vac} and the Fermi level, E_f), the electron affinity χ_1, χ_2 (difference between E_{vac} and conduction band edge E_c) and the band gap energies of the two semiconductors, E_{g1}, E_{g2} that determines the band diagram and the depletion region[1,2,36]. The built in potential ϕ_{bp} which arises between the p-type and N-type neutral regions is calculated from the difference in the work functions of the two materials, $(\phi_1 - \phi_2)$ which is equivalent to the sum of voltages that appear across the two semiconductors (i.e. $V_{b1} + V_{b2}$). At equilibrium the Fermi levels are aligned $E_{f1} = E_{f2}$ and are constant throughout the device.

The essential difference between a p-n homojunction and the p-n heterojunction is the formation of a discontinuity in the conduction band due to the difference in energies of the conduction band edges in the two materials. The discontinuity ΔE_c may be calculated from the difference in electron affinities according to:

$$\Delta E_c = \left| \chi_2 - \chi_1 \right| \qquad\qquad 3.32$$

Similarly the hole affinity difference can be used to determine the offset at the valence band edge ΔE_v and is given by;

$$\Delta E_v = \left| E_{g2} + \chi_2 - E_{g1} - \chi_1 \right| \qquad\qquad 3.33$$

Figures 3.20 and 3.21 indicate the formation of an energy band diagram constructed for an ideal N-p heterojunction under thermal equilibrium conditions. It is assumed that the transition region between the p and N-type regions is abrupt[1,2,36]. It must be noted that the actual energy band profile for the heterojunction is dependent on the relative values of E_g, χ and ϕ for the two semiconductors and therefore energy band profiles for different heterojunctions differ. A comprehensive description of types of heterojunctions has been given by Milnes and Feucht.[43]

Weakly coupled molecular crystals such as the phthalocyanines are not usually assigned to conventional band diagrams. The value of E_g simply refers to the difference between the HOMO (highest occupied molecular orbital) and LUMO (lowest occupied molecular orbital) rather than a distinct energy band gap. Nevertheless they are a useful aid in describing observed diode characteristics.

A band diagram for an IO heterojunction has been proposed by Anthoe, Tomozeiu and Gogonea[35] based on the organic materials PTCDI and CuPc in conjunction with p-type Si substrates. The proposed diagram includes the presence of an interfacial layer which can be attributed to range of factors such as cross-diffusion, chemical interaction, or surface damage.

In practical heterojunction devices a non-ideal situation occurs which modifies the idealised energy band diagram. In the CuPc/p-Si and PTCDI/p-Si devices the applied voltage V_a was the sum of V_{b1}, V_{b2}, and V_{ss} the voltage drop over the organic, inorganic, and the interfacial region respectively. The determination of a high ideality factor (m) for the Ag/CuPc/p-Si diodes indicated the existence of a high density of interface states.
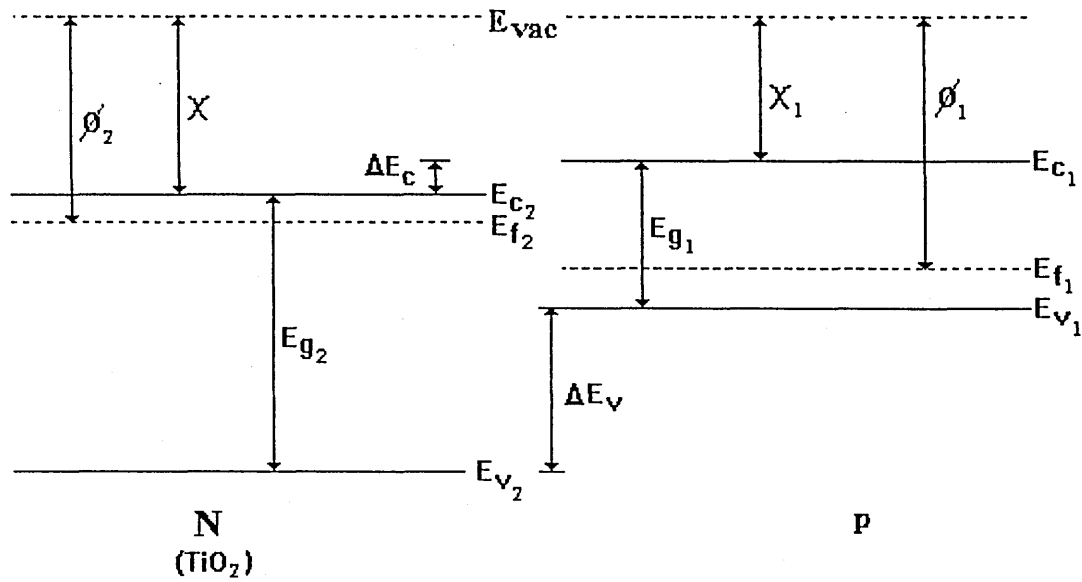
Figure 3.20. Two neutral, isolated semiconductors one N-type one p-type.
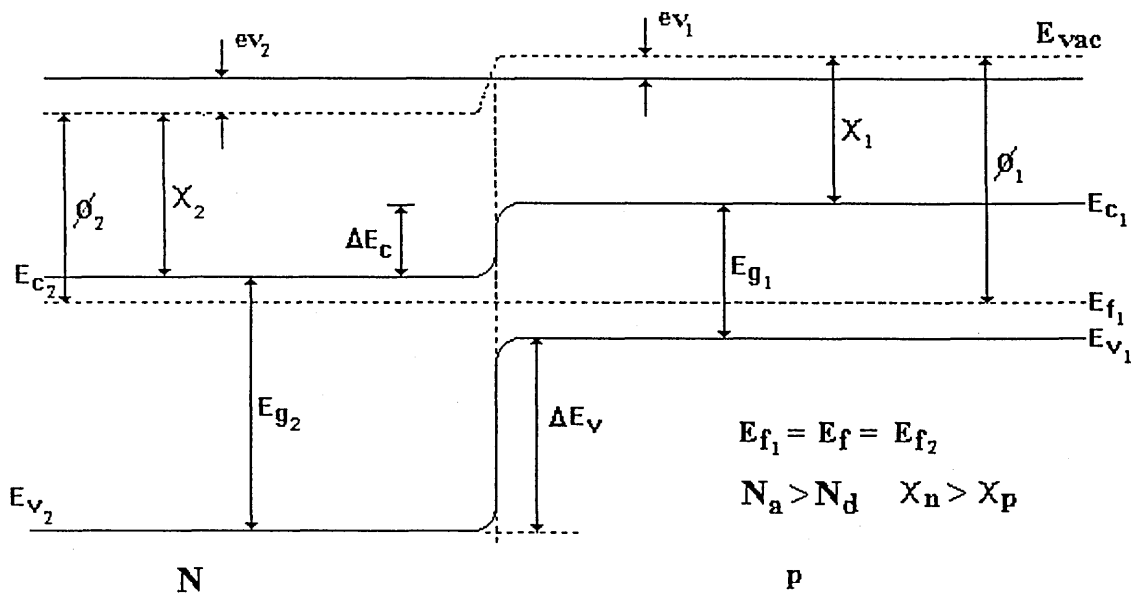
Figure 3.21. Energy band diagram for an ideal anisotype N-p heterojunction after contact has been made. It is assumed that the electron affinity χ of N type is greater than p-type and that the junction is abrupt.

In the current studies on TiO_2/MPc (IO) heterojunctions an energy band diagram for the device has been proposed (chapter 8), based on both available reported data and parameters measured during the course of these investigations.

3.4.3 Spectral Response

Comparison of the dyes absorption spectra with the short circuit (J_{sc}) photocurrent-density action spectra $J(\lambda)$ of dye sensitised cells is a direct indication of the ability of the dye to sensitise the wide band gap inorganic semiconductor to wavelengths outside its intrinsic sensitivity. A $J(\lambda)$ dependence which is similar to $A(\lambda)$ of the dye is strong evidence for spectral sensitisation as demonstrated in the recent photoelectrochemical cells of Shen[44] ($ZnPc/TiO_2$) and Kudo[45] (merocyanine/ZnO).

The spectral response is directly related to the cell's quantum efficiency, Z%. or the ratio of photocurrent collected at each wavelength to the number of photons incident on the surface at that wavelength. Measurements of the devices responsivity allows the calculation of Z according to the law[46];

$$Z = \frac{R h c}{e \lambda_g} \qquad\qquad 3.34$$

where R is the responsivity of the device and is defined as the ratio of photon generated current J_{sc} (A/cm^2) to the watts of optical power incident ϕ (mW/cm^2). λ_g is the wavelength of the incident radiation, and all other symbols have their usual meaning.

Quantum efficiency (Z) gives an indication of the potential of the cell to generate useful charge carriers per incident photon, the higher Z the more ideal the device. Low quantum efficiencies reported in p-n junctions have been attributed to the presence of recombination centres at the heterojunction interface[29]. It is also worth noting that in the literature often the only indication of a cell performance is the quoted maximum quantum efficiency measured for the cell at a specified wavelength and is therefore the only available performance parameter to compare against. Although Z is a useful parameter to indicate the cell potential, quality and aids in device optimisation, it is nevertheless the cell performance over the entire solar spectrum rather than over a small portion of the spectrum which is of most interest. i.e. the overall power conversion efficiency $\eta\%$ rather than Z%.

3.4.4 Current Transport

In a typical p-n heterojunction several current transport mechanisms may be present at the heterointerface[43,47]. These consist of (i) recombination-generation currents (ii) diffusion or emission currents (iii) recombination through interface states at the junction (iv) tunnelling from band states to localised defect states in the band gap across the heterointerface and (v) band to band tunnelling, as depicted in Figure 3.22.

In the case of an abrupt anisotype heterojunction, three models have been proposed to account for current transport.

(i) The Anderson model[42], in which the effects of dipoles and interface states are neglected as well as any recombination-generation within the space charge region. Current transport is believed to be by diffusion of one type of carrier only (electrons or

70

holes) due to the effects of the discontinuities in the band edges at the interface. (ii) Interface recombination as seen in Cu_2S/CdS heterojunctions[48]. and (iii) Tunnelling.[43,47] Heterojunctions are often dominated by a tunnelling current, due to the many energy states that are introduced within the band gap. This form of current transport has been observed as a major contributor to the dark current in heterojunction solar cells.[36]

Ag/CuPc/p-Si and In/PTCDI/p-Si heterojunction diodes have been studied by Antohe, Tomozeiu and Gogonea[35]. The observed temperature dependent J(V) behaviour was explained by a model of transport proposed by Forrest and So[31]. The current transport was believed to be limited by thermionic emission (TE) at low current densities and SCL as the current density was increased. Under low forward and reverse bias the device performance was analogous to a metal-insulator-semiconductor (MIS) structure, (the organic layer's behaviour being similar to a leaky insulator). Under large forward bias the diode behaviour was compared to that of a Schottky diode. In this regime the conduction in the organic film became space charge limited. Under moderate to high reverse bias the device performed in a heterojunction regime, whereby minority carrier generation in the semiconductor substrate was balanced by recombination at the IO heterointerface. The various modes proposed for IO heterojunction operation are shown in Table 3.4.

According to So and Forrest[31], under large reverse bias, the IO heterojunction interface is not strongly inverted due to the poor insulating properties of the organic layer. Charges must either recombine at the interface or diffuse to the ohmic metal contact made to the organic layer surface. A very large reverse current leads to a breakdown in the inorganic layer, after which charge transport is limited by space charge effects in the organic semiconductor.
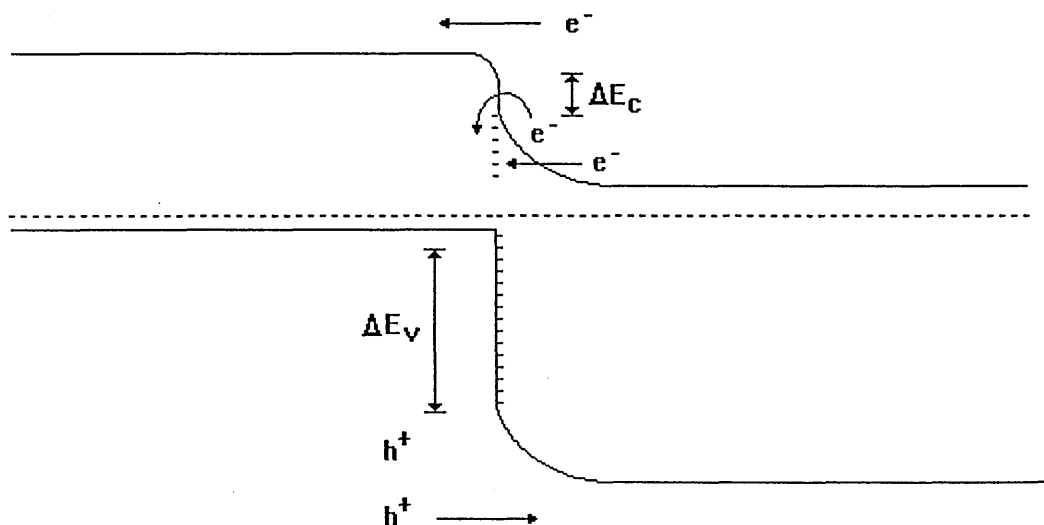
Figure 3.22. Current transport mechanisms in a typical heterojunction diode.

Regime	Voltage Range	Current Density	Organic Conductivity
Schottky	$-V_a \gg \phi_{bp}$	$J > J_s$	Space charge limited
MIS	$\lvert V_a \rvert < E_g/e$	$J < J_s$	Leaky insulator
Heterojunction	$V_a \ll \phi_{bp}$	$J \sim J_s$	Ohmic

Table 3.4 Operating regimes for organic/inorganic semiconductor heterojunctions. After Forrest and So[31]. J_s is the saturation current density, V_a the applied voltage, E_g is the energy band gap of the inorganic semiconductor. The organic conductivity describes the current transporting nature of the organic film.

3.4.5 Dark J(V) Characteristics

The dark J(V) characteristics are determined by the current transport mechanisms and can therefore reveal a great deal of information on the transport properties of the devices. They are also determined by any series or shunt resistances that may arise.

The current voltage characteristics of Schottky or p-n-junction diodes are often assumed to follow the empirical relationship[47];

$$J = J_s \left[\exp\left[\frac{eV}{mkT} \right] - 1 \right]$$
3.35

where J_s is the reverse saturation current density, m is the ideality factor and >1 (or diode quality factor) and is used to indicate the dominant type of conduction mechanism.

Values of m ~1 indicate the dominance of injected current (diffusion) whereas at low injection levels values of m~2 are attributed to recombination mechanisms. The ideality factor m and saturation current density J_s may then be determined from the slope and intercept of a ln(J) against V plot. These factors were therefore measured for the IO heterojunctions manufactured in these studies for dark forward biases.

It has been suggested[49] that this relationship (equation 3.35) cannot physically be realised since the reverse current must be affected by the same mechanisms that makes m>1 for the forward current. As such the term $(-J_s)$ must contain m also. An alternative test of the

ideality of a diode was therefore proposed by Missous and Rhoderick[50] using the J(V) relationship that results from tunnelling through the barrier;

$$J = J_s \exp\left(\frac{eV}{mkT}\right)\left(1 - exp\left(\frac{-eV}{kT}\right)\right)$$

3.36

This equation has been shown to be valid if departure from ideality is due to the voltage dependence of the barrier height[50], and describes J(V) characteristics resulting from all transport mechanisms. The ideality factor m can therefore be used to deduce junction parameters . The advantages are that in this case the reverse current also depends on m and a plot of ln{I/I[1-exp(-eV/kT)]} against V should be linear for reverse voltages and forward voltages less than 3kT/e. The plot reveals the ideality factor (m) and the saturation current J_s from the slope and intercept respectively.

This equation has been tested successfully on Al/GaAs[49] Schottky diodes, although the authors anticipated that it will hold true for p-n junction diodes. The J(V) characteristics of the TiO_2/ MPc devices have therefore been assessed according to the method of Missous and Rhoderick[50] for V<3kT/e, to both test the validity of the method and to derive m and J_s within this voltage regime.

In CuPc/CdS heterojunctions[32] for high forward voltages, the J(V) characteristics were better described by a $J \propto KV^Q$ dependence, where Q>2. This dependence was indicative of space charge limited currents, as a consequence of the organic layer, where the electrical characteristics were controlled by an exponential distribution of traps. In the current studies, the dark J(V) characteristics of the TiO_2/MPc (IO) heterojunction cells have also

74

been analysed in terms of this dependence. In order to identify whether the TiO$_2$/MPc contact formed is rectifying, the rectification ratio (r) of the devices was determined, where r is defined as the ratio of forward current to reverse current at an applied bias of +V and -V respectively.

3.4.6 Illuminated J(V) Characteristics

The overall photovoltaic cell performance is primarily assessed through illuminated J(V) characteristics[36,43,47,48]. Figure 3.23 is a typical example of the characteristics that would be obtained for a p-n junction cell under dark and illuminated conditions. The open circuit voltage V$_{oc}$, the short circuit current density J$_{sc}$, as well as V$_{mp}$ and J$_{mp}$ (defined below) are indicated on the figure. For an ideal p-n junction solar cell the current voltage characteristics may be described by;

$$J_{out} = J_L - J_o\left[\exp\left(\frac{eV_{out}}{mkT}\right) - 1\right]$$ 3.37

where J$_L$ is the photocurrent density, J$_o$ a pre-exponential factor, J$_{out}$ the measured output current density, V$_{out}$ the measured output voltage and all other parameters have been defined previously. J$_{out}$, J$_L$, and V$_{out}$ are shown in Figure 3.24 the solar cell equivalent circuit model.

The open circuit voltage V$_{oc}$ is defined as the light created voltage output for infinite load resistance (as shown on Figure 3.24). For an ideal PV cell it is related to the built in potential, ϕ_{bp} (and theoretically cannot be greater than ϕ_{bp}).

75
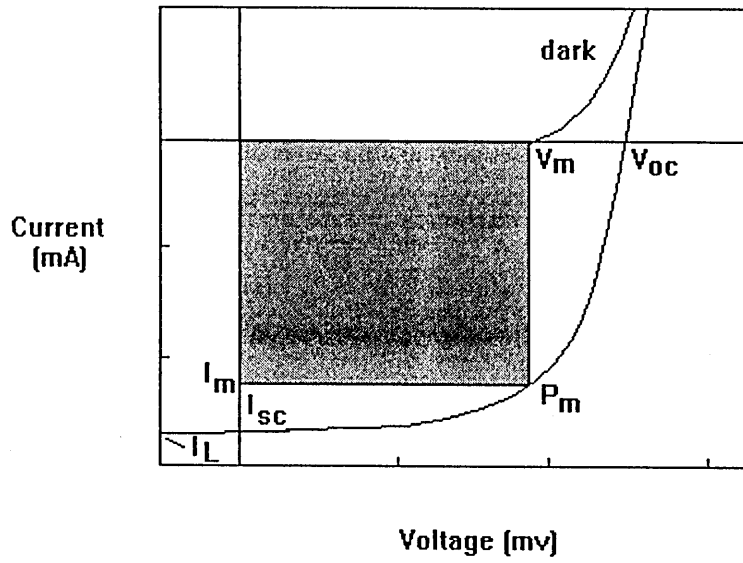
Figure 3.23. Typical J(V) characteristics of a p-n junction photovoltaic cell under dark and illuminated conditions. I_{sc} the short circuit current, V_{oc} the open circuit voltage.
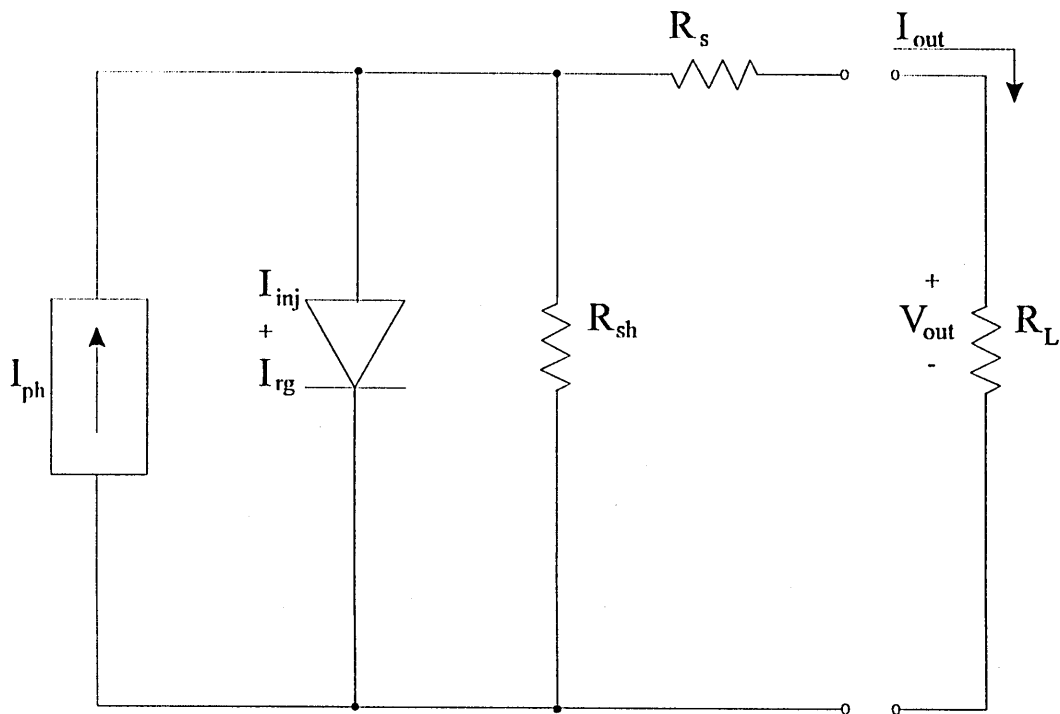
Figure 3.24. Equivalent circuit of a solar cell including series and shunt resistance's.

76

V_{oc} is given by;

$$V_{oc} = \left(\frac{mkT}{e}\right) \ln\left[\left(\frac{J_{sc}}{J}\right) + 1\right]$$

3.38

where J_{sc}, the short circuit current density is the current for zero net bias voltage across the device. It can differ from photocurrent if a large series resistance is present. Assuming the effects of series and shunt resistances are ignored then the short circuit current density J_{sc} for a p-n junction is theoretically predicted to increase linearly with increasing intensity[36], ϕ_o. A linear dependence of J_{sc} on ϕ_o therefore predicts a logarithmic dependence of V_{oc} with ϕ_o according to equation 3.38 and as shown in Figure 3.25.

The overall conversion efficiency $\eta\%$ is used to assess the device performance and is given by[36];

$$\eta = \frac{V_{oc} J_{sc} FF}{P_{in}}$$

3.39

where P_{in} are the watts of optical power incident on the cell, FF is the fill factor, defined as the fraction of the product of J_{sc} and V_{oc} available as power output and is given by;

$$FF = \frac{V_{mp} J_{mp}}{V_{oc} J_{sc}}$$

3.40

V_{mp} and J_{mp} represent the voltage and current density respectively at the maximum power point, as indicated on Figure 3.24.
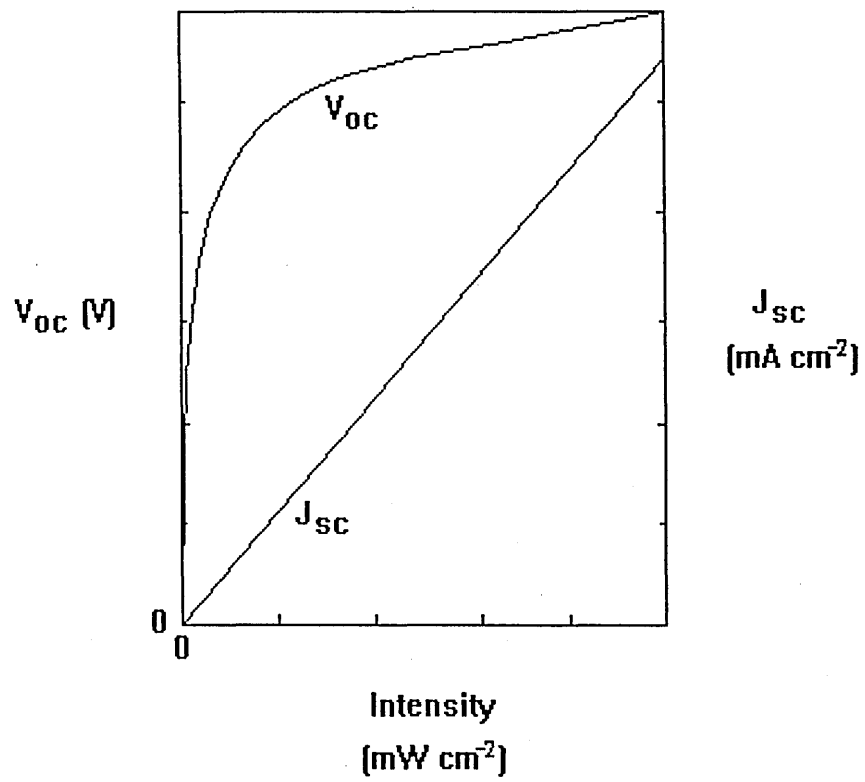
Figure 3.25. Theoretical variation of V_{oc} and J_{sc} as functions of incident light intensity, ϕ_o. for an ideal p-n junction PV cell.

In determining the performance and potential of a photovoltaic cell (PV) the effects of series and shunt resistances are considered. Shunt resistances (R_{sh}) indicate the presence of surface leakage caused by for example dislocations and grain boundaries. R_{sh} may be determined from the reverse bias J(V) illuminated characteristics where the reverse current changes linearly with the reverse bias voltage. In an ideal PV cell $R_{sh}=\infty$.

The series resistance (R_s) can be calculated from the slope of the illuminated characteristics at forward bias voltages $>V_{oc}$; where the forward current density does not vary exponentially with the applied bias. R_s indicates any contact resistance or the effects of the bulk film resistance. In an ideal PV cell $R_s=0$.

A great amount of work on Si, GaAs, and CdS based PV cells has revealed how R_s and R_{sh} affect the cells performance[36,48]. For example R_s is known to lower J_{sc} but does not affect V_{oc} while R_{sh} does the opposite. However both of these resistances are known to degrade the FF, and consequently η. For photovoltaic cells it is highly desirable that contacts are ohmic, therefore having minimal resistance and no rectification characteristics. Gold was chosen as the contact material in these studies as it is known to provide an ohmic contact to the MPcs used[51].

It is worth mentioning at this point the importance of carrier lifetime in a PV cell. Carrier lifetime is determined by the amount and nature of impurities and lattice imperfections in the semiconductor[36]. Their presence results in the formation of recombination centres, which may be either in the bulk (i.e. dislocations, vacant sites, impurities) or at the surface (i.e. dangling bonds, chemical residuals). An effective recombination centre has its energy level away from the band edges, deep within the forbidden gap, therefore the photogenerated carriers can be lost through bulk and surface recombination before they

can be collected, resulting in a reduction in the carrier lifetime. In traditional silicon and gallium arsenide p-n junction PV cells the minority carrier lifetime is one of the most important parameters in determining the cell performance, and is highly dependent on preparation procedures[36].

3.4.7 C(V) Characteristics

Measurement of the p-n heterojunction capacitance as a function of voltage allows the calculation of ϕ_{bp} the built-in-potential and W the depletion layer width. The unit area capacitance for an anisotype heterojunction based on Anderson's abrupt junction diffusion model[42] and reviewed by Chopra[48] is obtained by solving Poisson's equation and may be expressed as;

$$C = \sqrt{\frac{eN_{d1}N_{a2}\varepsilon_1\varepsilon_2\varepsilon_o}{2(\varepsilon_1 N_{d1} + \varepsilon_2 N_{a2})}\frac{1}{\phi_{bp} - V}}$$
3.41

where N_{d1} and ε_1 the donor concentration and permittivity respectively of the n-type material and N_{a2} and ε_2 the acceptor concentration and permittivity respectively of the p-type material. Taking the derivative of C^{-2} with respect to the applied voltage V, the slope of the (C^{-2} Vs. V) line can be given by;

$$\frac{dC^{-2}}{dV} = 2\frac{(\varepsilon_1 N_{d1} + \varepsilon_2 N_{a2})}{(a^2 eN_{d1}N_{a2}\varepsilon_1\varepsilon_2)}$$
3.42

where a is the active device area. Linearity of the C^{-2} plot indicates that the junction formed between the two materials is abrupt.

Extrapolation of C^{-2} against V to $C^{-2}=0$ provides the value of ϕ_{bp}. The total width of the depletion layer (W) is then calculated from;

$$W = \left[\frac{2\varepsilon_1\varepsilon_2\phi_{bp}(N_{a2}+N_{d1})^2}{e(\varepsilon_1 N_{d1}+\varepsilon_2 N_{a2})N_{d1}N_{a2}} \right]^{\frac{1}{2}}$$

3.43

The width of the space charge regions x_1 and x_2 (or the penetration depth of the depletion region into the respective semiconductors) may then be calculated according to;

$$x_1 = \left[\frac{2N_{a2}\varepsilon_1\varepsilon_2\varepsilon_o(\phi_{bp}-V)}{eN_{d1}(\varepsilon_1 N_{d1}+\varepsilon_2 N_{a2})} \right]^{\frac{1}{2}}$$

3.44

and

$$x_2 = \left[\frac{2N_{d1}\varepsilon_1\varepsilon_2\varepsilon_o(\phi_{bp}-V)}{eN_{a2}(\varepsilon_1 N_{d1}+\varepsilon_2 N_{a2})} \right]^{\frac{1}{2}}$$

3.45

REFERENCES

1. Wang, S. *Fundamentals of Semiconductor Theory and Device Physics*, Prentice-Hall, 1989.

2. Tyagi, M.S. *Introduction to Semiconductor Materials and Devices*, John Wiley & Sons, 1991.

3. Grant, F.A. *Reviews of Modern Physics*, **31**(3) (1959) 646-673.

4. Tauc, J., Grigorovici, R., and Vancu, A. *Phys. Status Solidi,* **15** (1966) 627.

5. Mott, N. F., and Davis, E. A. *Electronic Processes in Non-Crystalline Materials,* Clarendon Press, 1979.

6. Urbach, F. *Phys. Rev,* **92** (1953) 1324.

7. Tang, H., Levy, F., Berger, H., and Schmid, P.E. *Phy. Rev. B*, **52**(11) (1995) 7771-7774.

8. Murri, R., Schiavulli, L., Pinto, N., and Ligonzo, T. *J. Non-Crys. Solids.* **139**(1) (1992) 60-66.

9. Chopra, N., Mansingh, A., and Chadha, G. K, *J. Non-Cryst. Solids* **126** (1990) 194-201.

10. Tauc, J. *The Optical Properties of Solids,* Ed. F. Abeles, North-Holland Publ. Co., Amsterdam, (1970), P.277.

11. Davis, E. A., and Mott, N. F. *Phil. Mag.* **22** (1970) 903.

12. Khawaja, E. E., and Hogarth, C. A. *J. Phys. C: Solid State Phys.* **21** (1988) 607-613.

13. Simon, J., and Andre, J. J. *Molecular Semiconductors*, Springer, 1984.

14. Frenkal, J. *J Phys Rev.* **54** (1938) 647.

15. Ray, A. K., and Hogarth, C. A. *J. Phys. D. Appl. Phys.* **23** (1990) 458-459.

16. Manifacier, J. C., Gasiot, J., and Fillard, J. P, *J. Phys.E. Sci. Inst.* **9** (1976) 1002-1004.

17. Swanepoel, R. *J.Phys. E. Sci. Inst.* **16** (1983) 1214-1222.

18. Heavens, O. S. *Optical Properties of Thin Solid Films,* London:Butterworths, 1955.

19. Elliot, S. R. *Physics of Amorphous Materials*, John Wiley & Sons, Inc., New York, (1990).

20. Cohen, M. H., Fritzsche, H. and Ovshinsky, S. R. *Phys. Rev. Lett.* **22** (1969) 1065.

21. Abo El Soud, A. M., Mansour, B., and Soliman, L. I. *Thin Solid Films* **247** (1994) 140-143.

22. Mott, N. F. *Phil. Mag.* **13** (1966) 989.

23. Khawaja, E. E., and Hogarth, C. A. *J. Phys. C: Solid State Phys.* **21** (1988) 607-613.

24. Simmons, J. G. *J. Phys. D: Appl. Phys.* **4** (1971) 613-655.

25. Rudden, M. N., and Wilson, J. *Elements of Solid State Physics*. John Wiley & Sons, Inc., New York. 1980.

26. Tollin, G., Kearns, D.R., and Calvin, M. *J. Chem. Phys.* **32** (4) (1960) 1031-1020.

27. Ray, A. K., James, S. S., Thorpe, S. C., and Cook, M. J. *Thin Solid Films.* **226** (1993) 3-5.

28. Forro, L., Chauvet, O., Emin, D., Zuppiroli, L., Berger, H., and Lévy, F. *J. Appl. Phys.* **75**(1) (1994) 633-635.

29. Sravini, C., Reddy, K. T. R., Hussain, O. Md., and Jayarama Reddy, P. *Thin Solid Films* **253** (1994) 339-343.

30. Marsal, L. F., Pallarès, J., Correig, X., Calderer, J., and Alcubilla, R., *J. Appl. Phys.* **79** (11) (1996) 8493-8497.

31. Forrest, S. R., and So, F. F. *J. Appl. Phys.* **61** (1988) 399.

32. Antohe, S. *Rev. Roum. Phys.* **37**(3) (1992) 309-313.

33. Sakata, T., Hashimoto, K., and Hiramoto, M. *J. Phys. Chem.* **94** (1990) 3040-3045.

34. Antohc, S., and Vonsovici, A. *Phys. Stat. Sol. (a)* **124** (1991) 583-593.

35. Antohe, S., Tomozeiu, N., and Gogonea, S. *Phys. Stat. Sol. (a)* **125** (1991) 397-408.

36. Hovel, H. J. *Semiconductors and Semimetals, Solar Cells. Vol. 11.* Academic Press New York. (1975)

37. Nespurek, S. *Synthetic Metals.* **62** (1993) 55-60.

38. Fernando, C. A. N. *Solar Energy Materials and Solar Cells,* **39** (1993) 211-220.

39. Dähne, S. *J. Imag. Sci. Tech.* **38** (2) (1994) 101-117.

40. Sakata, T., Hashimoto, K., and Hiramoto, M. *J. Phys. Chem.* **94** (1990) 3040-3045.

41. Takada, J. *Jpn. J. Appl. Phys.* **34** (1995) 3864-3870.

42. Anderson, R. L. *Solid State Elec.,* **5** (1962) 341.

43. Milnes, A. G., and Feucht, D. L. *Heterojunctions and Metal-Semiiconductor Junctions.* Academic Press New York:London (1972).

44. Shen, Y., Wang, L., Lu, Z., Wei, Y., Zhou, Q., Mao, H., and Xu, H. *Thin Solid Films.* **257** (1995) 144-146.

45. Kudo, K., and Moriizumi, T. *Jap. J. Appl. Phys.* **19**(11) (1980) L683-L685.

46. Möller, H. J. *Semiconductors for Solar Cells,* Artech House, 1993.

47. Sze, S. M. Physics of Semiconductor Devices. Wiley, 1969.

48. Chopra, A. *Thin Film Solar Cells,* Plenum: New York:London, (1983) p. 85.

49. Rhoderick, E. H., *Metal-Semiconductor Contacts* Clarendon Press, Oxford 1978 p 87

50. Missous, M., and Rhoderick, E. H. *Elec. Letts.* **22** (9) (1986) 477-478.

51. Boudjema, B., Guillard, G., Gamoudi, M., Maitrot, M., Andre, J. J., Martin, M., and Simon, J. *J. Appl. Phys.* **56** (8) (1984) 2323.

<div align="right">

Chapter 4

</div>

Sol-Gel Processing

4.1 Introduction

A primary consideration in the present investigations was low cost and ease of fabrication. The required material parameters such as thickness, structure and conductivity must also be easily engineered. For the production of TiO_2 films a process that has potentially all of these attributes is Sol-Gel[1-2]. The possibility of using high purity starting materials and the ease with which large and complex shaped substrates can be coated has meant that this technique is becoming increasingly attractive to optoelectronic specialists[3-4].

The Sol-Gel process is a chemical route to preparing inorganic (oxide) compounds. There are two distinct variants of the process, known as the aqueous and alkoxide route respectively. The latter was employed in this case. The process consists of a two step, hydrolysis and polycondensation reaction of the precursor metal alkoxide molecules with water. The reaction produces a polymeric (or macro)molecular metal oxide network in the form of a colloidal dispersion (SOL) in a carrier liquid, which normally consists of an alcohol or diol. These macro-molecules subsequently cross link and/or join by

intermolecular forces to form a highly porous GEL product, characterised by a gradual increase in the viscosity of the medium.

The resultant gel, known as an alcogel, can be transformed to a rigid solid metal oxide by heat treatment at relatively low temperatures (typically 350-750°C) to remove residual organic material and sinter the porous gel to a dense film or monolith.

4.2 The Hydrolysis and Condensation Reactions

As previously explained, the Sol-Gel process involves a two stage chemical reaction with water. The two stages are known as the hydrolysis reaction and the polymerisation/condensation reaction. In the case of the Sol-Gel production of TiO_2, these take the following form.

(i) Hydrolysis.

Reaction formula = Ti (OR)$_4$ + 4H$_2$O → Ti (OH)$_4$ + 4ROH.
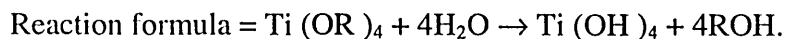
The metal alkoxide compound, Titanium Isopropoxide (TIP) undergoes a hydrolysis reaction with water present in the carrier solvent (e.g. ethanol) forming the intermediate compound Ti(OH)$_4$ when completely hydrolysed.

(ii) Polymerisation Condensation Reaction

Reaction = $(n)Ti(OH)_4 \rightarrow (n)TiO_2 + 2(n)H_2O$
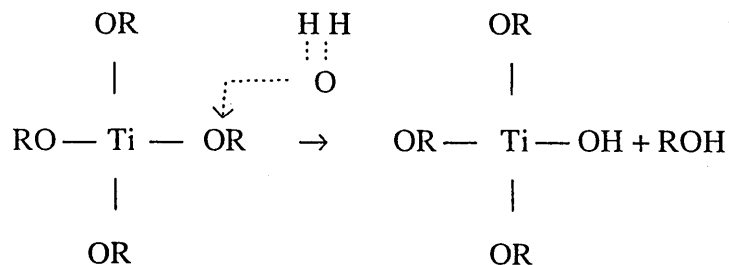
The polymerisation/condensation reaction involves the removal of unwanted OH groups, transforming the material into the oxide form in which the metal atoms are linked via oxygen linkages to form a polymeric network molecule. Water is evolved as the reaction occurs:

$$
\begin{array}{ccccccc}
 & \text{OH} & & & & \text{OH} & \\
 & | & & & & | & \\
\text{OH} - & \text{Ti} & - \text{OH} & + & \text{HO} - & \text{Ti} & - \text{OH} \\
 & | & & & & | & \\
 & \text{OH} & & & & \text{OH} &
\end{array}
$$

$$\downarrow$$

$$
\begin{array}{ccccc}
 & \text{OH} & & \text{OH} & \\
 & | & & | & \\
\text{OH} - & \text{Ti} - & \text{O} - & \text{Ti} & - \text{OH} \\
 & | & & | & \\
 & \text{OH} & & \text{OH} &
\end{array}
$$

$$H_2O$$

The molecular clusters grow and polymerisation takes place, to form a polymer network commonly termed the 'Gel'

$$
\begin{array}{ccccc}
 & \text{O} & & \text{O} & \\
 & | & & | & \\
\text{O} - & \text{Ti} - & \text{O} - & \text{Ti} & - \text{O} \\
 & | & & | & | \\
 & \text{O} & & \text{O} - & \text{Ti} - \text{O} \\
 & & & & | \\
 & & & & \text{O}
\end{array}
$$

Polymer network (Gel)
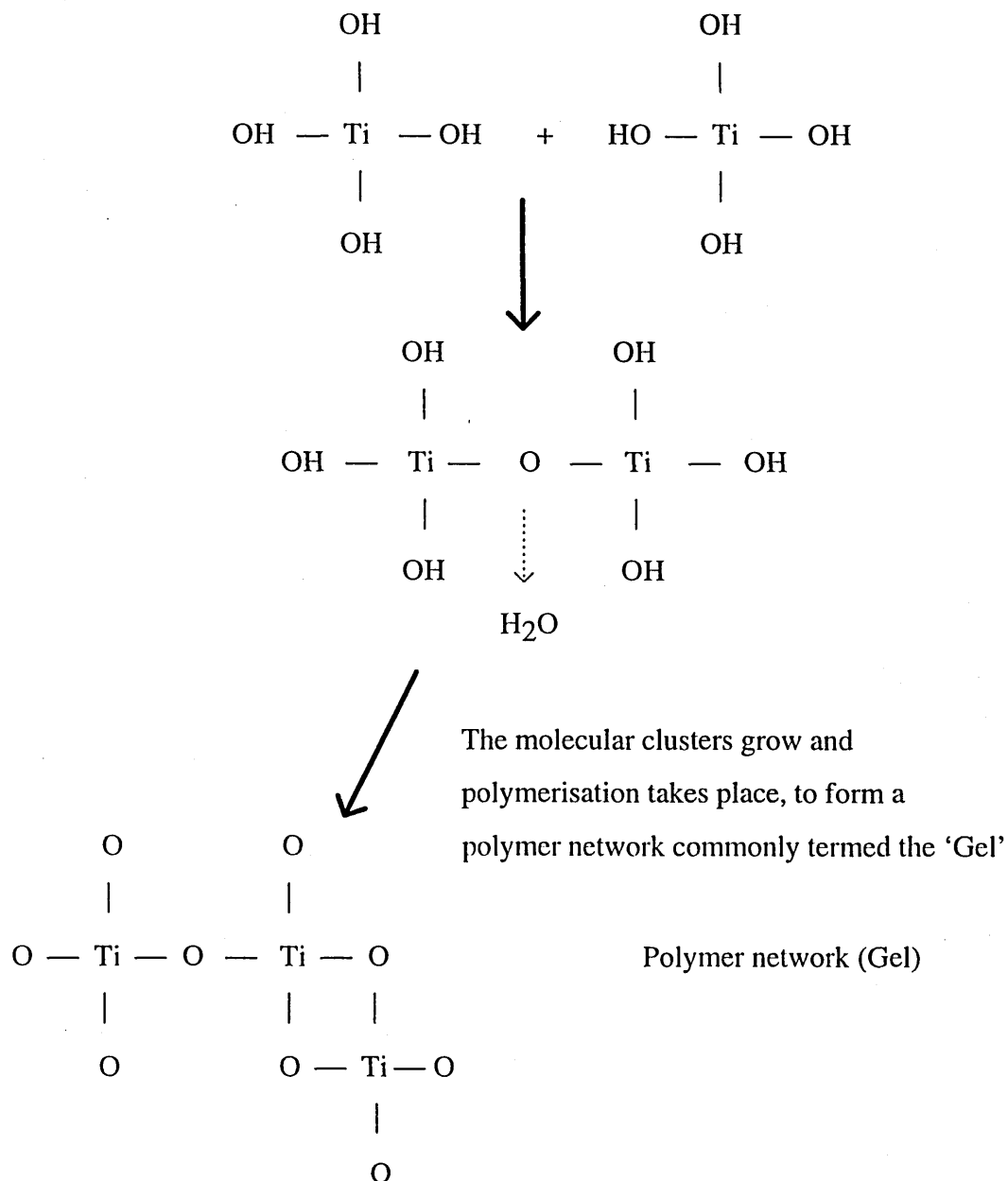
4.3 Reaction Modifiers

In the case of many alkoxides, particularly those of the transition metals, the compounds are highly susceptible to the hydrolysis reaction[5], and the nature of the reaction product from these rapidly reacting compounds tends to take the form of particulate rather than a three dimensional cross linked network or gel. Since these particulates are unsuitable for the production of thin films, it is necessary to add various modifying agents to the reactants to retard the hydrolysis reaction and allow the desired gel type products to be formed.

A number of additives have been successfully employed to control the reaction of TIP, either by chemically replacing the reactive alkyl groups with less reactive species, e.g. acetylacetone, acetic acid[6] or by controlling the hydrolysis reaction kinetics via the pH of the solution e.g Nitric and Hydrochloric acid[7]. In both cases, the reaction modifying additions increase the stability of the Sol, and produce changes in the Sol viscosity and subsequently film thickness.

4.4 Deposition Methods

Probably one of the greatest advantages of the Sol-gel technique over other film deposition methods is its versatility. Prior to gelation, the Sol can be spin-coated, sprayed, or dipcoated[1-2]. Each of these methods has respective advantages and drawbacks.

In the case of dip coating as used in this study, it is possible to achieve good control over thickness, and requires less expensive equipment than the other techniques. Homogeneity and uniformity are easily achieved as long as the withdrawal is smooth and vibration free.

4.5 Drying

The drying stage is an important aspect of the Sol-Gel process. This stage, which is normally carried out at temperatures between ambient and approximately 150°C, causes the mobile alcogel to transform to a rigid solid known as a xerogel or aerogel[1-2].

During this time most of the residual solvent and water is removed. This process causes the gel film to shrink and to eventually form a solid which is highly porous in nature[1,2,8]. The drying procedure alone does not however remove all of the trapped solvent and water. For that, a subsequent higher temperature heat treatment is required that essentially densifies the gel and results in the diffusion of the residual aqueous and organic components to the surface from where they are removed by evaporation and/or pyrolysis[1,8].

4.6 Sintering and Densification

Yet another attractive feature of the Sol-Gel process is that compared to conventional ways of producing glasses, i.e. by fusion of oxides, the densification takes place at much lower temperatures[9,10]. In an extensive study by Brinker and Scherer[1] it was proposed

that the densification process is a combination of four mechanisms each occurring in varying degrees and at varying temperatures.

At low temperatures during the drying stage the gel will shrink as the solvent evaporates and the pores begin to contract. As the temperature begins to increase condensation polymerisation occurs and density of cross-links increases, the overall effect is to shrink the Gel further. If the temperature reaches the glass transition temperature (T_g) for the material then structural relaxation will occur where the excess free volume (or the volume available to an atom not including that required for thermal vibrations) is decreased. After this temperature a further increase results in 'viscous sintering' when the pores remaining in the gel collapse, the material increases in viscosity and begins to flow eventually forming a dense, solid material. At even higher temperatures the gels can begin to crystallise, an effect which has been observed in the TiO_2 gel residues prepared in these studies is outlined in chapter 6.

4.7 The Effects of Sol-Gel Process Parameters on Thin Films

It is recognised that process parameters have a major influence on the properties of Sol-Gel derived thin films. Parameters such as heat treatment conditions, Sol reactivity and viscosity, oxide ratio and the number of coatings have been shown in some cases to drastically alter the electrical, optical and structural properties of the films[11-16,19].

Heat treatment conditions are known to have an effect on the structural properties of Sol-Gel derived films. TiO_2 films prepared from Sols manufactured from TIP in ethanol, and stabilised with CH_3COOH have been found to be amorphous when annealing temperatures of 350°C have been used[11]. Sol-Gel derived TiO_2 films heat treated to 400°C are reported to be anatase in structure[12]. Changes in crystalline structure have been shown to correspond to changes in the measured refractive index (n) of TiO_2. Sol-Gel processing is used to engineer refractive index[13] for a variety of optical and optoelectronic applications.

Many process parameters have been shown to have effects on film thickness. For example the thicknesses of SiO_2 films were dependent on the Sol viscosity [14]. The oxide concentration of the solution, heat treatment temperature and time are also used to control film thickness.[14,15] Dip-coating is a common technique for the film manufacture. The variation of thickness as a function of withdrawal rate has been examined by Huang[15] on Na^+ Super ionic conductor (NASICON) thin films. Thickness increased linearly with increasing withdrawal rate. For multidipping coatings the thickness of the first layer was observed to be thicker than subsequent layers. The thickness had relatively little dependence on the number of sinterings.

The effect of heat treatment on the dielectric constant (ε) and resistivity (ρ) of TiO_2 Sol Gel films deposited on Silicon substrates were assessed by Vorotilov[16]. ρ decreased as the heat treatment temperature was raised >700°C. Values of ε and n were observed to increase with increasing temperature and these rises were attributed to observed structural changes.

The models developed to explain and predict the behaviour of the types of observations described have tended to characterise the role of individual factors in the process, and remain of limited general applicability. Consequently the development of novel systems has tended to occur on a largely empirical basis. Little published work exists on the role and nature of interactions between the process parameters to allow a more general understanding of the role of the process parameters to be developed.

Factorial experimental design (FED)[17] is a useful, highly efficient statistical technique for assessing and predicting the effect of both individual factors (i.e. process parameters), and any interaction between factors that may exist. (described in more detail in chapter 5.) Originally developed by Fisher in 1926[18], it is a technique that offers a number of advantages (outlined in 5.4) over the traditional 'one-factor-at-a-time' approach, in which the effect of changing any one variable is assessed independently of the others.

As well as characterising the TiO_2 films manufactured in these investigations, for example in terms of their conductivity, refractive index and optical band gap, the effects of process parameters on properties such as thickness and absorption of the TiO_2 films have been assessed using FED[19] (see Appendix C). It is anticipated that these observations will be applicable to a wide variety of similar alkoxide systems, and that elucidation of the nature of interactions between the process parameters will lead to a greater understanding of their role.

REFERENCES

1. Brinker, C. J., and Scherer, G. W. *Sol-Gel Science:The Physics and Chemistry of Sol-Gel Processing*. Academic Press: London, (1990).

2. Jones, R. W. *Fundamental Principles of Sol-Gel Technology*. Insitute of Metals (1989).

3. Nogués, J. L., and Hunt, P. B. *Laser Focus World*. Dec (1995) p. 90.

4. Dislich, H. *J. Non-Cryst. Solids*. **57** (1983) 371-388.

5. Sanchez, C., Livage, J., Henry, M., and Babonneau, F. *J. Non-Cryst. Solids*. **100** (1988) 65-76.

6. Livage, J. *Mat. Res. Symp. Proc.* **73** (1986) 717-723.

7. Yoldas, B. E. *J. Mat. Sci.* **21** (1986) 1087-1092.

8. Anderson, M. A., Gieselmann, M. J., and Xu, Q. *J. Mem. Sci.* **39** (1988) 243-258.

9. Sorek, Y., Reisfeld, R., Finkelstein, I., and Ruschin, S. *Appl. Phys. Letts.* **63** (24) (1993) 3256-3258.

10. Keddie, J. L., and Giannelis, E. P. *J. Am. Ceram. Soc.* **75** (10) (1991) 2669-2671.

11. Ozer, N., Demiryont, H., and Simmons, J. H., *Appl. Optics*. **30** (1991) 3661-3666.

12. Kohno, K. *J. Mat. Sci.* **27** (3) (1992) 658-660.

13. Takahashi, Y., and Matsuoka, Y. *J. Mat. Sci.* **23** (1988) 2259-2266.

14. Sakka, S., Kamiya, K., and Yoko, Y. *Inorganic and Organometallic Polymers*, Amer. Chem. Soc. Symp. Series. **360** (1988) 345-353.

15. Huang, Y. L., Caneiro, A., Attari, M., and Fabry, P. *Thin Solid Films*.**196** (1991) 283-294.

16. Vorotilov, K. A., Orlova, E. V. and Petrovsky, V. I. Thin Solid Films. 207 (1992)

    180-184.

17. Montgomery, D.C. *Design and Analysis of Experiments,* John Wiley & Sons, New

    York, 2nd ed. 1984.

18. Fisher, R. A. "The Arrangement of Field Experiments," *J. Ministry of Agriculture* 33

    (1926) 503-513.

19. Tracey, S. M., Hodgson, S. N. B., Ray, A. K., and Ghassemlooy, Z., *Adv. Mat.*

    Proc. Tech. 3 (1995) 1268-1277.

Chapter 5

Experimental Methodology

5.1 Introduction

This chapter is divided into two sections the first describes the device fabrication procedures used during these investigations and the precautions necessary to ensure high quality films. The second section is concerned with the characterisation techniques and the equipment employed for an accurate compilation of experimental data. Safety precautions are also reviewed.

5.2 Device Fabrication

5.2.1 Substrate Type and Preparation

A variety of substrate types were used depending on the characterisation method employed. The substrates were either one of four types (i) Pre-fabricated Yoshi slides (lithographically interdigitated platinum electrodes), (ii) glass slides (manufactured from clear white glass as supplied by BDH) (iii) Indium Tin Oxide coated glass or (iv) Fluorine doped Tin Oxide coated glass, both as supplied by Pilkington Glass. Figure 5.1 shows the %transmission as a function of wavelength for the $InSnO_2$ and Fluorine doped SnO_2 coated substrates used in the construction of the dye sensitised cells. Both exhibit

an average of 80% transmission in the visible region. The sheet resistance (R_{ST}) of the conductive glass substrates was determined using the four point probe technique and found to be 11.6 Ω/ and 18.6 Ω/ for the $InSnO_2$ and F-doped SnO_2 respectively.

5.2.1.1 Substrate Cleaning

The structure and properties of thin films are known to be affected by the quality of the substrate surface onto which they are deposited[1]. A rough or dirty surface can lead to a R_{ST} which varies across the substrate surface causing 'hot spots' and eventually device failure, particularly for dielectric films[1]. Cleaning the substrate will improve its adherence to the deposited film and remove the minute particles of dust and debris which can have catastrophic effects on film quality, resulting problems are likely to include pinholes, cracking and unhomogeneity[2]. The cleansing processes employed were therefore very thorough and carried out under a class 100 specification clean room environment. Table 5.1 summarises the substrate cleansing procedure. The use of the ultrasonic bath not only agitates the solution for effective cleaning but also has a heating effect which enhances the effectiveness of the solvents. The solvents were all supplied by BDH. After each step the substrates were spray rinsed in de-ionised water prepared in-house by a Milli-pore water purification system. The water had an electrical resistance of 18 MΩ and can therefore be regarded as contaminant free. The substrates were finally dried in air, ready for film deposition.
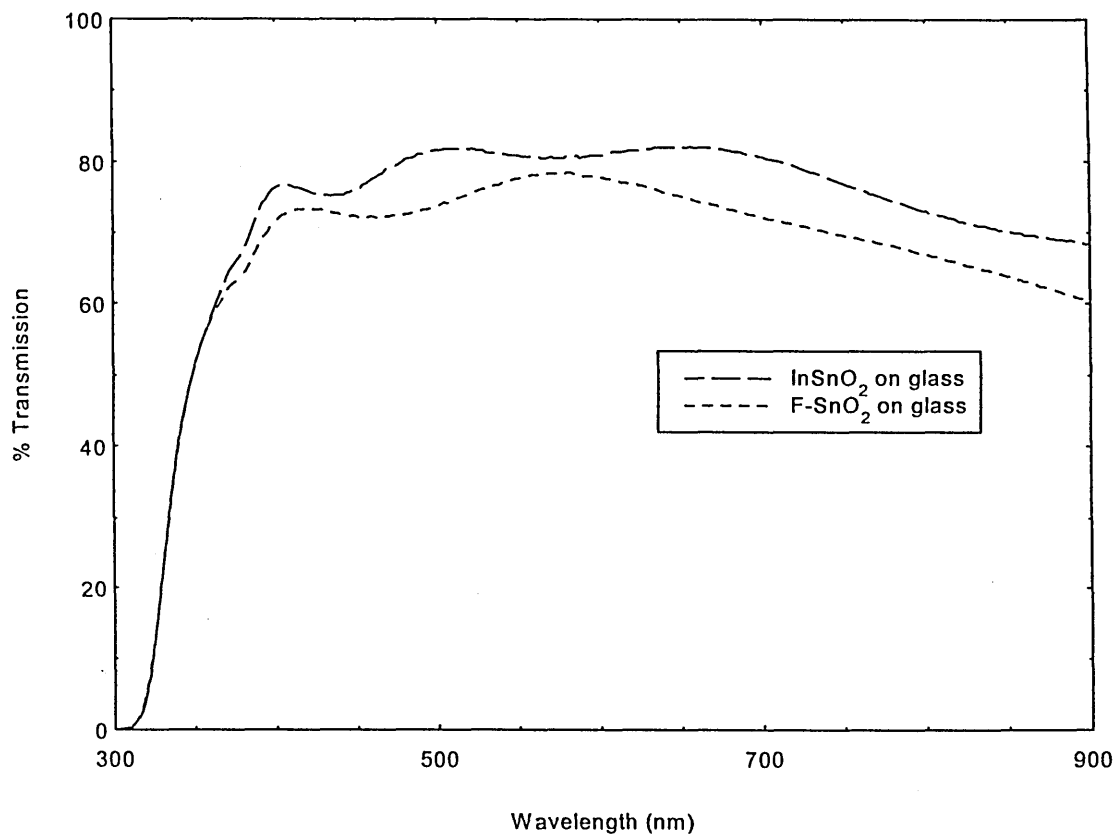
Figure 5.1. % Transmission versus wavelength (nm) for the conducting glass substrates used in the production of the dye sensitised cells.

Chemical	Formula and Purity	Sonification Time (mins)
Dilute Decon 90	Mixed with de-ionised water approx. 1part in 10	10
Analar *DCM	CH_2Cl_2 99.5%	5
Analar Propan-2-ol	$(CH_3)_2CHOH$ 99.7%	5
Aristar *DCM	CH_2Cl_2 99.5%	5
Aristar propan-2-ol	$(CH_3)_2CHOH$ 99.8%	5

Table 5.1. Order of cleansing procedure for all substrates used. *DCM (Dichloromethane).

5.2.1.2 Preparation for Film Deposition and Device Configurations

Both sandwich and planar device configurations were used throughout these studies, as shown in Figure 5.2 with a summary of the corresponding materials used and characterisations performed. A scanning electron micrograph of the Yoshi slide as shown in Plate 5.1 was used to determine the electrode dimensions. Each of the 15 electrodes were 186µ wide and 60µ apart, and overlapped by 3.125mm. The intrinsic conductivity of films on such slides could then be calculated according to the formula[3];

$$\sigma = \frac{S}{t}\frac{d}{P} \qquad\qquad 5.1$$

where σ is the intrinsic conductivity (S/cm), S is the measured conductance, t the film thickness (cm), P the electrode perimeter and d the electrode spacing.

For refractive index measurements it was necessary to deposit a TiO_2 film onto one side of the glass substrate. A consequence, was that one side of the substrate had to be shielded from the Sol-Gel mixture. This was successfully achieved by covering the selected area with heated wax, allowing it to solidify, depositing the required film and finally removing the wax by peeling and subsequent cleaning with acetone. This method was also used to shield the platinum electrical contacts from the Sol mixture in order that a clean electrical contact could be made.

A,B,C,D	Au / MPc / TiO$_2$ / InSnO$_2$/F-SnO$_2$ / Glass
A,B,C,D	Au / PbPc / TiO$_2$ / Glass, InSnO$_2$ / F-SnO$_2$
A,E,G	Au / TiO$_2$, InSnO$_2$ / Glass
E,F,G	MPc / Glass, TiO$_2$ / Glass
A	TiO$_2$/Pt
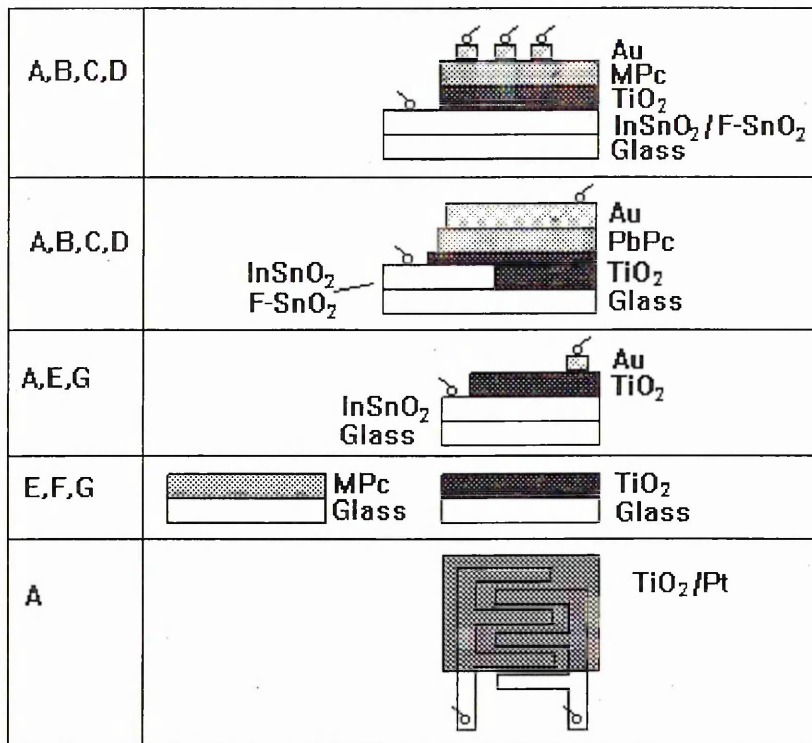
Figure 5.2. Summary of device configurations and characterisations performed during these investigations. Where letters denote characterisation performed; A=dark J(V); B= illuminated J(V); C=J(λ); D=C(V); E=optical absorption/transmission; F=n, E$_o$'; G=thickness.
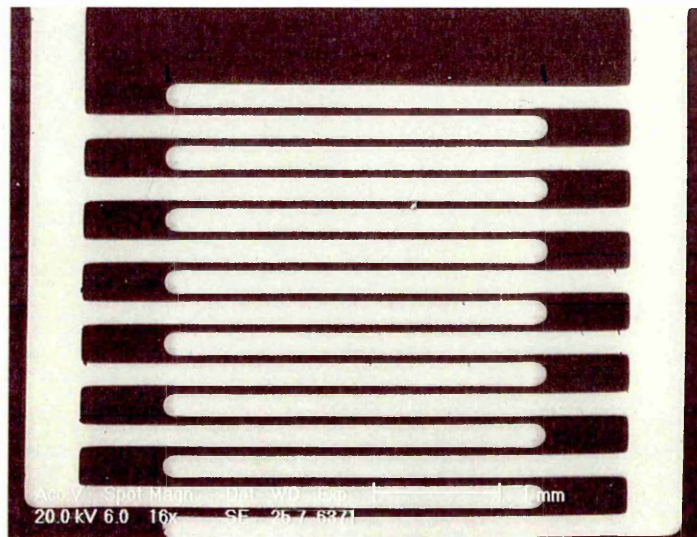
Plate 5.1. Scanning electron micrograph of the platinum interdigitated electrodes (x16 mag).

As shown in Figure 5.2, for the construction of the PbPc/TiO$_2$ device a section of the InSnO$_2$ or F-SnO2 coating film from the glass substrate was removed. This was achieved by preparing a paste of zinc powder and water which was subsequently coated over the area of the conductive glass film to be removed, this was allowed to dry in air. Placing the zinc coated area into concentrated Hydrochloric acid for approximately five seconds removed the InSnO$_2$ or F-SnO$_2$ effectively, leaving the insulating glass exposed[5]. The substrates were then ready for phthalocyanine or titanium dioxide deposition.

5.2.2 Film Deposition

5.2.2.1 Titanium Dioxide via the Sol-Gel Process

The three components used in the production of the TiO$_2$ Sol-Gel films were as follows: Titanium Isopropoxide (TIP) Ti[OCH(CH$_3$)$_2$]$_4$ = Ti(OR)$_4$ purity 97%, Acetic acid CH$_3$COOH purity 99.5% and Ethanol CH$_3$ CH$_2$OH purity 99.7-100%, all chemicals were as supplied by Aldrich Chemicals Ltd. TIP is a metal alkoxide, where metal alkoxides have the general formula M(OR)$_n$ M=metal R=alkyl group and n is the valence of the metal atom (in this case 4).

The required volume of TIP was added by pipette to a beaker containing a mixture of glacial acetic acid and ethanol that had been mixed for five minutes. The mixture was continually stirred using a magnetic stirrer during addition and for a further two minutes after addition of the precursor. The volumes of TIP used were calculated, relative to the volume of ethanol solvent to give the required concentration (either 6.3% or 12.6% by volume) of TIP solution. The volume of acetic acid used was calculated to give the

required molar ratio (either 3.14:1 or 4.16:1) of acetic acid to the TIP. The Sol concentration was altered in order to assess the effects of ratios and concentrations.

The effects of altering molar ratios of acid:TIP on the thickness and absorption properties of the films were investigated in these studies and are discussed in chapter six. The Sols manufactured according to the method described above were immediately used to produce coatings on the various substrates.

The dipcoating apparatus used, shown in Plate 5.2 was developed by Nima technology. The apparatus contained a linear motor, ensuring that the dipping rate was constant and that the resulting films were homogeneous. The apparatus allowed the withdrawal rate to be altered in the range 2-200mm/min. This was an important variable as it has proved to be significant with regard to the quality of the films and in particular film thickness.

After dipcoating the films contain residual ethanol and very probably water from the condensation reaction. The TiO_2 deposited film samples were therefore left to dry in ambient temperatures under a clean room environment for approximately 24 hours, prior to the sintering heat treatment.

Plate. 5.2. Linear dipping apparatus developed by Nima Technology.

For the densification process a Carbolite type CSF 11/3 furnace was used, which has a temperature range of 28-1100°C and is accurate to +/-5°C. The temperature and duration of sintering are dependent on the film requirements, and the limitations of the substrate. In this study a variety of sintering times and temperatures up to 500°C have been investigated to assess their effects on overall film quality.

5.2.2.2 Metal-Substituted Phthalocyanine (MPc)

The organic materials used during the course of these investigations were Copper Phthalocyanine (CuPc), Lead Phthalocyanine (PbPc) and Chloroaluminium Phthalocyanine (ClAlPc).

The PbPc and CuPc were obtained in powder form from commercial suppliers such as Kodak and Fluka AG, and subsequently purified to remove contaminants used in their synthesis by the process of entrainer sublimation[6]. The ClAlPc was prepared within the Physics department at Lancaster University according to the following method. A mixture of 40g Phthalonitrile, 10g $AlCl_3$ and 200ml Quinoline (doubly distilled and deoxygenated under a Nitrogen gas atmosphere) was refluxed for 1.5 hours. The resulting hot mixture was then filtered using a glass filter, then cooled to room temperature and filtered again. The solid, isolated, was washed sequentially with toluene, carbon tetrachloride and acetone, then dried under vacuum to 150°C.

Semiconducting materials have a wide range of vapour pressures[7]. The vapour pressure is that pressure at which the gaseous phase of the material is in equilibrium with the liquid or solid phase of the material when both phases are at the same temperature. This can be equated to the resulting equilibrium gas pressure of the material at that temperature when the gas atom condensing on the substrate surface are at the same rate as atoms evaporating from the material surface. As organic materials such as the phthalocyanines have vapour pressures below their fusion temperatures they sublime easily (where the material undergoes direct transition from a solid to a vapour form) and are therefore well suited to this technique[8]. The process sublimation has the added advantage as acting as a further purification step.

The method of vacuum sublimation was therefore employed to manufacture the MPc thin films. All of the phthalocyanines used during these investigations have been previously vacuum sublimed[9-11].

The PbPc and the CuPc films were prepared at the HSE (Health and Safety Executive) and the ClAlPc films at Lancaster University though the preparation procedures were similar. The phthalocyanines were sublimed from resistively heated metallic boats constructed from either molybdenum or tantalum depending on the sublimation temperatures. Upon heating the MPc turned into vapour and was deposited onto the required substrates which were held at a distance of ~15cm above the boat. The sublimation process took place in a well degassed vacuum chamber, the vacuum was ~10^{-5} mbar. For consistency all substrates were held at room temperature during the sublimation process and a low deposition rate of 1-10A/sec was used.

5.2.2.3 Electrical Contacts and Thickness Monitoring

For any electrical or photoelectrical characterisation it is necessary to apply metal electrodes to the film surface. Metals have high vapour pressures[7] so evaporation is a simple technique to employ. The procedure was again carried out using a resistively heated source mounted inside a vacuum chamber. The choice of source is dependent upon the evaporation temperature of the electrode material. For the evaporation of Gold contacts a molybdenum boat was used. This prevented the occurrence of metallic impurity contamination in the electrodes.

The choice of electrode material and configuration when studying semiconducting materials is extremely important. Knowledge of the work function of the electrode metal is required to ascertain the type of contact made to the material i.e. rectifying, ohmic or neutral . For the heterojunction devices investigated in these studies it is desirable to have ohmic contacts on both sides of the junction. Gold was therefore chosen as this is known to provide good ohmic contacts to phthalocyanine[12]. The gold, supplied by Aldrich Chemicals Ltd was of high purity ~99.999%.

For all contacts a masking system determined the electrode configuration, the dimensions of which were known in order that an accurate determination of device active areas could be deduced. Evaporation was carried out under a background pressure of 10^{-3}Pa. The evaporation rates of the contact material were initially very low ~0.1nm/s, especially if deposition was directly onto an organic film and gradually increased to 0.5nm/s.

This prevents any thermal damage to the underlying organic layer, for example in the form of resublimation. Copper wires were used for electrical connections from the measuring equipment to the devices which were attached to the electrodes using a silver conducting paste.

An Edwards Bir-Vac vacuum evaporation chamber was used for both the deposition of organic films and for electrode fabrication. A schematic representation of the system is shown in Figures 5.3 and 5.4. The vacuum system consists of a rotary pump and an oil diffusion pump. The rotary pump is used to obtain a vacuum of around 10^{-1} torr, by roughing the sample chamber and backing the diffusion pump. The diffusion pump (Figure 5.4) provides the high vacuum of up to 10^{-6} torr.

A Maxtek quartz crystal oscillator was used to determine the deposition rate and to obtain an estimation of electrode and MPc thicknesses in situ. The monitor measures the change in oscillating frequency of the quartz crystal (due to its change in mass) and is placed as close as possible to the sample to obtain the highest accuracy. The amount of material actually deposited on the crystal is therefore proportional to its change in oscillating frequency.
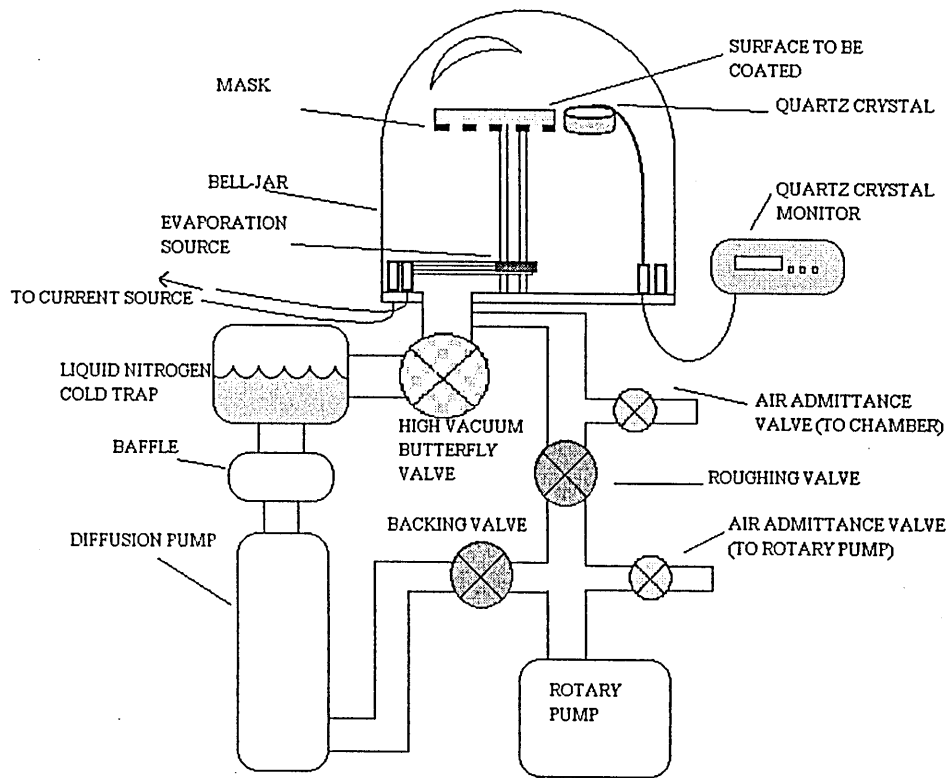
Figure 5.3. A schematic representation of the vacuum evaporator system used for thin film deposition.
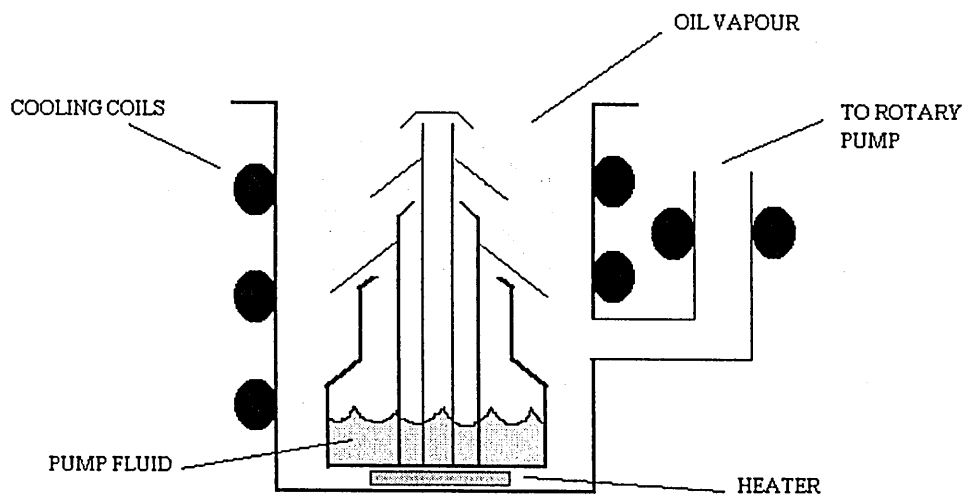
Figure 5.4. A schematic representation of the diffusion pump.

5.2.3 Safety Considerations

The processes that have been described involve a variety of chemicals some of which can be dangerous if contact is made with the skin. All chemical procedures were therefore performed in a fume cupboard supplied with an adequate grade of filter, and the appropriate protective clothing was worn e.g. lab coat, gloves. In the case of acids and TIP a mask provides an extra precaution against inhalation. Gloves were also worn when handling phthalocyanines which can be toxic. These procedures also prevent grease contamination of both materials and equipment.

5.3 Characterisation Equipment

5.3.1 Optical Absorption/Transmission

Analysis of optical absorption/transmission spectra allows determination of a variety of fundamental material parameters such as film thickness t, refractive index n, absorption coefficient α and the optical band gap E_o.

To obtain absorption and/or transmission data in the wavelength range 300-900nm an ATI Unicam UV/Visible spectrometer in conjunction with 'Vision' software was used. As depicted in figure 5.5 the Unicam spectrometer measures light transmitted by a thin film along the axis of a probe beam at wavelength (λ), and compares it with intensity of the probe beam before the interaction at the same wavelength. A bandwidth of 2nm was used which prevented the need for slit width correction according to Swanepoel[4] (1983).

In order to remove the effects of substrate absorption an uncoated substrate was measured and used as a baseline. The absorption (A) measured by the instrument is related to transmission (T) by the following formula, $A=2-\log(\%T)$. The 'Vision' software was consequently able to convert absorbance data into % transmission as and when required.

The signal to noise ratio of the absorbance peaks was increased using the specially designed 'Intelliscan' function. The instrument monitored the energies in both the sample and reference beams, reducing the scan speed during absorbance peaks where noise tends to be higher. This has the effect of increasing the time available for measurement at each data point. The instrument then increased the signal to noise ratio by averaging out random noise in the signal. The peaks were therefore measured with an improved signal to noise ratio. In the low absorbance areas of the spectrum, the scan speed was increased so that little time was spent on these areas.

5.3.2 The Electrical and Photoelectrical Characterisation System

The electrical characterisations performed on the materials and devices throughout these studies can be divided into three main areas AC , DC and photoelectrical. To make these characterisations easier to perform much of the equipment used was interfaced with a Farnell SW1B IEEE-488 switching unit and from there to an IBM-PC. The software developed in house enables the user to perform automatic Capacitance/voltage C(V), and current/voltage I(V) investigations for temperatures in the range 77K-300K. Plates 5.3 and 5.4 display the electrical characterisation system used.
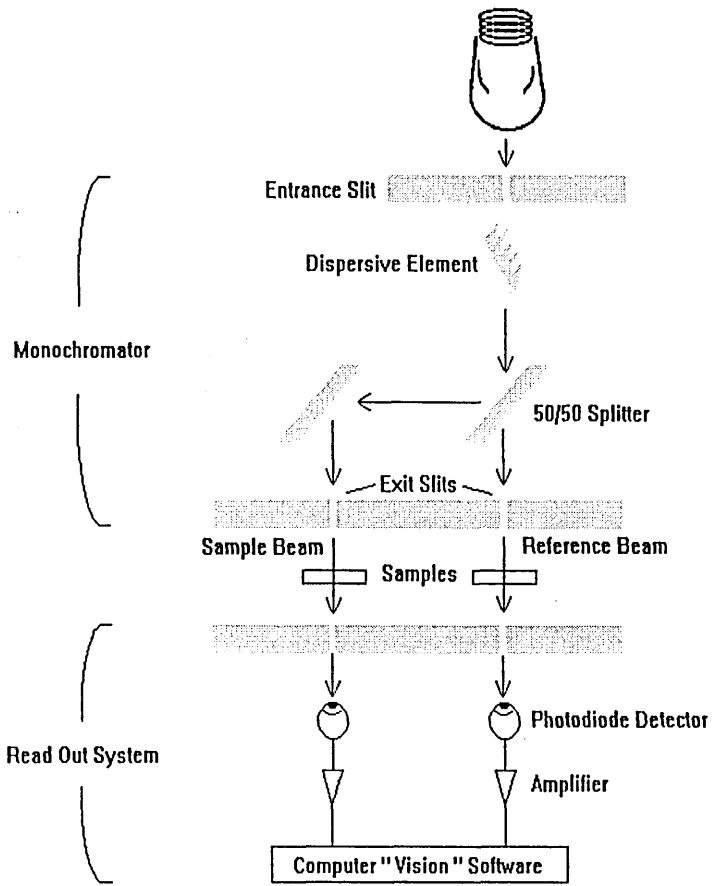
Figure 5.5 Schematic representation of the principle components for optical absorption/transmission.
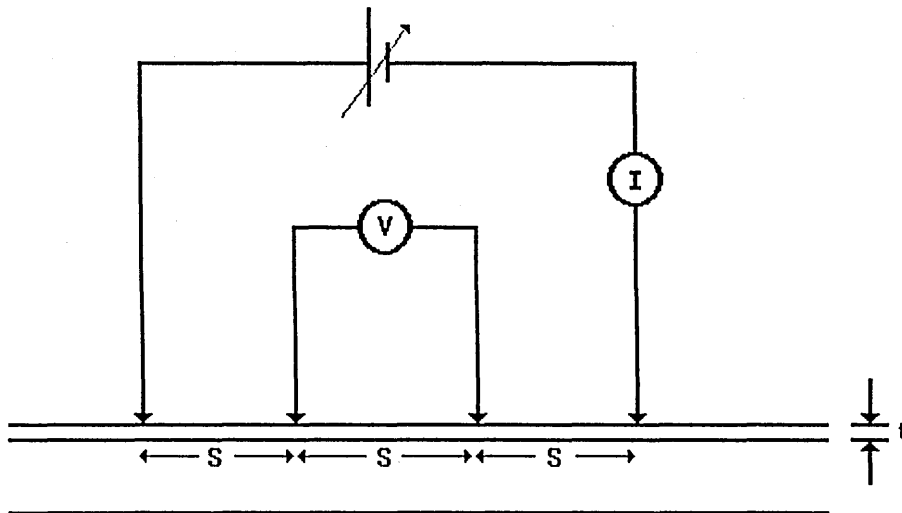
Figure 5.6. 4-Point probe analysis for determination of base electrode sheet resistance, where s=1mm.
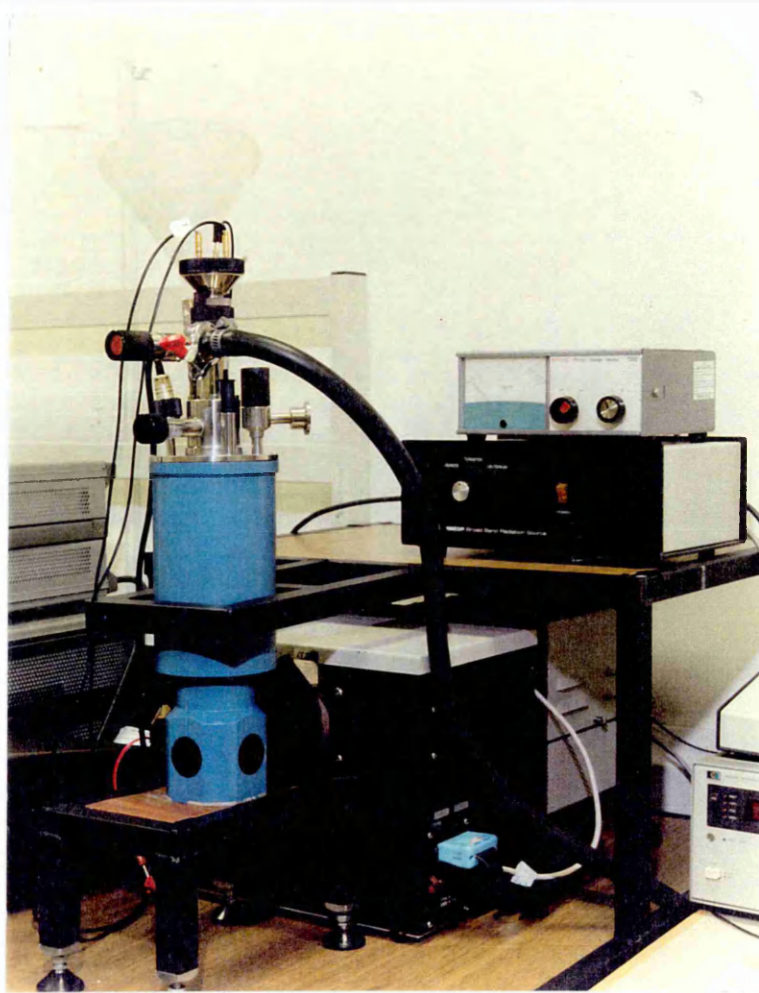
Plate 5.3
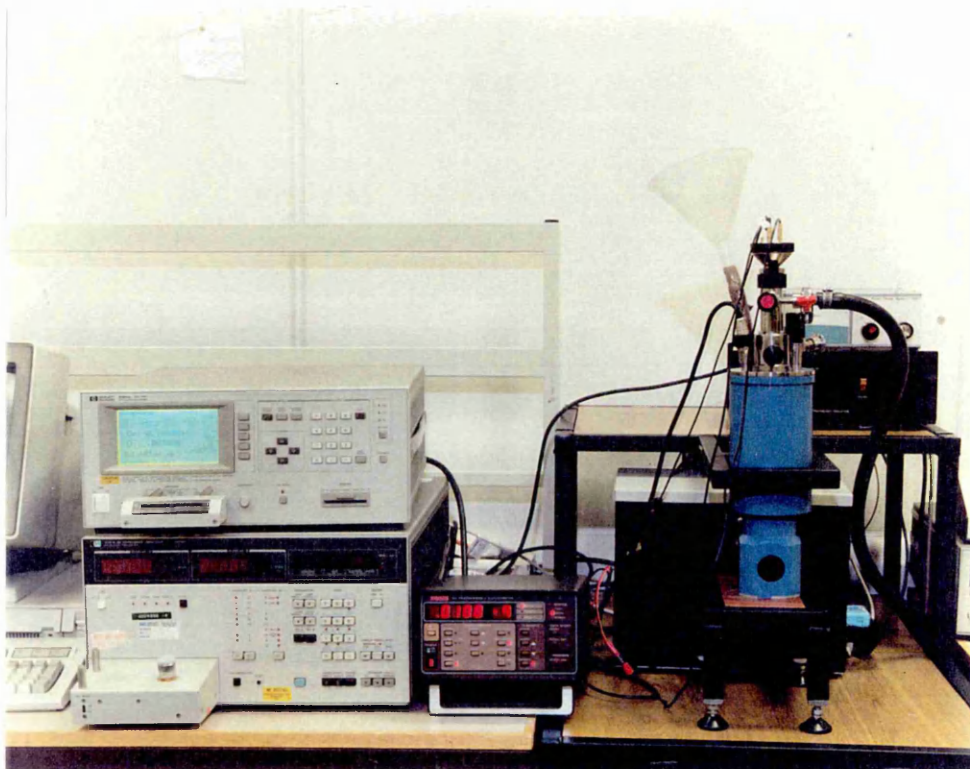
Plate 5.4

For electrical measurements a Keithley 617 electrometer was used as a voltage source and ammeter to record I as a function of the applied bias potential. The electrometer is capable of supplying a voltage in the range +/- 100V in steps of 0.05V and measuring currents from 2mA to as low as 10^{-12}A. The electrometer has a cut off at 2mA, therefore for more conductive samples the electrometer was replaced for a Farnell LT30-1 stabilised power supply and a Fluke 8010A digital multimeter.

DC conductivity (σ_{DC}) was then calculated according to the formula;

$$\sigma_{DC} = \frac{Jt}{V} \qquad\qquad 5.2$$

where J is the measured current density, V the applied bias and t is the material thickness. For determination of the sheet resistance (R_{ST}) of the conducting glass electrodes a 4 point probe analysis was performed as depicted in Figure 5.6. R_{ST} was then calculated according to the formula;

$$R_{ST} = 4.53\frac{V}{I} \qquad\qquad 5.3$$

For C(V) measurements a precision Hewlett Packard LCR meter with an oscillating voltage of 1V peak to peak and a frequency range of 20Hz-1MHz was used. A DC bias could be varied across the device, which allowed C(V) analysis to be performed for constant frequencies. A schematic representation of the electrical characterisation system is shown in Figure 5.7.

Illumination for wavelength dependent measurements was provided by a SPEX 1682p broad band radiation source. The 1683L tungsten/halogen incandescent lamp supplies illumination over 300 to 3000nm although the wavelength range of interest in these studies was kept within the visible region 300-900nm. The intensity was found to be in the order of 32 $\mu W/cm^2$ measured using an Anritsu optical power meter model ML9001A.

Intensity stability over the wavelength range was provided by an optical feedback circuit that regulates the magnitude of the current applied to the lamp by the 1683P power supply. Any fluctuations due to line voltage or lamp ageing were therefore avoided. The lamp intensity varies by +/- 1.25% / hour after warm up.

The radiation source was used in conjunction with a Spex1681 0.22m spectrometer and 1673 minidrive which provided and controlled the desired wavelength respectively.
A model 9500 solar simulator with a 1kW high pressure metal halide lamp supplied by Applied Photophysics was used as a light source. The lamp had a spectral distribution closely matching that of the AM2 solar spectrum (equivalent to the sunlight reaching the earth's surface).

The simulator was not equipped with the ability to vary intensity although moving the lamp nearer or further from the cryostat optical window allowed a range of stable intensities from 2-25 W/m^2. The photocurrent was therefore measured for 5 intensities within this range. The intensity was corrected for absorption losses due to the cryostat. The actual range of intensities used in these studies was 0.16-2 mW/cm^2.
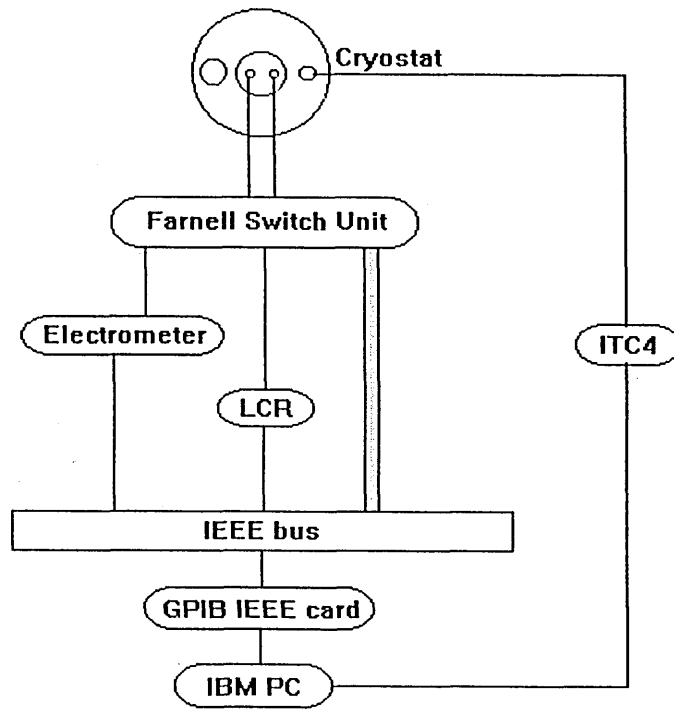
Figure 5.7 Schematic representation of the electrical characterisation system.
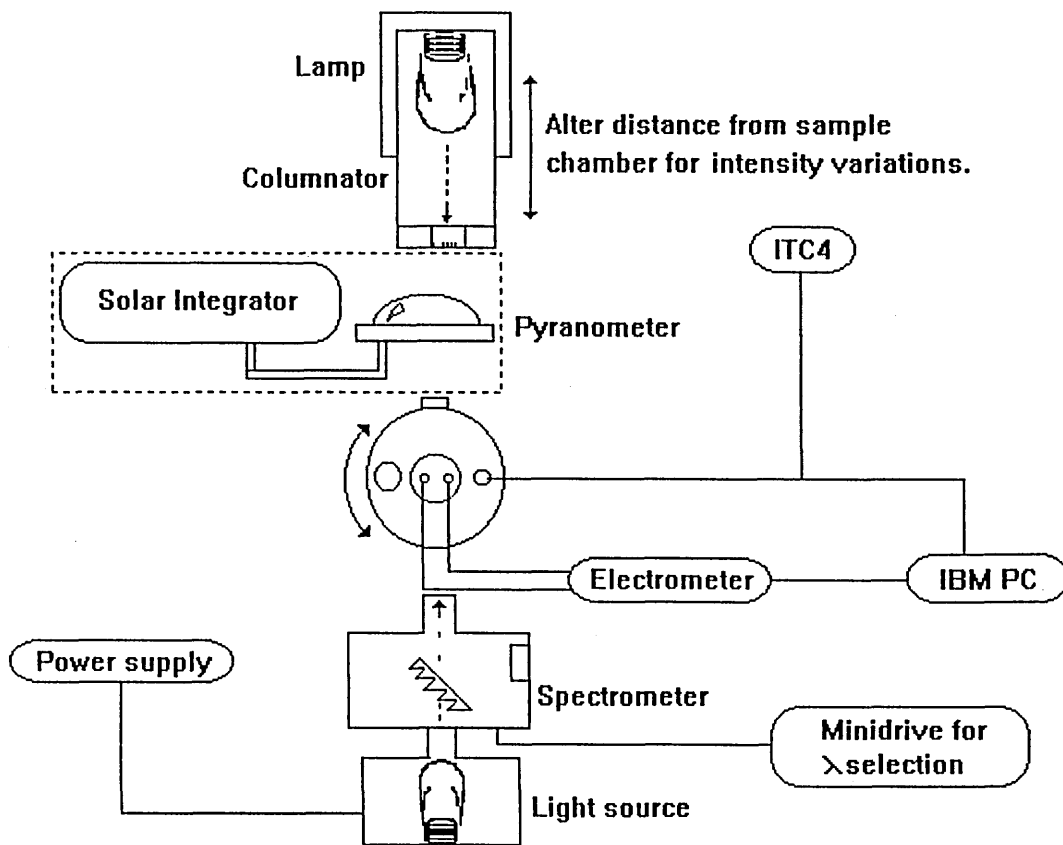
Figure.5.8 A schematic of the photoelectrical characterisation system.

114

For the determination of the Solar simulator intensity, values were measured using a CM11 Kipp and Zonen Pyranometer in conjunction with a CC10 Kipp and Zonen Solar integrator. The pyranometer measures global radiation (the downward component of the direct and diffuse solar radiation) in a spectral range of 305-2800nm. It produces a voltage which is directly proportional to the solar irradiance level. The voltage is read by the integrator where it is amplified to a normalised value. The irradiance is then converted to Wm^{-2} by dividing the output voltage in μV by the sensitivity of the pyranometer in $\mu V/Wm^{-2}$. The sensitivity of the pyranometer was pre-determined in the manufacturers lab as 4-6.5 $\mu V/Wm^{-2}$. The integrator had a measurable range of 2-200Wm^{-2} and a resolution of 1Wm^{-2}. Irradiance measurements were taken automatically every 0.6 seconds. A diagram of the photoelectrical characterisation set-up is shown in Figure 5.8

A thorough electrical and photoelectrical characterisation of materials and devices ideally requires measurements to be taken at a range of temperatures and if possible ambient conditions, i.e. under Nitrogen, vacuum or atmospheric conditions.

For temperature and/or ambient dependent measurements the devices were mounted in an Oxford Instruments Liquid Nitrogen cryostat. The cryostat in conjunction with an ITC4 Intelligent temperature controller allowed measurements to be taken in the temperature range 77K to 292K and under a variety of ambient conditions. For temperature dependent measurements surrounding the devices in nitrogen gas prevented ice formation on their surface. Figure 5.9 is a cross section of the liquid Nitrogen cryostat.
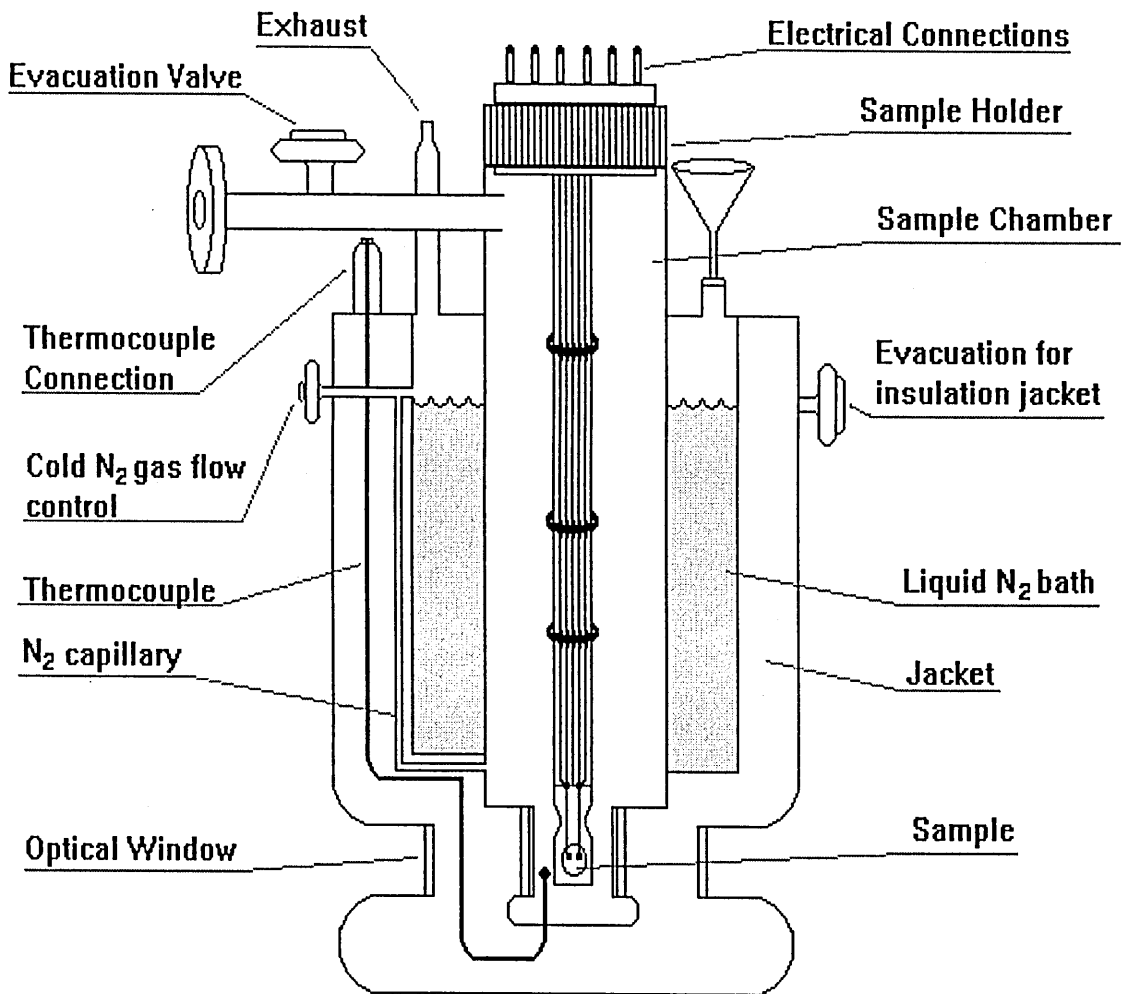
Figure. 5.9 Cross sectional view of the Oxford Instruments Liquid Nitrogen Cryostat.

5.3.3 Structural Characterisation Techniques

The chemical and physical properties of materials are strongly influenced by their structure at an atomic level[13]. Therefore, in order to understand the properties of materials, it is necessary to understand their structures. Structural characterisation involved X-ray diffraction studies, thickness measurements, scanning electron microscopy and optical microscope studies.

5.3.3.1 Infra Red

Infra red analysis was carried out using an ATI Mattson Genesis Series FTIR spectrometer in the wavenumber range 500 to 4000 cm^{-1}. These studies were necessary in order to identify the presence of any organic residue, water or solvent left after heat treatment of the Sol-Gel derived products. Due to problems associated with substrate absorption all infra red analysis was carried out on Sol-Gel residues.

The KBr disc method[14] proved to be the most appropriate. Approximately 1% by mass of the powdered sample was added to KBr powder and crushed into a thin pellet suitable for infra red analysis. A pure KBr pellet. was formed to provide a baseline.

5.3.3.2 X-Ray Diffraction

X-ray diffraction studies highlight any internal regularity and in the case of TiO_2 will distinguish between the various forms (i.e., anatase, rutile, brookite) or will reveal if the films are amorphous[15]. In order to determine the effect of the process route and heat treatment conditions on the structure of the Sol-gel product powder X-ray diffraction studies were performed on residues of the Sol mixture. Gels were dried and subjected to identical heat treatment to the coating films. These experiments were carried out using a Philips PW1710 diffractometer with monochromated Cu radiation and a scan speed of 0.01 degree (2θ) per second.

5.3.3.3 Scanning Electron and Optical Microscopy

A Philips XL40 Scanning Electron Microscope and a Zeiss optical microscope were required to investigate the surface quality of the materials used , i.e. whether the films were cracked/homogeneous/porous. SEM studies were also used to determine TiO_2 film thickness, the samples were investigated in cross section and were therefore snapped or cut using a diamond saw.

For SEM studies, it was necessary for the samples to be coated in conductive materials such as gold, platinum or carbon. This prevented 'shadowing' which can inhibit viewing. Shadowing is caused by highly charged areas repelling electrons, the result is a dark patch around a very bright charged area. SEM studies were also used to accurately

calculate electrode width and interelectrode spacing of the interdigitated electrodes as shown in Plate 5.1.

5.3.3.4 Surface Profiling for Thickness Determination

A planar surfometer (Surfcom 300) was used to measure the TiO_2 film thickness to an accuracy of approximately $\pm 0.01\mu$. The surface profiler measured the thickness of the TiO_2 coating by traversing a stylus across the slide to the coating edge and beyond for a total distance of 2mm. For each coated sample a total of 4 thickness measurements was made (2 on each side of the sample). Vertical movement of the stylus under the application of a small force is amplified electronically and reordered as a graphical representation of the difference in level between the surface of the substrate and the TiO_2 coating. As the stylus traverses it reveals information on the surface contour, therefore as well as thickness, to some extent surface quality may be assessed.

5.4 Factorial Experimental Design

Factorial experimental design is a useful statistical technique for analysing variation in experimental results, which may be caused by an individual factor (i.e. feature of the experimental conditions) or an interaction of two or more factors[16]. Each factor may take on a number of levels where a specific combination of factor levels is called a treatment combination. The numerical results of treatment combinations are termed the responses or observations, which must be expressed quantitatively. An experiment refers to the whole set of treatment combinations carried out.

It must be noted that there are two types of factors, qualitative and quantitative. A qualitative factor is one for which the different levels cannot be assigned in order of magnitude, for example a particular brand or make of a similar material used. The quantitative factors can be arranged in order of magnitude, temperature or applied voltage for example.

The factorial design technique is the most efficient to use when two or more factors are to be examined. It offers many advantages over the traditional one-factor-at-a-time approach in which the effect of changing any one variable is assessed independently of the others. Most importantly the factorial experiment detects and estimates any interaction, which a one-at-a-time analysis cannot do. When there are interactions, (although initially unknown) a factorial design is necessary to avoid misleading conclusions. When no interactions exist the factorial design method gives maximum efficiency in the estimation of the effects. In addition, for n factors the design will require n times fewer measurements than the traditional approach to achieve the same precision.

The procedure for designing an experiment for factorial analysis is straight forward, though the analysis requires a knowledge of statistical techniques. In particular the area of hypothesis testing, which also includes an understanding of the analysis of variance method (ANOVA)[17].

The technique was used to investigate the effects and interactions between various Sol-Gel process parameters on the thickness and absorption properties of the TiO_2 films.

5.4.1 For TiO$_2$ Analysis

There are a number of types of factorial designs which may be used, the simplest and most efficient is a design that involves factors at 2 levels, a 2^n design where n is the number of factors. This was the design adopted in the current studies. The Sol-Gel parameters or factors studied are given in Table 5.2, along with the corresponding levels (2 levels for each factor representing high and low).

The factors are conventionally denoted using higher case letters, hence A-D, while the treatment combinations denoted using lower case letters a-d. The absence of the lower case letter demonstrates that a particular factor is at a low level. For example, the combination 'acd' represents a treatment where the withdrawal rate used was high (250mm/min), the molar ratio of acetic acid:TIP was low (3.14:1), the number of coatings was high (4) and the concentration of coating solution was high (12.6%). The observations or results of the particular experiment are written in a standard order shown in Appendix B, Tables 1, 3, 5 and 7. These observations are numerical and in these studies represented overall coating thickness, individual layer thickness, absorption and absorption coefficient. As such n=4, and consequently this is a 2^4 design which represents 16 combinations (or samples to produce).

The total effects of each treatment combination were calculated using the systematic tabular method derived by Yates[18], where columns of sums and differences are derived. For a 2^n design the calculation is carried out n times to obtain n columns of sums and differences.

To demonstrate this procedure, the results obtained for the overall coating thickness are used as a worked example. The corresponding Yates table is shown in Appendix B, Table 1. Referring to the table, the effects of each treatment combination are written beside the corresponding letters of the treatment combination, i.e. the overall coating thickness measured on a sample prepared according to the condition 'ac' (where the withdrawal rate and the number of coating layers were at a high level and all other factors were at a low level) was 0.15μ. This is continued for all factors and combinations as far as 'abcd', (which had an overall coating thickness of 0.38μ).

In order to carry out the statistical analysis an estimate of the experimental error is required. There are a number of ways in which this can be obtained, the most accurate was used which is to replicate the observations, (i.e. repeat the experiment). The replicate observations are entered into the table in a similar fashion to the original measurements. For experiments with replication, the sum of the original and repeated measurements (i.e. the sum of the replicate observations) are entered in the standard order depicted in Appendix B, Table 1. Then a series of columns are generated (4 columns for a 2^4 design.) in the manner now described. The first 8 numbers in each column are obtained by adding together successive pairs of the numbers in the preceding column (e.g. the first number in column (1) is 0.29 which is (0.15+0.14)), with the final 8 numbers being obtained by subtracting successive pairs of numbers in the preceding column, (e.g. the last figure in column (1) is 0.41 which is (0.77-0.36)). This process is continued for columns (2) to (4) (e.g. the final figure in column (4) is 0.12 which is (0.25-0.13)).

Code	Factor	High Level	Low Level
A	Withdrawal Rate	250 mm/min	100 mm/min
B	Molar Ratio acetic acid:TIP.	4.16:1	3.14:1
C	No of coatings.	4	1
D	Concentration of TIP to anhydrous ethanol.	12.6%	6.3%

Table 5.2. Factors studied with corresponding high and low levels.

Order	Procedure	Comments
1	Decide on null hypothesis H_o	The null hypothesis implies no difference, i.e. in these investigations it represents no significant effects or interaction between factors
2	Decide on alternative hypothesis H_1	i.e. that the opposite of H_o is true
3	Decide on significance level	i.e. 5% level states that there is a 5% risk of rejecting H_o in favour of H_1 when H_o is actually correct
4	Calculate appropriate test statistics	
5	Find from tables appropriate tabulated test statistic	
6	Compare tabulated and calculated	If $F_{calc} > F_{tab}$ then reject H_o
7	State conclusions and assumptions of test	i.e. if H_o is rejected the effect or interaction is significant at the chosen significance level.

Table 5.3. Complete hypothesis test.

The figures in column (4) represent the total factorial effects of the factors and interactions [A] to [ABCD]. The mean factorial effects and interaction effects are calculated by dividing the total factorial effect by 2^{n-1}, where n, in this case, equals 4. The next step is to carry out a complete hypothesis test. The procedures for this test are outlined in Table 5.3.

Parts 4-7 of the hypothesis test use the analysis of variance (ANOVA) method[17] in order to decide if the main effects and/or the interactions are significantly large. Again, the ANOVA table derived for the overall coating thickness given in Appendix B, Table 2 is used as an example. The test statistic used is the F-distribution. F_{calc} is derived for each observation, this is obtained by first calculating the sum of squares (SS) for each observation given by equation 5.4, where r = number of replicates and in this case is equal to 2.

$$SS = \frac{(total\_effect)^2}{2^n r} \qquad\qquad 5.4$$

e.g. the sum of squares of the effect of withdrawal rate [A] is given by;

$$SS = \frac{(0.78)^2}{2^4 \times 2} = 0.019$$

The means squares (MS) for each observation is then calculated using equation 5.5, where df = degrees of freedom.

$$MS = \frac{SS}{df} \qquad\qquad 5.5$$

F_{calc} for each effect is then the ratio of the mean square of that effect to the error (residual) mean square. This is the difference between the total sums of squares of all ($2^n.r$) individual observations and the 'sum of' the sum of squares for the treatments divided by the degrees of freedom.

F_{calc} is then compared with F_{tab} (which is obtained from statistical tables of the F-distribution using the appropriate degrees of freedom and significance level). If F_{calc} is greater than F_{tab}, H_o is rejected and the effect or interaction can be concluded to be significant at that level.

A large interaction indicates that the effect of one factor is markedly dependent on the level of the other, yet when quoting the effect of one factor the level of the other is specified. When the interaction can be assumed to be negligible it may be inferred that the factors operate independently. A single factor need only be tested for significance if it does not interact with other factors.

REFERENCES

1. Schwartz, N., and Berry, R. W. *Physics of Thin Films*, Vol 2, Academic Press 1964.

2. Stuart, R. V. *Vacuum Technology, Thin film and Sputtering: An Introduction.* Academic Press Inc. 1983.

3. Kutzler, F. W., Barger, W. R., Snow, A. W., and Wohltjen, H. *Thin Solid Films.* **155**(1) (1987) 1-16.

4. Swanepoel, R. *J. Phys. E: Sci. Instrum.* **16**(1983) 1214-1222.

5. *Personal Communication*, School of Science: Chemistry Department Sheffield Hallam University.

6. Exley, J. PhD Thesis. *Electrical and Optical Properties of Novel Phthalocyanine Compounds for Sensor Devices* (1995). p. 80.

7. Lide, D. R. *Handbook of Chemistry and Physics.* CRC Press. 72nd ed. (1991-1992).

8. Yase, K., Takahashi, Y., Arakato, N., and Kawazua, A. *Jap. J. Appl. Phys. Part 1.* **34** (2A) (1995) 636-637.

9. Yanagi, H., Kataura, H., and Ueda, Y. *J. Appl. Phys.* **75**(1) (1994) 568-576.

10. Krier A, Abass A. K., and Collins, R. A. *Adv. Mat. Opt. Elec.* **2** (1993) 289-293.

11. Gould, R. D., and Hassan, A. K. *Thin Sold Films.* **223** (1993) 334-340.

12. Boudjema, B., Guillard, G., Gamoudi, M., Maitrot, M., Andre, J. J., Martin, M., and Simon, J. *J. Appl. Phys.* **56** (8) (1984) 2323.

13. Elliot, S. R. *Physics of Amorphous Materials. 2nd ed.* Longman; John Wiley & Sons. (1992) p.71.

14. Roberts, J. D., and Caserio, M. C. *Basic Principles of Organic Chemistry.* W. A. Benjamin Inc. (1964) p.29.

15 Takahashi, Y., and Matsuoka, Y. *J. Mat. Sci.* **23** (1988) 2259-2266.

16. Montgomery, D.C. *Design and Analysis of Experiments,* John Wiley & Sons, New York, 2nd ed. 1984.

17. Ogawa, J., *Statistical Theory of the Analysis of Experimental Design*. M. Dekker. (1974).

18. Yates, F. *Imp. Bur. Soil Sci. Tech Comm.* **35** (1937)

Chapter 6

TiO$_2$ Characterisation : Results

6.1 Introduction

In the Sol-Gel process there are many parameters that may be considered, for example, relative concentrations of the precursor, acid and solvent, number of coatings layers, withdrawal rates, annealing temperature, annealing time and substrate type. An in depth examination of the effects and interactions of all these would be outside the limits of this programme of research. Consequently, the study was restricted to those factors which, after preliminary investigations, were observed as having notable effects on the Sol stability and the optical, structural and electrical properties of the resulting films.

Initial studies conducted on TiO$_2$ samples were to discover a suitable procedure for film production, this could then be used to fabricate samples for a factorial design experiment and ultimately in the construction of the dye sensitised cell.

6.2 Sol Stability

Factors that affected the overall Sol stability and lifetime were found to include respective concentrations of acetic acid and Titanium Isopropoxide (TIP), and the procedure used for Sol preparation. The effect on Sol stability on omitting the reaction modifying acetic acid was an immediate precipitation and films produced from this Sol were inhomogenous. Pre-reacting the TIP with the acetic acid resulted in a strong initial exothermic reaction, and rapid gelation. On adding this mixture to the solvent, gel residues were left on equipment used, which had catastrophic effects on the accuracy of the volumes added. Films prepared from Sols of this type were also inhomogenous and contained small clusters of TiO_x, these were visible under the SEM shown in Plate 6.1. Mixing the TIP with a pre-acidified solution proved to be a more accurate method and reduced cloudiness in the Sols as observed by Yoldas[1]. This procedure was adopted for the production of all TiO_2 films.

For Sols containing less than 4 moles of acetic acid per mole of TIP, and low concentration of TIP the Sols became cloudy after a period of approximately 1 hour and underwent gelation in approximately 2 hours. Sols prepared with more than 4 moles of acetic acid per mole of TIP and of high concentration were found to remain stable and clear for at least 24 hours after which precipitation appeared. Plate 6.2 shows a variety of gels as a function of time. The most stable Sol was that in which the TIP was added to a acidified ethanol solution in a molar ratio of TIP:acid, 1:4.16 and where the TIP concentration in ethanol was 12.6%.
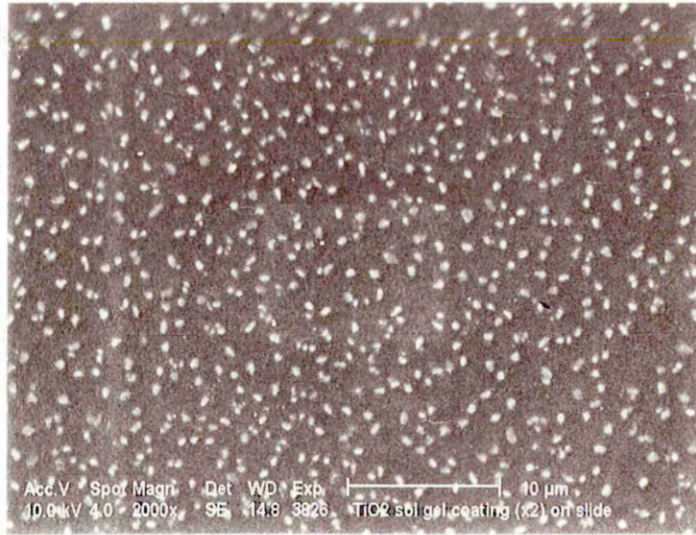
(i)
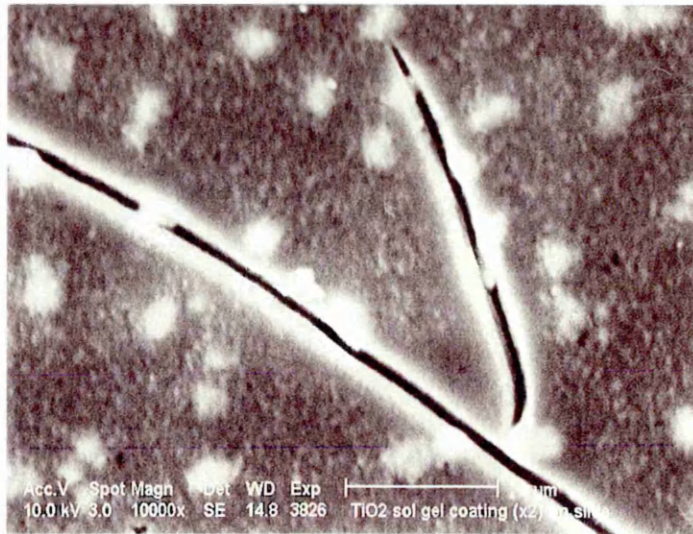
(ii)

Plate 6.1. SEM Micrographs of TiO$_2$ film surface. The Sol was prepared by pre-reacting the TIP with the acetic acid before adding to ethanol. (i) x2000 magnification (ii) x10000 magnification. Clusters are estimated to be between 0.5-1μm in diameter.
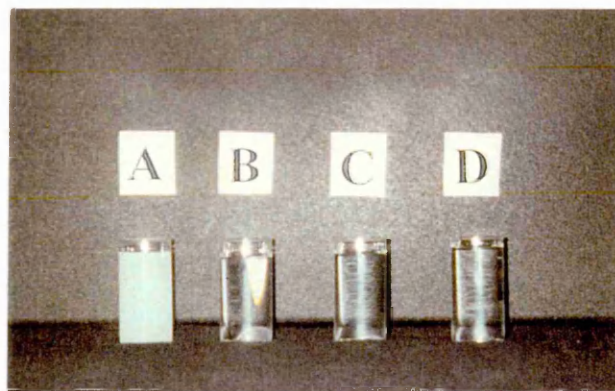
(i)
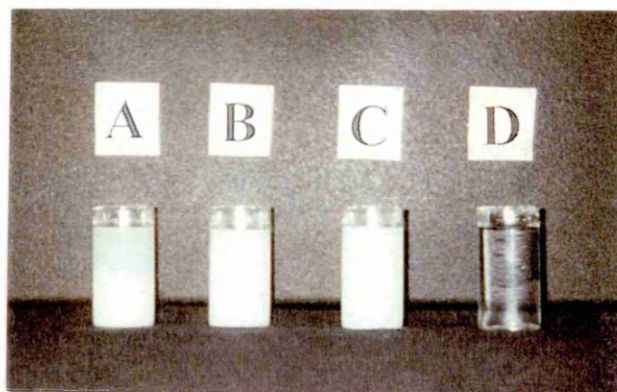
(ii)
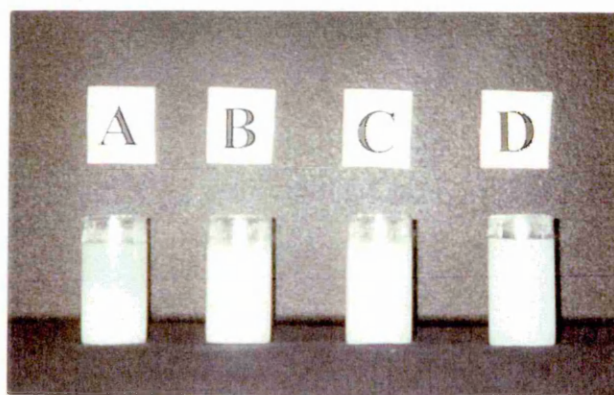
(iii)

Plate 6.2. Degradation of Sols as a function of time. Molar ratios of acid:TIP and TIP concentration in ethanol are as follows, (A) 3:1:1 and 6.3% (B) 3:1:1 and 12.6% (C) 4.1:1 and 6.3% (D) 4.1:1 and 12.6%. Plate (i) after 1 hour (ii) after 12 hours (iii) after 1 day.

131

6.3 Surface Quality: Optical Microscopy

The annealing temperature, annealing time and the TIP:Acetic acid molar ratio, all had an effect on the overall film surface quality. Plate 6.3 is an optical micrograph obtained for a TiO_2 film. The film was prepared from a Sol containing a low concentration of TIP in ethanol and a molar ratio TIP:acid of 1:1.6. The film was annealed to a temperature of $500^{\circ}C$ for 30mins. Plate 6.4 shows the surface of a film prepared from an identical Sol, however the film was heated to $120^{\circ}C$ again for 30mins. Both films exhibit a degree of porosity, however the film heated to $500^{\circ}C$ appears to have a higher pore density/unit area. Qualitative analysis revealed that low heat treatment temperatures and times resulted in larger pore sizes and consequently a visibly lower pore density/unit area. Films that did not undergo any annealing procedure were also highly porous, but had poor adherence to the glass substrates. The annealing is an important part of the Sol-Gel process densifying the gel and removing residual organics and solvent as discussed in chapter 4.

Plate 6.5 shows the surface of a film prepared from the most stable Sol, containing a high concentration of TIP and an increased proportion of Acid to TIP.. Annealing films of this nature for longer times (~5 hours) and to high temperatures (up to $500^{\circ}C$) resulted in densification of the film. The films were visibly transparent, uniform, robust and had no visible porosity at the highest magnification available (x900). The micrograph in Plate 6.5 was taken in an area close to the film edge and cracks are therefore visible. Away from the film edge the films were completely crack free.
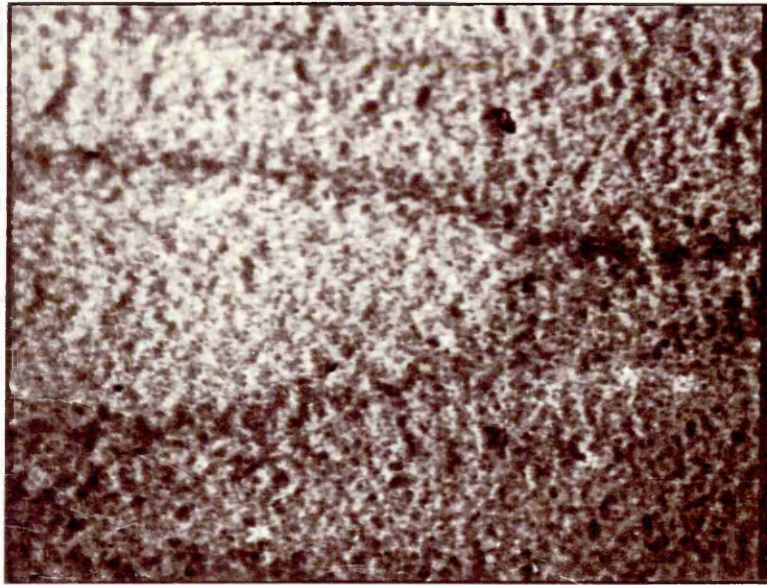
Plate 6.3. Optical Micrograph, (magnification x900) of a TiO$_2$ film surface. TIP in ethanol concentration (~1.4%), Molar ratio of Acetic acid:TIP was 1.6:1. Film was annealed to 500°C for 30mins.
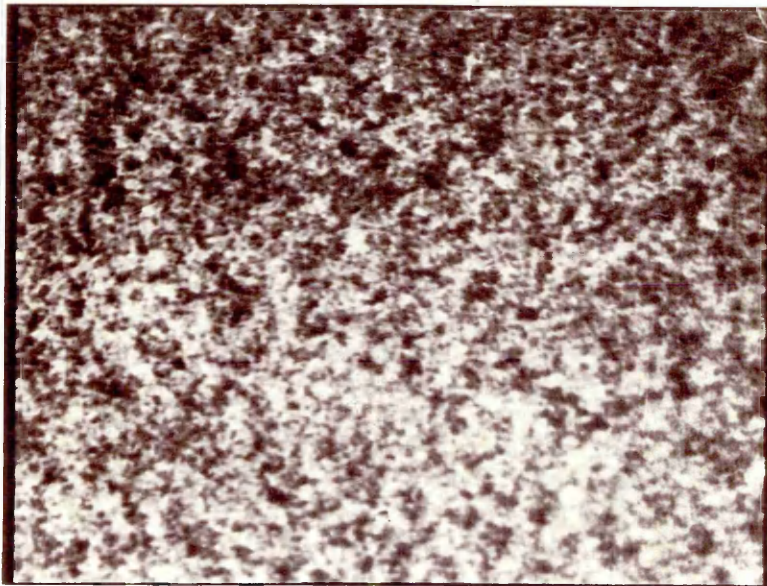
Plate 6.4. As for plate 6.3. In this case film was annealed to 120°C for 30mins.

Plate 6.5. TiO$_2$ film surface, produced from a Sol prepared with a concentration of TIP (12.6%) and a ratio of 1:4.1 TIP:acid. The film was left to dry in air for 24 hours and subsequently annealed to 500°C for 5 hours. (x 900mag).
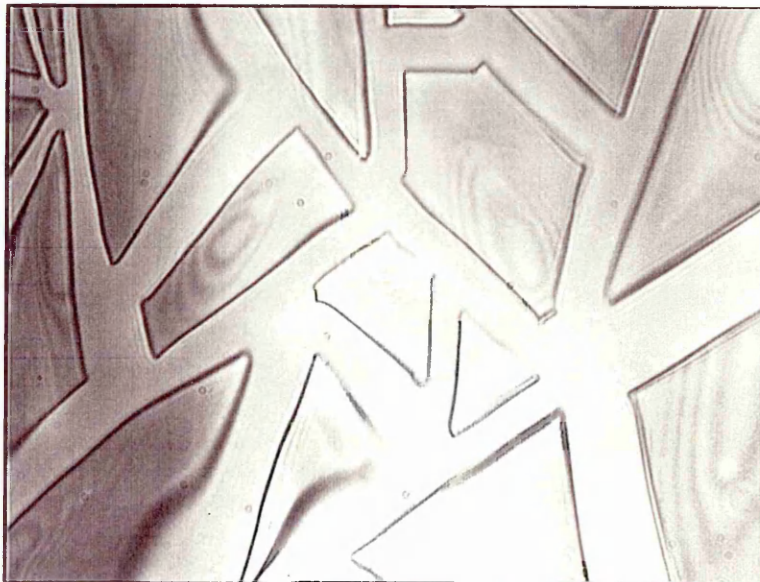
Plate 6.6. Example of film shrinkage and cracking at film edge. (x 900mag).

134

Shrinkage and as a consequence cracking are known to occur during the annealing process as the organics and solvent are removed from the Sol[2], both Plates 6.5 and 6.6 are examples of this effect. The causes of shrinkage have been examined by Brinker[3] in a study of multicomponent borosilicate glass. At low temperatures negligible shrinkage occurs at higher temperatures cross linking and polymerisation of the network results in some shrinkage, however at even higher temperatures large shrinkage results, explained as viscous flow sintering which causes the pores in the gel to collapse. Large shrinkage and little or no pores are visible in the films prepared from the most stable Sols which could be explained by viscous flow sintering.

6.4 X-Ray Diffraction

Figures 6.1 and 6.2 are examples of the powder X-ray diffraction patterns obtained from Sol residues, heated to 350°C and 500°C respectively. Both were heated for five hours and manufactured under identical conditions. A good correlation between the measured interplanar spacings (d-values) of a Gel heated to 500°C and TiO_2 anatase reference d-values obtained from Philips PC-APD diffraction software was observed, as is shown in the table inset of Figure 6.2. It is therefore concluded that an increase in the heat treatment temperature to 500°C caused a gradual crystallisation of the material to the anatase structure. The amorphous phase of TiO_2 was obtained from Sols that underwent no heat treatment. The rutile and brookite forms of TiO_2 were not observed during these investigations.
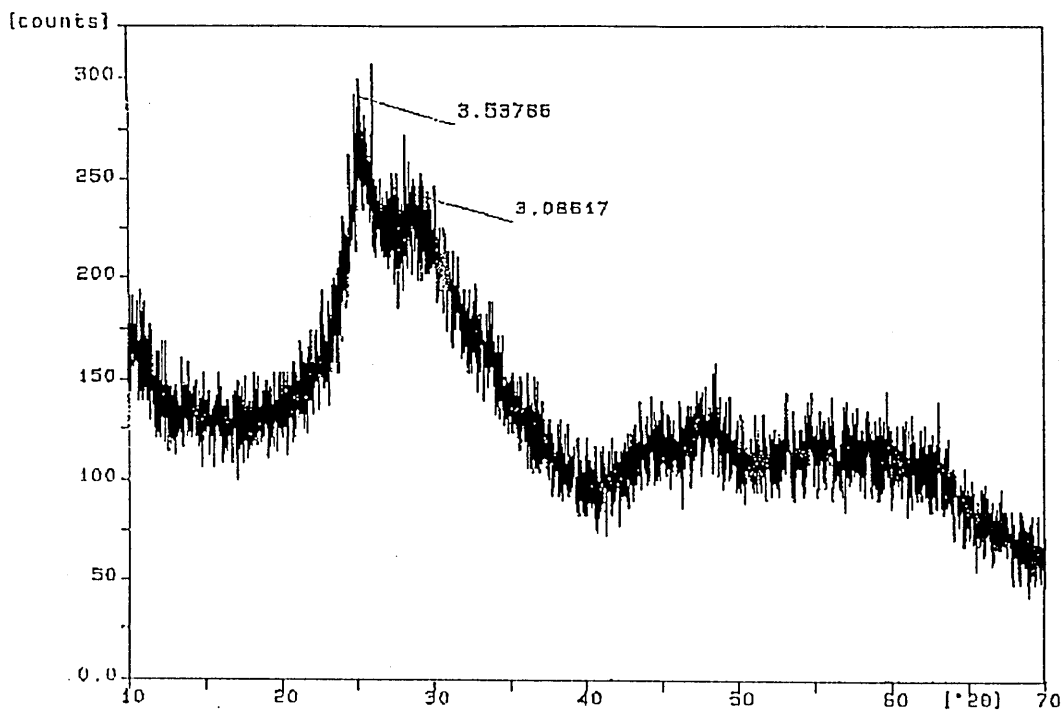
Figure.6.1. The effect of heat treatment temperature on the X-ray diffraction patterns of TiO_2 Sol-Gel residues for a gel heated to 350°C

Angle (°2θ) (a)	d-values [Å] (a)	Angle (°2θ) (b)	d-values [Å] (b)
25.38	3.5065	25.281	3.52
37.78	2.3793	37.801	2.378
48.03	1.8927	48.05	1.892
53.83	1.7017	53.891	1.6999
55.215	1.6622	55.062	1.6665
62.79	1.4787	62.69	1.4808
68.725	1.3647	68.762	1.3641
70.255	1.3387	70.311	1.3378
75.075	1.2643	75.032	1.2649
82.7	1.166	82.662	1.1664
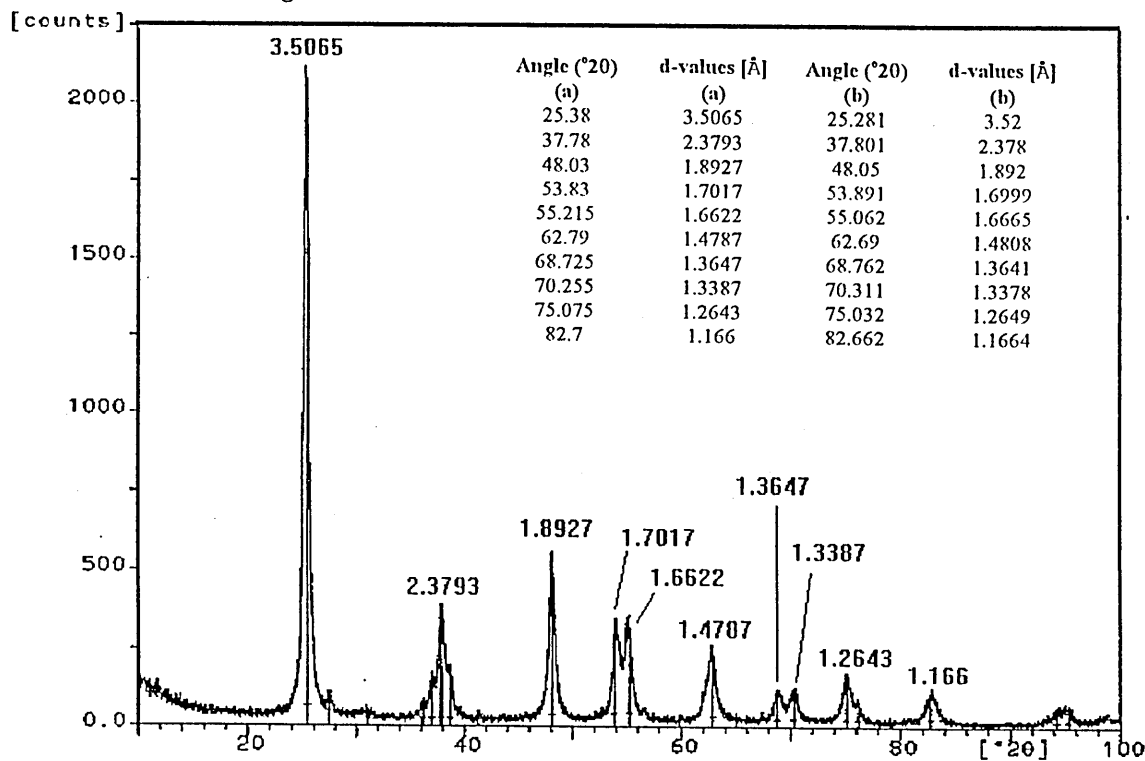
Figure 6.2. As figure 6.1 for a gel heated to 500°C. Table inset shows (a) measured d-values and (b) reference d-values for TiO_2 anatase. Where d is the interplanar spacing, [Å].

136

6.5 Infra Red Studies

The infra red results are shown in Figure 6.3 for residual gels that are a) unheated b) heated to 350°C and c) heated to 500°C for a time period of five hours. The doublet observed for the unheated gel located at 1500cm^{-1} has been attributed previously to chelating acetates[4]. As the heat treatment temperature increases reduction in the intensity of the doublet is observed. The frequency separation of these peaks also noticeably reduces. It is suggested therefore that only the chelating acids remain[4].

At 500°C the spectra shows that there is some absorption remaining from the organic residues, although this is minimal. It is suggested that this absorption may have been eliminated in submicron thickness films rather than the bulk gels. Higher heat treatment temperatures were not be investigated due to the limitations of the glass substrates used.

6.6 Thickness Studies

6.6.1 Via Scanning Electron Microscopy.

Plate 6.7 and 6.8 are SEM micrographs showing fracture cross sections of TiO_2/ glass substrates. The samples were prepared via a diamond saw or by snapping the sample into cross sections. In both cases the TiO_2 layer is visible. For the sawn sample, (Plate 6.7) the film appears to be less than a 1μm thick. Contrary to this for the snapped sample (Plate 6.8) the film appears to be much thicker by ~2-3μm. The SEM was not an exact method of accurately determining TiO_2 film thickness.
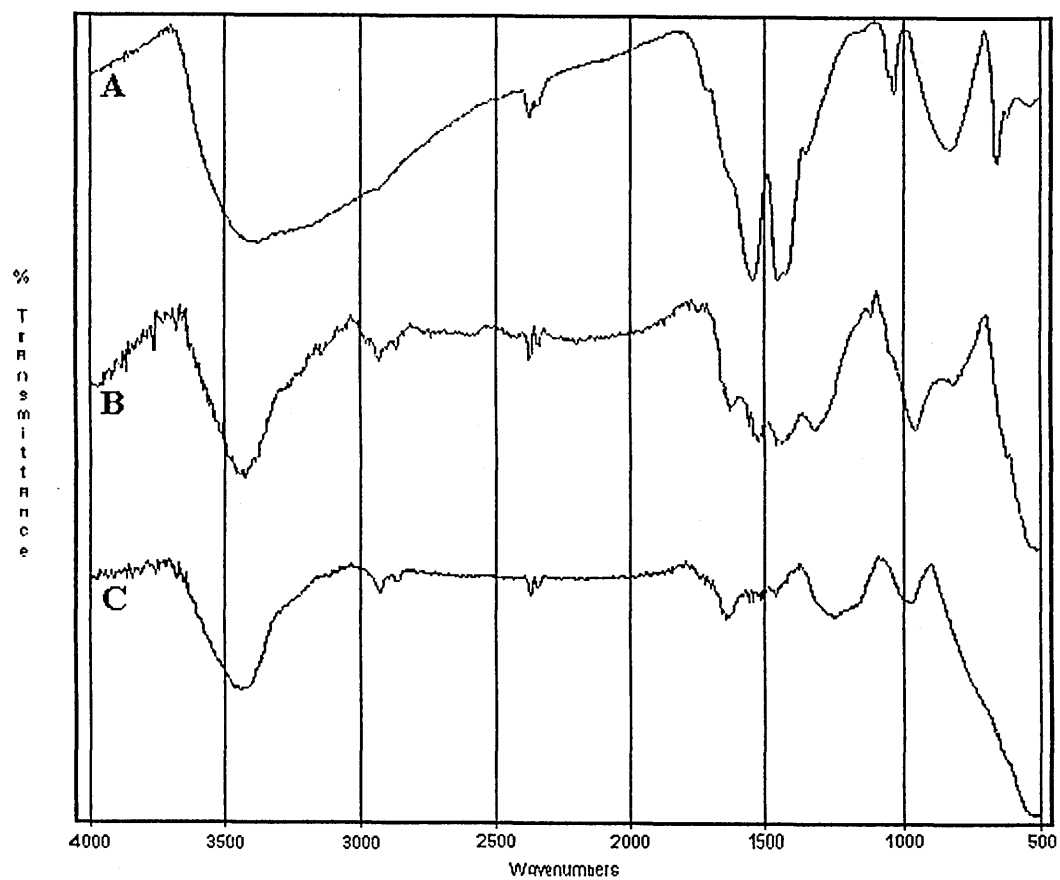
Figure.6.3. Infra Red absorption spectra for variously heat treated TiO_2 gels.
(A) unheated (B) 350°C and (C) 500°C. All gels were heated for 5 hours.

The insulating nature of the substrate, and the identification of glass/TiO_2 boundaries were factors that contributed to this. The appearances of the fracture cross sections confirmed the excellent adherence of the films to the substrates.

6.6.2 Via Surface Profiling

An example of a surface profiling trace is shown in Figure 6.4. In all cases there was evidence of a small region of considerably greater thickness (approximately 1 μm) close to the top edge of the coated region. Although this increase in thickness may be attributed to the jump of the 'stylus' as it traverses the slide and hits the film. Further to this, there was some evidence of a slight and gradual reduction in coating thickness towards the bottom of the dip coated substrate. This latter point was extremely difficult to confirm due to variations in the flatness of the substrate at this scale.

However, outside of these areas the results of the thickness determinations carried out on the coated glass substrates indicated that this was generally consistent across the coatings, with total film thickness' in the range 0.03 to 0.37 μm being produced according to the process parameters used. The results obtained for thicknesses determined via the surface profiling technique were analysed using FED as discussed in section 5.4 the results of which are detailed in section 6.6.4.
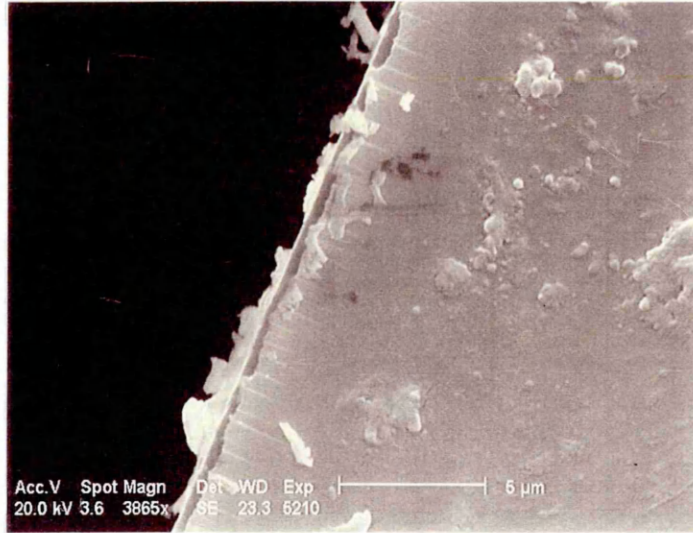
Plate 6.7. SEM of fracture cross section showing TiO$_2$/glass boundary. Section was prepared using a diamond saw.
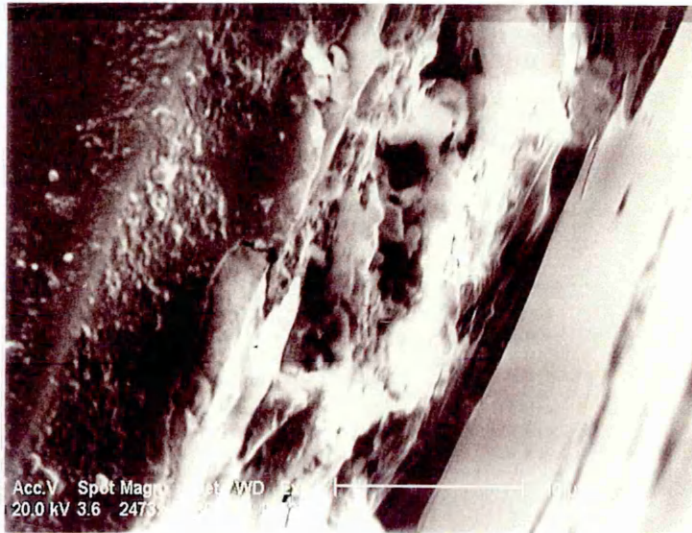
Plate 6.8 Similar cross section sample was prepared by snapping.

6.6.3 Via the Swanepoel Method of Interference Fringes

Interference spectra were not observed for samples with less than 4 coatings. This suggested that the total coating thickness for samples with more than 4 coatings must be in the order of the wavelength of visible light. The samples under investigation were prepared from the most stable Sol, where the molar ratio of Acetic acid:TIP was 4.16:1 and the concentration of TIP in ethanol 12.6%, the films were annealed to 500°C for 5 hours.

Typical transmission interference fringes observed for the Sol-Gel derived TiO_2 films are shown in Figure 6.5, for 5, 6, and 7 TiO_2 layers. The transmission spectrum of the glass substrate, (T_s) is also shown. As the number of layers (hence thickness) increased more interference maxima and minima became visible.

An approximately linear relationship was observed between the number of applications and the overall coating thickness, as shown in Figure 6.6. The film thickness was likely to be controlled by the number of coating applications. The effect of withdrawal rate on the TiO_2 film thickness was considered. Two withdrawal rates, a high rate of 250mm/min and a low rate of 100mm/min were used. Figure 6.7 is an example of the effect of each withdrawal rate on the interference fringe patterns. The higher rate caused more fringes to become visible, again implying an increase in film thickness. Analysis of the transmission fringes according to the Swanepoel[5] method confirmed that this was the case. A higher rate produced thicker films.

$\lambda c =$ _____ mm
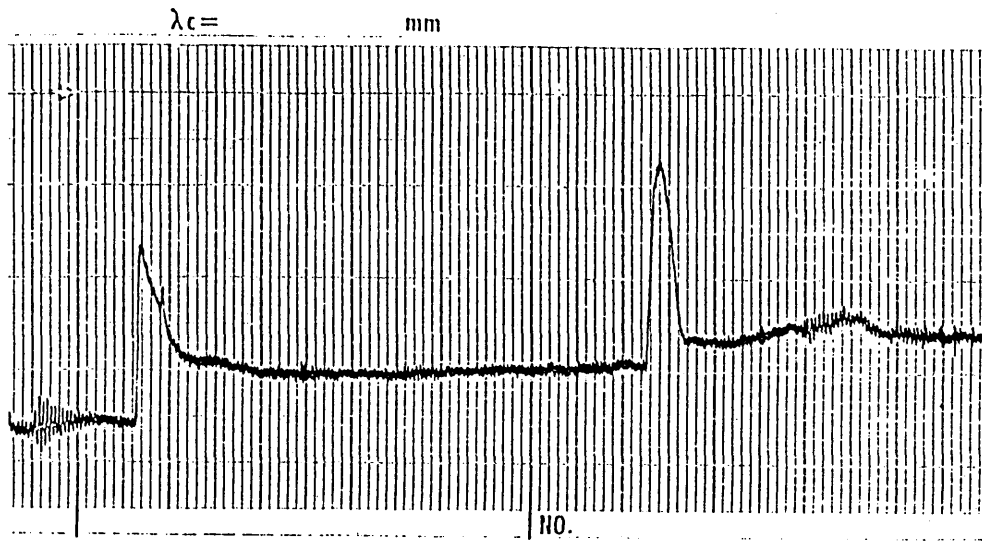
Figure 6.4. Example of surface profiling trace for a TiO$_2$ film on a glass substrate. Trace shows layers 3 and 4. Average total coating layer thickness for this 4 layer sample (sample C in factorial experiment was estimated to be 0.12μm.+/- 0.02μm.
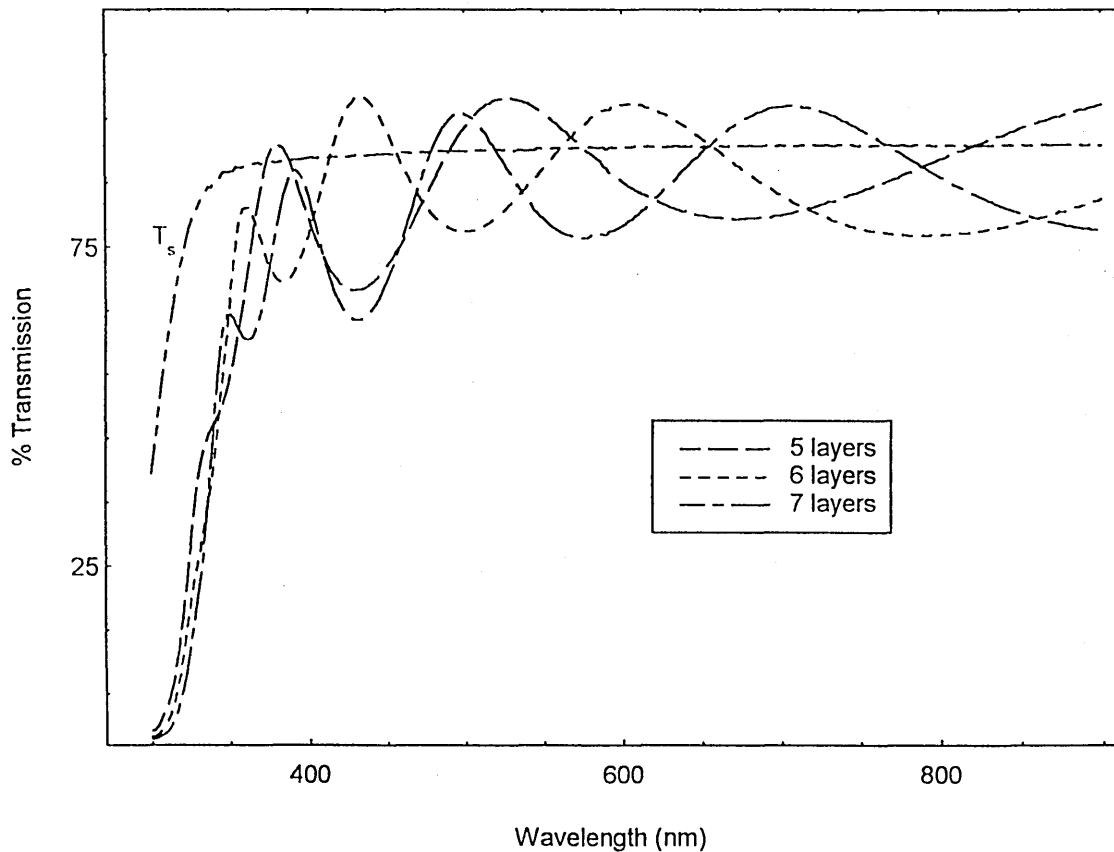
Figure 6.5. Example of transmission interference fringes observed for TiO$_2$ coatings with 5,6 and 7, and layers, the transmission spectra (T$_s$) for the glass substrate is also shown.
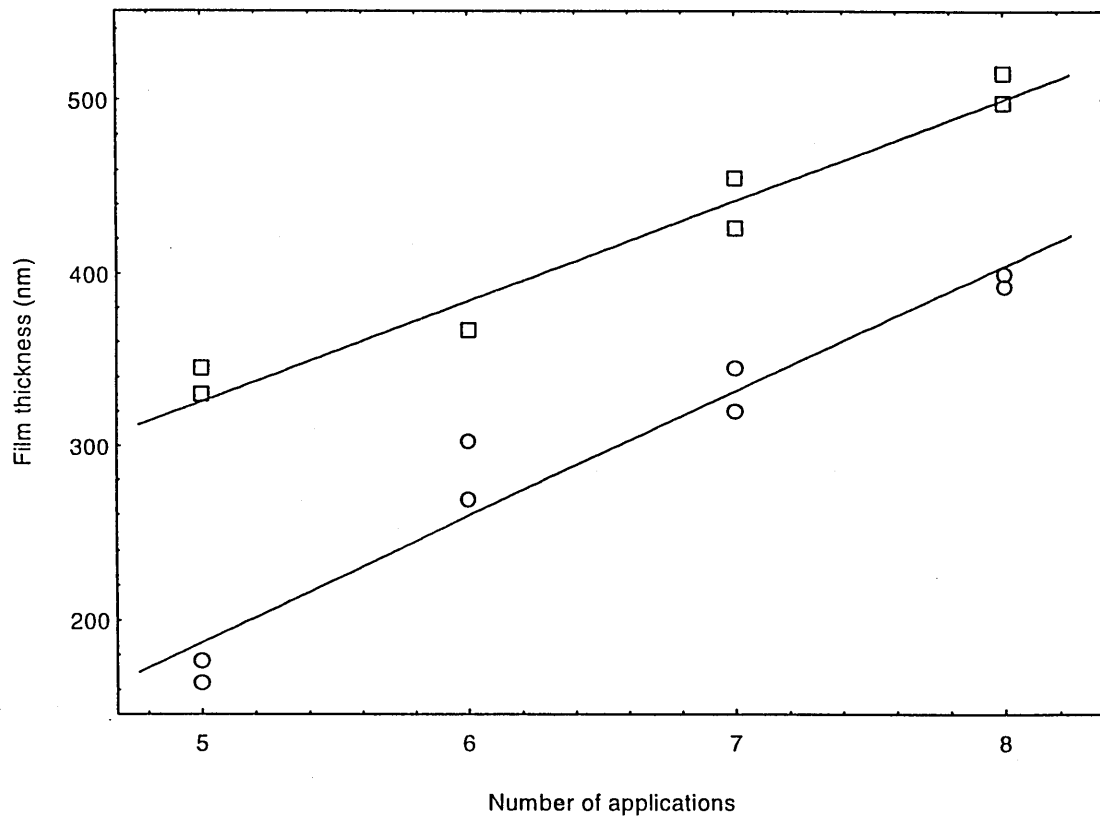
Figure 6.6. Graph showing relationship between TiO₂ film thickness and the number of applications for a withdrawal rate of 250 ( ) and 100 (O) mm/min. TiO₂ film thickness was calculated according to the method of Swanepoel[5].
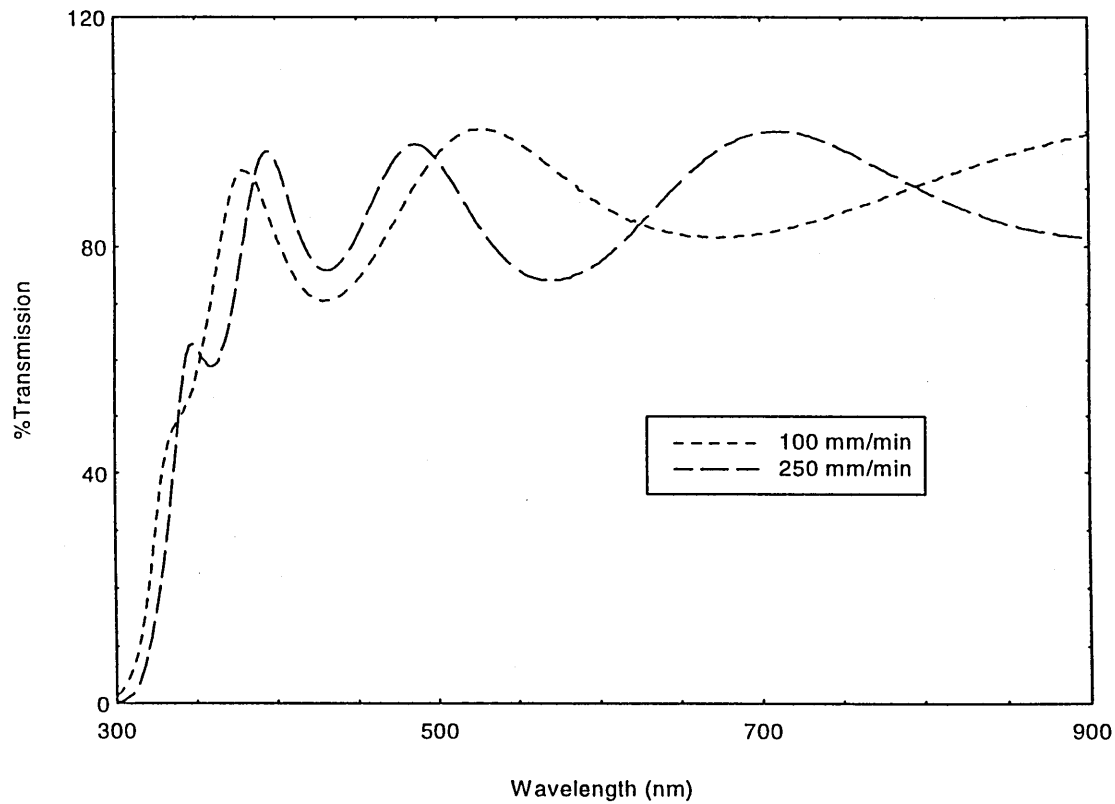
Figure 6.7. Effect of withdrawal rate on the interference fringes observed in transmission spectra for TiO₂ films. (In this case coated with 5 layers).

A dependence of withdrawal rate on film thickness has been observed for a variety of materials prepared by dip-coating. Yang[6] found that ultrathin polymer coatings could be prepared via dipcoating and that the thickness of the films was dependent on the square root of the substrate withdrawal speed. Takahashi and Matsuoka[7] found a similar dependence on a study of dip-coated TiO_2 films, prepared from a Sol derived from a $Ti(O-I-PrOH)_4$-diethanolamine-H_2O-i-PrOH system. The significance of the withdrawal rate on the coating thicknesses has been discussed in these studies using the FED technique.

Examples of tables produced for the TiO_2 Sol-Gel films using the Swanepoel[5,] method can be found in Appendix A. The tables list n and the film thickness (t) and in conjunction aid in the demonstration of the Swanepoel[5] procedure.

6.6.4 Factorial Investigations of Film Thickness

Section 5.4 details the FED experiment and contains Table 5.2 which displays the factors studied, namely the withdrawal rate, acetic acid:TIP molar ratio, number of coatings applied, and the concentration of TIP in ethanol. The corresponding high and low levels are also stated. A summary of the results of factorial experiments on film thicknesses are shown in Table 6.2, for both the overall coating thickness and the average coating layer thickness, (or the average thickness of an individual layer). The associated analysis of variance tables and results of Yates[8] analysis may be found in appendix B.

The main effects for a factorial experiment represent the effect of each factor, averaged over all levels and combinations of the other factors. Thus in systems in which considerable multi-factor interaction occurs, the main effects are believed to be of limited significance, since the effect of each factor is dependent upon the levels of the other factors present, and should be interpreted with some caution.

The calculated main effects of the dipping speed, ([A] in Table 6.2) indicates an increase in both overall coating thickness and average coating layer thickness as the dipping speed is increased. No significant effect could be identified for the acetic acid:TIP mole ratio [B] in the thickness factorial experiments. This was somewhat unexpected since, as discovered during tests on Sol stability, the level of acid present resulted in a change in the reactivity (and gelation times) of the alkoxide precursor, and might therefore be expected to result in a change in the viscosity of the coating solution. This discrepancy may be due to the short time elapsed between alkoxide addition and the dip coating process, resulting in relatively small differences between the progress of the relative reactions of the Sols containing different levels of acid addition. However, it is also possible that the presence of such an effect may be masked by the large interaction effects involving this factor.

The total thickness of the coating showed the expected increase as the number of coating layers [C] was increased from 1 to 4 (by an average of 0.16μm averaged over all levels and combinations of the other factors).

However, the estimated factorial effect of the number of coatings on the thickness of the individual coating layers was not found to be significantly large. Significant interaction effects were found involving this factor, and are discussed in detail in section 8.1.1.

The estimated main effects of TIP concentration ([D] in the factorial experiments) showed an increase in both total coating thickness and individual layer thickness with an increase in the concentration of the TIP, as might be intuitively expected. However, the magnitude of the calculated factorial effect for this factor has little practical significance due to the presence of numerous interactions involving this factor. The effect of changing TIP concentration on the coating thickness depends upon a number of other factors.

As shown in Table 6.2 the results of the factorial experiments for both overall coating thickness and average coating layer thickness indicated the presence of numerous interaction effects. A number of significant two and three factor interaction effects were identified in the experiment for the overall coating layer thickness which appear to be not significant in the experiment for the individual average coating layer thickness. However, this apparent discrepancy is most probably due to the increased sensitivity of the former experiment in detecting what are in all cases relatively small effects relative to the error in the thickness determinations.

Overall coating thickness				Average coating layer thickness			
Treatment	Mean Measured Coating Thickness (um)	Mean factorial Effect (um)	Significance	Treatment	Mean coating layer thickness (um)	Mean factorial Effect (um)	Significance
1	0.055			1	0.055		
a	0.050	[A] = 0.049	***	a	0.050	[A] = 0.015	***
b	0.040	[B] = 0.006	N/S	b	0.040	[B] = -0.004	N/S
c	0.120	[C] = 0.164	***	c	0.030	[C] = -0.002	N/S
d	0.070	[D] = 0.068	***	d	0.070	[D] = 0.390	***
Two Factor Interactions							
ab	0.045	[AB] = 0.026	***	ab	0.045	[AB] = 0.008	**
ac	0.120	[AC] = 0.041	***	ac	0.030	[AC] = 0.008	**
ad	0.085	[AD] = 0.030	***	ad	0.085	[AD] = 0.010	***
bc	0.170	[BC] = 0.021	***	bc	0.043	[BC] = 0.011	***
bd	0.050	[BD] = -0.033	***	bd	0.050	[BD] = -0.160	***
cd	0.260	[CD] = 0.048	***	cd	0.064	[CD] = 0.004	N/S
Three Factor Interactions							
abc	0.245	[ABC] = 0.024	***	abc	0.061	[ABC] = 0.005	N/S
abd	0.065	[ABD] = 0.005	N/S	abd	0.065	[ABD] = 0.000	N/S
acd	0.335	[ACD] = 0.023	***	acd	0.084	[ACD] = 0.003	N/S
bcd	0.160	[BCD] = -0.028	***	bcd	0.040	[BCD] = -0.005	N/S
Four Factor Interactions							
abcd	0.365	[ABCD] = 0.008	N/S	abcd	0.091	[ABCD] = 0.003	N/S

KEY: a,b,c,d, ab = treatment includes specified factor at high level
[A],[B],[C],[D],[ABC] = calculated mean effect of that factor or interaction
A = effect of withdrawal rate,   B = effect of acetic acid:TIP mole ratio
C = effect of number of coatings,   D = effect of T.I.P. concentration
*** = Significant at f<1% level   '** Significant at f<5% level
*   = Significant at f<10% level,   'N/S = Not significant

Table 6.2. Summary of results of FED experiment on overall coating and individual average coating layer thickness for Sol-Gel derived TiO_2 films.

6.7 Optical Characterisation

Figure 6.8 displays the optical absorption spectra obtained for films obtained from the most stable Sol (molar ratio acetic acid:TIP 4.16:1 and TIP concentration in ethanol 12.6%). Such films were used in the fabrication of the (inorganic:organic) IO heterojunctions. Films were prepared using a dipping speed of 250mm/ min. The spectra shown are for a varying number of coating layers. The optical absorption edge is clearly visible (Figure 6.9 displays the absorbance as a function of photon energy in the range 3.5-4.1eV). The absorption edge was observed to increase to higher wavelengths with increasing number of coating layers. This is expected to correspond to a decrease in the value of the optical band gap, E_0. The effect was later confirmed from investigations of E_0 detailed in the following section. The absorption coefficient (α) of the TiO_2 films and its dependence on Sol-Gel process parameters was analysed using the FED technique the results of which are shown in section 6.7.2.

6.7.1 Optical Band Gap and Nature of Optical Transitions

From the optical absorption spectra, the optical band gap E_0 was calculated according to Tauc[9] from plots of $(\alpha h\nu)^{1/\delta}$ against $h\nu$ and for comparison according to the technique developed by Ray and Hogarth[10]. Figures 6.10 to 6.13 are Tauc plots where δ (which must be assumed) was taken to be 1/2, 3/2, 3 and 2 respectively. Analysis was performed for photon energies ($h\nu$) greater than the absorption edge.
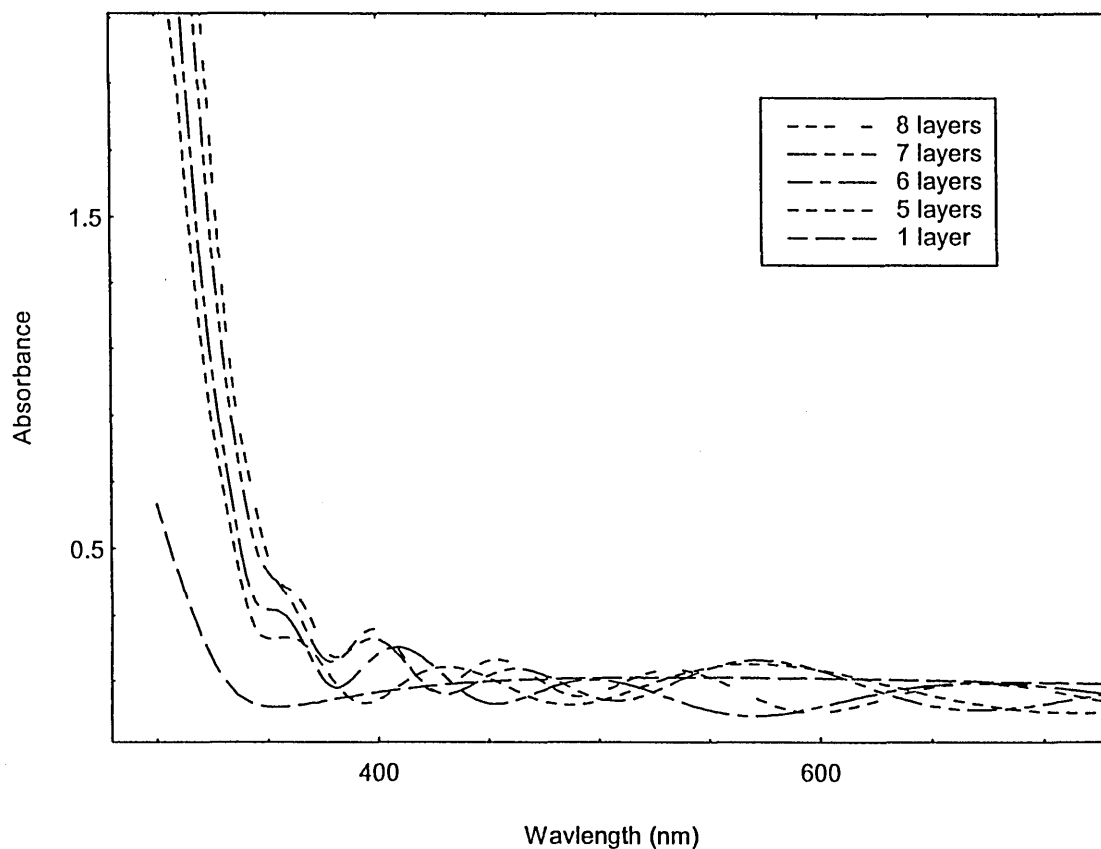
Figure 6.8. . Absorption as a function of no of coating layers of TiO$_2$ films prepared from 4.16:1 (acetic acid:TIP) ,molar ratio and TIP concentration in ethanol of 12.6%. Films heat treated to 500°C for 5 hours. A withdrawal rate of 250mm/min was used.
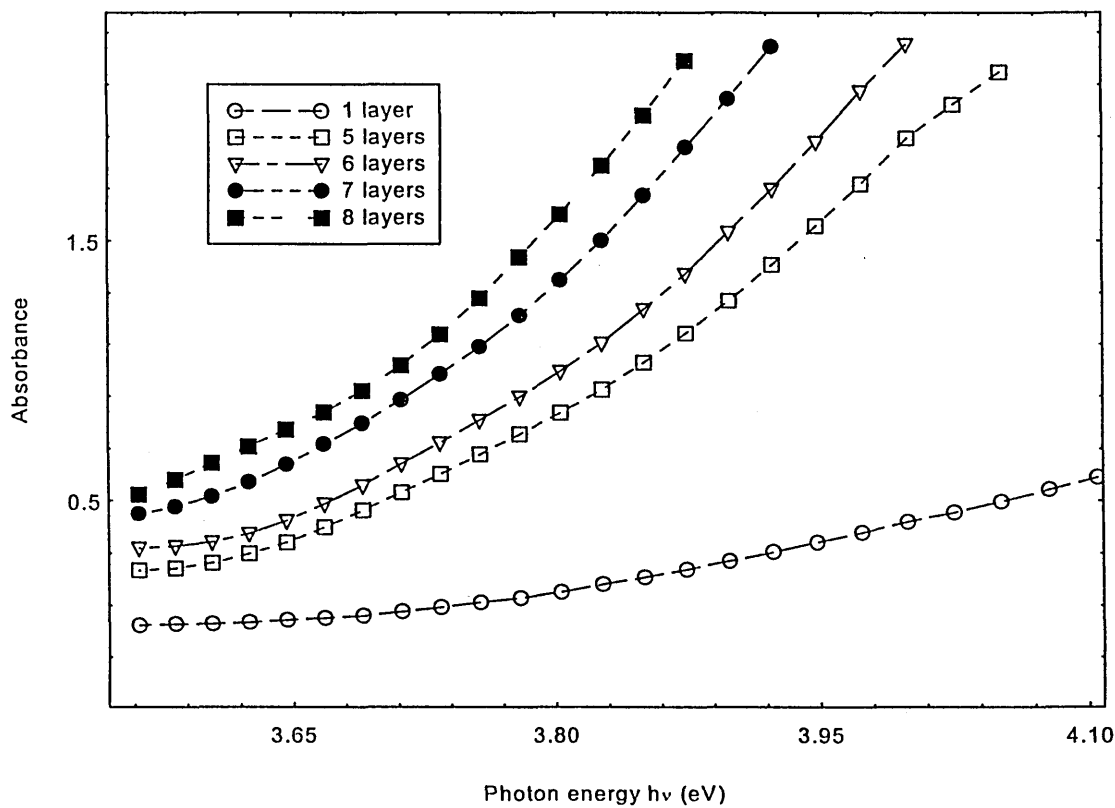
Figure 6.9. As for figure 6.10 ; For the absorption edge wavelength range of 300 nm to 350nm.

149

For hv less than the absorption edge interference effects were observed and therefore not used in the analysis.

Straight line fits were applied to the curves for $hv>3.6eV$, and the deviation from linearity measured. The worst fits were for $\delta=1/2$ and $\delta=3/2$. Particularly for $\delta=1/2$ where extreme deviation was observed. The electronic transitions responsible for absorption in these films are therefore not expected to be allowed direct transitions or forbidden direct transitions. Better fits were observed for $\delta=2$ and $\delta=3$. The calculated deviation from linearity is given in Table 6.3. A slightly better fit to the experimental data was observed when $\delta=3$ for 5-8 layers, however for 1 layer $\delta=2$ provided the best fit. The most favoured nature of electronic transitions in these films is anticipated to be through an indirect allowed transition (where $\delta=2$) for thin films (1 coating layer) and an indirect forbidden transition (where $\delta=3$) as the thickness increases.

The room temperature experimental values of E_o as a function of the number of coating layers were derived from the $\delta=3$ and $\delta=2$ plots. The values of E_o (listed in Table 6.3) generally decreased as the number of coating layers increased. A further observation was that as the number of layers increased the values of E_o converged. $E_o \sim 3.2eV$ for the indirect forbidden transition and $E_o \sim 3.4-3.35$ eV for the indirect allowed transition. The value of E_o was also calculated according to the technique of Ray and Hogarth[10] in this technique the value of δ need not be assumed but is calculated from the experimental data. Values of Y and Y' were determined from Figure 6.9 for each of the curves at different photon energies within the absorption edge.
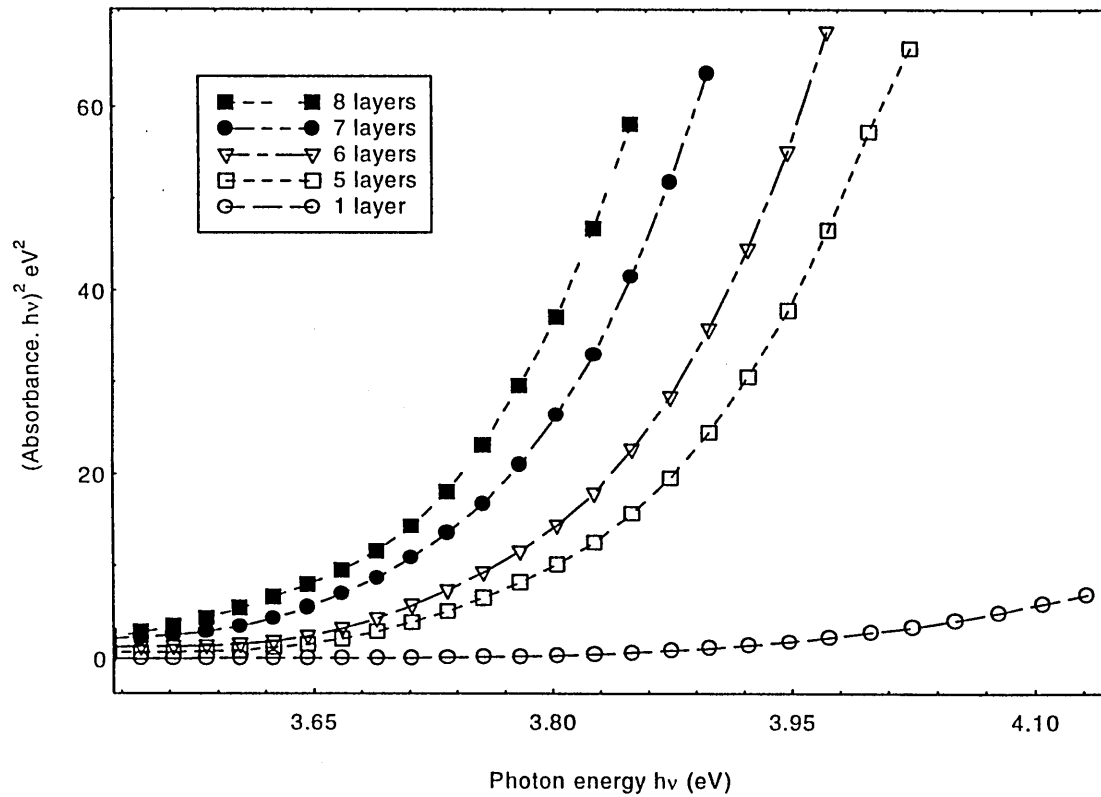
Figure 6.10. Plot of $(\text{Absorbance.hv})^{1/\delta}$ against hv for TiO_2 Sol-Gel derived films where $\delta=1/2$.
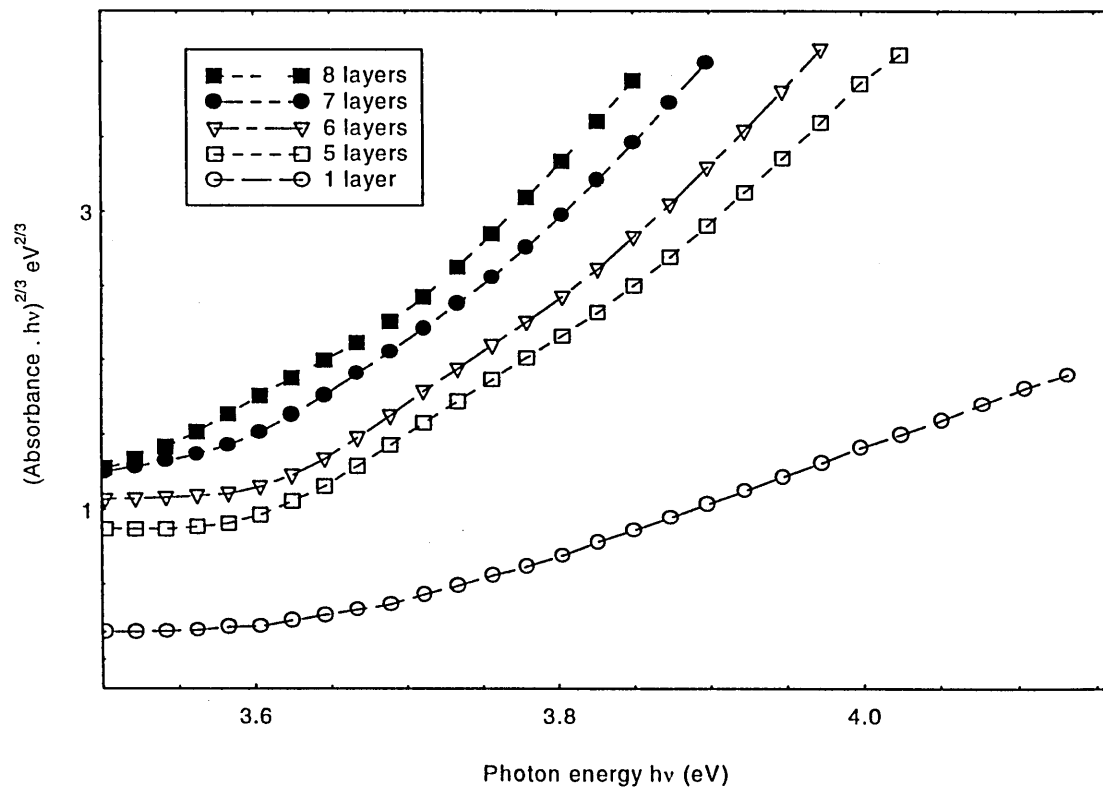
Figure 6.11. Plot of $(\text{Absorbance.hv})^{1/\delta}$ against hv for TiO_2 Sol-gel derived films where $\delta=3/2$.
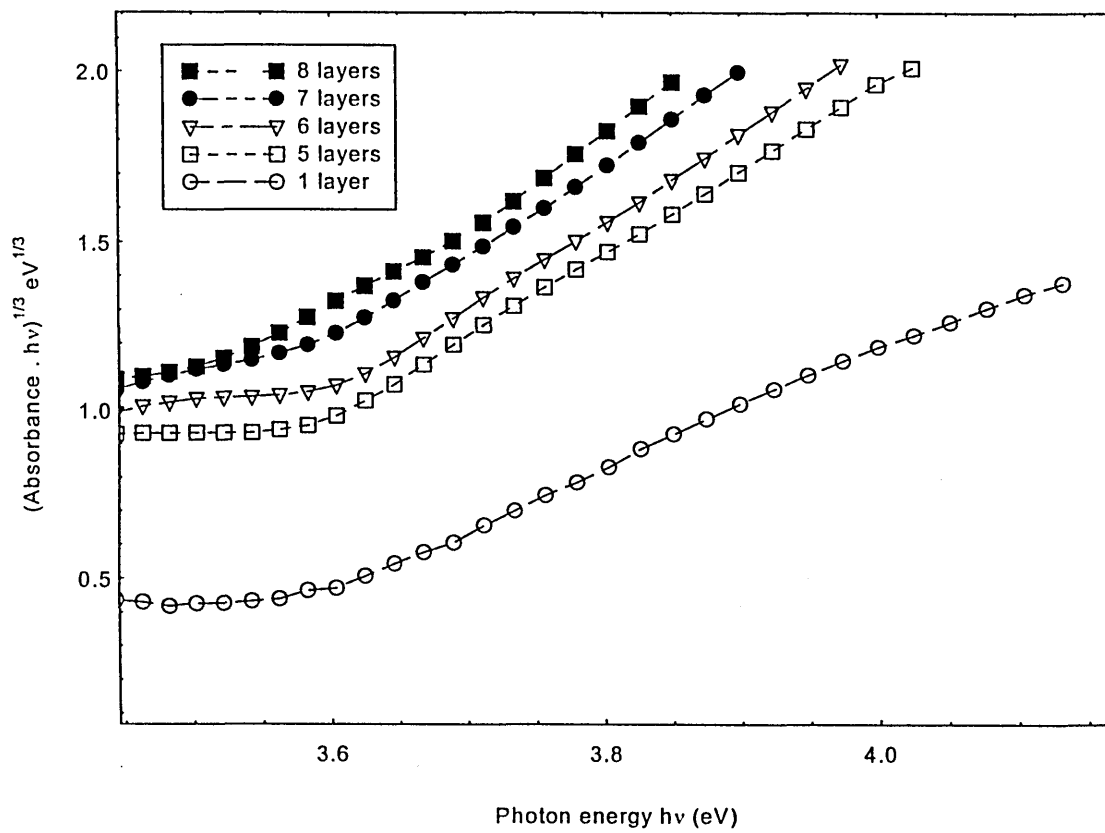
Figure 6.12. Plot of $(Absorbance.h\nu)^{1/\delta}$ against $h\nu$ for TiO_2 Sol-Gel derived films where δ=3.
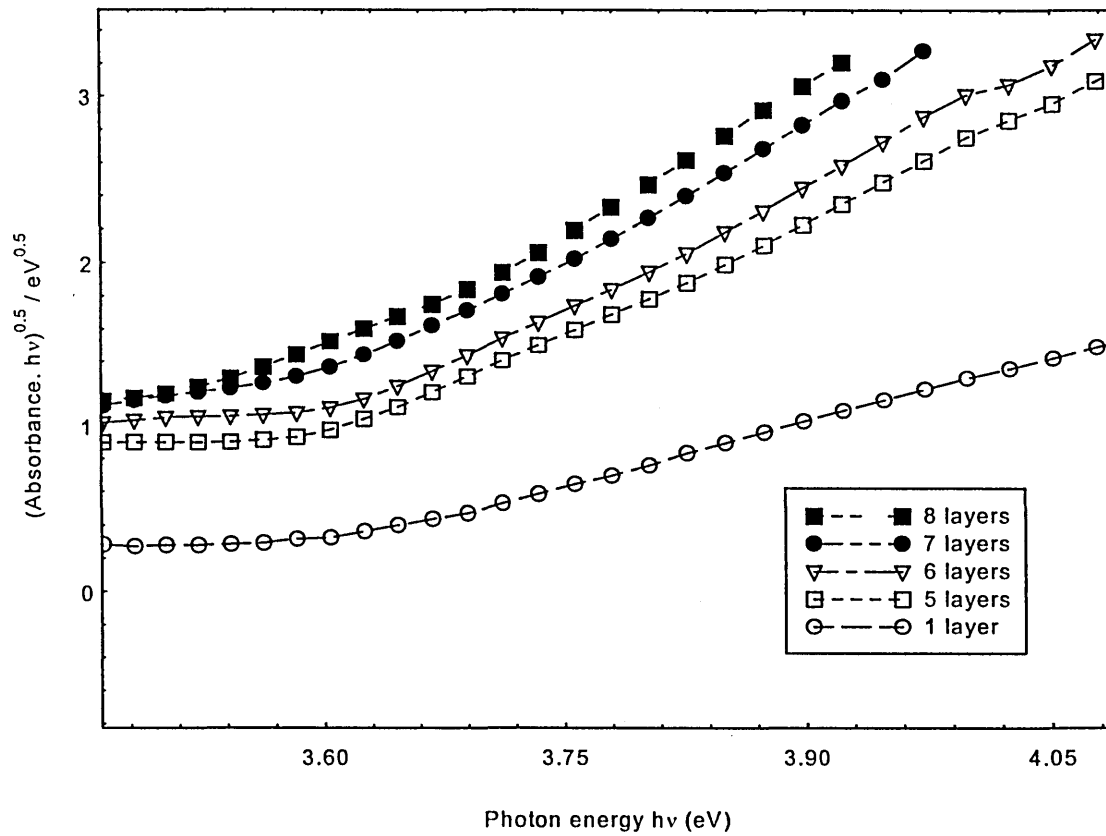
Figure 6.13. Plot of $(Absorbance.h\nu)^{1/\delta}$ against $h\nu$ for TiO_2 Sol-Gel derived films where δ=2.

Method	Number of coating layers				
	1	5	6	7	8
(a)	3.36 (0.035)	3.2 (0.0106)	3.2 (0.0107)	3.16 (0.0133)	3.17 (0.0232)
(b)	3.5 (0.012)	3.41 (0.0336)	3.4 (0.0507)	3.36 (0.0449)	3.35 (0.0327)
(c)	3.55 $\delta=1.81$	3.25 $\delta=2.9$	3.16 $\delta=3.2$	3.27 $\delta=2.64$	3.21 $\delta=2.8$

Table 6.3. The optical band gap E_0 (eV) as a function of the number of coating layers. E_0 calculated according to the following methods. (a) Tauc[9] where $\delta=3$, (b) Tauc[9] where $\delta=2$, (The deviation from linearity of the fitted data is shown in brackets) (c) Ray and Hogarth[10] where calculated value of δ is shown.
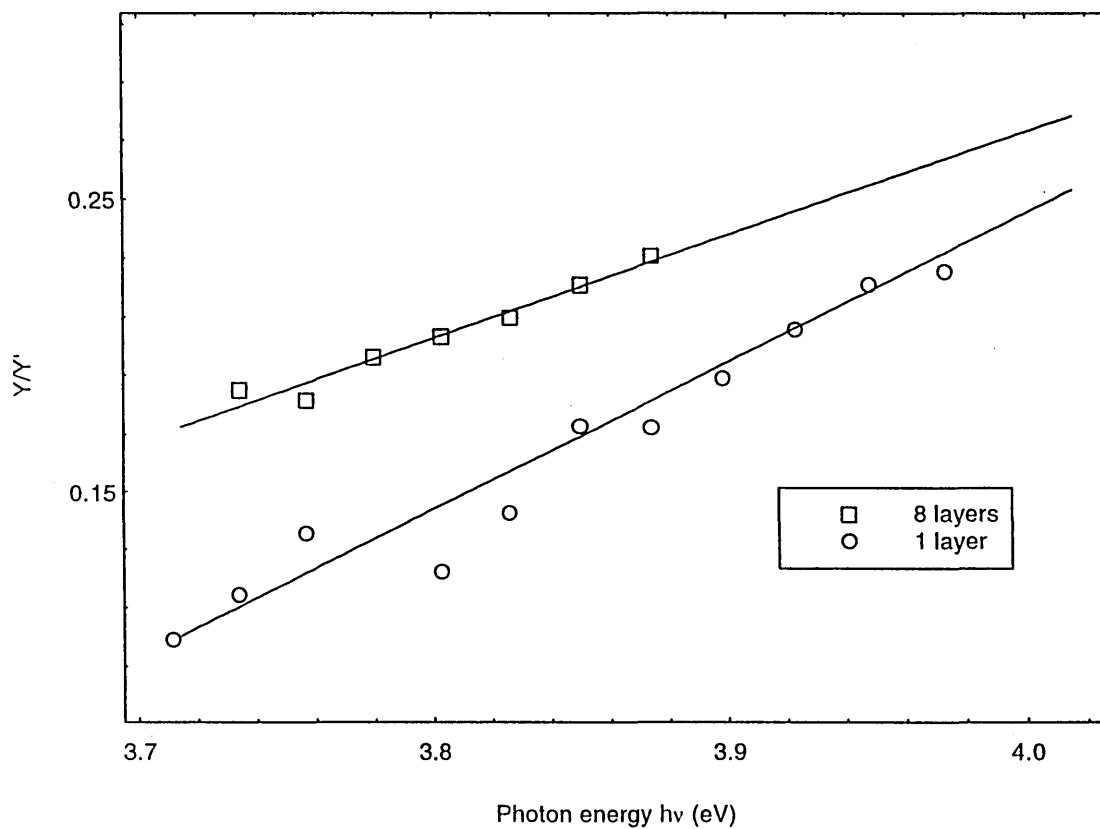
Figure. 6.14. Example of Y/Y' as a function of photon energy in the range 3.7-4eV, observed for Sol Gel derived TiO_2 films.

153

Figure 6.14 is an example of the resulting (Y/Y') plots as a function of photon energy. Table 6.3 contains the values of δ and E_0 derived from this technique. The results supported those obtained from the Tauc plots. The optical band gap and nature of electronic transition was again found to be dependent on the number of coating layers. For very thin (1 layer) film, $E_0 \sim 3.55$ and $\delta \sim 1.8$ in close agreement with that which was observed from Tauc plots when $\delta = 2$ giving the best fit. For higher number of coating layers the values of E_0 and δ were in agreement with that which was observed from Tauc plots when $\delta = 3$, which again provided the best fit. It is suggested therefore that both the nature of electronic transitions giving rise to absorption in these films and the optical band gap E_0 is thickness dependent.

6.7.2 Factorial Investigations of Absorbance and α

The optical absorption (at standard photon energy of 4eV, within the absorption band edge) and the optical absorption coefficient α (cm^{-1}) at this photon energy were measured for the TiO_2 Sol-Gel derived films together with the estimated factorial effects and associated analyses of variance. The recipe of calculation was described in section 5.4. The results are shown in Table 6.4 and the complete ANOVA table can be found in Appendix B.

The results of the experiments for optical absorption indicate the presence of large numbers of apparent effects of interactions. However, when these effects are converted to absorption coefficient, to incorporate the effect of film thickness, the majority of these are eliminated, indicating that these changes in optical absorption can be attributed

154

to the variation in film thickness associated with changes in the process parameters. The remaining effects which were significant in both optical absorption and absorption coefficient experiments, indicate effects which cannot be attributed solely to changes in film thickness. These effects must arise due to changes in the behaviour of the coating films themselves.

The most significant effects in both experiments were associated with the effect of the number of coating layers applied, which was also the largest factor affecting the thickness of the coating. The main effects of the number of coating layers [C] showed the expected increase in overall optical absorption as the number of coating layers, and hence coating thickness increased (manifested as a positive factorial effect). However, once the effects of coating thickness are taken into account (i.e. in the absorption coefficient), the calculated effect of this factor was found to change from a positive to a negative effect (-0.472).

One possible explanation of this phenomena is that a large contribution to the apparent optical absorption may be due to reflectance at the coating/substrate interface due to refractive index mismatch. This effect will occur only for the initial coating layer (since subsequent layers will have identical refractive index to the first), and thus subsequent coating layers will produce a smaller effect on absorption, and apparent absorption coefficient than the first. This would be manifested as a negative factorial effect for the number of coatings in the absorption coefficient experiment.

Measured absorption at 4eV				Calculated absorption coefficient at 4eV			
Treatment	Mean absorbance	Mean factorial effect	Significance	Treatment	Mean calculated absorption coefficient	Mean factorial effect	Significance
1	0.56			1	1.175		
a	0.607	[A] = 0.532	***	a	1.425	[A] = 0.178	N/S
b	0.804	[B] = -0.140	***	b	1.870	[B] = 0.065	N/S
c	0.900	[C] = 1.077	***	c	0.868	[C] = -0.472	***
d	0.520	[D] = 0.645	***	d	0.860	[D] = -0.057	N/S
Two Factor Interactions							
ab	0.544	[AB] = -0.076	*	ab	1.490	[AB] = -0.234	N/S
ac	1.555	[AC] = 0.322	***	ac	1.523	[AC] = -0.028	N/S
ad	1.025	[AD] = 0.257	***	ad	1.390	[AD] = 0.048	N/S
bc	0.917	[BC] = -0.082	*	bc	0.628	[BC] = -0.328	**
bd	0.564	[BD] = -0.059	N/S	bd	1.343	[BD] = 0.159	N/S
cd	1.835	[CD] = 0.469	***	cd	0.830	[CD] = 0.108	N/S
Three Factor Interactions							
abc	1.305	[ABC] = -0.009	N/S	abc	0.623	[ABC] = -0.052	N/S
abd	0.840	[ABD] = 0.000	N/S	abd	1.740	[ABD] = 0.089	N/S
acd	3.060	[ACD] = 0.076	*	acd	1.048	[ACD] = -0.222	N/S
bcd	1.545	[BCD] = -0.046	N/S	bcd	1.112	[BCD] = 0.148	N/S
Four Factor Interactions							
abcd	2.695	[ABCD] = 0.048	N/S	abcd	0.850	[ABCD] = -0.045	N/S

KEY: a,b,c,d, ab = treatment includes specified factor(s) at high level
[A], [B],[C],[D], [ABC] =Calculated mean effect of that factor, or interaction.
A = effect of withdrawal speed   B = effect of acetic acid:TIP mole ratio.
C = effect of number of coatings, D = effect of T.I.P. concentration
*** = Significant at f<1% level   ** Significant at f<5% level
* = Significant at f<10% level,   N/S = Not significant

Table 6.4. Summary of results of FED experiment for optical absorption and absorption coefficient, $(10^5 cm^{-1})$ for Sol-Gel derived TiO_2 films.

6.7.3 Transmission

Typical transmission spectra observed for the TiO_2 films annealed to $500^{\circ}C$ for 5 hours are shown in Figures 6.15 and 6.16 as a function of withdrawal rate, Sol concentration and molar ratio of acetic acid:TIP. The % transmission spectra have been corrected for the effects of substrate absorption. The transmission spectra of the glass substrate is shown and was measured to be in the order of 90.8% over the wavelength range ~550nm to ~900nm.The transmission of the films was dependent on the withdrawal rate of the substrate from the Sol. Three dipping speeds were chosen in the range 50-200mm/min speeds less than 20mm/min produced visibly unhomogenous, low quality films and were disregarded. Previous studies on thickness indicated that as the withdrawal rate increases the thickness increases. These results also confirm that lower transmission results from thicker films as may be intuitively expected. Transmission decreases from 93% for a speed of 50mm/min to 89.3% for a withdrawal rate of 100mm/min to 83.8% for 200mm/min measured at wavelength of 600nm.

The molar ratio of acetic acid:TIP and TIP concentration also had a visible effect on the transmission properties of the TiO_2 films. Of the films prepared from a Sol with a low TIP concentration (6.3%) those which contained a molar ratio of 3.14:1 (acetic acid:TIP) had lower transmission than the 4.16:1 (acetic acid:TIP) films. Similarly, of the films produced using the higher TIP concentration (12%) Sols, those with an acetic acid:TIP molar ration of 4.16:1 possessed a higher transmission than the 3.14:1 films for films $\lambda > 600nm$.
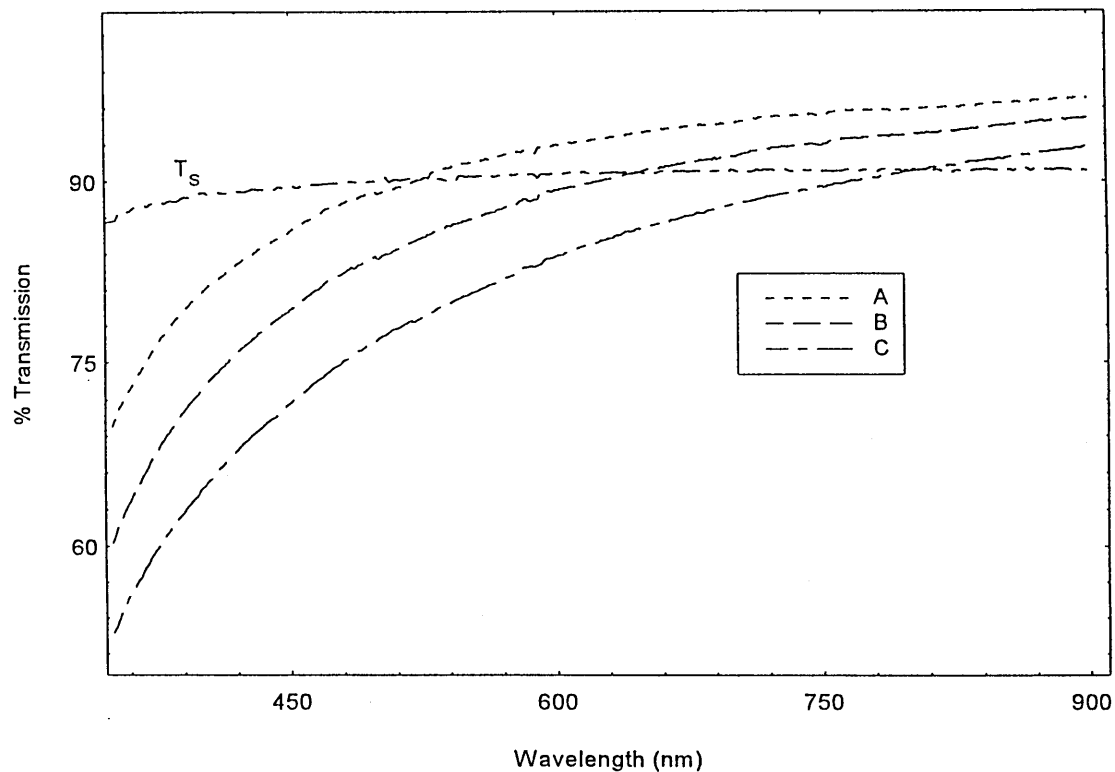
Figure 6.15. Transmission spectra of Sol-Gel TiO$_2$ films (molar ratio acid:TIP 4.16:1; TIP concentration in ethanol 6.3%; samples annealed at 500°C for 5 hours; 2 coating layers). Withdrawal rates used were A=50mm/min, B=100mm/min,. C=200mm/min T$_s$ represents the glass substrate.
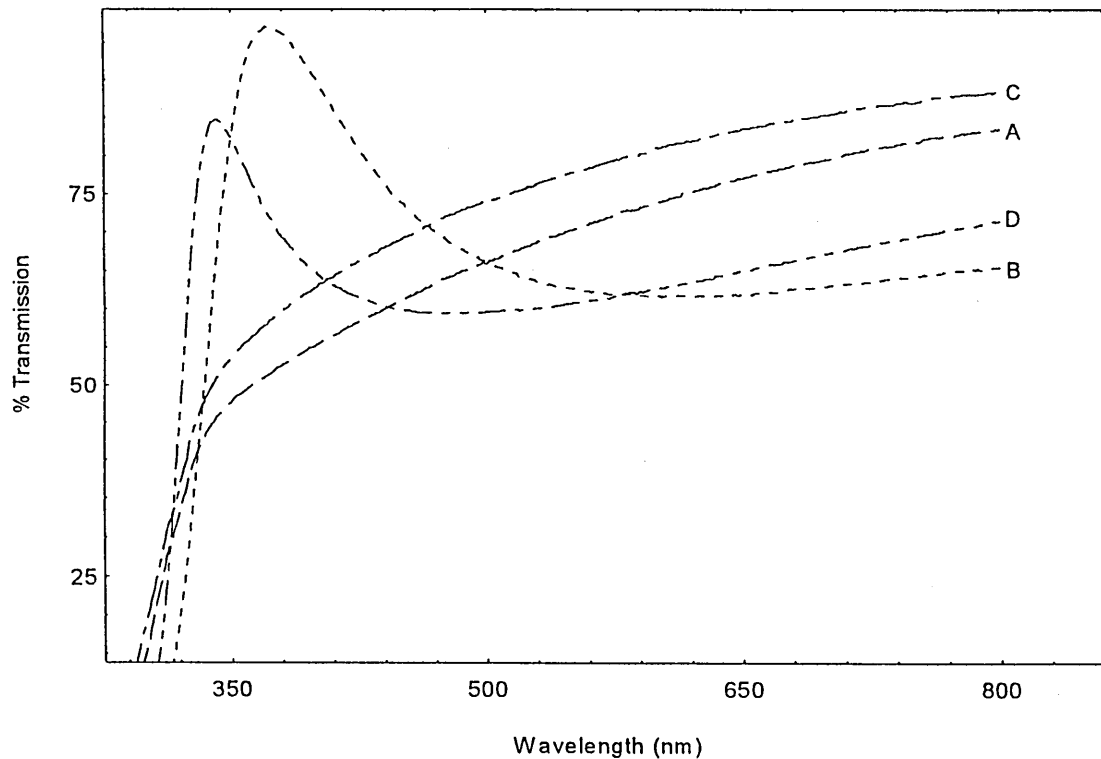
Figure 6.16. Transmission spectra of TiO$_2$ films where A,B,C,D were prepared according to 'a','ad','ab', and 'abd' respectively as described in section 5.4.1.

The opposite was true for $\lambda < 600nm$. In all cases the transmission of the films was observed to decrease rapidly from between 340nm-370nm into the UV region. The average transmission of the films obtained from the most stable Sols (molar ratio acetic acid:TIP 4.16:1 and TIP concentration in ethanol 12.6%) exhibited an average transmission of 87% in the wavelength range 350-900nm. These films were subsequently used for the fabrication of the IO heterojunctions.

6.7.4 Refractive Index Determination

The refractive index $n(\lambda)$ was calculated from the interference fringes using the Swanepoel[5] method.

Values of n for the TiO_2 films are listed in Appendix A and were found to vary between 2.73 and 1.81 measured as a function of the number of coating layers (5,6,7,8), the dipping speed (100 mm/min or 250mm/min) and the wavelength, λ (in the range 300nm to 900nm). For all films the calculated n was observed to decrease as λ increased. Figure 6.17 is a typical example of the $n(\lambda)$ against λ dependence observed in the films.

The wavelength dependent refractive index was analysed in terms of the single oscillator model[11] where the optical dispersion may be expressed mathematically as;

$$n^2 - 1 = \frac{E_d E_s}{E_s^2 - (h\upsilon)^2} \qquad 6.1$$

E_s is the single effective oscillator energy, E_d the dispersion energy and $h\nu$ the photon energy. The parameter E_d is a measure of the strength of interband transitions. The average oscillator strength is defined as $S_o = E_d E_s / (\hbar^2 c^2)$ and the average oscillator position, λ_o, is related to the natural frequency of the particles, ν_o by the equation $\lambda_o = c/\nu_o$ where c is the speed of light. It may be deduced from equation (6.1) that a plot of $1/(n^2-1)$ against $(h\nu)^2$ should be linear. Such plots were derived for the TiO$_2$ films, an example is shown in Figure 6.18 for a TiO$_2$ coating film 8 layers thick. The oscillator energy, E_o and dispersion energy, E_d were derived from the slope and zero energy intercept of the straight line. The values estimated from the linear plots as a function of number of coating layers are shown in Table 6.5. As shown in Figure 6.19 the theoretical curve of refractive index as a function of photon energy was generated using the estimated values of E_s and E_d. The theoretical curves were in good agreement with the experimental values over the energy range studied. The refractive index was found to be relatively independent of the sample thickness indicated in Table 6.5, for the thickness ranges studied.

6.8 Electrical Characterisation

The measured conductivity of the Sol-Gel derived TiO$_2$ films varied depending on the type of device configuration used. TiO$_2$ films (prepared according to the 'high level' in Table 5.2 and heat treated to 500°C for 5 hours) deposited on InSnO$_2$ base electrodes with Au counter electrode (hence in sandwich configuration) had a measured conductivity of 4.27×10^{-4} S/m under atmospheric conditions and 4.26×10^{-4} S/m when measured under vacuum.

160
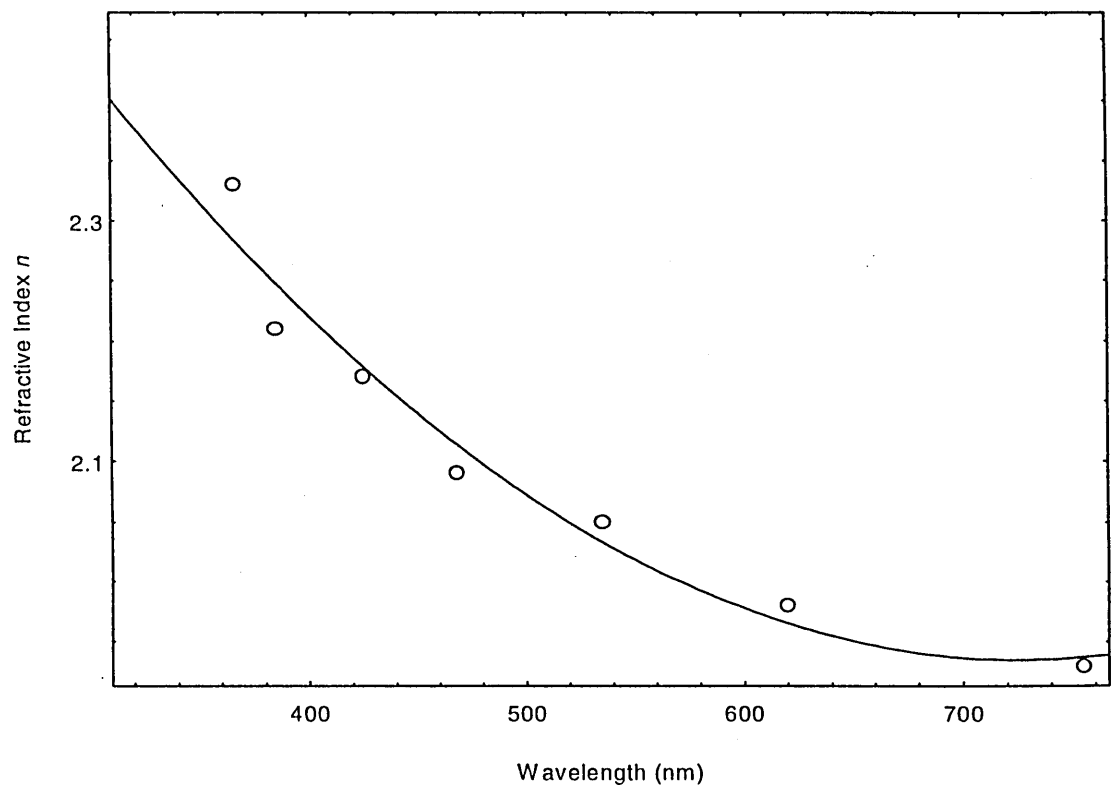
Figure 6.17. Example of the spectral dependence of the refractive index *n* at room temperature, for a
TiO$_2$ coated with 8 layers. A withdrawal rate of 100mm/min was used. (denoted sample A8
in appendix A)
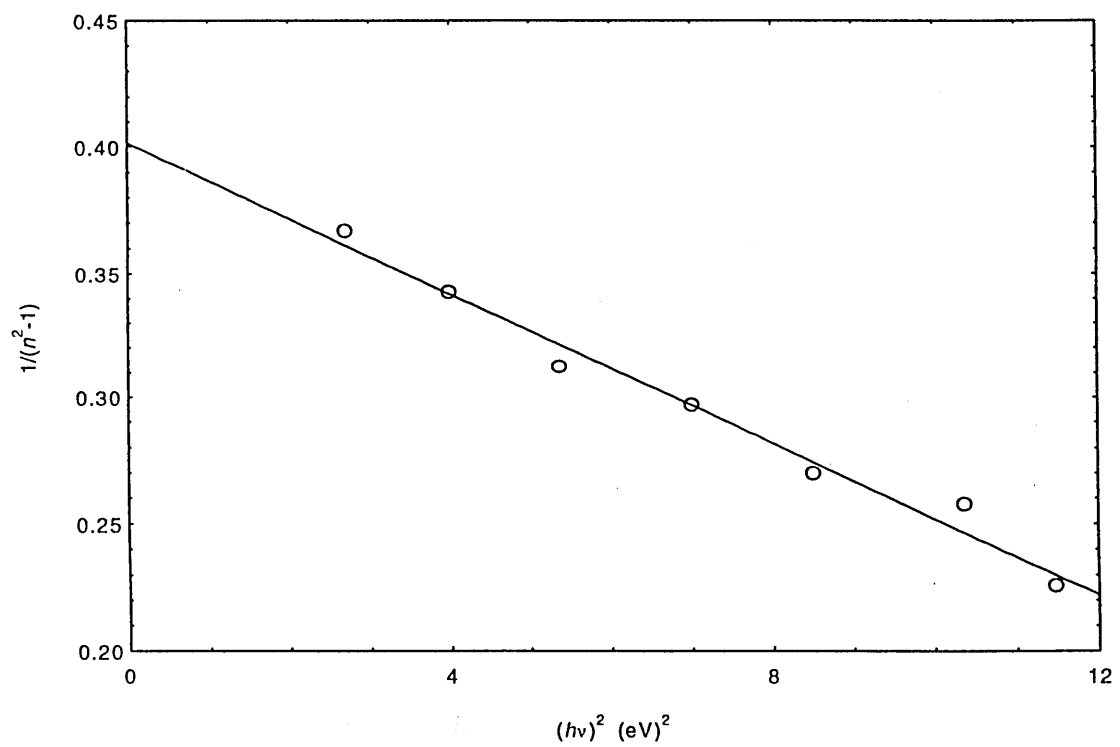
Figure 6.18 The plot of $1/(n^2-1)$ against $(h\nu)^2$ for sample 'A8' as shown in Appendix A.

Withdrawal Speed (mm/min)	Number of layers	Overall coating thickness (nm)	E_s (eV)	E_d (eV)	n (at 500nm)
100	5	164	4.09	8.29	2.18
"	5	176	4	7.91	2.19
"	6	302	5.24	13.36	2.07
"	6	268	3.79	10.03	2.41
"	7	345	5.21	14.64	2.16
"	7	320	4.39	10.55	2.12
"	8	399	5.16	13.45	2.1
"	8	392	5.18	12.88	2.07
250	5	330	4.84	13.4	2.18
"	5	345	2.86	8.38	2.12
"	6	367	3.99	7.85	2.02
"	6	367	3.68	6.21	2.07
"	7	426	4.28	9.5	2.03
"	7	455	4.88	13.56	2.18
"	8	515	4.48	11.34	2.13
"	8	498	4.22	9.63	2.18

Table 6.5 Optical paramters of the TiO_2 films (prepared from a Sol consisting of ; molar ratio acetic acid:TIP 4.16:1, concentration TIP in ethanol 12.6%, films annealed to 500°C for 5 hours)
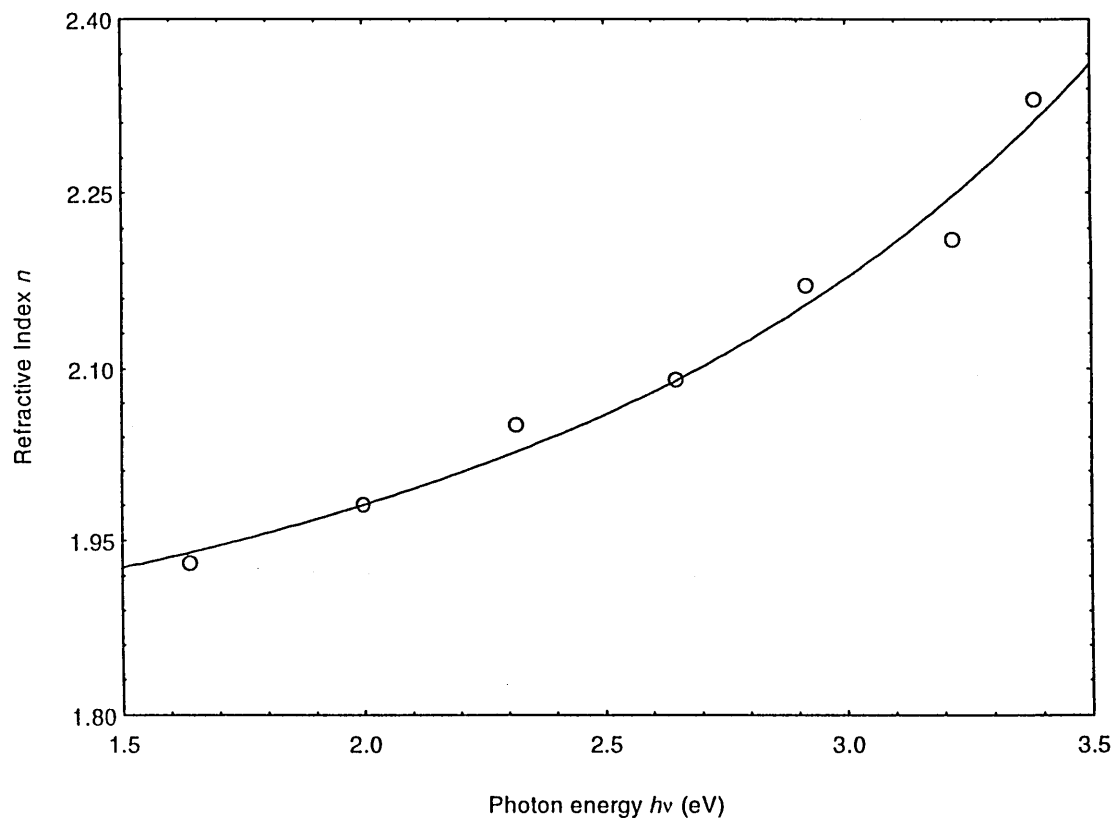
Figure 6.19. Comparison of single oscillator model (———) with experimental data for sample 'A8' (as described in appendix A)

Ambient conditions were observed to have little effect on the film conductivity. Conversely, for TiO_2 films (heated to $350^{\circ}C$) deposited on Pt interdigitated electrodes (planar configuration) the measured conductivity was in the order of $1 \times 10^{-5} S/m$.

It was not possible to determine the conductivity of the films heat treated to temperatures in excess of $350^{\circ}C$ in planar configuration due to degradation of the Pt electrodes at heat treatment temperatures in excess of this. The effects of heat treatment temperature up to $350^{\circ}C$ on the conductivity of the TiO_2 films was measured. The results are shown in Figure 6.20. Conductivity measurements were taken for 3 heat treatment temperatures and repeated at each temperature. The results show that there was an apparent decrease in conductivity in the films heat treated at $200^{\circ}-300^{\circ}C$ compared to the non heat treated films. The results also show that increasing heat treatment temperature in the range $200-300^{\circ}C$ produced a diminishing reduction in the conductivity of the film.

The temperature dependence of the electrical conductivity was measured in the range 77K-290K for the TiO_2 films. The conductivity increased with increasing temperature and began to saturate as room temperature was reached. In order to determine the activation energy associated with the material within this temperature regime, Arrhenius plots were produced as shown in Figures 6.21 and 6.22 for TiO_2 films 0.36μ and 0.455μ thick respectively.

The activation energies were calculated from the slopes of the $\ln\sigma$ against $1/T$ curves. In both cases very low activation energies were deduced $\Delta E{\sim}0.49meV$ for $TiO_2(0.455\mu)$ and $\Delta E{\sim}0.64meV$ for $TiO_2(0.36\mu)$. These results are discussed further in section 8.1.3.

163
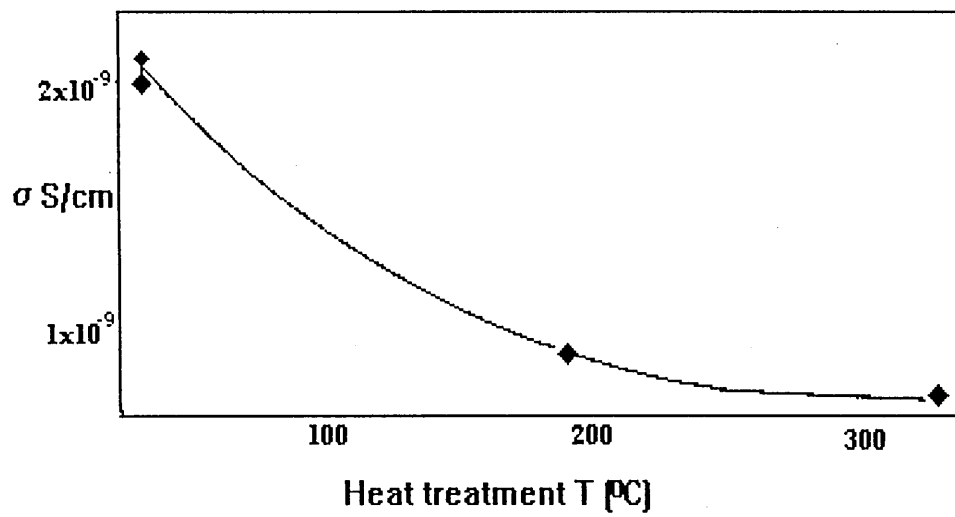
Figure 6.20.The effect of heat treatment on the conductivity σ (S/cm) of TiO₂ film. Films deposited
onto platinum interdigitated electrodes conductivity therefore measured in planar
configuration.
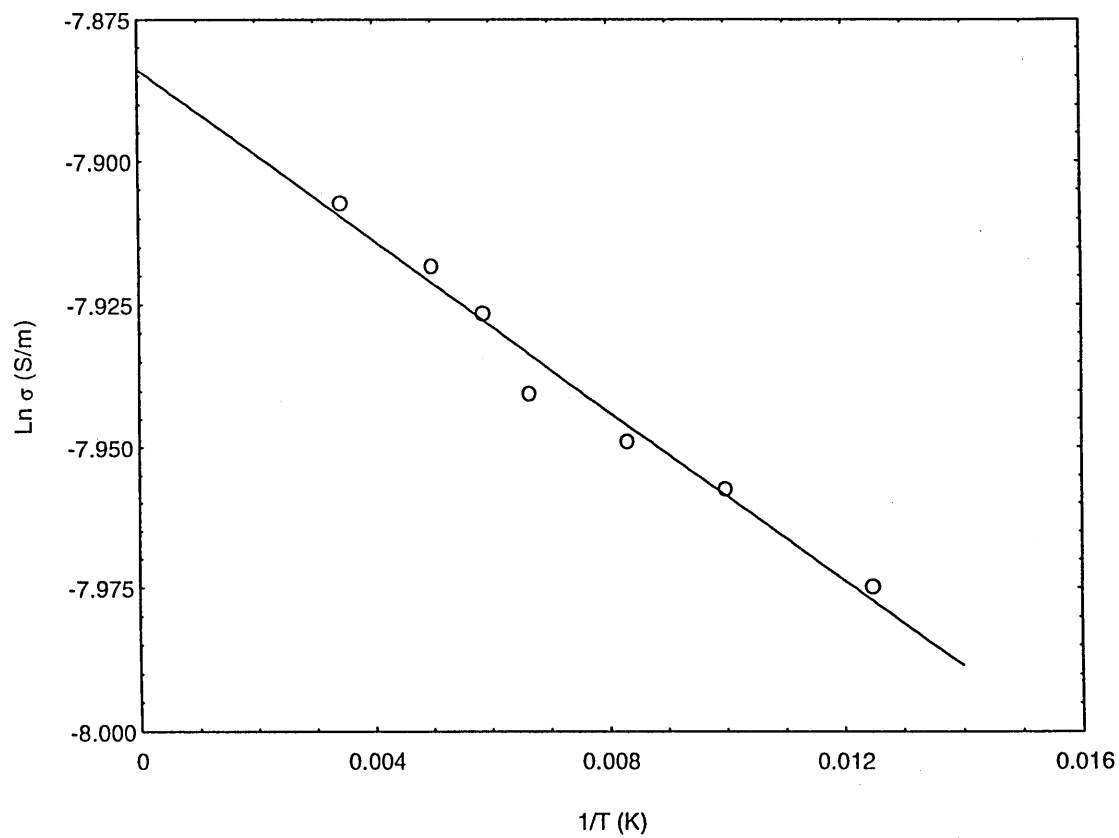
Figure 6.21. Graph showing variation of conductivity σ with reciprocal temperature for a
Au/TiO₂/InSnO₂ device.(TiO₂ thickness ~0.36μ)

164
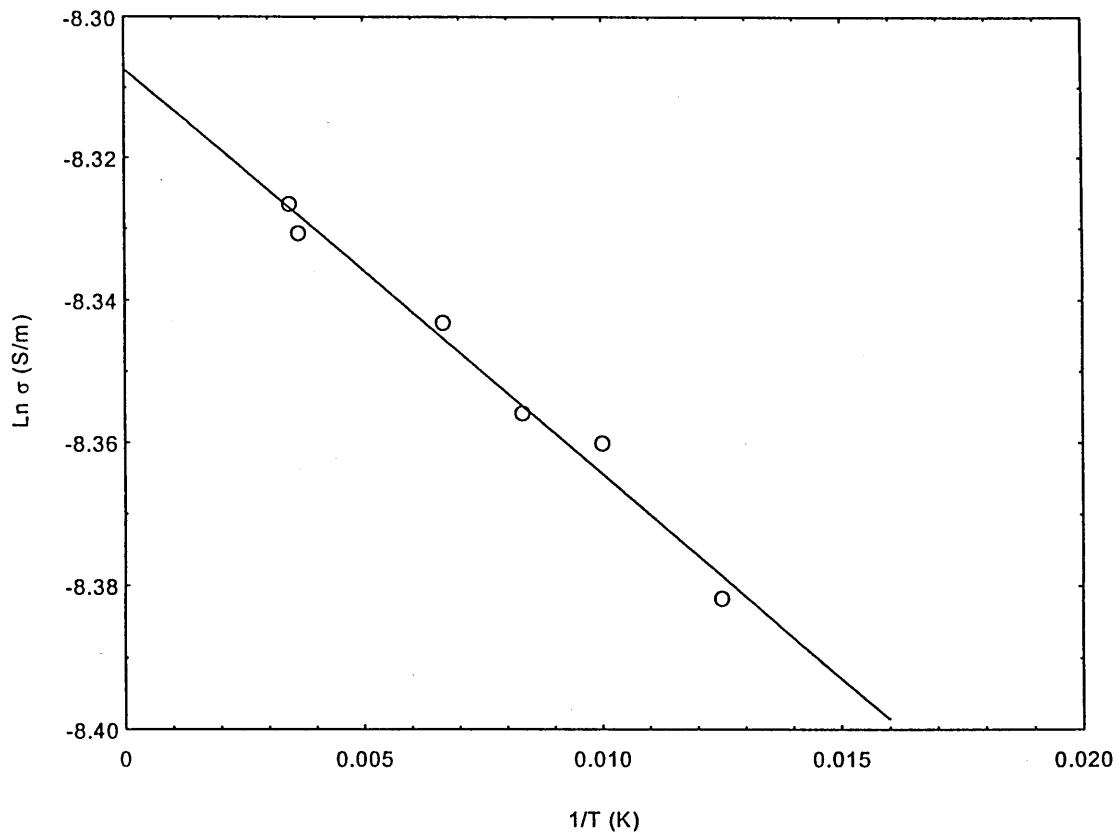
Figure 6.22. Graph showing variation of conductivity with reciprocal temperature for a Au/TiO$_2$/InSnO$_2$ device. (TiO$_2$ thickness ~0.455μ))

REFERENCES

1. Yoldas, B. E. *J. Mat. Sci.* **21** (1986) 1087-1092.

2. Jones, R. W. *Fundamental Principles of Sol-Gel Technology.* The Institute of Metals 1989.

3. Scherer, G. W., Brinker C. J., and Roth, E. P. *J. Non-Cryst. Solids.* **72**(2-3) (1985) 369-389..

4. Livage, J. *Mat. Res. Soc. Symp. Proc.* **73** (1986) 717-724.

5. Swanepoel, R. *J. Phys. E:Sci. Instrum.* **16** (1983) 1214-1222.

6. Yang, C. C., Josefowicz, J. Y., and Alexandru, L. *Thin Solid Films.* **74** (1980) 117-127.

7. Takahashi, Y., and Matsuoka, Y. *J. Mat. Sci.* **23** (1988) 2259-2266.

8. Yates, F. *Imp. Bur. Soil. Sci. Tech. Comms.* **35** (1937).

9. Tauc, J. *The Optical Properties of Solids,* Ed. F. Abeles, North-Holland Publ. Co., Amsterdam, 1970.

10. Ray, A. K., and Hogarth, C. A. *J. Phys. D. Appl. Phys.* **23** (1990) 458-459.

11. Wemple, S. H., and DiDomenico, Jr. M., *Phys Rev B.* **3** (4) (1971) 1338-1351.

Chapter

Dye Sensitised IO Heterojunction : Results

7.1 Introduction

This chapter reports the photovoltaic and electrical measurements carried out on the TiO_2/MPc, inorganic:organic (IO) heterojunction cells. Three devices are constructed containing chloroaluminium phthalocyanine (ClAlPc), copper phthalocyanine (CuPc) and lead phthalocyanine (PbPc) as the photogenerating layer respectively. The properties investigated include the spectral response in relation to the absorption of the dyes, dark current density/voltage (J(V)), illuminated J(V), and capacitance-voltage (C(V)) characteristics.

For all illuminated J(V) measurements, irradiation of the TiO_2/MPc junction was directed through the $InSnO_2$/TiO_2 or F-SnO_2/TiO_2 faces. In all measurements the polarity of the forward voltages was always positive at the Au electrode. The devices being of the form Au/MPc/TiO_2/F-SnO_2 or $InSnO_2$, where the Sol-Gel TiO_2 film was manufactured according to code 'B' in Table 5.3 and annealed to a temperature of $500°C$ for 5 hours unless otherwise stated. A table containing all solar cell parameters obtained for the devices tested in these studies may be found in Appendix C.

C(V) characteristics were analysed in terms of Anderson's abrupt junction model[1] as discussed in chapter 3. Values of ε_1 (the permittivity of TiO_2 anatase), ε_2 (the permittivity of the MPc) and N_d as required by the formula are well reported in the literature[2-5]. Therefore the depletion layer width W, depletion layer penetration into the TiO_2 and the MPc's, x_1 and x_2, respectively and N_a the ionised acceptor concentration were estimated using the following values $N_d \sim 9 \times 10^{18} cm^3$, $\varepsilon_1 \sim 1.77 \times 10^{-12} Fcm^{-1}$ and $\varepsilon_2(CuPc) \sim 3.19 \times 10^{-13} Fcm^{-1}$, $\varepsilon_2(ClAlPc) \sim 3.54 \times 10^{-13} Fcm^{-1}$ and $\varepsilon_2(PbPc) \sim 3.45 \times 10^{-13} Fcm^{-1}$.

7.2 SEM Micrographs

Plate 7.1, 7.2 and 7.3 are scanning electron micrographs of the surface of vacuum sublimed PbPc, ClAlPc and CuPc respectively. The films were all sublimed onto TiO_2 Sol-Gel films which had been coated onto $InSnO_2$ coated glass substrates. The micrographs indicate that the MPc films were not compact but discontinuous and granular in appearance.

The elongated nature of the PbPc 'crystallites' are highly visible and could be a consequence of the non-planar nature of the PbPc molecule. The length of the PbPc crystallites were between 0.2-0.3µm.

The CuPc and ClAlPc 'crystallites' are spherical in appearance. The CuPc were of slightly smaller diameter at ~0.1µm than the ClAlPc which were between 0.2-0.3µm.
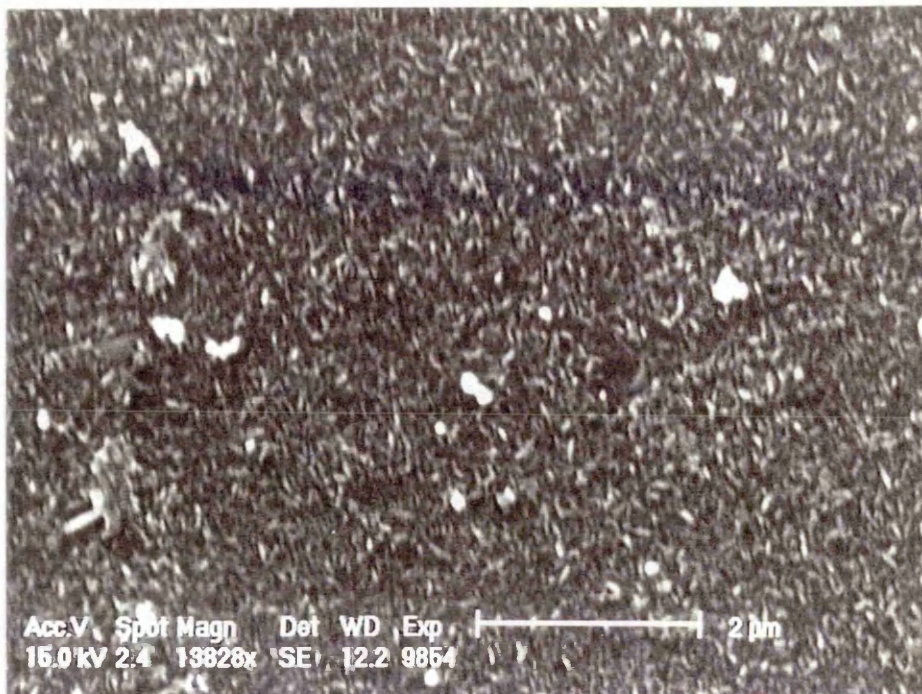
Plate 7.1. SEM micrograph of the PbPc sublimed film surface deposited onto TiO_2 Sol-Gel derived film.
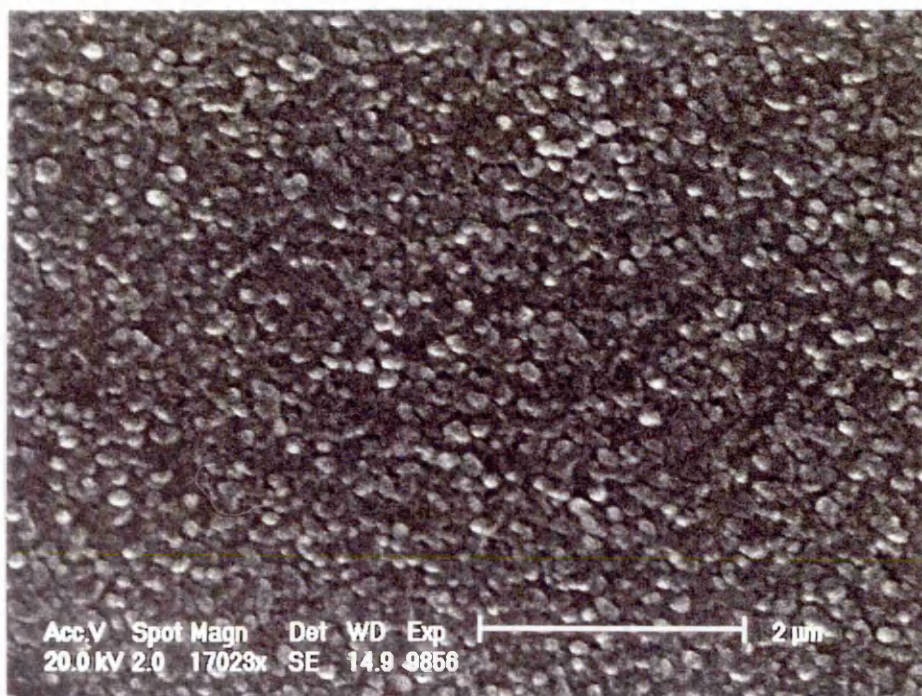
Plate 7.2. SEM micrograph of the ClAlPc sublimed film deposited on Sol-Gel derived TiO_2 film.
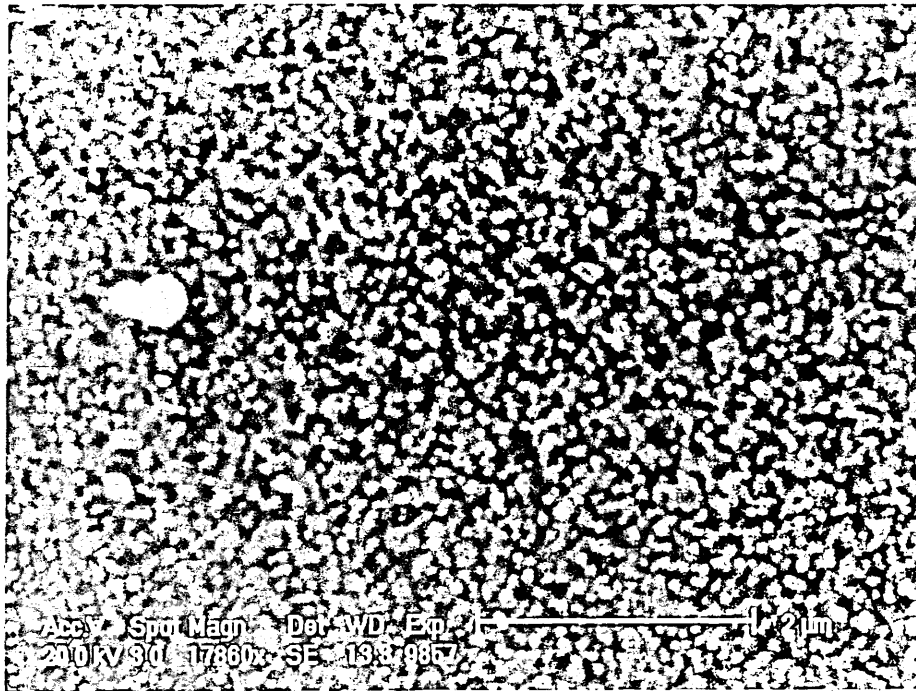
Plate 7.3. SEM micrograph of a sublimed CuPc film surface deposited on a Sol-Gel derived TiO$_2$ film.
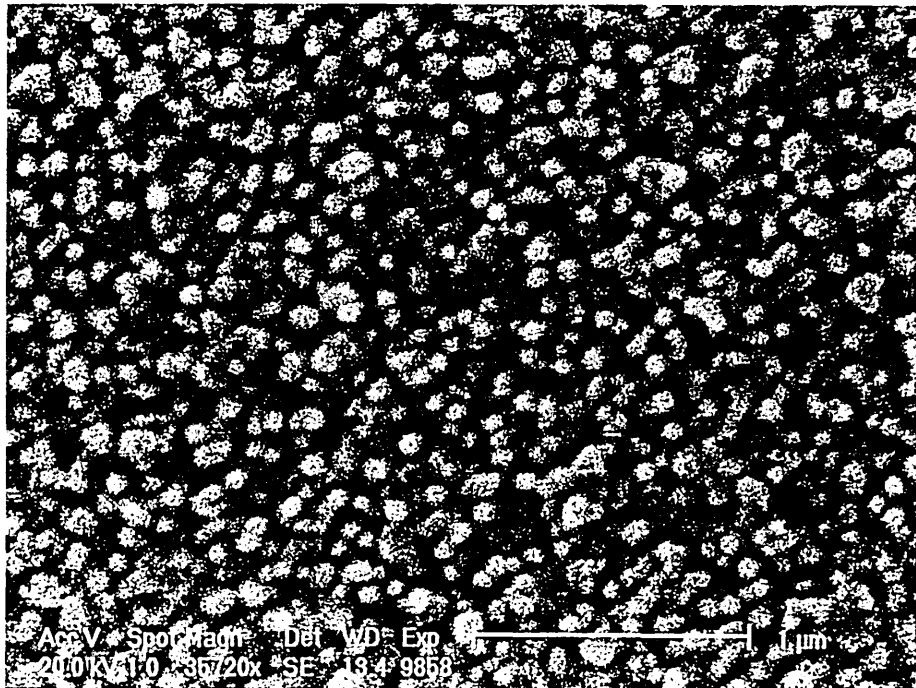
Plate 7.4. As for Plate 7.3 at ~ x2 higher magnification.

7.3 ClAlPc/TiO$_2$

7.3.1 Spectral Response

Figures 7.1 and 7.2 display the short circuit photocurrent density J$_{sc}$ as a function of wavelength (λ) for a Au/ClAlPc($\sim$500nm)TiO$_2$($\sim$50nm)/InSnO$_2$ heterojunction cell, measured at room temperature under vacuum and atmospheric conditions respectively. The wavelength dependence of J$_{sc}$ in both cases is similar to the absorption spectra of the ClAlPc sublimed film. Photocurrent maxima are located at approximately 380nm and 700nm. Under vacuum the maximum J$_{sc}$ was 0.133μA/cm^2 at 700nm, and 0.029μA/cm^2 at 380nm. Using equation (3.34) this corresponded to a maximum calculated quantum efficiency (Z) of 0.74% and 0.3% at 700nm and 380nm respectively. A reduction in the short circuit photocurrent was observed when measurements were taken under atmospheric conditions. At 700nm the measured photocurrent density, J$_{sc}$ was $\sim$0.038μA/cm^2 such that Z$\sim$0.21%. At 380nm J$_{sc}$$\sim$0.027$\mu$A/cm^2 and Z$\sim$ 0.28%.

The photocurrent action spectra were found to be fairly reproducible with F-SnO$_2$ base electrodes, as shown in Figure 7.3. A change of substrate base electrode material to F-doped SnO$_2$ resulted in lower J$_{sc}$ $\sim$0.087μA/cm^2 and a corresponding quantum efficiency of 0.48% at 700nm under vacuum. A shift in the second maxima to 345nm was observed, the photocurrent density was higher at this wavelength than the device consisting of an InSnO$_2$ substrate at $\sim$0.07μA/cm^2 where Z$\sim$ 0.79%. A suppression in the magnitude of J$_{sc}$, was observed at 380nm in the device containing an InSnO$_2$ substrate when measured under vacuum. This suppression was observed in subsequent measurements using the alternative dyes and is discussed section 8.3.1.

Figure 7.1. J_{sc} ($\mu A/cm^2$) (□) action spectra of a Au/ClAlPc(~500nm)/TiO$_2$(~50nm)/InSnO$_2$ cell.
Absorption spectra of ClAlPc film only (——). Absorption spectra of TiO$_2$ film only (---).
Measurements taken under vacuum at room temperature.

Figure 7.2. J_{sc} ($\mu A/cm^2$) (O) action spectra of a Au/ClAlPc(~500nm)/TiO$_2$(~50nm)/InSnO$_2$ cell.
Absorption spectra of ClAlPc film only (——). Absorption spectra of TiO$_2$ film only (---).
Measurements taken in air at room temperature.

172

Figure 7.3. J_{sc} action spectra ($\mu A/cm^2$) (O) of a Au/ClAlPc(~500nm)/TiO$_2$ (~50nm)/F-SnO2 cell. (□) represents a repeat measurement. Absorption spectra of ClAlPc film only (——), Absorption spectra of TiO$_2$ film only (---). Measurements taken at room temperature and under vacuum.

173

7.3.2 Dark J(V) Characteristics

The forward and reverse dark J(V) characteristics typically observed for the Au/ClAlPc(~500nm)/TiO$_2$(~50nm) heterojunction cells are shown in Figure 7.4, the base electrode was InSnO$_2$. Similar characteristics were observed for devices consisting of F-SnO$_2$ base electrodes. Measurements were made at room temperature under both vacuum and atmospheric conditions. The cells exhibited rectifying properties, although the rectification ratios (r) were very low (between 1.3 and 4.94 at 0.3V), a summary is shown in Table 7.1. The devices exhibit a degree of reproducibility, the repeat of the measurements taken under atmospheric conditions is shown in Figure 7.4 for comparison.

As previously discussed, a plot of $\ln[I/\{1-\exp(-eV/kT)\}]$ against the bias voltage V(V) will be linear for all values of V, for both reverses voltages and forward voltages less than $3kT/e$, which corresponds to 75.5 mV. Figures 7.5 and 7.6 are such plots for devices consisting of InSnO$_2$ and F-SnO$_2$ base electrodes respectively. For V< $3kT/e$, a linear dependence is observed. The ideality factor, m and the saturation current density, J$_s$ were calculated from the slope and interrcept respectively and are given in Table 7.1. The diode ideality factors were 1<m<1.2 for all devices comprising of both types of base electrodes. Although, those consisting of F-SnO$_2$ base electrodes had consistently slightly higher factors than the devices constructed with InSnO$_2$ electrodes. Ambient conditions had negligible effect on the ideality factors.

Slight variations in the saturation current density, J$_s$ were observed depending on the ambient conditions and base electrodes, although high values of J$_s$ were observed in all the ClAlPc/TiO$_2$ devices studied.

174

Figure 7.4. Dark forward and reverse J(V) characteristics of a Au/ClAlPc(500nm)/TiO$_2$(50nm)/InSnO$_2$ cell. Measurements were made at room temperature and under vacuum or atmospheric conditions as indicated. A repeat measurement is also shown.

Figure 7.5. Plot of ln(I/[1-exp(-eV/kT)]) against V for the Au/ClAlPc(500nm)/TiO$_2$(50nm)/InSnO$_2$ cell.

175

Figure 7.6. Logarithmic plot of I/[1-exp(-eV/kT)] against V for the Au/ClAlPc(500nm)/TiO$_2$(50nm)/F-SnO$_2$ cell.

Substrate	Ambient	m	J$_s$ (x 10^{-9}A/cm^2)	γ	T$_c$	Rectification Ratio, r at 0.3V
InSnO$_2$	Air	1.01	5.1	1.93	564	1.62
"	"	1	5.64	1.87	546	1.47
"	Vacuum (~10^{-3}torr)	1.01	3.42	1.98	578	4.94
*"	"	1.15	5.11	3.28	958	1.33
F-SnO$_2$	"	1.11	10.3	0.52	152	1.3
"	Air	1.18	0.93	0.47	137	3.06

Table 7.1. Electrical characteristics of the ClAlPc/TiO$_2$ heterojunction cells, m and J$_s$ were obtained from reverse characteristics and for V<3kT/e according to Missous and Rhoderick[6].
* TiO$_2$ layer annealed to a temperature of 100°C for 5 hours.

176

The forward characteristics were fitted to the standard diode equation, (equation (3.35)). Plots of lnJ against applied bias V are therefore displayed in Figures 7.7 and 7.8. In all cases m>2, regardless of ambient conditions, substrate type or forward voltage range. Very high values of m were determined for higher forward voltages. An improvement in device performance was observed for the ClAlPc/TiO_2 cell measured under vacuum with $InSnO_2$ base electrode, although m~2.6 the saturation current density J_s ~7x10^{-11}A/cm^2 which is relatively low. At higher forward voltages (V>~0.4V) a dependence J∝KV^Q was observed where Q>1. This is similar to the situation of space charge limited conduction[7]. Under these circumstances the current density is described according to Helfrich[8];

$$J_{SCLC} = \frac{BV^{\gamma+1}}{t^{2\gamma+1}}$$
7.1

where J_{SCLC} the the space charge limited current density, B is a constant, t the film thickness and $\gamma = T_c/T$, where T_c is a parameter characteristic of the trap distribution. Values of T_c and γ were calculated from logarithmic plots of the high forward J(V) characteristics. Significantly lower values of T_c were observed for those devices comprising of F-SnO_2 base electrodes.

Figure 7.9 shows the dark forward and reverse characteristics obtained for a ClAlPc/TiO_2 cell in which the TiO_2 had been densified to a much lower temperature of 100°C. The significant difference observed was the measured value of T_c ~958 compared to T_c~578 for a similar device in which the TiO_2 had been heated to 500°C. All the deduced electrical parameters are shown in Tables 7.1 and 7.2.
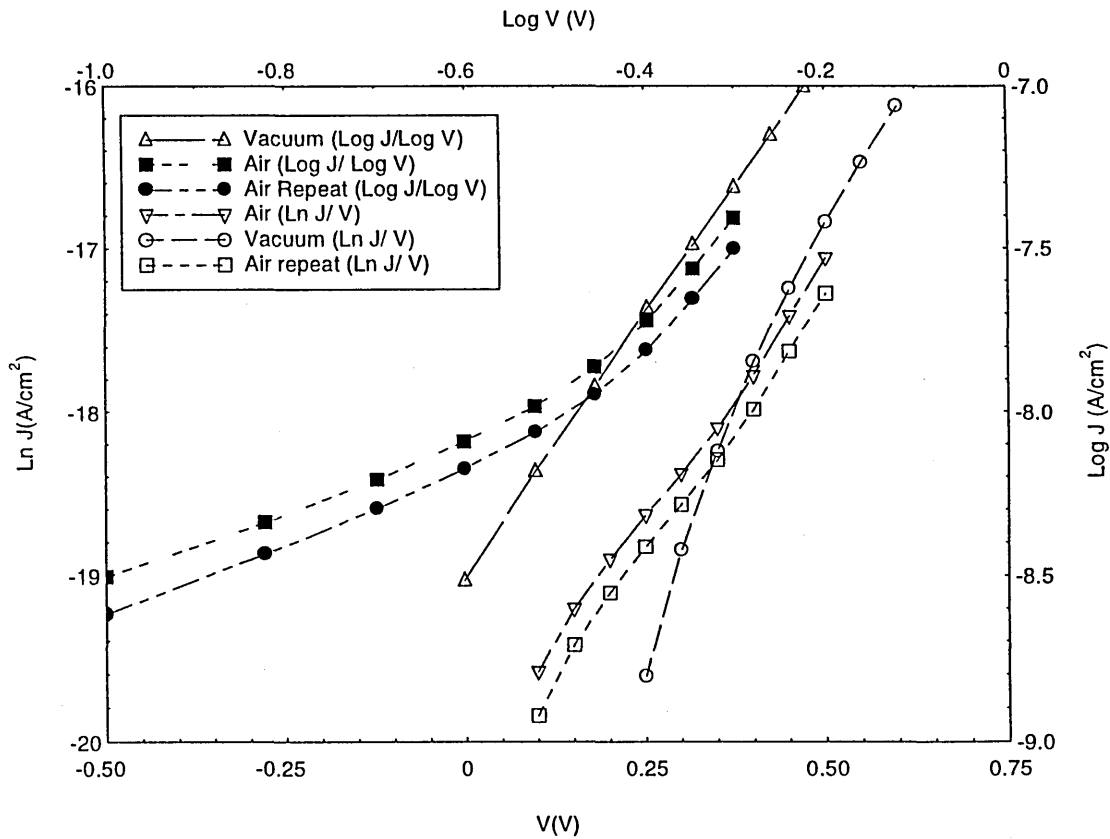
Figure 7.7. ln (J) Vs V and log J Vs log V for the Au/ClAlPc(500nm)/TiO$_2$(50nm)/InSnO$_2$ cell..
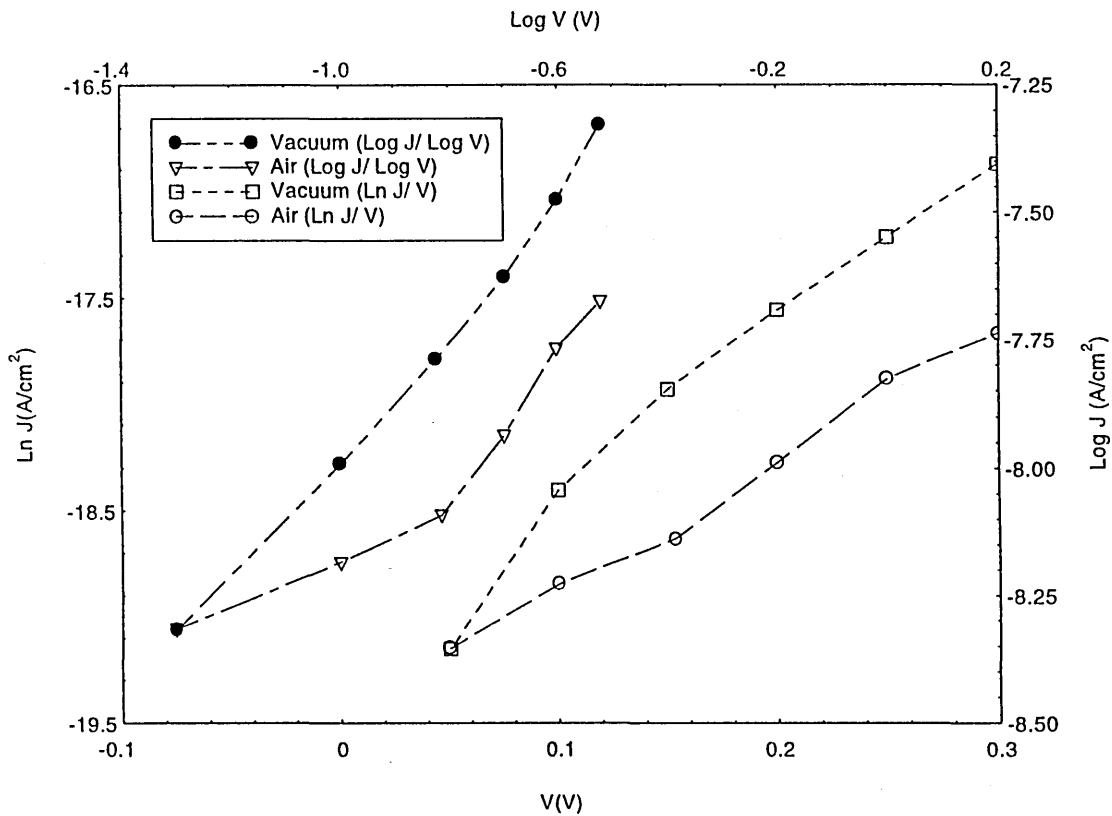
Figure 7.8. ln (J) Vs. applied forward bias for the Au/ClAlPc(500nm)/TiO$_2$(50nm)/F-SnO$_2$ cell.

178

Substrate	Ambient	Voltage Range (V)	Q	m	$J_s(\times 10^{-9} A/cm^2)$
InSnO₂	Air	0.17-0.2		5.2	1.53
"	"	0.2-0.37	3.23	7.48	2.06
"	"	0.37-0.5	V>0.4V	5.5	1.02
"	"(Repeat)	0.17-0.2		4.72	1.02
"	"	0.2-0.37	3.18	7.41	1.67
"	"	0.37-0.5	V>0.4V	5.6	9.26
"	Vacuum	0.25-0.36		2.6	0.07
"	"	0.3-0.4	3.96	3.46	0.21
"	"	0.4-0.6	V>0.4V	5.08	0.93
* "	"	0-0.3		4.4	4.59
* "	"	0.3-0.6	4.28	4.03	2.28
* "	"	0.6-0.8	V>0.4V	8.08	41.4
F-SnO₂	Air	0.05-0.12		6.6	3.76
"	"	0.12-0.22	1.47	5.17	2.52
"	"	0.22-0.3	V>0.15V	9.26	5.6
"	Vacuum	0.05-0.12		2.65	2.28
"	"	0.12-0.22	1.68	5.3	5.07
"	"	0.22-0.3	V>0.15V	5.82	6.19

Table 7.2. Electrical parameters of the ClAlPc/TiO₂ heterojunction cell as obtained from forward characteristics using standard diode equation. * where TiO₂ annealed to 100°C for 5 hours.
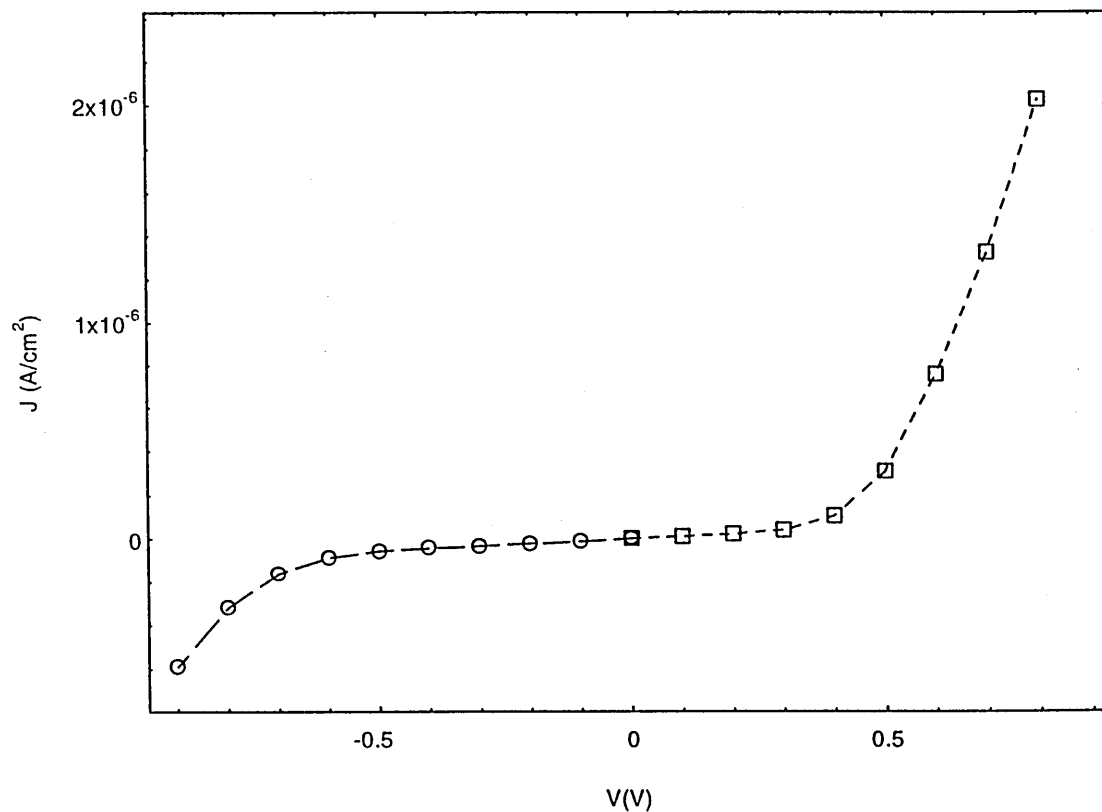
Figure 7.9. Room temperature J(V) characteristics of a Au/ClAlPc(500nm)/TiO₂(50nm)/InSnO₂ device in darkness and under vacuum
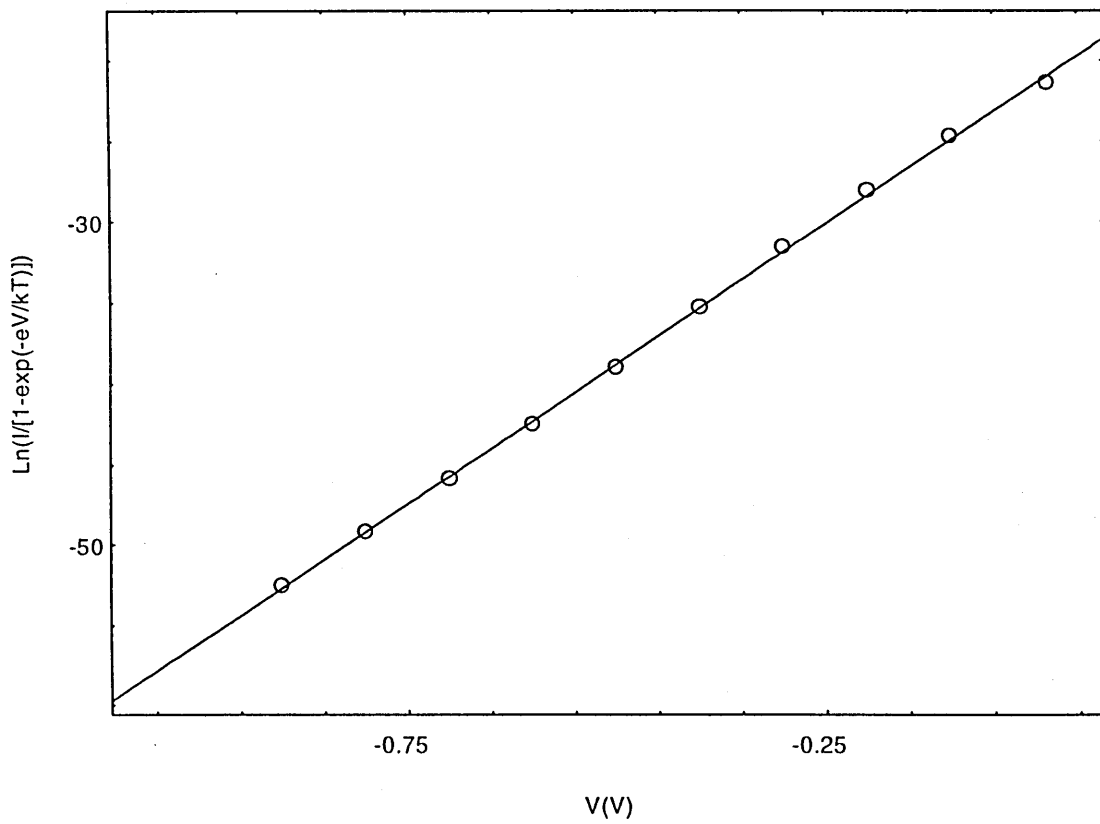
Figure 7.10. Logarithmic plot of I/[1-exp(-eV/kT)] Vs. V for the Au/ClAlPc(500nm)/TiO$_2$ 50nm)/InSnO$_2$ device.
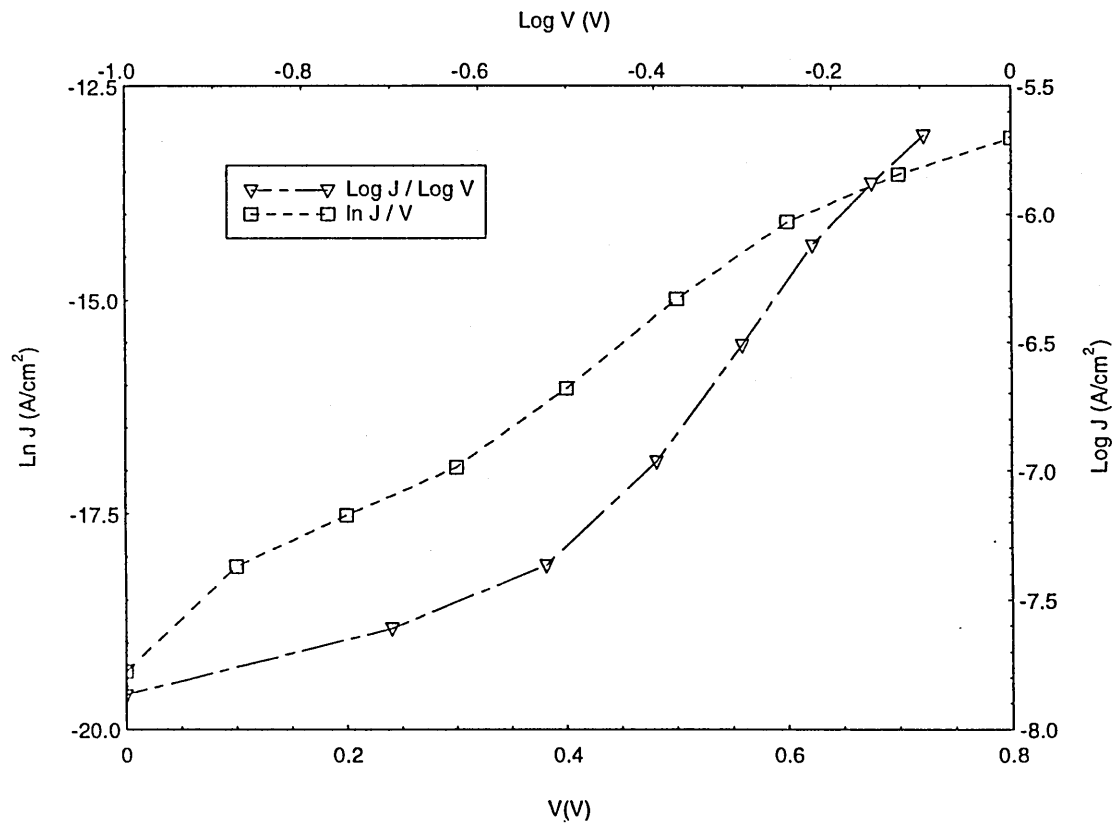
Figure 7.11 ln J Vs. V and log J Vs. log V of forward characteristics for ClAlPc/TiO$_2$ device

7.3.3 Illuminated J(V) Characteristics

The J(V) characteristics of a $Au/ClAlPc(500nm)/TiO_2(50nm)/InSnO_2$ device measured under atmospheric conditions are shown in Figure 7.12, for a variety of intensity levels. The highest overall conversion efficiency obtained for the cells was $\eta\sim0.0015\%$ at an intensity level of $1.12mW/cm^2$, the corresponding FF, V_{oc} and J_{sc} at this intensity were 0.165, 0.468V, and 2.19×10^{-7} A/cm^2 respectively.

The intensity dependence of J_{sc}, V_{oc} and subsequently FF and $\eta\%$ of the cells was investigated. The dependencies are shown in Figures 7.13 and 7.14. It is observed that V_{oc} is virtually proportional to the logarithm of the incident light intensity, increasing with intensity to a relatively high maximum value of $\sim0.5V$.

The photocurrent increased approximately linearly with the light intensity ϕ. An exponent of y=0.88 was derived according to $J_{sc}\propto\phi^y$. The FF generally increased as the incident intensity increased, although the behaviour was erratic at low intensities. A corresponding increase in the overall conversion efficiency with increasing intensity was also observed, however at high intensities $\eta\%$ reduced slightly even though FF, V_{oc} and J_{sc} were at the maximum observed values.

From the J(V) plots under illuminated conditions, the average series resistance, (R_s) for the cell was determined from the slope of the plots in forward bias where $V>V_{oc}$. From the reverse characteristics where $J\propto V$, R_{sh} was calculated (for ideal p-n junction PV cells $R_s\sim0\Omega cm^{-2}$, $R_{sh}\sim\infty\Omega cm^{-2}$). R_s and R_{sh} were calculated to be $1.2M\Omega cm^{-2}$ and $5.2M\Omega cm^{-2}$ respectively.

181
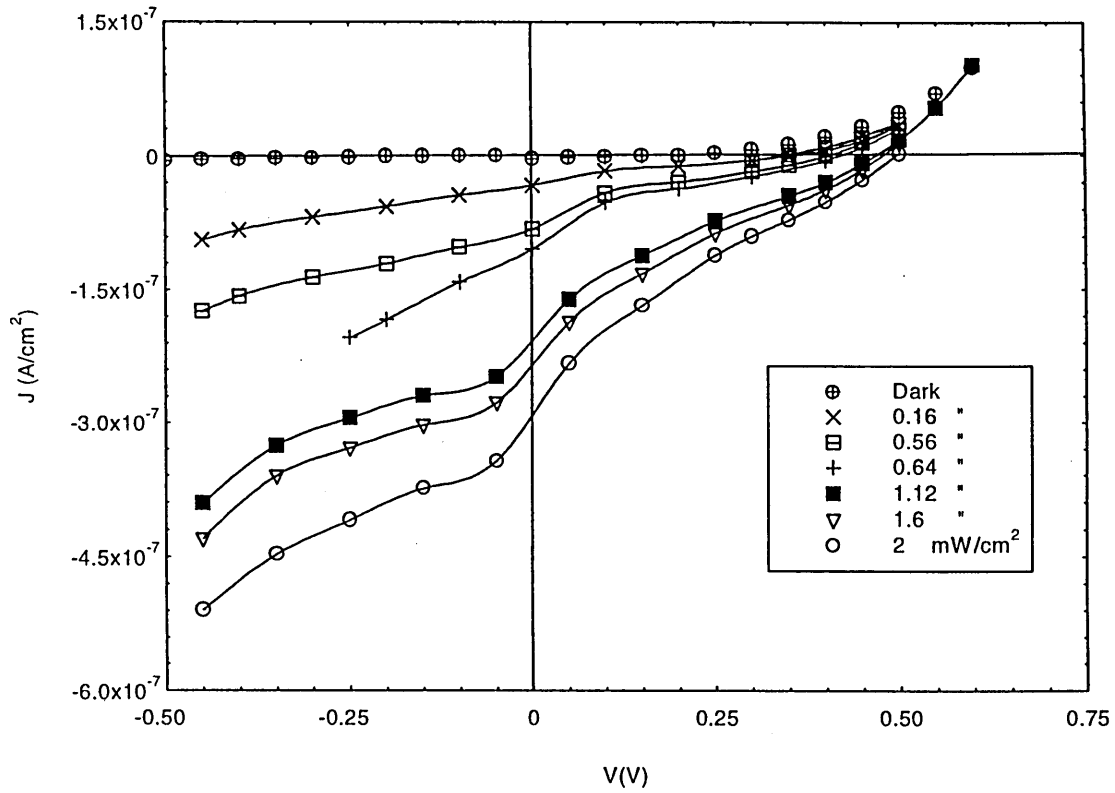
Figure 7.12. J(V) characteristics obtained for a Au/ClAlPc(500nm)/TiO$_2$(50nm)/InSnO$_2$ heterojunction cell under atmospheric conditions. In darkness and under simulated AM2 radiation. at a variety of intensities as indicated. Illumination through the InSnO$_2$ side.
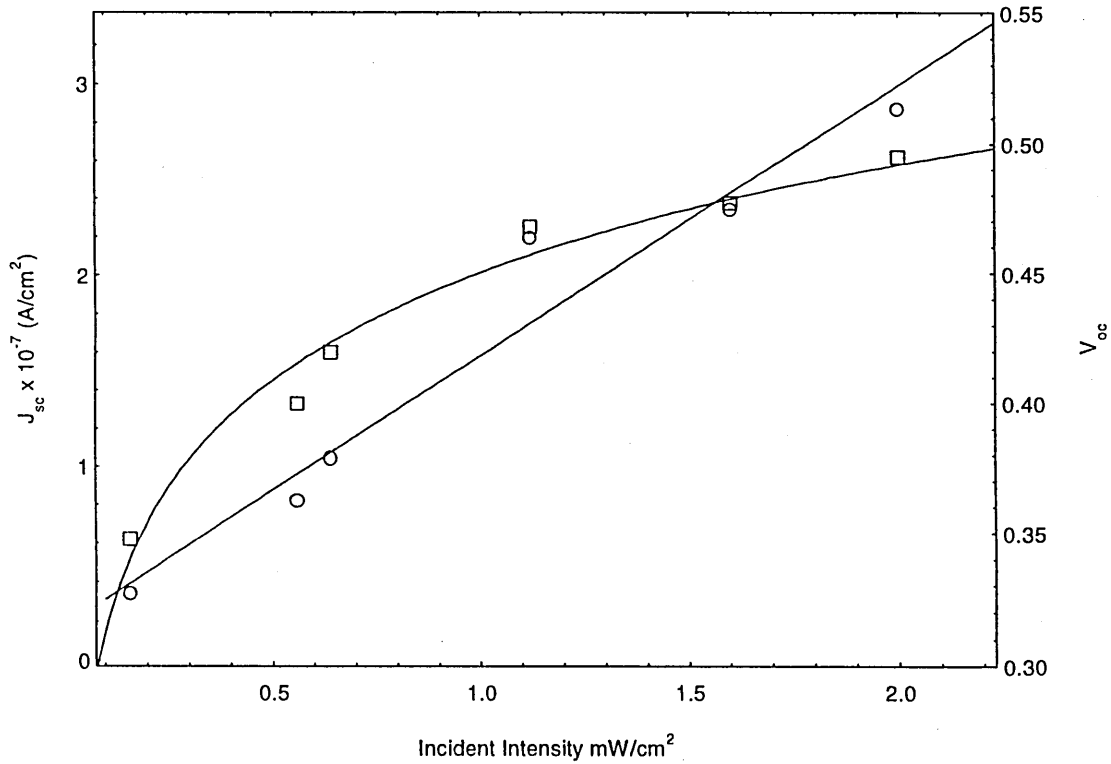
Figure 7.13 Graph showing V$_{oc}$ ( ) with logarithmic fitting and J$_{sc}$ (O) with linear fitting as a function of incident light intensity for the Au/ClAlPc(500nm)/TiO$_2$(50nm)/InSnO$_2$ heterojunction cell under atmospheric conditions

In order to investigate the effects of ambient conditions the measurements were repeated for the same cell measured under vacuum ($\sim 10^{-3}$ torr). The J(V) characteristics of the cell in darkness and under illumination for a variety of intensity levels are shown in Figure 7.15. The highest overall conversion efficiency $\eta\%$ obtained for the cell under vacuum was 0.0047% at an intensity level of 1.12mW/cm^2, this corresponded to V_{oc}, FF, and J_{sc} values of 0.479V, 0.304 and 3.64x10^{-7} A/cm^2 respectively. The value of $\eta\%$ for cell measured under vacuum represents an increase of ~200% compared to the cell measured under atmospheric conditions.

Figures 7.16 and 7.17 show the dependencies on the intensity of J_{sc}, V_{oc}, FF and $\eta\%$. V_{oc} increased with increasing intensity although a weaker dependence was observed compared to that measured for the device under atmospheric conditions. J_{sc} also increased with the increasing intensity and saturated at higher intensities. A fit of $J_s \propto \phi^y$ resulted in y=0.32. The values of R_s and R_{sh} were 2.27MΩcm^{-2} and 0.7MΩcm^{-2} respectively.

The FF increased with increasing intensity to a maximum at 1.12mW/cm^2 which coincides with a peak in $\eta\%$. At high intensities the FF decreased which was followed by a decrease in $\eta\%$. At low intensities $\eta\%$ increased, which could be a consequence of the relatively high V_{oc} measured at these intensities. The peak in $\eta\%$ was observed under both atmospheric and vacuum conditions at 1.12mWcm^{-2}.
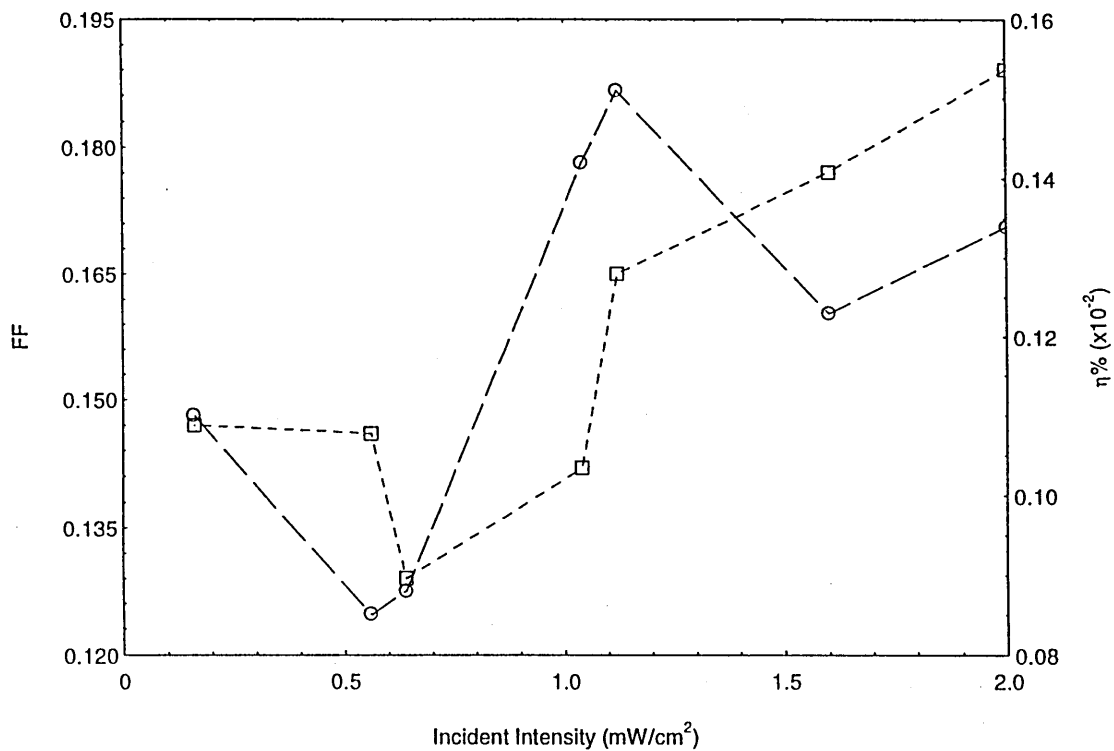
Figure 7.14. Fill factor ( ) and overall conversion efficiency η% (O) as a function of incident light intensity φ, mW/cm². Measurements made under atmospheric conditions.
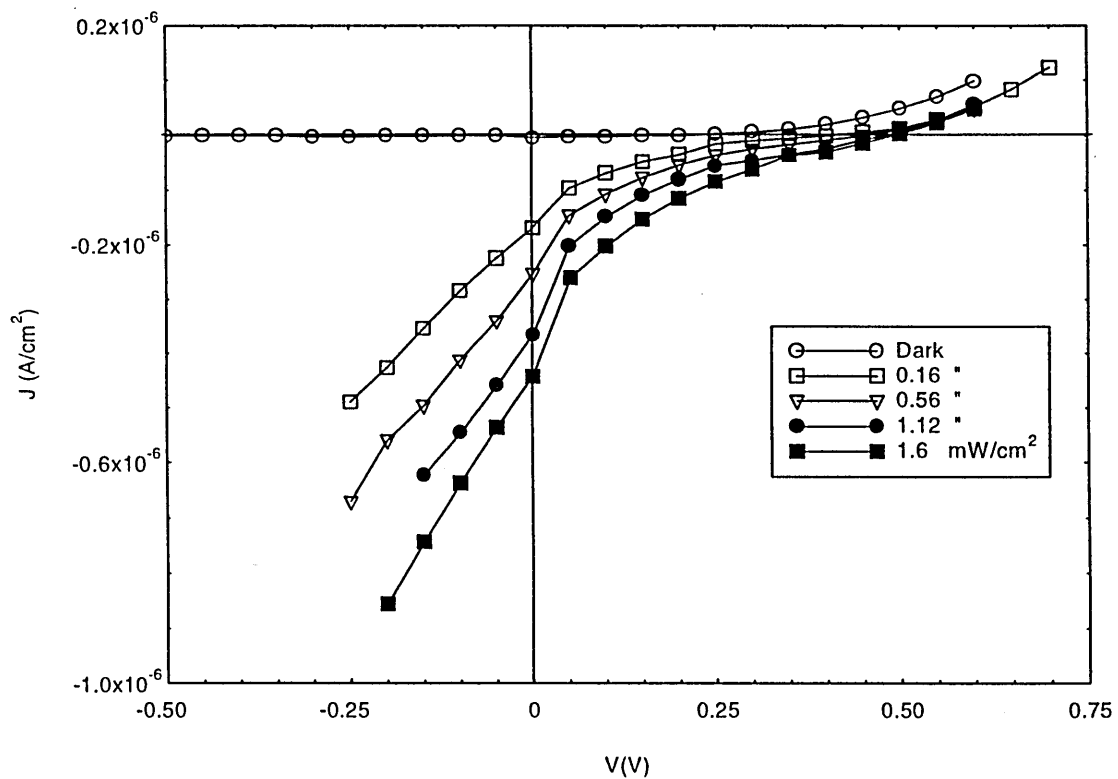
Figure 7.15. J(V) characteristics obtained for Au/ClAlPc(500nm)/TiO₂(50nm)/InSnO₂ heterojunction cell under vacuum, in darkness and under simulated AM2 radiation, at a variety of intensities as indicated.
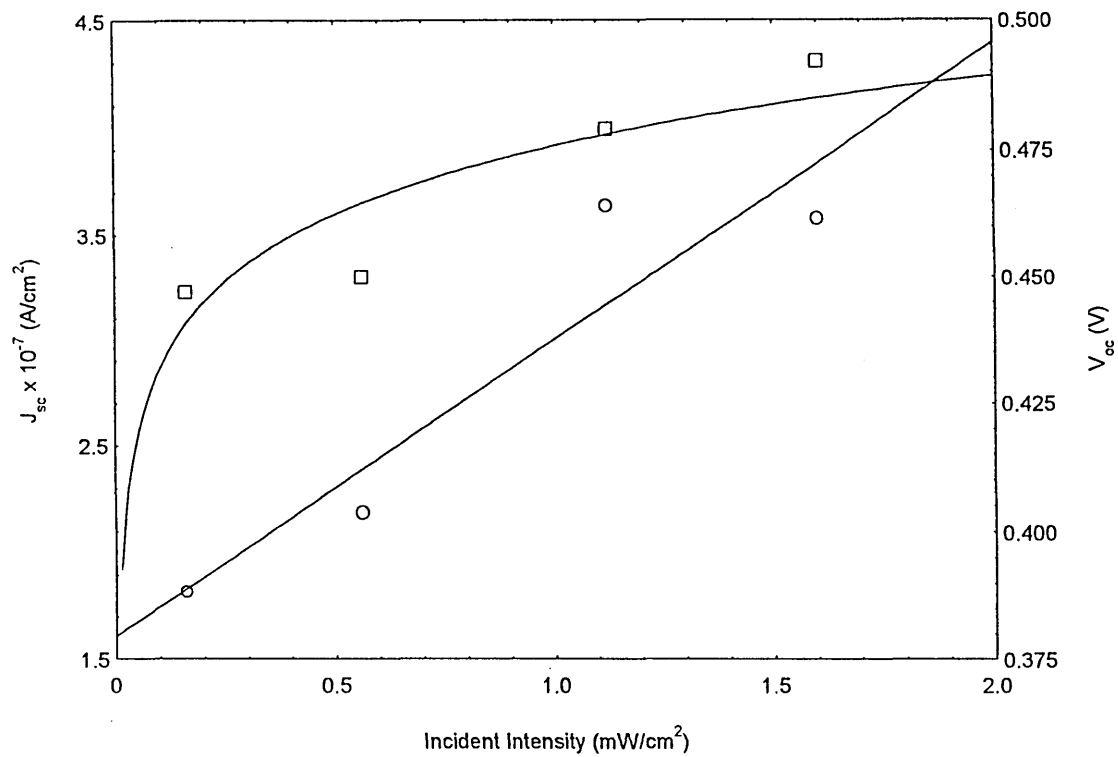
Figure 7.16. Graph showing variation of V_{oc} (□) with logarithmic fitting and J_{sc} (O) with linear fitting as a function of incident light intensity ϕ for the cell as in Figure 7.15.
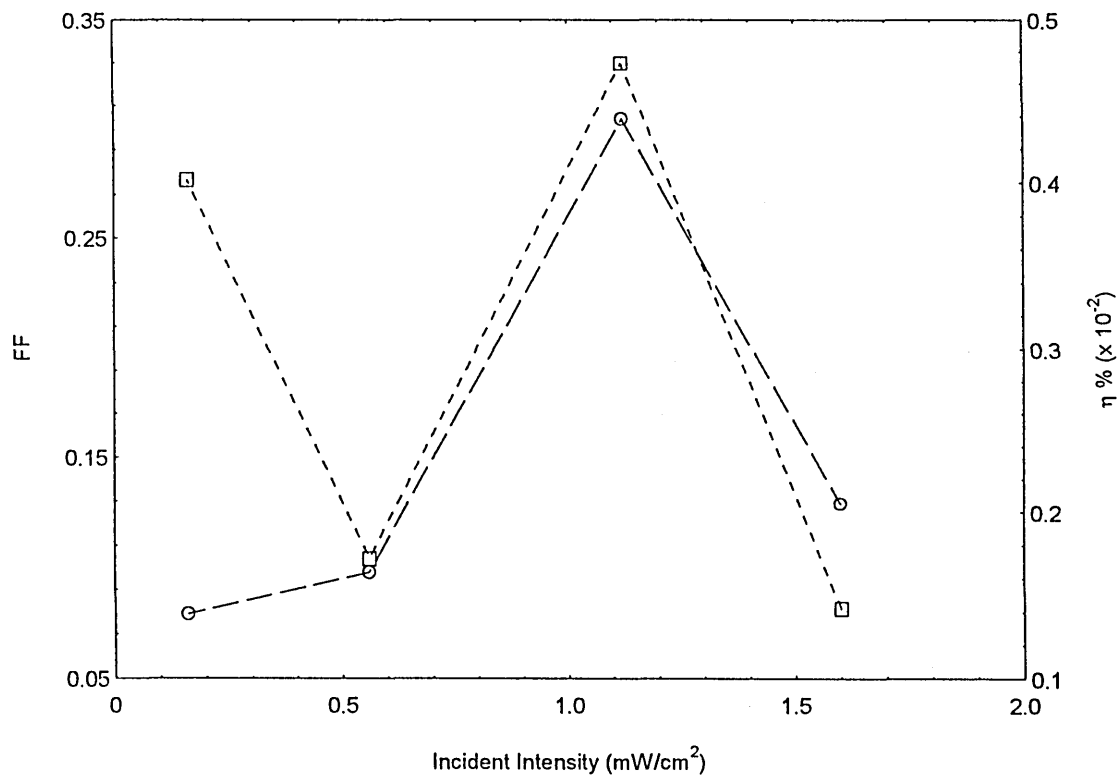
Figure 7.17. Fill factor (O) and $\eta\%$ (□) as a function of incident light intensity ϕ of the cell as in Figure 7.15.

185

7.3.4 C(V) Characteristics

The dark C(V) measurements of Au/ClAlPc(500nm)/TiO$_2$(50nm)/InSnO$_2$ heterojunction cells were carried out at room temperature, atmospheric conditions and at a fixed frequency of 500Hz, with an oscillating voltage level of 1V. Figure 7.18 presents a plot of C^{-2} as a function of reverse applied bias V(V). The linearity of C^{-2}(V) characteristics indicates the presence of an abrupt junction.

Using equation (3.42) a value of N$_a$~4.6x10^{19}cm^{-3} was deduced. However the capacitance was found to be virtually independent of the reverse bias voltage. Most of the applied bias may have therefore been dropped over the high series resistance ((R$_s$~1.2MΩ) as observed from illuminated J(V) data) of the cells rather than the junction. As a consequence the junction capacitance would be insensitive to the applied bias. However, the independence may also have been attributed to high interface state density and pin holes. Nevertheless, this resulted in an unrealistic value for the built in potential ϕ_{bp} which was deduced from the intercept (i.e. ~192V). The value of N$_a$ as calculated above must therefore be taken with caution. Indeed, calculation of the transition region width using this model leads to W~544nm, practically the thickness of the device.

Observation of the entire C^{-2}(V) characteristics, shown in Figure 7.19, indicates that a Bethe type[9] type barrier may be present. According to the Bethe model[9] the intercept of the 1/C^2 against V plot with the horizontal asymptote , rather than the base lines gives the built in potential ϕ_{bp}.

186

A value of ϕ_{bp} ~0.02V was obtained. From the Bethe model[9] the density of ionised trapping centres contributing to the barrier capacitance is H~$1.41 \times 10^{18} cm^{-3}$ and the barrier width (where C_o ~224.328pF) is W~473nm, which is still unrealistic. However, combining the Bethe model[9] with Andersons abrupt junction model[1], the substitution of ϕ_{bp} gives a depletion layer width of 5.55nm, which is comparable with later studies of the depletion layer width on the $CuPc/TiO_2$ and $PbPc/TiO_2$ cells.
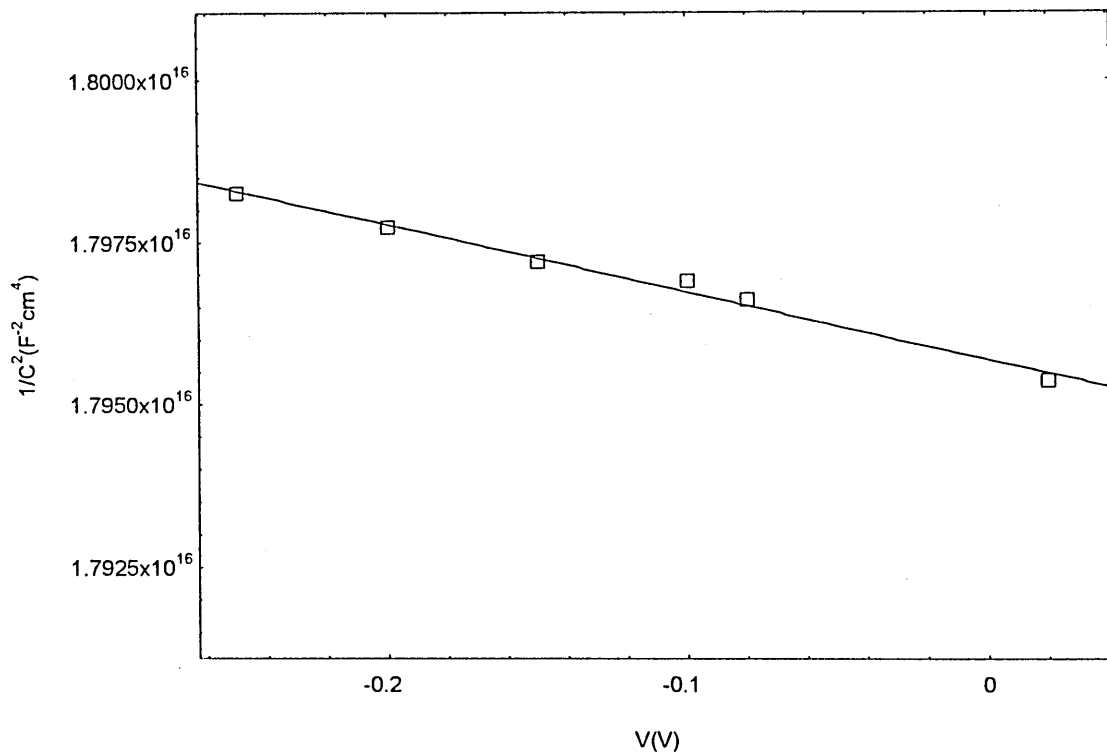
Figure 7.18. $1/C^2$ against reverse applied bias V(V) for a Au/ClAlPc(500nm)/TiO$_2$(50nm)/InSnO$_2$ heterojunction cell under darkness and atmospheric conditions.
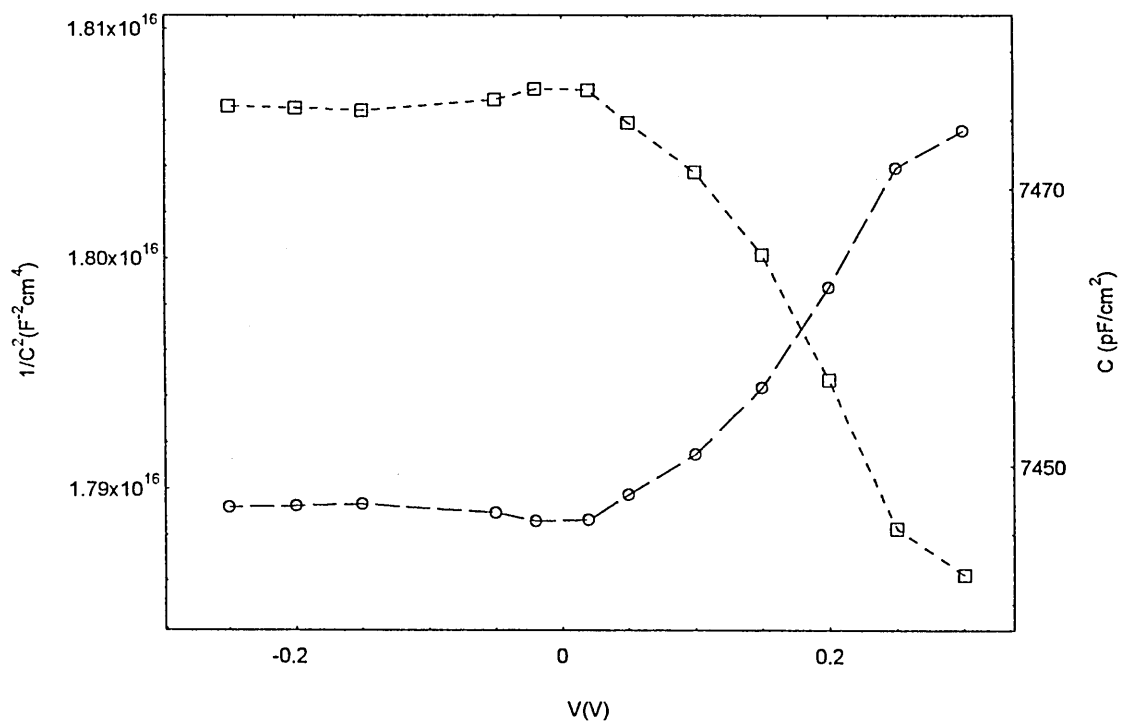
Figure 7.19. C^{-2}(V), (O) and C(V) ($\square$) characteristics of the Au/ClAlPc(500nm)/TiO$_2$(50nm)/InSnO$_2$ heterojunction cell under darkness and atmospheric conditions.

7.4. CuPc/TiO$_2$

7.4.1 Spectral Response

Figures 7.20 and 7.21 show the J$_{sc}$ and V$_{oc}$ action spectra respectively as a function of wavelength, λ for a Au/CuPc(~500nm)/TiO$_2$(50nm)/InSnO$_2$ cell, measurements were taken under both atmospheric conditions and under N$_2$ gas. The maximum observed quantum efficiencies, Z under both N$_2$ and atmospheric conditions occurred at λ~350nm as Z~ 0.34% and Z~0.43% respectively. The corresponding J$_{sc}$ at this wavelength were 0.031μA/cm^2 and 0.039 μA/cm^2 respectively. Under both conditions higher J$_{sc}$ was observed at the λ~590nm maxima. (J$_{sc}$~0.034 μA/cm^2 under N$_2$ and J$_{sc}$~0.043 μA/cm^2 under atmospheric conditions). However this did not give rise to a corresponding increase in Z. (Z~0.22% under N$_2$ and Z~0.28% under atmospheric conditions). A decrease in J$_{sc}$ and Z was observed at the λ~700nm maxima. Where Z~ 0.15% and J$_{sc}$~0.027 μA/cm^2 under N$_2$, and Z~0.2% and J$_{sc}$~ 0.036 μA/cm^2 under atmospheric conditions. The open circuit voltage V$_{oc}$ was found to vary as a function of incident wavelength under both N$_2$ and atmospheric conditions. The values of V$_{oc}$ under N$_2$ at peak wavelength positions were 16mV at 350nm, 12mV at 590nm and 6.5mV at 700nm. Under atmospheric conditions maximum V$_{oc}$ observed were 15.5mV at 350nm, 14.8mV at 590nm and 8.3mV at 700nm.

Maxima in the absorption spectra coincided with observed maxima in the J$_{sc}$ and V$_{oc}$ action spectra. Therefore indicating that the dye had sensitised the TiO$_2$ to wavelengths outside the materials intrinsic sensitivity. An increase in both open circuit voltage and short circuit current density were observed for measurements carried out under atmospheric conditions.

189
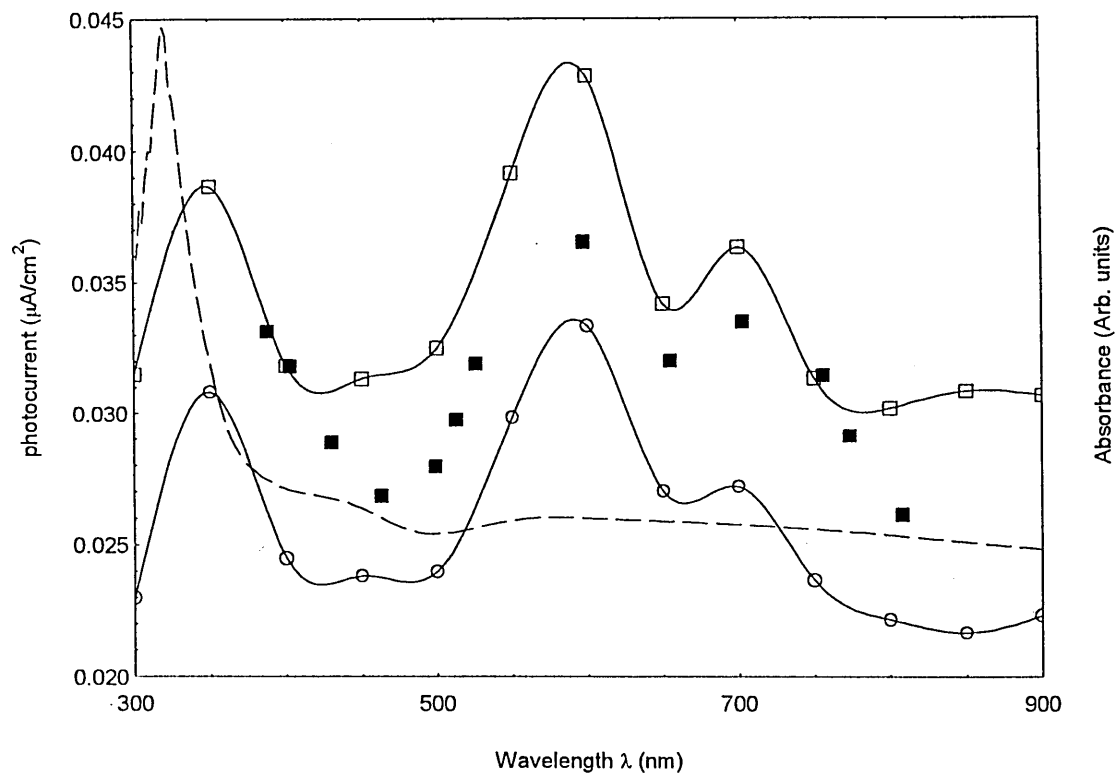
Figure. 7.20 J_{sc} (μA/cm^2) as a function of wavelength under Nitrogen (O) and air ($\square$) of a
Au/CuPc(500nm)/TiO$_2$(50nm)/InSnO$_2$ cell. ($\blacksquare$) and (---) represent the absorbance of a
CuPc film and TiO$_2$ film respectively
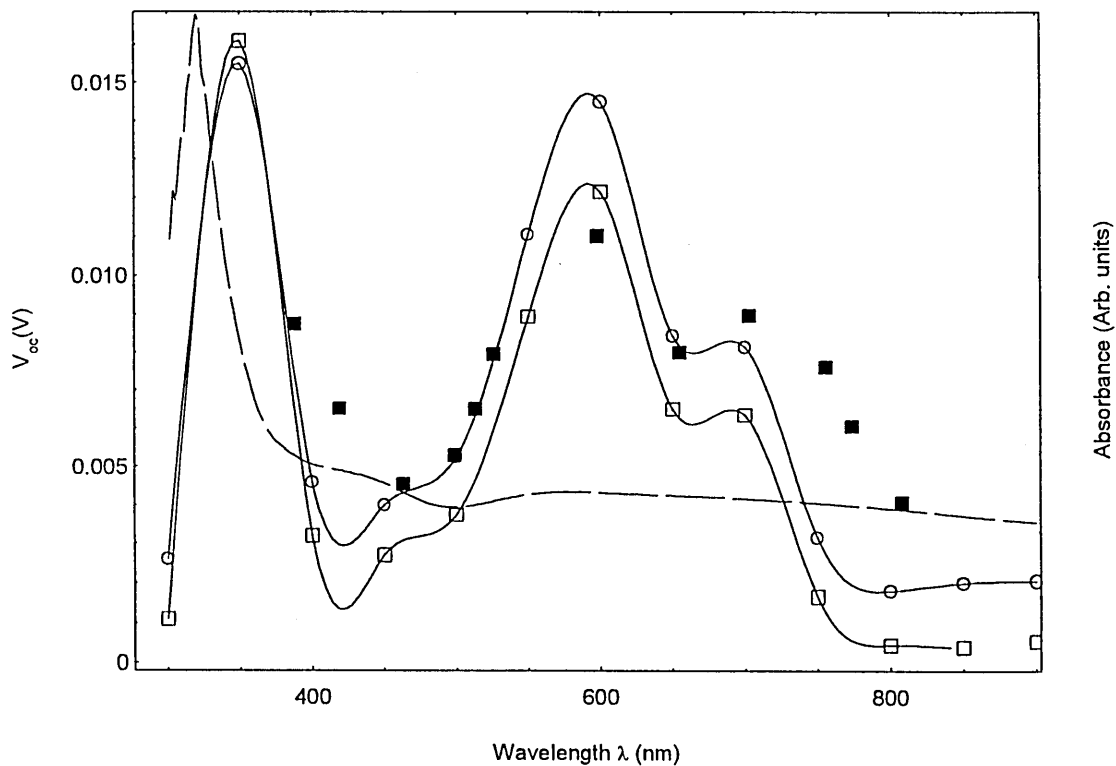
Figure 7.21. V_{oc} (V) as a function of wavelength under air (O) and Nitrogen ($\square$) of a
Au/CuPc (500nm)/TiO$_2$(50nm)/InSnO$_2$ cell. ($\blacksquare$) and (---) represent the absorbance of a
CuPc film and TiO$_2$ film respectively.

7.4.2 Dark J(V) Characteristics

Figure 7.22 shows typical dark forward and reverse J(V) characteristics of a Au/CuPc(500nm)/TiO$_2$(50nm)/InSnO$_2$ heterojunction cell, the measurements were taken under vacuum and at room temperature. Identical devices measured under N$_2$ and atmospheric conditions exhibited similar characteristics. Rectification effects were observed under all conditions, the ratios (r) are given in Table 7.3. The lowest values of r were for those cells measured under vacuum r~11 and increased to r~30 for devices measured under N$_2$ gas.

For bias voltages V<3kT/e, values of the saturation current density J$_s$ and the ideality factor m (summarised in Table 7.3) were deduced from plots of ln[I/{1-exp(-eV/kT}] against V(V), shown in Figure 7.23. Both m and J$_s$ were found to be reproducible. The ideality factor was in the range 1>m>1.2 and the saturation current density in the range 2.2<J$_s$<4.6 (x10^{-7}A/cm^2).

Table 7.4 summarises the results obtained from the forward characteristics when fitted to the standard diode equation (equation (3.35)), over the voltage ranges as indicated. Reasonable fits to the equation were observed at low forward voltages ~V<0.15V. In this range values of m ~ 2, though m~2.3 under vacuum. Very high J$_s$~(3-5)x10^{-7}A/cm^2 was observed under all conditions. For V>0.15V deviation from the standard diode equation was observed. At these applied bias the J(V) characteristics displayed a good fit to the relation J=KV^Q.

191
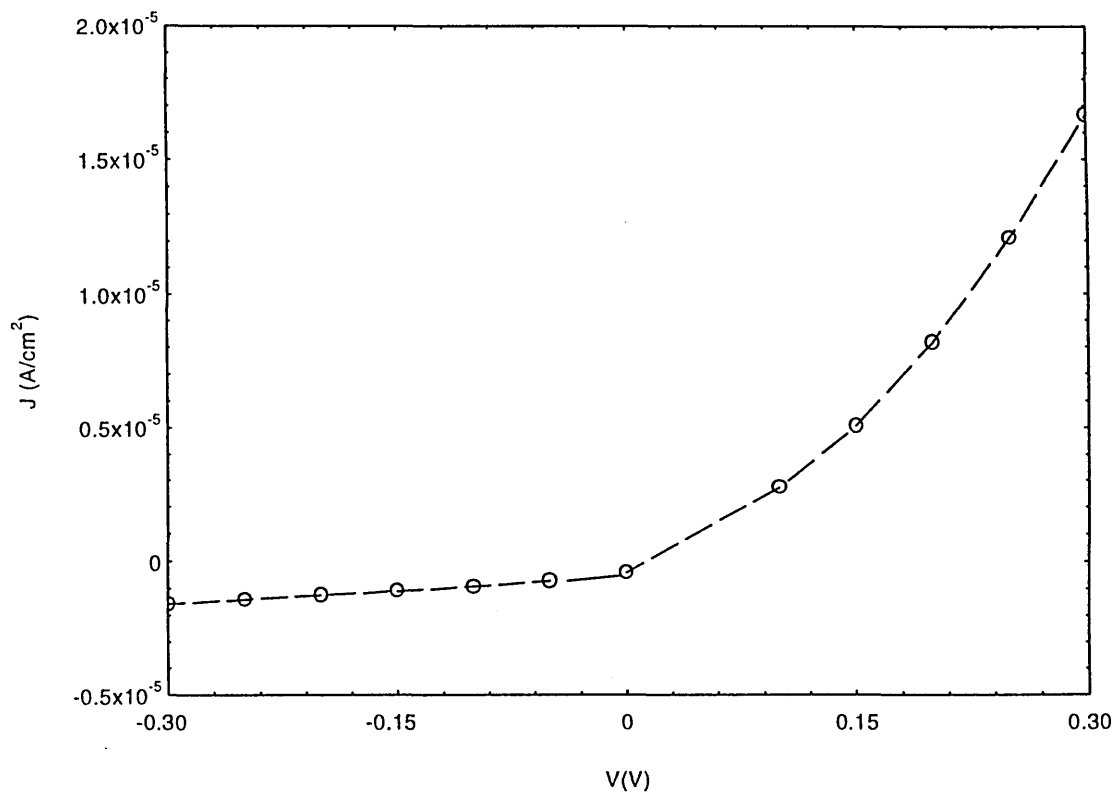
Figure 7.22. Dark forward and reverse J(V) characteristics of a Au/CuPc(500nm)/TiO$_2$/(50nm)/InSnO$_2$ cell. Measurements were made at room temperature and under vacuum.

Ambient	Rectification Ratio, r at 0.3V	m	J$_s$ (x10^{-7}A/cm^2)	γ	T$_c$
Air	21.3	1.13	2.79	0.9	263
" repeat	19.8	1.13	2.79	0.9	263
N$_2$	30.4	1.09	2.52	0.82	239
" repeat	29.3	1.11	2.28	0.81	237
Vacuum	10.64	1.15	4.59	0.73	213
" repeat	11	1.15	4.16	0.78	228

Table 7.3. Electrical characteristics of the Au/CuPc/TiO$_2$/InSnO$_2$ heterojunction cells, m and J$_s$ were obtained from reverse characteristics and where V<3kT/e according to Missous and Rhoderick[6].

192
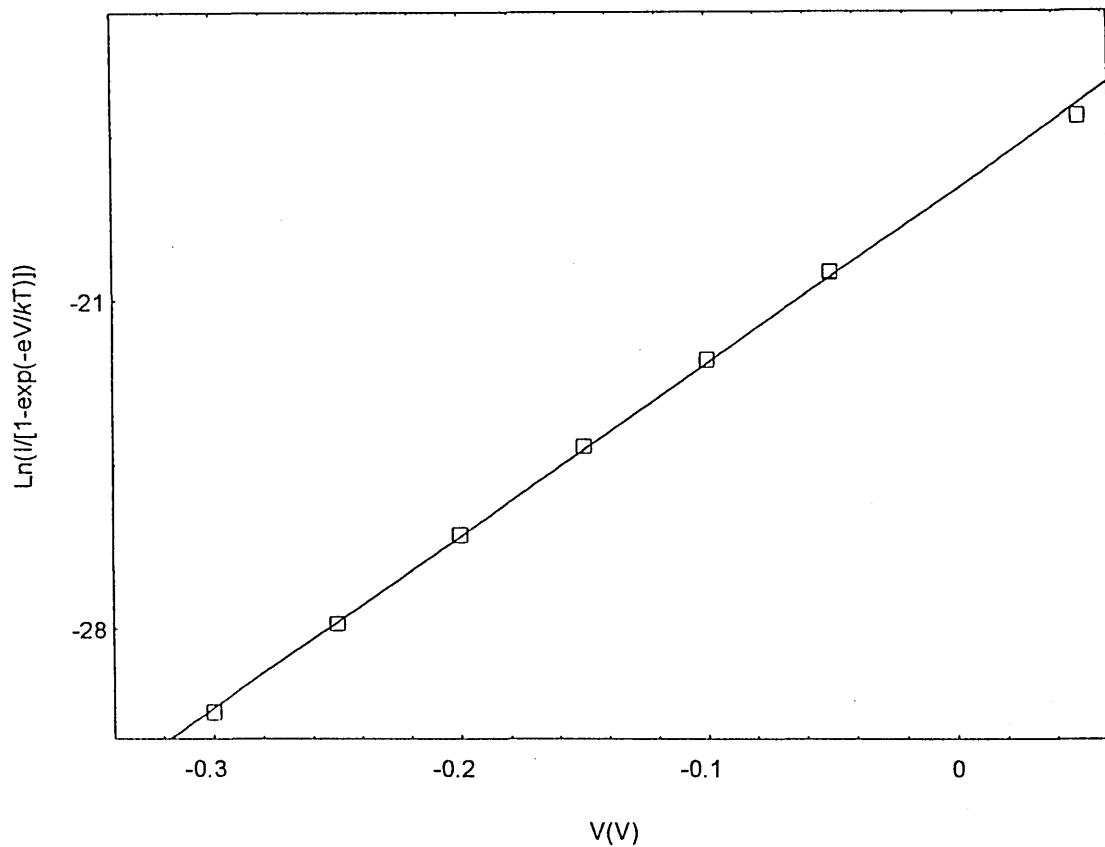
Figure 7.23. Logarithmic plot of I/[1-exp(-eV/kT)] against V for the Au/CuPc/TiO$_2$/InSnO$_2$ cell measured under N$_2$.

Ambient	Voltage Range V	m (a)	J$_s$ (x10^{-7}A/cm^2) (a)	Q, V>0.15V (b)
Air	0.05-0.15	1.99	3.38	
	0.15-0.3	4.69	15.2	1.84
" repeat	0.05-0.15	2.2	3.74	
	0.15-0.3	4.68	15.2	1.83
N$_2$	0.05-0.15	2.06	4.13	
	0.15-0.3	5.03	16.7	1.75
" repeat	0.05-0.15	1.81	3.06	
	0.15-0.3	5.15	18.5	1.7
Vacuum	0.05-0.15	2.3	5.04	
	0.15-0.3	5.27	18.5	1.64
" repeat	0.05-0.15	2.26	4.56	
	0.15-0.3	5.13	17	1.68

Table 7.4. Electrical parameters of the Au/CuPc/TiO$_2$/InSnO$_2$ heterojunction cell as obtained from forward characteristics using (a) standard diode equation for V<0.15V and (b) Using J$\propto$V^Q relationship at V> 0.15V.

Values of the exponent Q are displayed in Table 7.4. These values were fairly reproducible. An example of such characteristics are shown in Figure 7.24 for a cell measured under atmospheric conditions.

Values of T_c and γ were derived from $\log(J)/\log(V)$ plots in the high forward voltage region, these are shown in Table 7.3. T_c was found to be highest under atmospheric conditions, the lowest values of T_c were derived under vacuum. However all values were in the range ~210-265.

7.4.3 Illuminated J(V) Characteristics

The $\eta\%$, FF, V_{oc}, and J_{sc} obtained from the illuminated J(V) characteristics of the Au/CuPc(500nm)/TiO$_2$(50nm)InSnO$_2$ cells under vacuum and atmospheric conditions are shown in Appendix C. Figure 7.25 is an example of the characteristics obtained from the cells measured under atmospheric conditions after two days. The effects of prolonged exposure to air were assessed including the effects of vacuum for a constant incident intensity of 2.4mW/cm^2.

The maximum calculated $\eta\% \sim 0.063$ (x10^{-2}) % for a cell which had been immediately exposed to air, the corresponding FF, V_{oc} and J_{sc} were 0.217, 0.109V, and 6.35x10^{-7}A/cm^2 respectively. After 24 hours exposure the conversion efficiency fell to $\eta\sim0.05$ (x10^{-2})% and after two days a further decrease was measured to $\eta\sim0.038$ (x10^{-2})%. The FF increased with prolonged exposure to air from 0.217 to 0.246 while J_{sc} decreased.

194
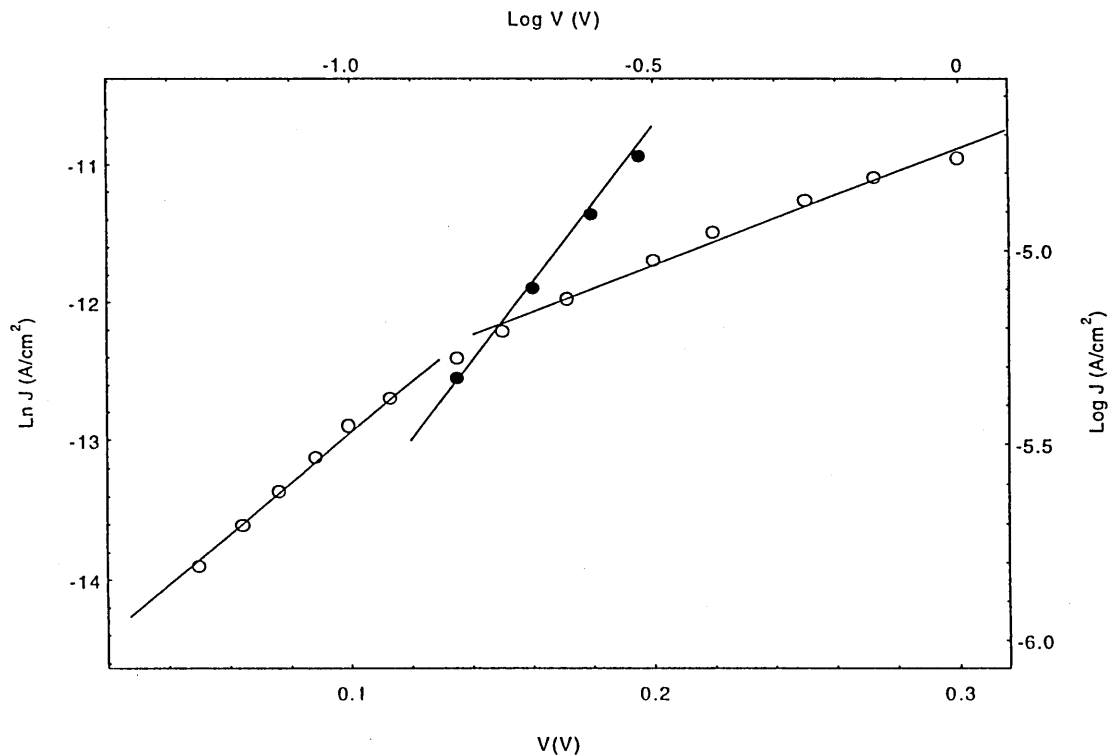
Figure 7.24. ln J Vs. V(V) (O) as required according to standard diode equation, and log J Vs. log V (●) according to J∝V^Q relation for a Au/CuPc/TiO$_2$/InSnO$_2$ heterojunction cell measured under atmospheric conditions.
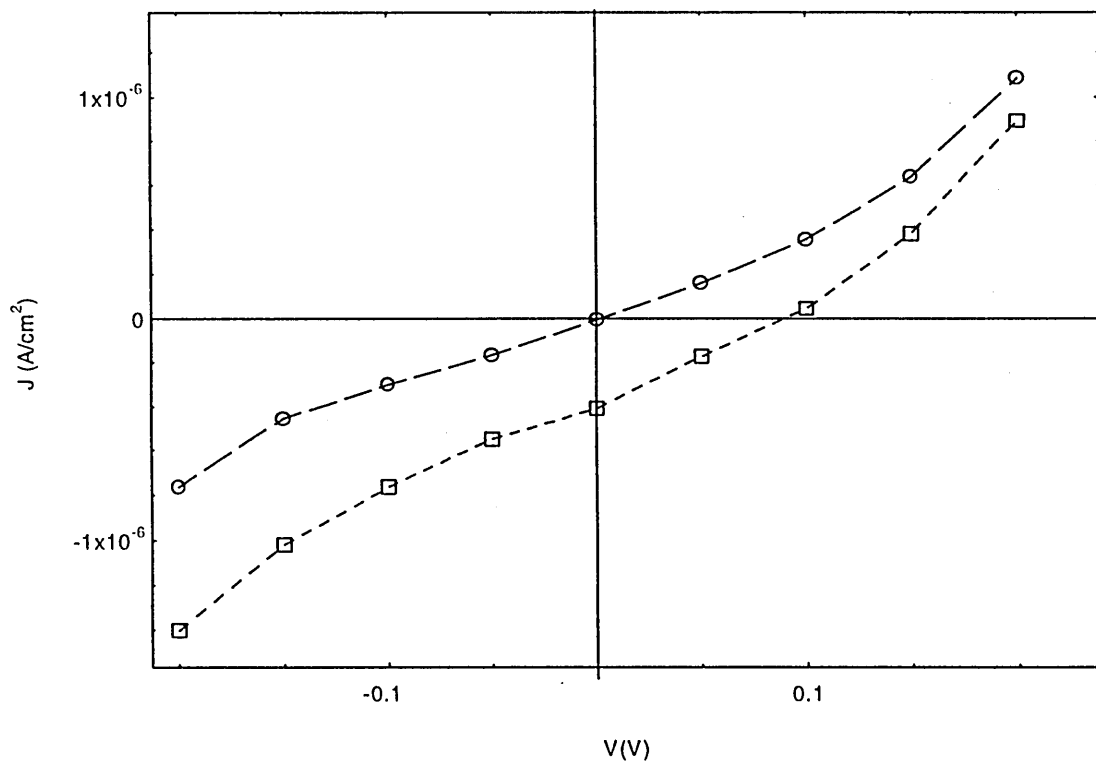
Figure 7.25. J(V) characteristics of a Au/CuPc(500nm)/TiO$_2$(50nm)/InSnO$_2$ heterojunction cell under darkness (O) and simulated AM2 radiation (2.4mW/cm^2) (□). Held under atmospheric conditions for 2 days.

Under vacuum the FF dropped to 0.198, though little change was observed in the value of η% when compared to cells which had been exposed to air for two days.

The effects of the incident intensity on the cell parameters were examined under vacuum conditions. Very high incident intensities (~60.6mW/cm^2) had detrimental effects on the cell performance. Although a comparably high J_{sc} was observed the V_{oc} was very low (~0.024V). This therefore led to a correspondingly low η~0.022 (x10^{-2})% one of the lowest measured for the CuPc/TiO$_2$ devices. Accordingly at low intensities (ϕ~0.56mW/cm^2) a low J_{sc} was observed and although the FF increased, η~0.026 (x10^{-2})% . The series resistances R_s determined from the illuminated plots where $V>V_{oc}$ and R_{sh} where the reverse voltage has an approximately linear dependence on the reverse current density J are shown in Table 7.5. In all cases a very high series resistance was observed, and this is believed to inhibit the cell performance especially at high intensities where R_s is known[10] to significantly reduce the V_{oc} in p-n junction cells.

Ambient	Light Intensity mW/cm^2	R_s (MΩ)/cm^2	R_{sh} (MΩ)/cm^2
Vacuum	60.6	2.36x10^{-3}	2.33x10^{-3}
"	2.4	0.127	0.102
"	0.56	0.455	1.29
Air	2.4	0.143	0.163
Air (1 day)	"	0.157	0.236
Air (2 days)	"	0.098	0.203

Table 7.5. Series and Shunt resistance's obtained from the Au/CuPc(500nm)/TiO$_2$(50nm)/InSnO$_2$ cell.
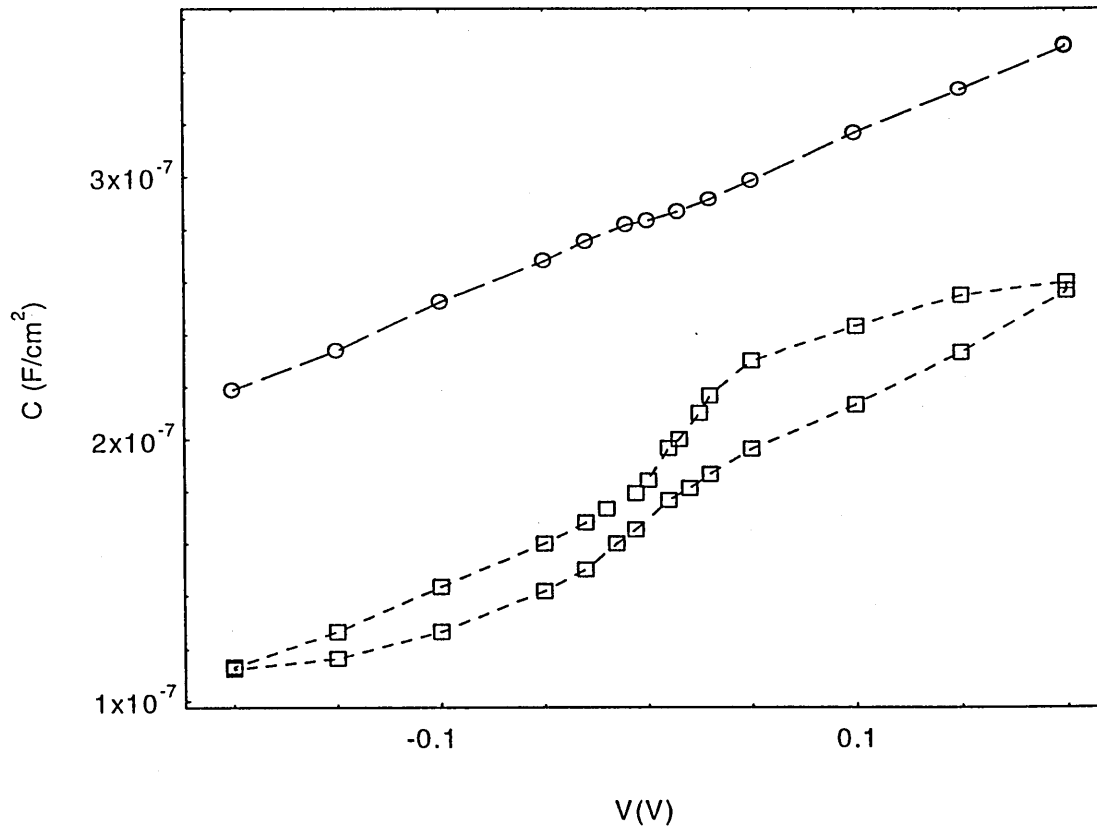
Figure 7.26. C(V) characteristics of Au/CuPc(500nm)/TiO$_2$(50nm)/InSnO$_2$ heterojunction cell for two fixed frequencies of 1kHz (□) and 100Hz (O). Measurements taken under darkness and atmospheric conditions.

7.4.4 C(V) Characteristics

C(V) characteristics are shown in Figure 7.26 for a Au/ CuPc(500nm) /TiO$_2$(50nm) /InSnO$_2$ heterojunction cell under vacuum, using fixed frequencies of 1kHz and 100Hz. At 1kHz, a hysteresis loop was observed which is believed to be attributed to the polarisation charges of the device. A plot of 1/C^2 against V was linear for the reverse applied bias as shown in Figure 7.27. From the intercept of the curve the built in potential was measured to be $\phi_{bp} \sim$ 0.14V. Using Anderson's abrupt junction model[1], N$_a$ the net ionised acceptor concentration was N$_a \sim$ 6.8x10^{19}cm^{-3}. The depletion layer width, W was estimated to be W$\sim$9.82nm, where the depletion width penetration x$_1$ and x$_2$ into the TiO$_2$ and the CuPc layer was calculated as x$_1 \sim$ 8.67nm and x$_2 \sim$ 1.15nm respectively. x$_2$ is less than x$_1$ which is as expected since N$_a$ is less than N$_d$.

1/C$_2$ against V is shown in Figure 7.27 for a fixed frequency of 100Hz. Again a linear dependence was observed which indicates an electrically abrupt junction. From the V axis intercept the built in potential ϕ_{bp} was $\sim$ 0.32V. In this case, using similar values for N$_d$, ε_1 and ε_2 the value of N$_a \sim$5.2x10^{19}cm^{-3}, and the depletion layer width W$\sim$34.5nm. The penetration of the depletion region into the TiO$_2$ and the CuPc layers was 29.4nm and 5.1nm respectively. Again the depletion layer penetrated further into the least heavily doped side of the junction, namely the TiO$_2$.
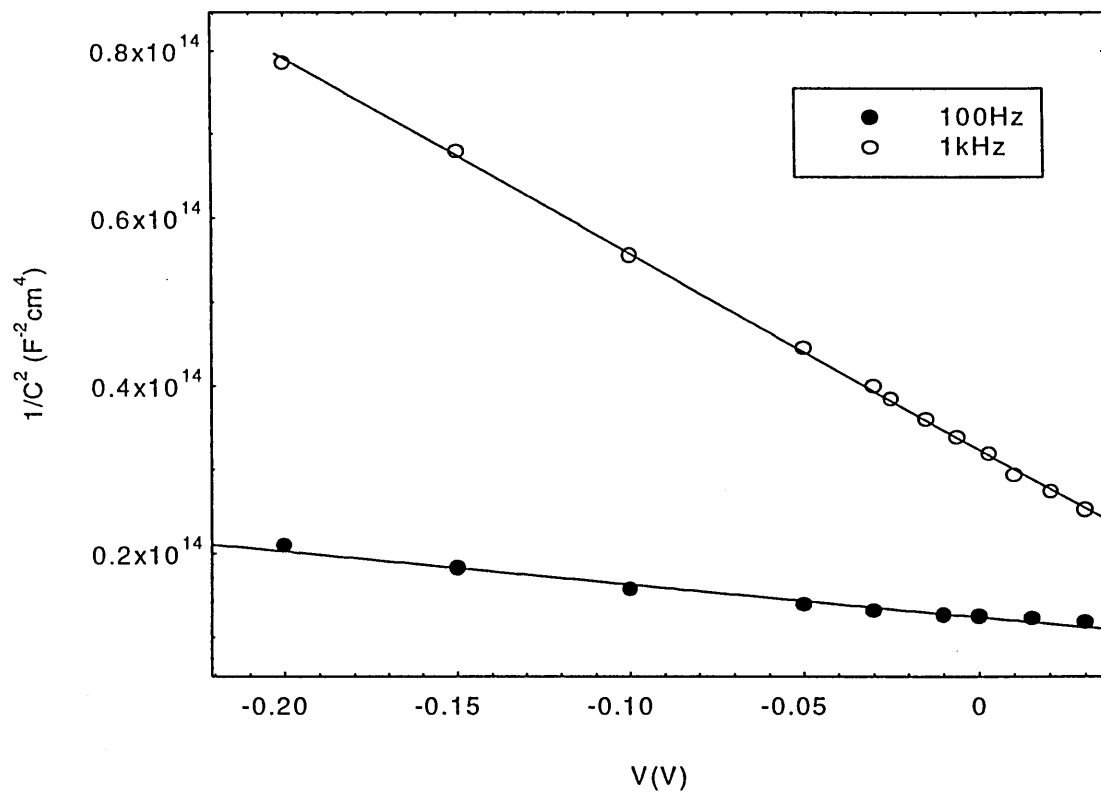
Figure 7.27. C^{-2} as a function of reverse applied bias V(V) for the Au/CuPc(500nm)/TiO$_2$(50nm)/InSnO$_2$ heterojunction measured under darkness and atmospheric conditions.

7.5 PbPc/TiO$_2$

7.5.1 Spectral Response

Figures 7.28 and 7.29 are typical action spectra obtained for short circuit current density J$_{sc}$ and open circuit voltage V$_{oc}$ respectively of a Au/PbPc(100nm)/TiO$_2$(50nm)/InSnO$_2$ heterojunction cell. Measurements were taken under atmospheric conditions. Both spectra have a distinct maximum located in the Q-band region at approximately 665nm. A photocurrent maximum of 0.067μA/cm^2 was measured at λ~665nm. This maximum is located at a wavelength which is in close agreement with the absorbance maximum the PbPc film. The measured photocurrent corresponds to calculated quantum efficiency of Z~0.4%. A second maxima in J$_{sc}$ is located at ~335nm again corresponding to a maxima in the PbPc absorption spectra. A lower J$_{sc}$ was measured (~0.059μA/cm^2) however the calculated quantum efficiency was higher at Z~0.68%. The spectral dependence of V$_{oc}$ matched that of the absorption spectra of the PbPc films with maximum of 61mV and 66mV at ~665nm and 335nm respectively.

The measurements were repeated on similar devices held under vacuum The observed photocurrent action spectra is shown in Figure 7.30. Maximum J$_{sc}$ were significantly higher reaching 0.14μA/cm^2 at ~375nm and 0.363μA/cm^2 at ~680nm. The corresponding quantum efficiencies were also increased to Z~1.45% and Z~2.07% at 375nm and 680nm respectively. The measured maximum V$_{oc}$ increased reaching 92mV at 680nm. Measurements were taken under atmospheric conditions on a similar cells in which the thickness of the PbPc film was increased to 500nm. Figures 7.31 and 7.32 display the photocurrent action spectra and V$_{oc}$ for such a device.
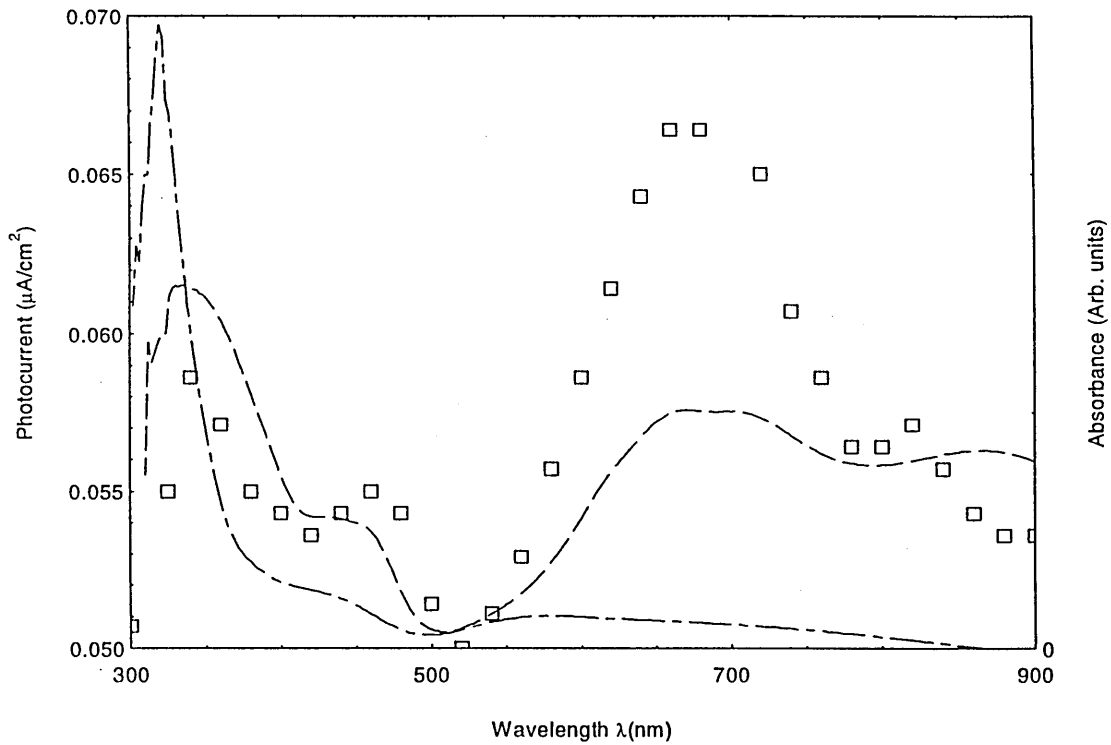
Figure 7.28. Photocurrent action spectra ($\mu A/cm^2$) ( ) of a Au/PbPc(100nm)/TiO$_2$(50nm)/InSnO$_2$ cell. Absorption spectra of a PbPc film only (------) and a TiO$_2$ film (— - — -). Measurements were taken in air at room temperature.
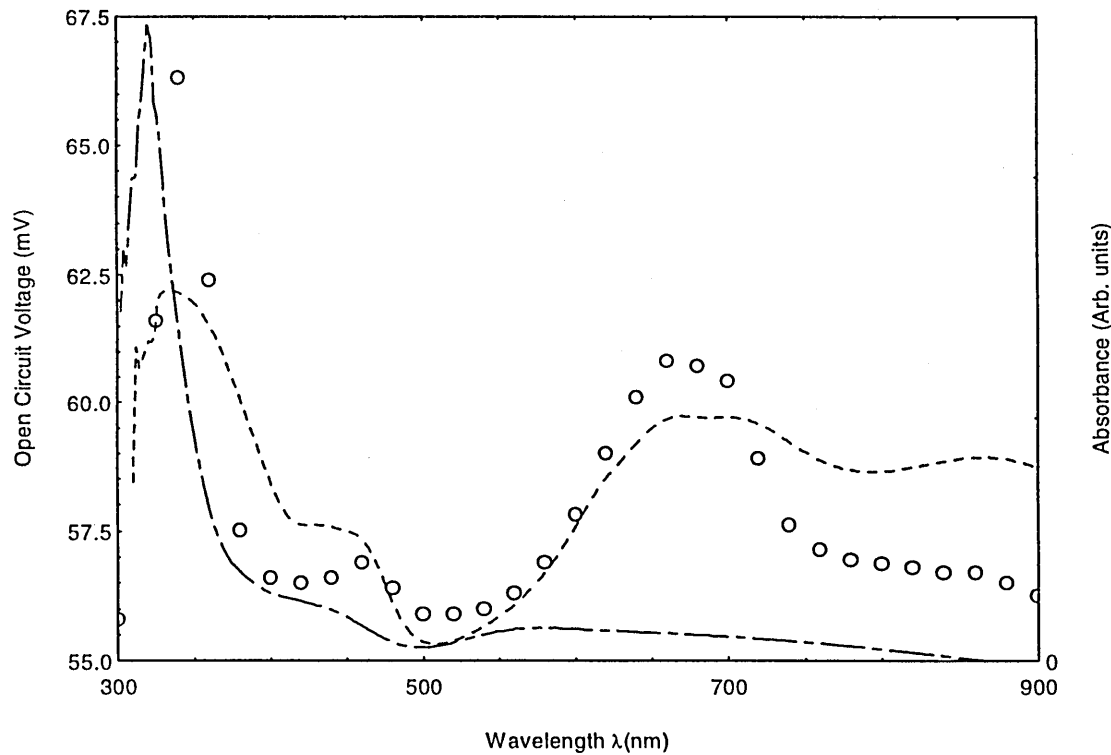
Figure 7.29 Absorption spectra of a PbPc film only (------) and a TiO$_2$ film (— - — -). Measurements were taken in air at room temperature V_{oc} (mV) (O) as a function of λ for the Au/PbPc(100nm)/TiO$_2$(50nm)/InSnO$_2$ cell.
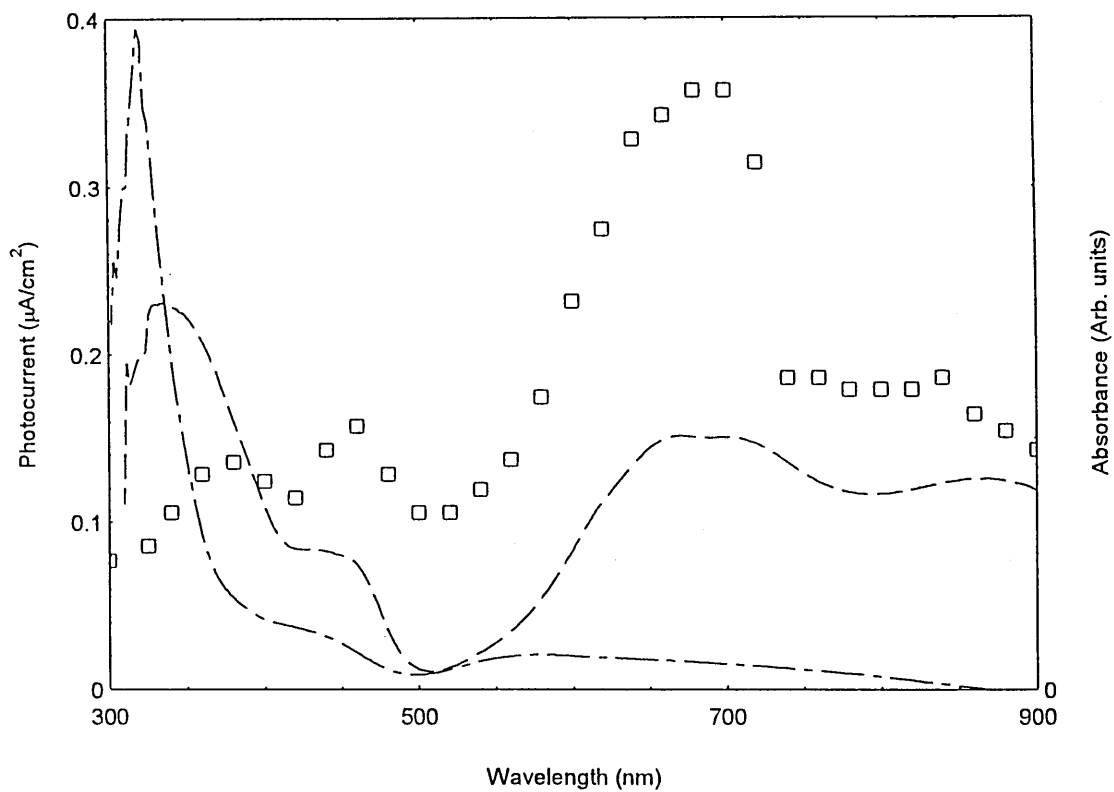
Figure 7.30. As for Figure 7.28. Measurements taken under vacuum at room temperature.
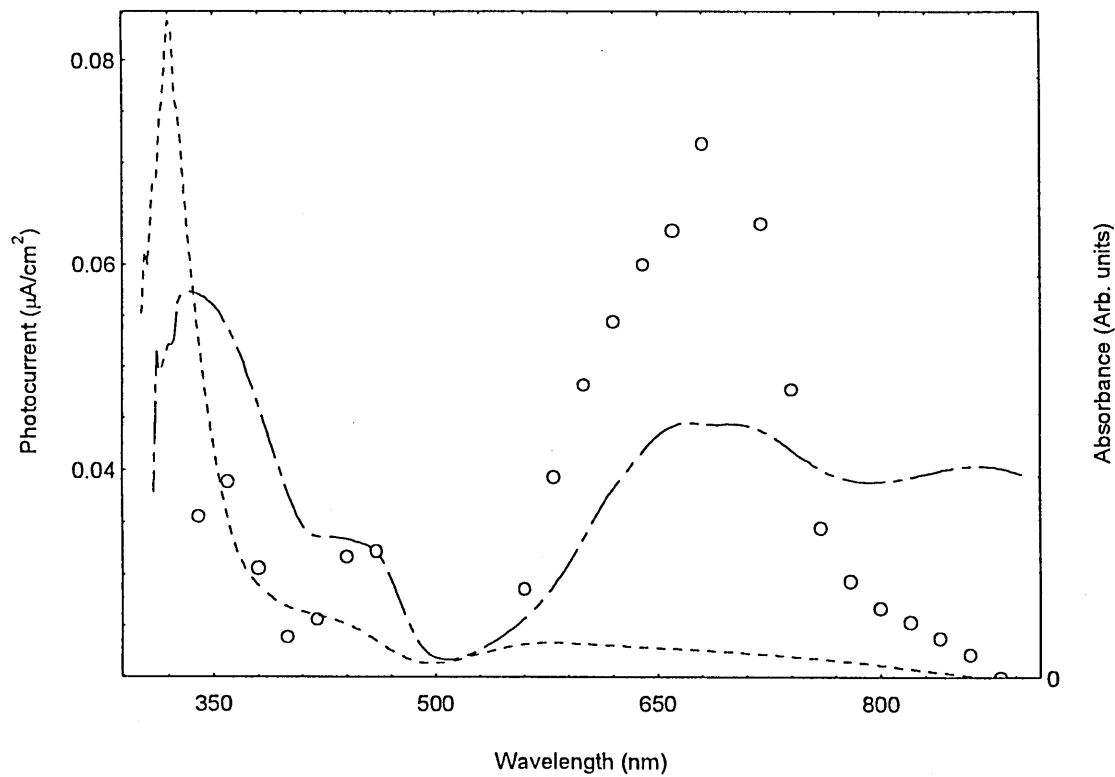
Figure 7.31. Photocurrent action spectra (O) of a Au/PbPc(500nm)/TiO₂(50nm)/InSnO₂ cell. Absorbance of TiO₂ and PbPc film given by (---) and (— - — -) respectively. Measurements taken in air at room temperature.

202
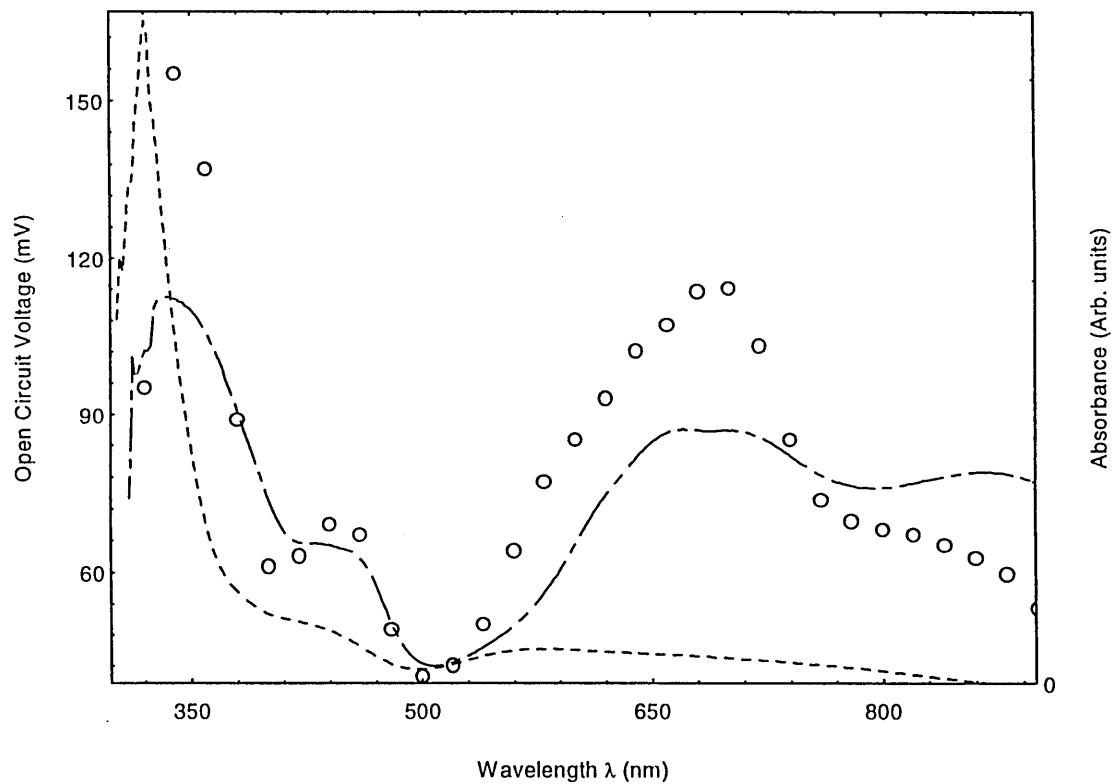
Figure.7.32. Absorption spectra of a PbPc film only(— – — -). and a TiO₂ film (------). Measurements were taken in air at room temperature V_oc (mV) (O) as a function of λ for the Au/PbPc(500nm)/TiO₂(50nm)/InSnO₂ cell.
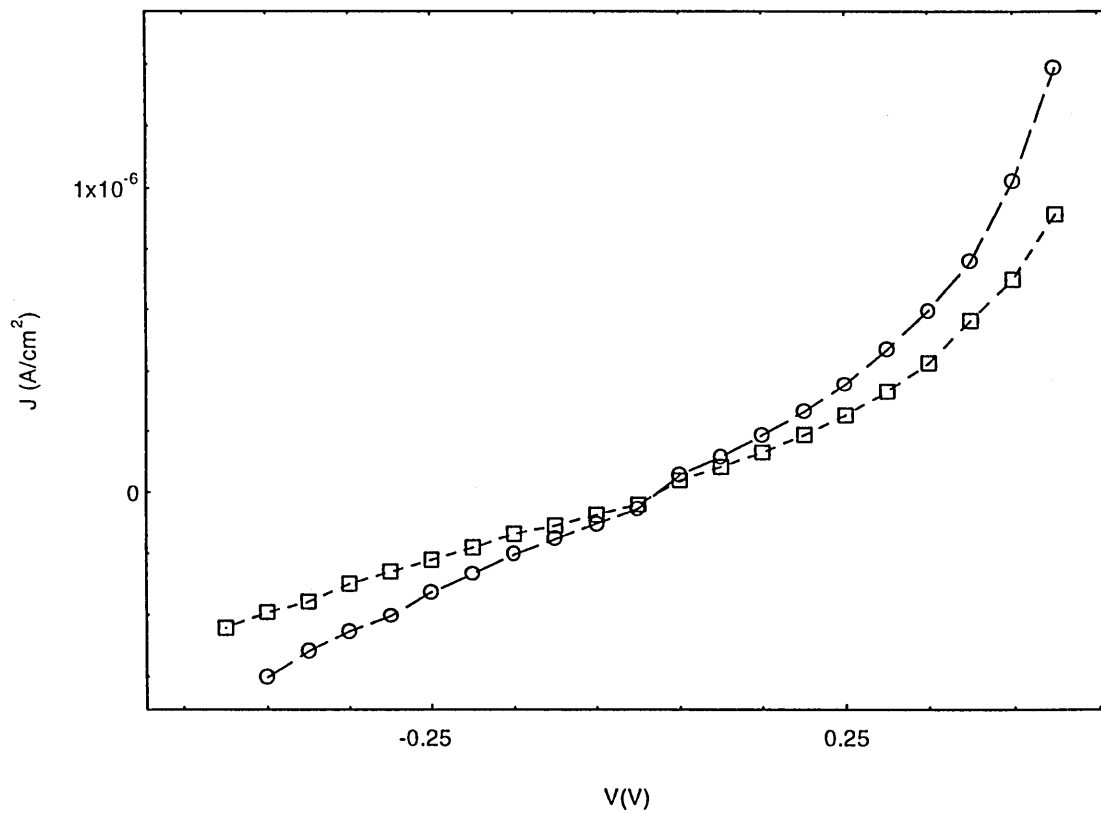
Figure 7.33. Room temperature dark J(V) characteristics under vacuum (□) and air (O) of Au/ PbPc(100nm)/TiO₂(50nm))/InSnO₂ heterojunction cell.

203

A good correlation between the absorption spectra of the PbPc film and the spectral dependencies of V_{oc} and J_{sc} was observed. The quantum efficiency decreased for the thicker film to Z~0.42% at the lower maxima ~360nm. At the higher maxima ~680nm, little change in the value of Z~ 0.41% was observed for the cell containing a thicker PbPc film. However the values of V_{oc} were observed to increase to 155mV at 340nm and 115mV at~700nm.

In all cases a suppression in the photocurrent was observed at ~350nm which corresponds to a maximum absorption for the PbPc film and the onset of absorption in the TiO_2 film.

7.5.2 Dark J(V) Characteristics

Figure 7.33 displays the typical forward and reverse, dark, room temperature J(V) characteristics obtained for a $Au/PbPc(100nm)/TiO_2(50nm)/InSnO_2$ heterojunction cell. The characteristics obtained for this cell under both atmospheric and vacuum conditions are shown. The cell exhibited rectifying properties although the rectification ratios were very low r~1.3. The ideality factor, m and saturation current density, J_s were calculated according to both Missous and Rhoderick[6] and using the standard diode equation (equation (3.35)). A summary of the electrical characteristics obtained from this cell are shown in Table 7.6. As predicted by equation 3.36 a plot of $\ln[I/\{1-\exp(-eV/kT\}]$ against V was linear over the expected voltage range (V< 3kT/e) as shown in figure 7.34. From this curve the ideality factor m~1.2, and was found to be relatively independent of ambient conditions. J_s increased from $3.6 \times 10^{-8} A/cm^2$ under vacuum to $4.85 \times 10^{-8} A/cm^2$ under atmospheric conditions.

For forward voltages ~>$3kT/e$ V a non-linear dependence of $\ln[I/\{1-\exp(-eV/kT)\}]$ on V was observed. Very high values of m were observed when the forward characteristics were fitted to the standard diode equation m~2.8 for example for low forward voltages and increased to as high as 7.3. A change of ambient conditions from atmospheric to vacuum do not appear to influence m. Very high values of J_s were again obtained from the forward characteristics. For voltages >0.3V a theoretical fit to the relation $J=KV^Q$ as shown in Figure 7.35 revealed that values of Q were >2.

The measurements were repeated for a similar device where the PbPc film was 5000Å thick. The J(V) characteristics obtained from this device under both vacuum and atmospheric condition are shown in Figure 7.36. Rectification was again observed with r~6.4 and 2.9 at 0.3V under air and vacuum respectively. A good fit to equation 3.36. was observed as shown in Figure 7.37. From this curve the ideality factor m~1.15 and 1.05 under air and vacuum respectively. A fit to the standard diode equation revealed that for low applied voltages V<0.25V under vacuum conditions m~1.03. As the forward voltage was increased departure from ideality was observed and for V>0.25V m~3.1 and 3.2 under vacuum and air respectively. Fits to the high forward voltage regime according to $J=KV^Q$ produced values of Q>2 under both conditions. Values of J_s were lower than those measured for the Au/PbPc(100nm)/TiO_2(50nm)/$InSnO_2$ cell. The values of T_c calculated from the high forward characteristics within the SCL regime were very high for the Au/PbPc(500nm)/TiO_2(50nm)/$InSnO_2$ cell T_c ~1065 and 1203 under air and vacuum respectively, compared to T_c~ 321 and 400 under vacuum and air respectively for the Au/PbPc(100nm)/TiO_2(50nm)/$InSnO_2$ cell. A summary of the electrical parameters obtained is contained within Table 7.7.
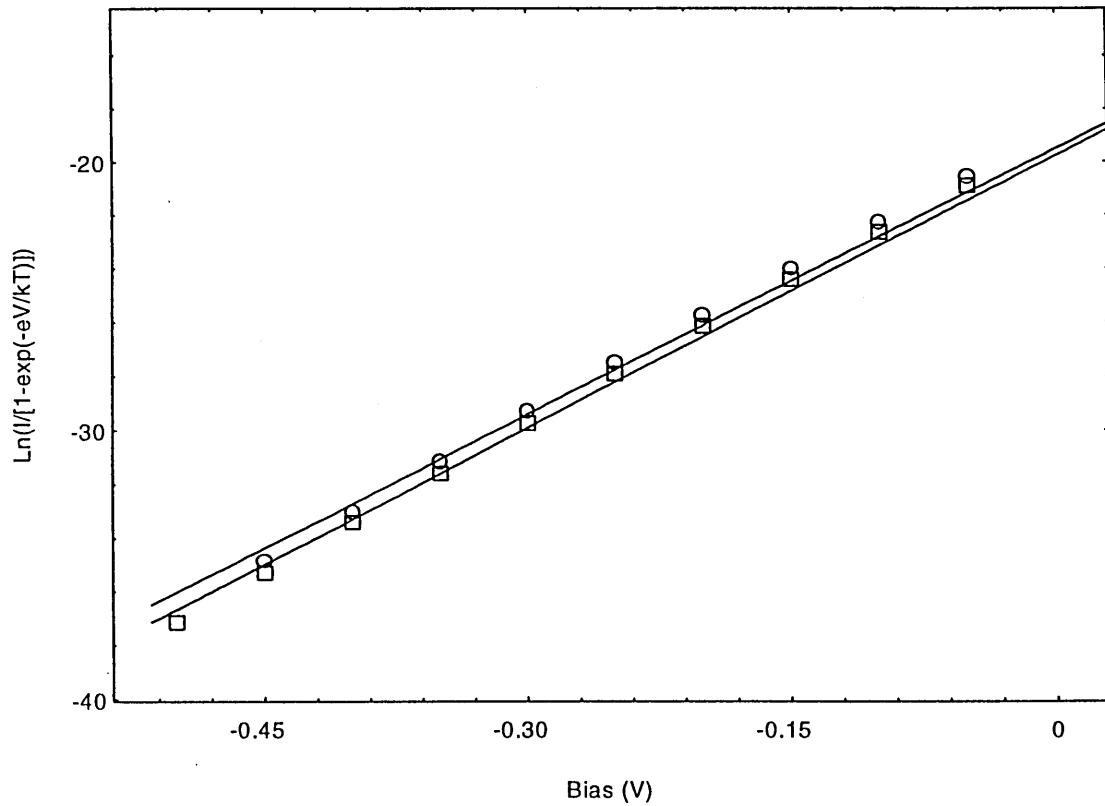
Figure 7.34 Logarithmic plot of I/[1-exp(-eV/kT)] Vs. V for the Au/PbPc(100nm)/TiO$_2$(50nm)/InSnO$_2$ heterojunction cell under vacuum (□) and Air (O) for V<3kT/e V.
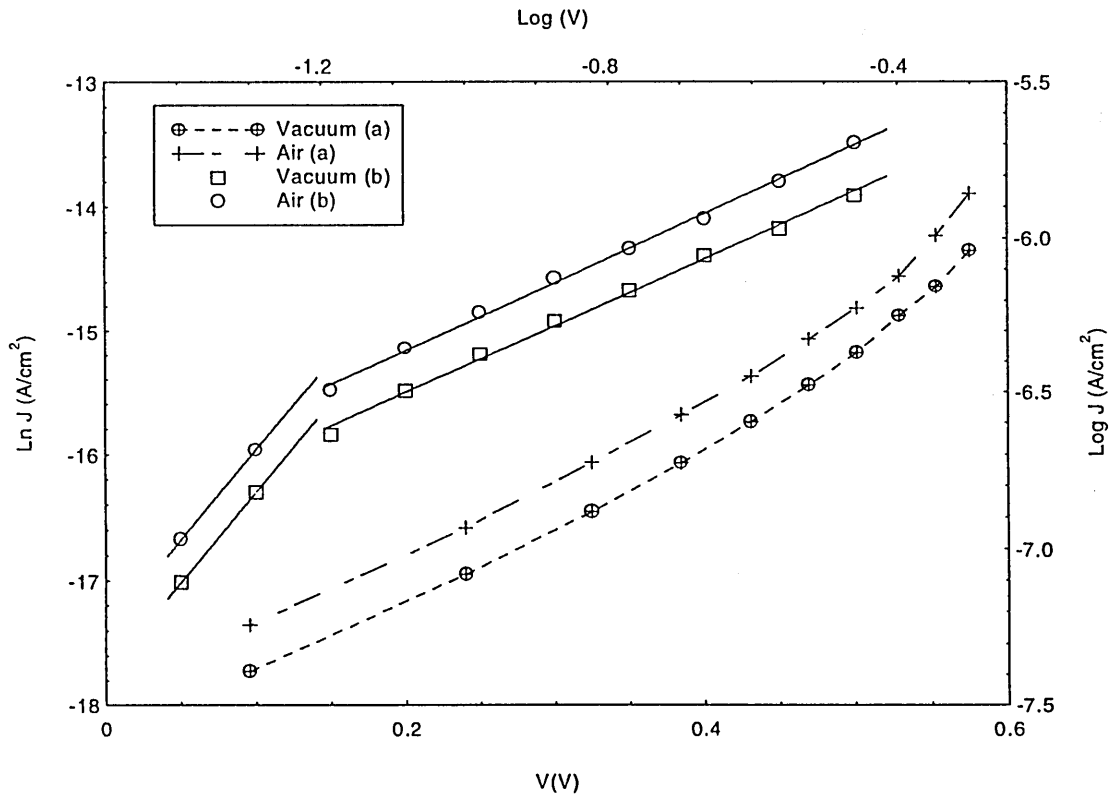
Figure 7.35 Plot of (a) log(J) Vs. log(V) and (b) ln J Vs. V for Au/PbPc(100nm)/TiO$_2$(50nm)/InSnO$_2$ cell. Forward characteristics.

Ambient	m (a)	J_s(x10^{-8} A/cm^2) (a)	m (b)	J_s(x10^{-8} A/cm^2) (b)	γ	T_c	Q	r (0.3V)
Vacuum	1.18	3.6	*(0.05<V<0.1)* 2.8 --------------- *(0.1<V<0.5)* 7.3	2.1 -------- 6.2	1.1	321	*(V<0.3V)* 1.12 ----------------- *(V>0.3V)* 2.1	1.3
Air	1.2	4.85	*(0.05<V<0.1)* 2.8 --------------- *(0.1<V<0.5)* 7.2	2.78 -------- 8.3	1.37	400	*(V<0.3V)* 1.13 ----------------- *(V>0.3V)* 2.37	1.17

Table 7.6. Electrical characteristics of a Au/PbPc(1000Å)/TiO$_2$(500Å)/InSnO$_2$ heterojunction cell. (a) According to Missous and Rhoderick where V<3kT/e. (b) Standard diode equation (equation 3.35). Values obtained for T$_c$, r (rectification ratio) , and Q are also shown.
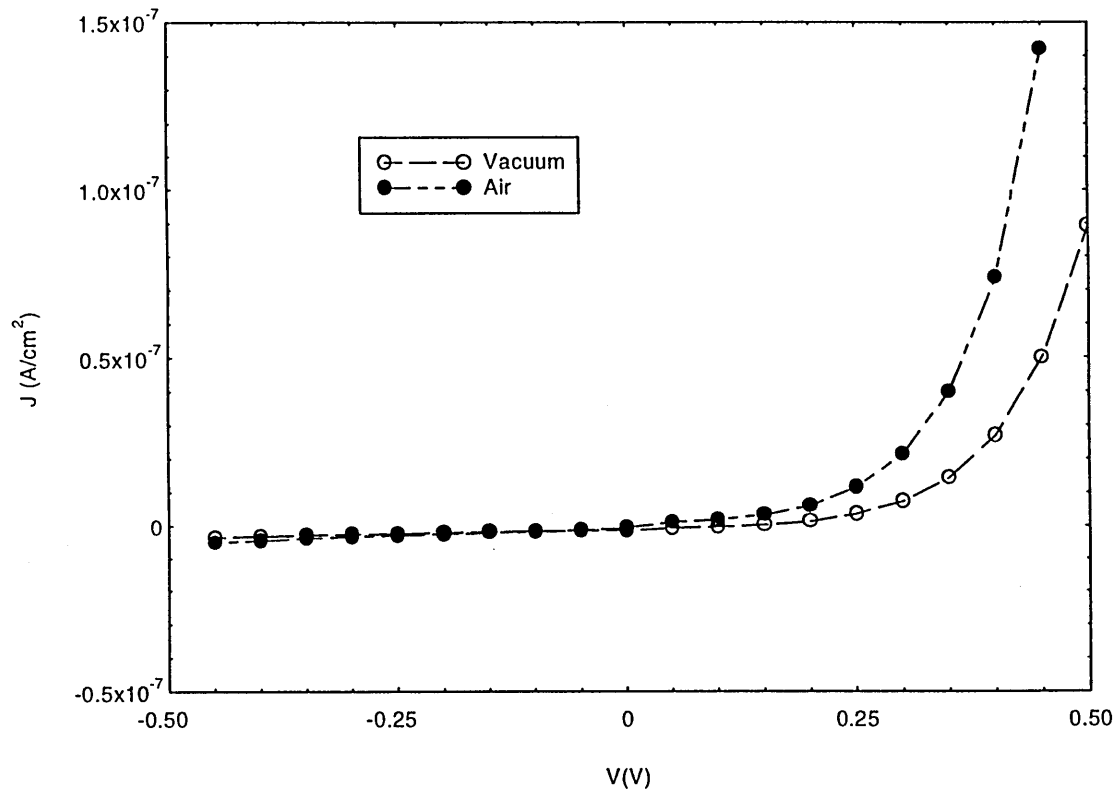
Figure 7.36. Room temperature dark J(V) characteristics of a Au/PbPc(500nm)/TiO$_2$(50nm)/InSnO$_2$ heterojunction cell under both vacuum and atmospheric conditions as indicated.
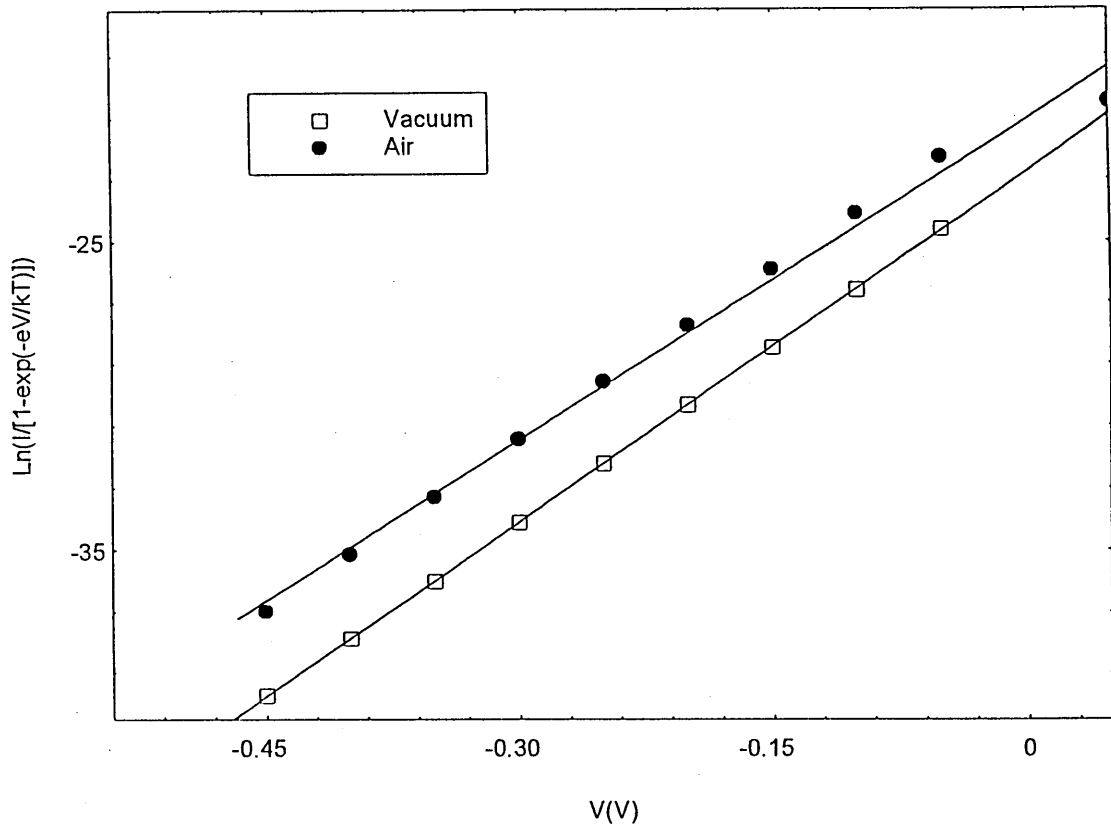
Figure 7.37. Logarithmic plot of I/[1-exp(-eV/kT)] Vs. V for the Au/PbPc(500nm)/TiO₂(50nm)/InSnO₂ heterojunction cell under vacuum and atmospheric conditions where V<3kT/e V.
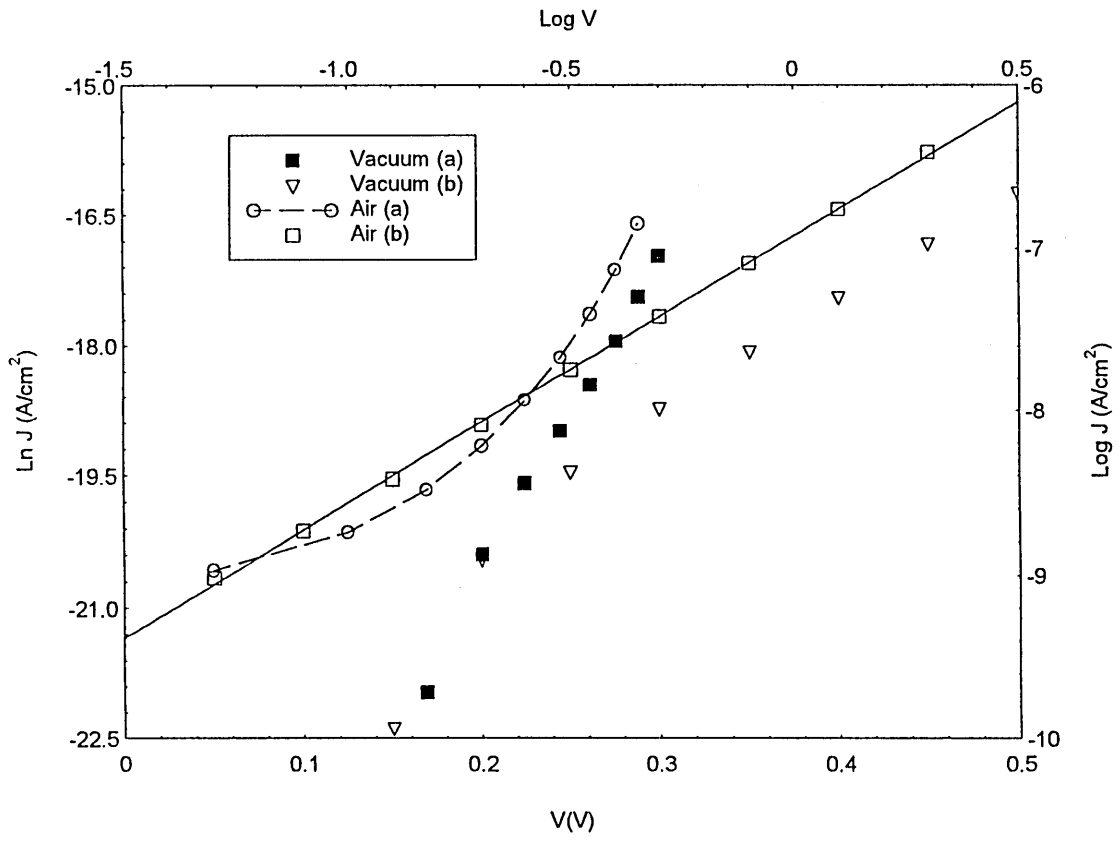
Figure 7.38. Plot of (a) log(J) Vs. log(V) and (b) ln J Vs. V for Au/PbPc(500nm)/TiO₂(50nm)/InSnO₂ cell. Forward characteristics.

208

Ambient	m (a)	J_s (x10^{-8} A/cm^2) (a)	m (b)	J_s (x10^{-8} A/cm^2) (b)	γ	T_c	Q	r (0.3V)
Air	1.15	0.76	(0.05<V<0.5) 3.2	0.056	3.65	1065	(V>0.3) 4.65 -------------- (0.15>V>0.3) 2.7 -------------- (V<0.15) 0.76	6.4
Vacuum	1.05	0.014	(0.25<V<0.5) 3.1 -------------- (V<0.25) 1.03	0.015	4.12	1203	(V>0.3) 5.12 -------------- (0.2<V<0.3) 4.24 -------------- (V<0.2) 6.73	2.9

Table 7.7. Electrical characteristics of a Au/PbPc(500nm)/TiO$_2$(50nm)/InSnO$_2$ heterojunction cell. (a) According to Missous and Rhoderick where V<3kT/e. (b) Standard diode equation (equation 3.35). Values obtained for T$_c$, r (rectification ratio) , and Q are also shown
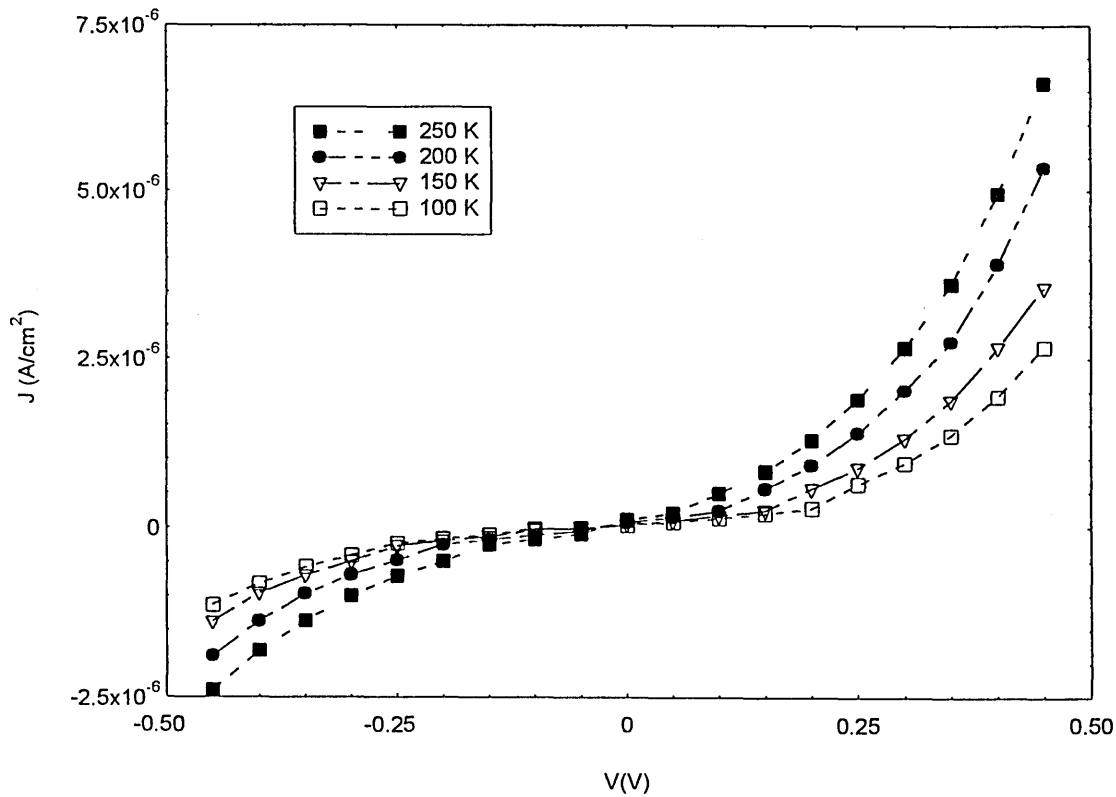
Figure 7.39. Typical J(V) characteristics of a Au/PbPc(100nm)/TiO$_2$/(50nm)/InSnO$_2$ cell as a function of temperature in the range 250-100K.

209

A study of the temperature dependence of the dark characteristics provides information on the junction transport mechanisms. Figures 7.39 to 7.41 are typical plots obtained for the PbPc/TiO$_2$ devices at various temperatures within the range 100 to 250K. From analysis of the characteristics it was found that both the saturation current density J$_s$ and the ideality factor m are temperature dependent parameters.

The ideality factor (as shown in Table 7.8) increased with decreasing temperature varying from m~1.45 at 250K to m~3.64 at 100K according to method (a) and 6.3 at 250K to 12.94 at 100K according to method (b).

The saturation current density was thermally activated increasing with increasing temperature. In reverse bias the slopes of the lnI/[1-exp(-eV/kT)] against V characteristics were practically independent of temperature (over the temperature range studied). In forward bias the slopes of ln J(V) characteristics became temperature independent at very low temperatures T<150K. As the temperature decreased the saturation current density became less temperature dependent.
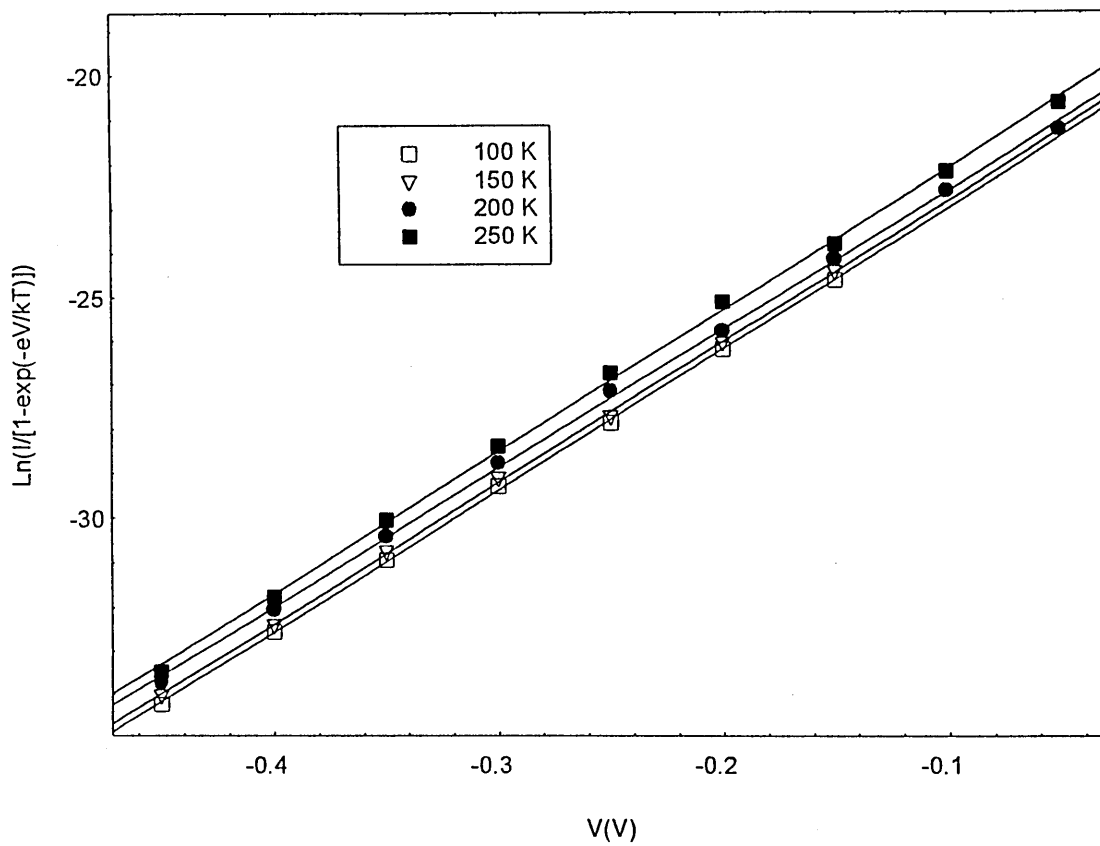
Figure 7.40. Logarithmic plot of I/[1-exp(-eV/kT)] Vs. V for a Au/PbPc(100nm)/TiO$_2$(50nm)/InSnO$_2$ heterojunction cell as a function of temperature in the range 250-100K.
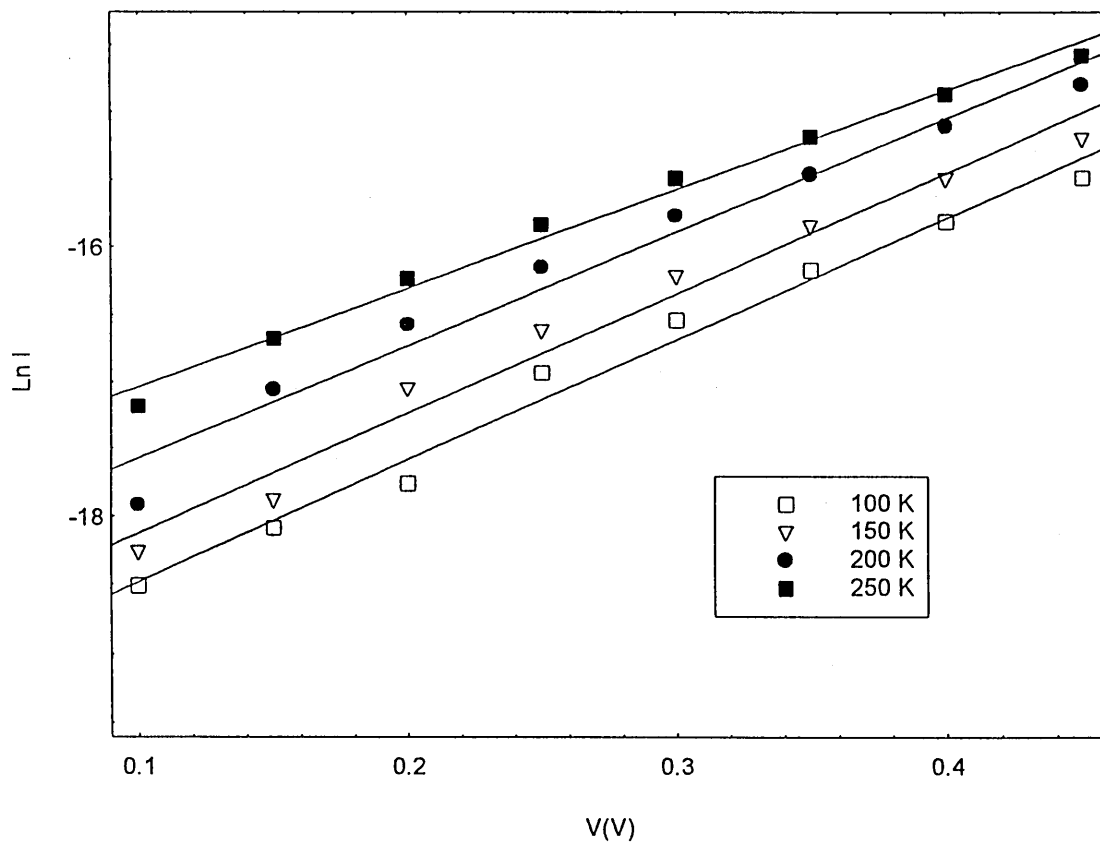
Figure 7.41. Plot of ln(I)/V for a Au/PbPc(100nm)/TiO$_2$ (50nm)/InSnO$_2$ cell as a function of temperature. Forward characteristics.

Temperature (K)	m (a)	J_s (x10^{-8} A/cm^2) (a)	$3kT/e$ (mV)	m (b)	J_s (x10^{-8} A/cm^2) (b)
100	3.64	3.6	25.8	12.94	5.36
150	2.43	3.97	38.8	8.69	8
200	1.85	4.85	51.7	6.9	14.6
250	1.45	8.85	64.6	6.3	26.6

Table 7.8. Summary of the temperature dependent electrical parameters obtained or a
Au/PbPc(100nm)/TiO$_2$(50nm)/InSnO$_2$ cell. Ideality factor , m and saturation current density
were calculated according to (a) Missous and Rhoderick[6] and (b) From the forward
characteristics using equation 3.35.
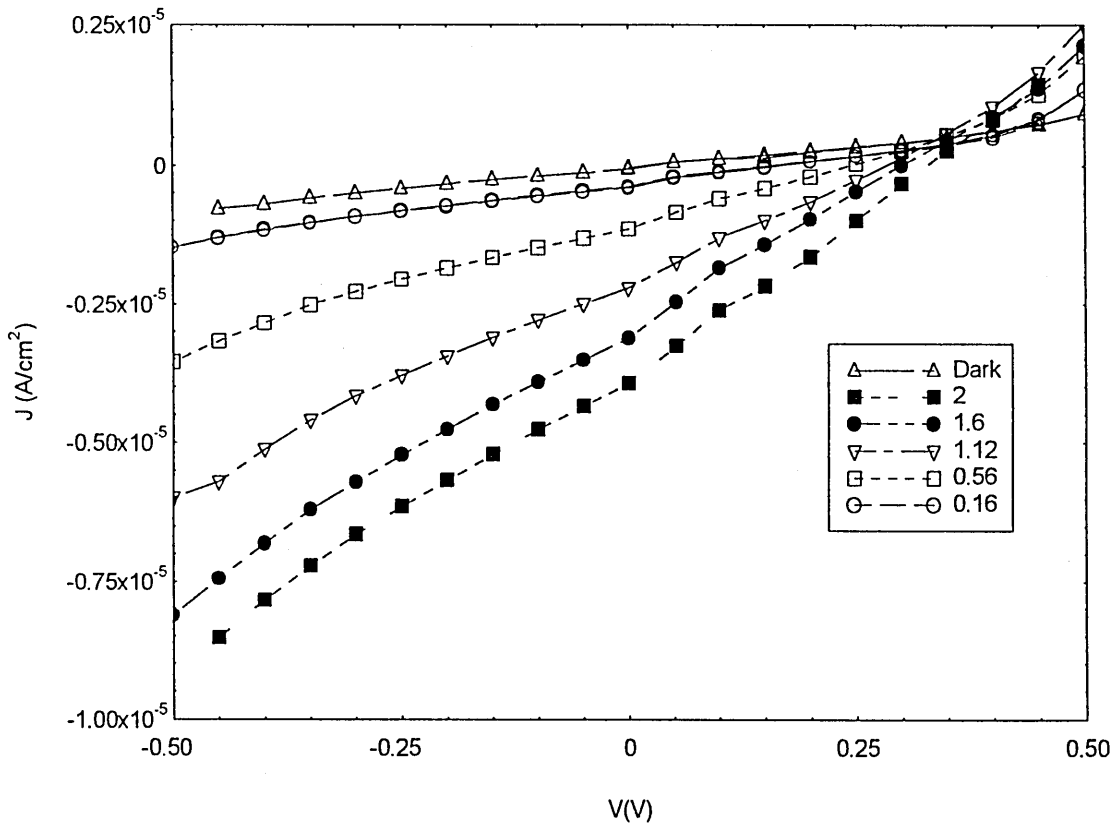
Figure 7.42. The J(V) characteristics obtained for a Au/PbPc(100nm)/TiO$_2$(50nm)/InSnO$_2$
heterojunction cell under vacuum. Measurements made in darkness and under simulated
AM2 radiation for a variety of intensity levels as indicated, (mW/cm^2).

7.5.3. Illuminated J(V) Characteristics

Figure 7.42 and 7.43 are typical J(V) characteristics obtained for the Au/PbPc/TiO$_2$(50nm)/InSnO$_2$ heterojunction cell under vacuum and at room temperature where the PbPc was 100nm and 500nm thick respectively. The characteristics shown are in darkness and under simulated AM2 radiation for a variety of intensities as indicated. Higher photocurrent densities were measured in the cell containing a 100nm thick PbPc film. This cell also exhibited higher overall conversion efficiencies. The highest η% measured was 4.6 x10^{-2} % at an incident intensity of 1.12mW/cm^2 compared to 0.14x10^{-2}% at the same intensity for the cell consisting of a 500nm thick PbPc film. This represents a 30 fold increase in conversion efficiency. Consistently higher values of FF, J$_{sc}$, and V$_{oc}$ were measured at all intensities investigated in the device consisting of the thinner 100nm PbPc film.

The intensity dependence (φ) of J$_{sc}$, V$_{oc}$, FF, and η% for both cells was investigated. The dependencies are shown in Figures 7.44 and 7.45.

V$_{oc}$ was found to increase logarithmically with increasing intensity for both cells studied, increasing with increasing intensity to maximum values of 0.328 and 0.296 for the cells consisting of PbPc(100nm) and PbPc(500nm) respectively. J$_{sc}$ had a linear dependence on incident intensity. A fit to the relation J$_{sc} \propto \phi^y$ produced values of y~ 0.95 and y~1.31 for the cells containing a PbPc(100nm) and PbPc(500nm) thick films respectively.
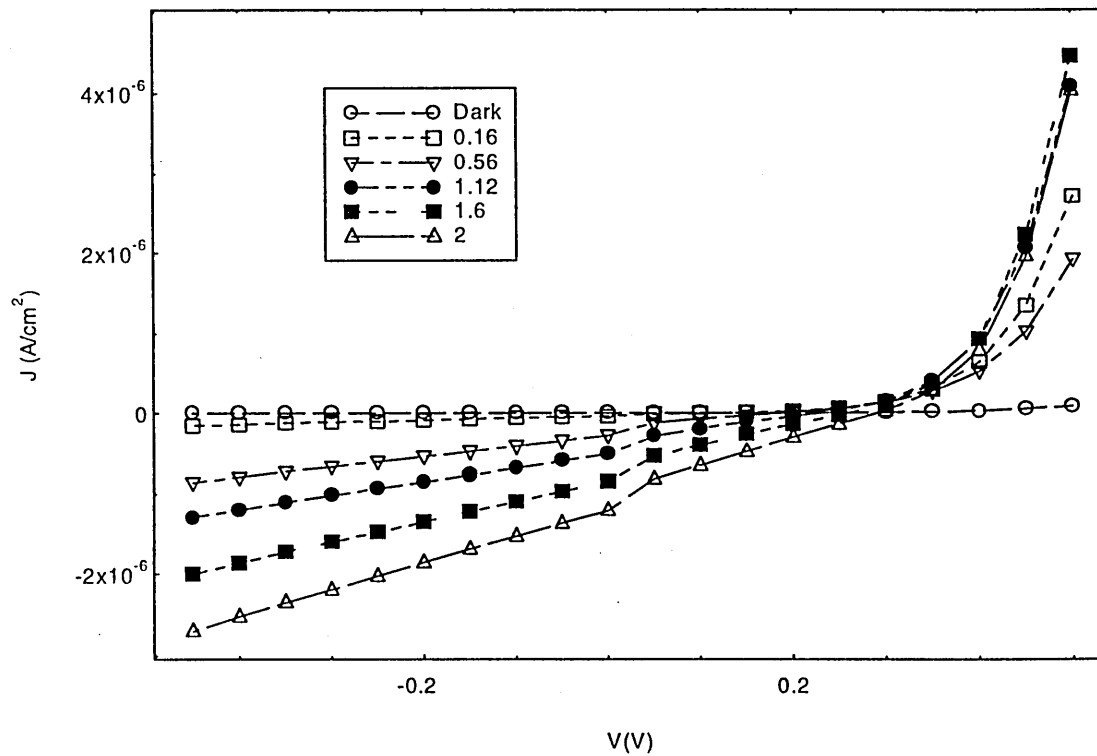
Figure 7.43. Dark and illuminated J(V) characteristics for a Au/PbPc(500nm)/TiO$_2$(50nm)/InSnO$_2$ heterojunction cell under vacuum. Measurements made in darkness and under simulated AM2 radiation at a variety of intensity levels as indicated (mW/cm^2).
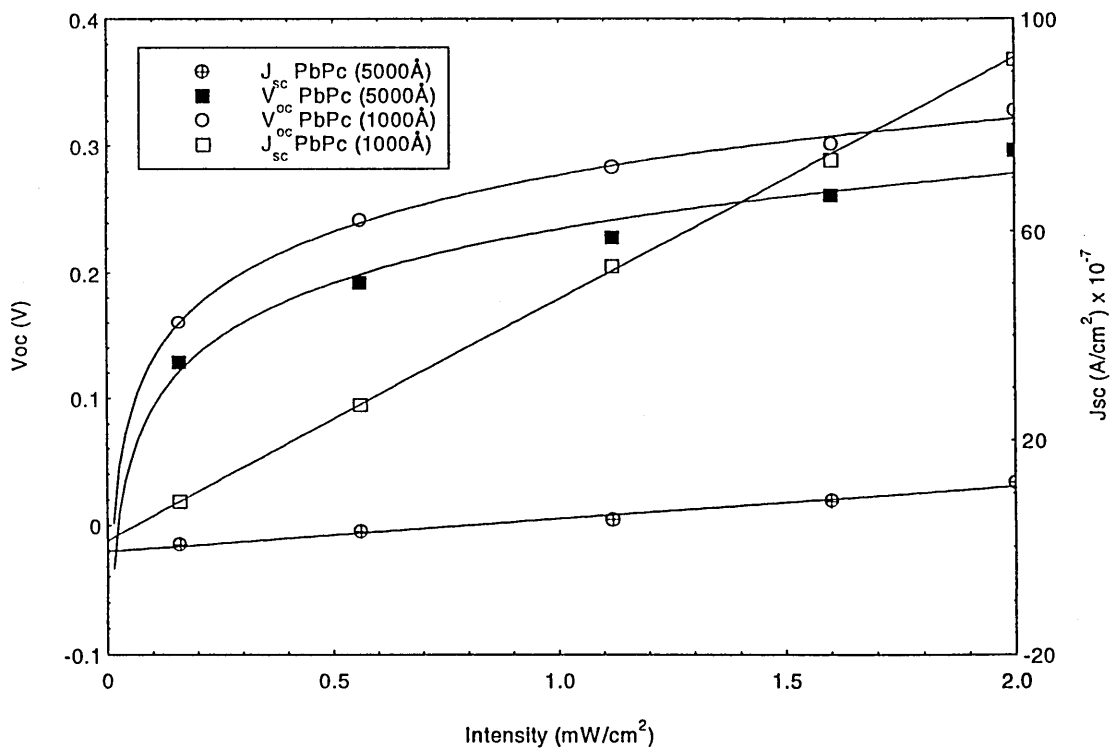
Figure. 7.44. Graph showing V$_{oc}$ with logarithmic fitting and J$_{sc}$ with linear fitting. as a function of incident light intensity (ϕ), for the Au/PbPc/TiO$_2$(50nm)/InSnO$_2$ cells under vacuum. PbPc film thickness as indicated on graph.

214
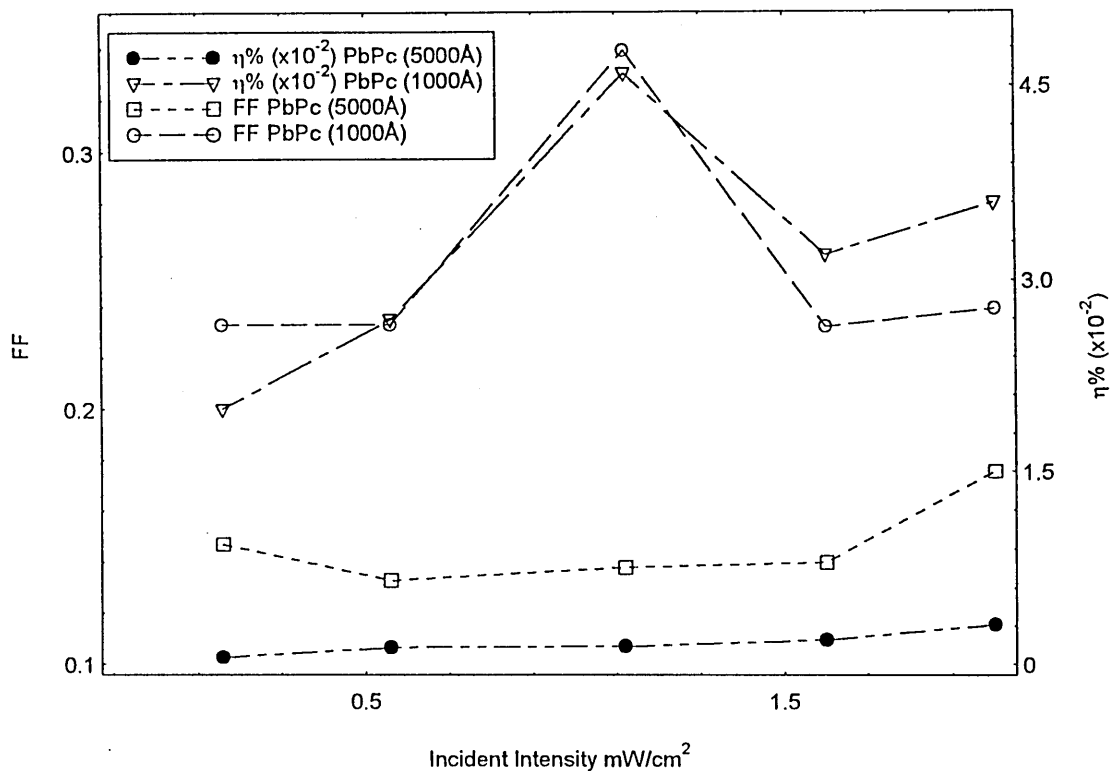
Figure 7.45. FF and η% as a function of incident intensity (φ), for cells as described in Figure 7.44.

PbPc film ~thickness nm		Incident Intensity (φ) mW/cm^2					
		Dark	0.16	0.56	1.12	1.6	2
100	R_s	570	85.5	74.6	86.2	98	85.5
100	R_{sh}	610	490	210	130	100	100
500	R_s	1610	48.3	71.9	31.7	28.4	24.1
500	R_{sh}	195700	3860	780	570	390	300

Table. 7.9 Series (R_s) and Shunt (R_{sh}) resistance's (kΩcm^{-2}) obtained for the Au/PbPc/TiO$_2$(50nm)/InSnO$_2$ heterojunction cells under vacuum.

215

In the cell containing PbPc(500nm), $\eta\%$ increased slightly with increasing intensity, while the FF slightly increased only at the highest and lowest intensity. However both factors displayed a relatively weak intensity dependence in comparison to the PbPc(100nm) cell. In this cell the FF and the $\eta\%$ had a similar intensity dependence. A maximum was observed at an intensity level of ~1.12mW/cm^2. Both factors decreased at intensities where 1.12mW/cm$^2 < \phi < 1.12$mWcm^2.

It has been previously stated that the J(V) characteristics are dependent upon R_{sh} and R_s the shunt and series resistance respectively of the cell[10]. Table 7.9 summarises R_{sh} and R_s obtained for the both cells in darkness and under various intensity levels.

In all cases $R_s < R_{sh}$ as expected. For both cells the measured series resistances were less under illumination than those measured in darkness. Similarly, the measured shunt resistances R_{sh} were less under illumination than those measured in darkness. In both cells the R_{sh} reduced with increasing intensity and the values of R_{sh} were poorer in the PbPc(100nm) device (note that ideal $R_{sh} \sim \infty$). The series resistances R_s in all cases were relatively high and far from the ideal ($R_s = 0$). Nevertheless, the values of R_s and R_{sh} measured for the cell consisting of PbPc(500nm) is an improvement over the devices containing ClAlPc(500nm) and CuPc (500nm).

Figure 7.46 displays the J(V) characteristics of a Au/PbPc(500nm)/TiO$_2$(50nm)/InSnO$_2$ cell under atmospheric conditions. The measured V_{oc} and J_{sc} were lower when the device was measured under atmospheric conditions. However both J_{sc} and V_{oc} saturated at high intensities.
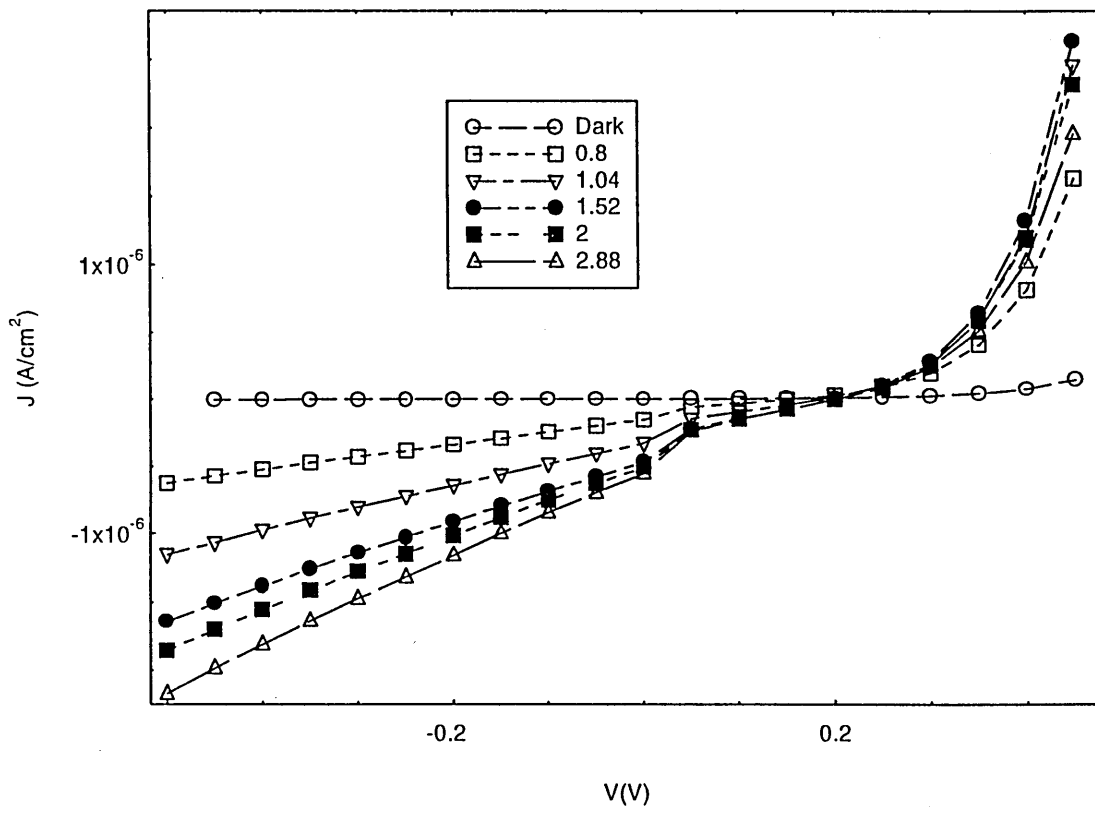
Figure 7.46. Dark and illuminated J(V) characteristics of a Au/PbPc(500nm)/TiO$_2$(50nm)/InSnO$_2$ heterojunction cell under atmospheric conditions. Measurements made in darkness and under simulated AM2 radiation at a variety of intensity levels as indicated.
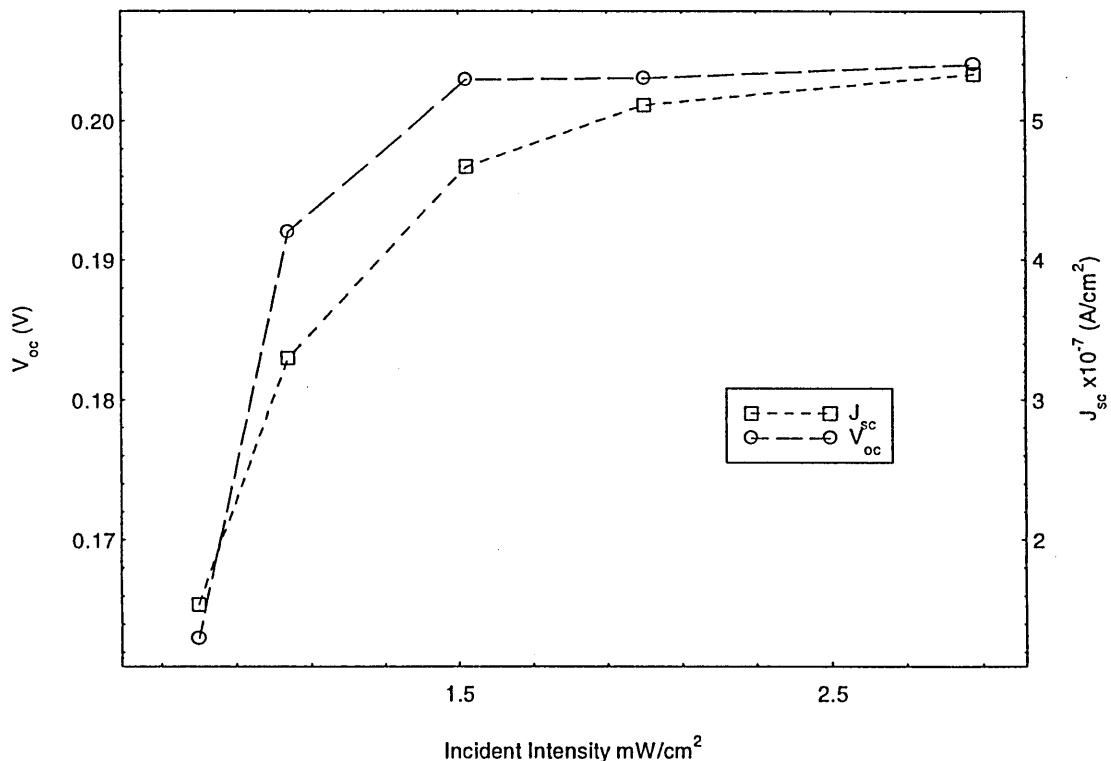
Figure 7.47. V$_{oc}$ and J$_{sc}$ as a function of intensity (ϕ) mW/cm^2, for a Au/PbPc(500nm)/TiO$_2$(50nm)/InSnO$_2$ cell under atmospheric conditions.
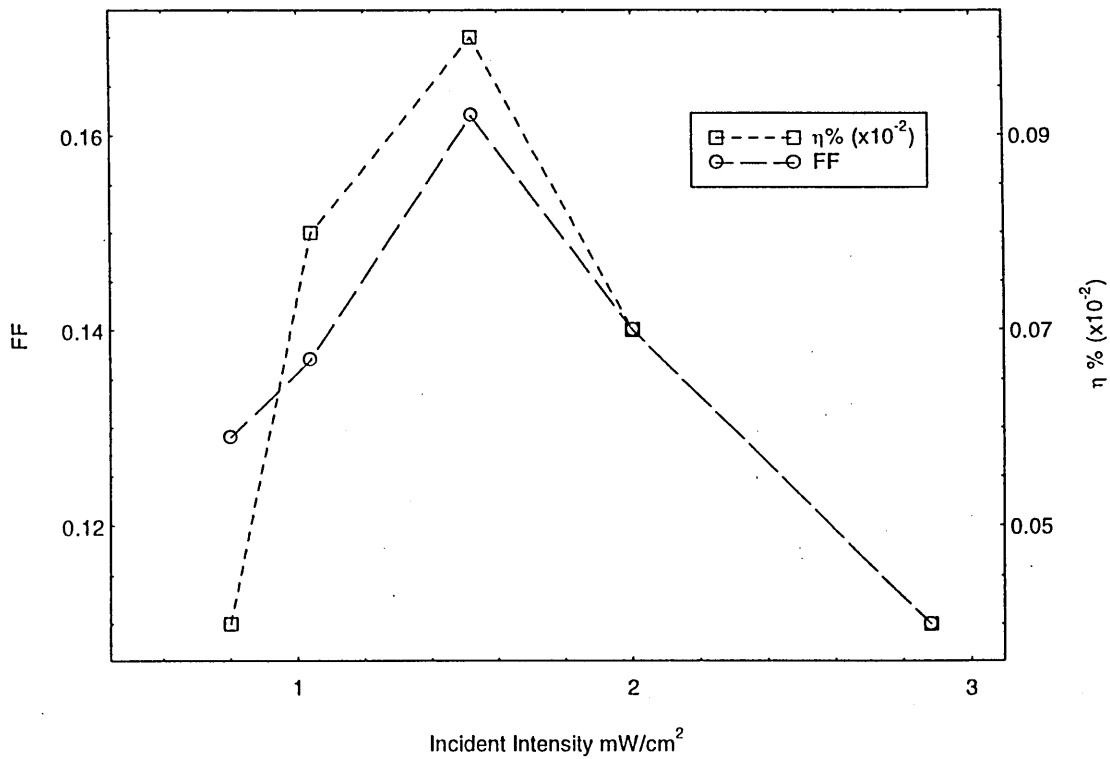
Figure 7.48. FF and $\eta\%$ as a function of intensity (ϕ) mW/cm^2 for the cell as described in Figure 7.47, under atmospheric conditions.
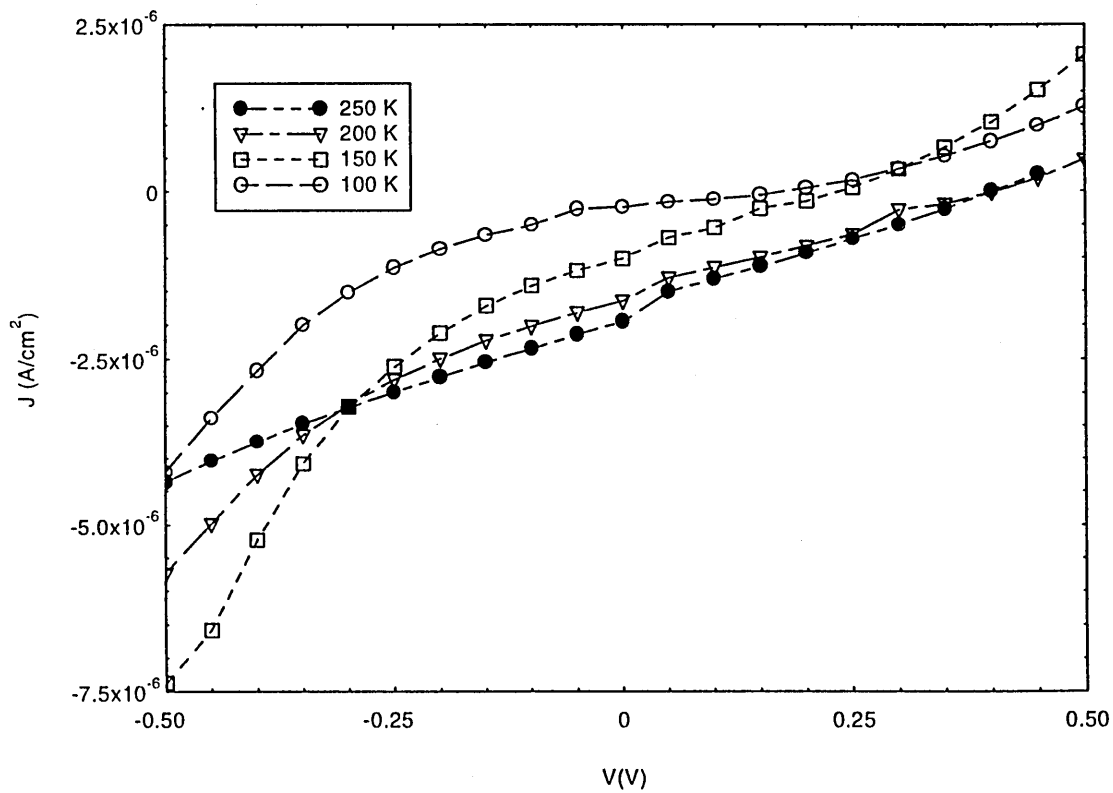
Figure 7.49. Illuminated J(V) characteristics (Intensity: 1.12mW/cm^2) of the Au/PbPc(100nm)TiO$_2$(50nm)InSnO$_2$ cell at a variety of temperatures as indicated.
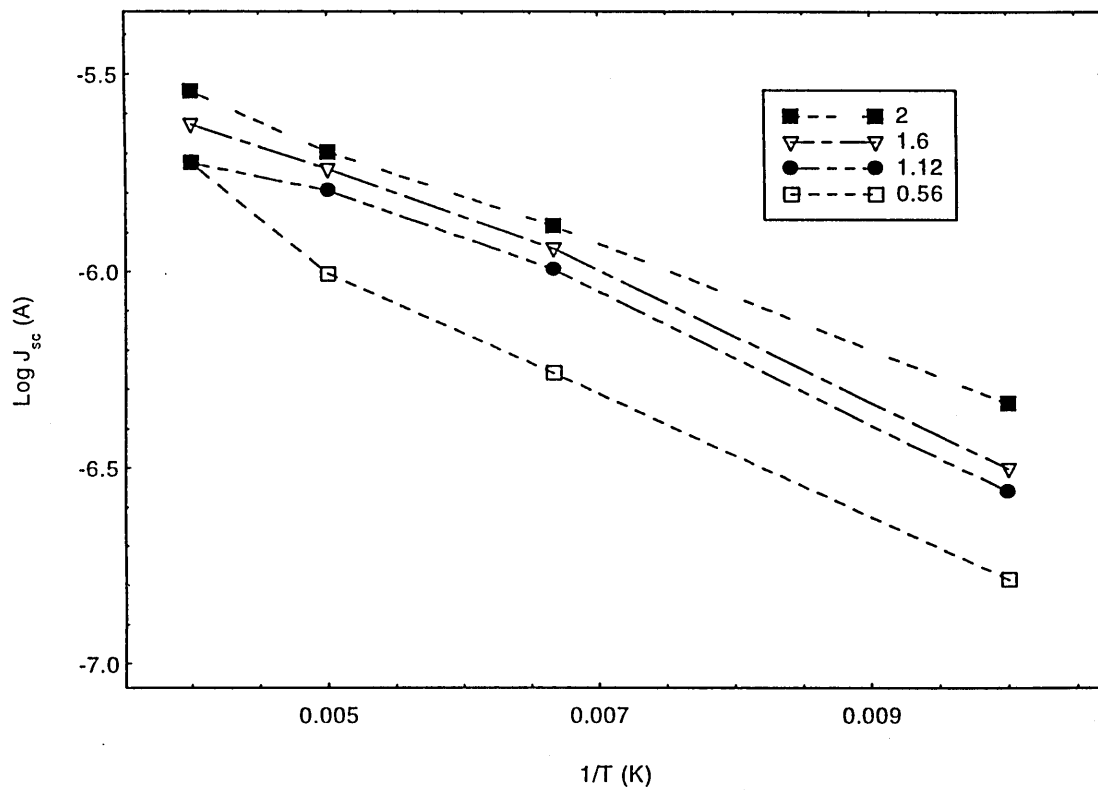
Figure 7.50. Arrhenius plot of J_{sc} for the Au/PbPc(100nm)/TiO$_2$(50nm)/InSnO$_2$ cell in dependence of temperature. For four intensities as indicated.
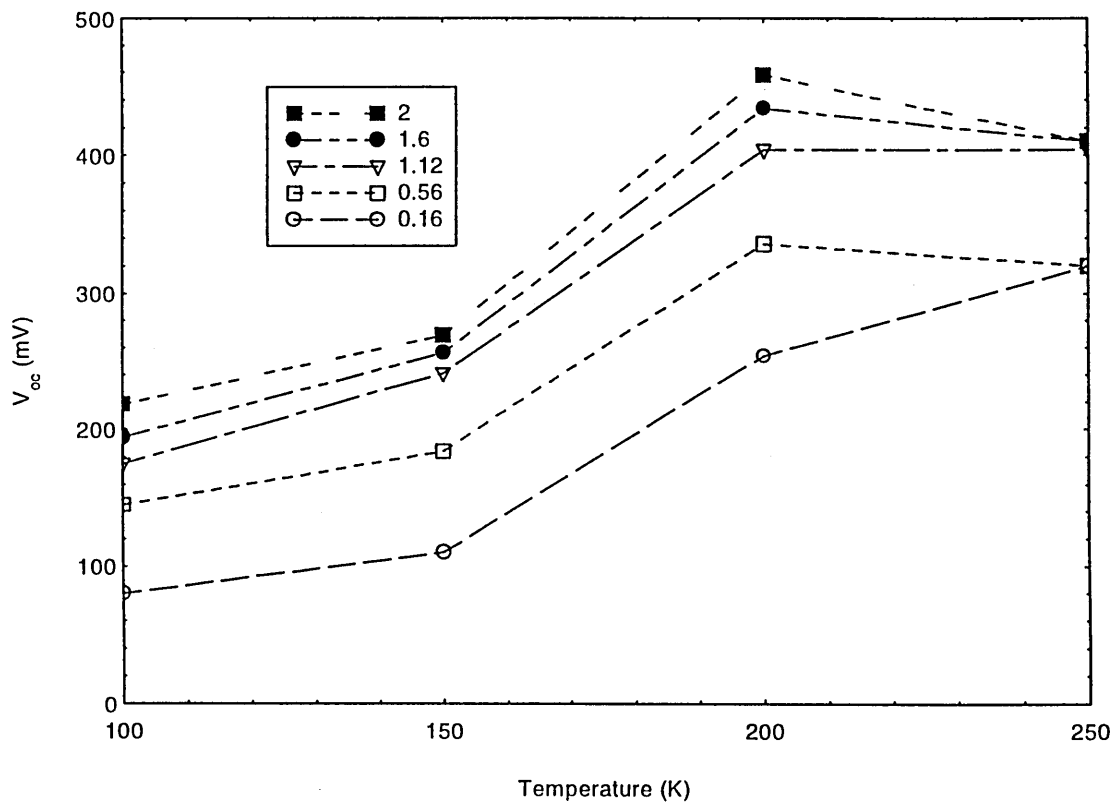
Figure 7.51. Open circuit voltage as a function of temperature for the cell as described in Figure 7.50.

R_{sh} again decreased as the intensity increased The value of R_{sh} is reduced under atmospheric conditions, both in darkness to $111.2 M\Omega cm^{-2}$ and under illumination to $370 k\Omega cm^{-2}$ at $2mWcm^{-2}$. R_s in darkness was decreased under atmospheric conditions to $\sim 971\ k\Omega cm^{-2}$ but under illumination R_s was higher than that measured under vacuum (i.e., $57.5\ k\Omega cm^{-2}$)

The temperature dependent J(V) characteristics are shown in Figure 7.49 for a $Au/PbPc(100nm)/TiO_2(50nm)/InSnO_2$ heterojunction cell at an intensity level of $1.12mW/cm^2$. It is clearly seen from the characteristics that J_{sc} is temperature dependent. Figure 7.50 is therefore an Arrhenius plot of J_{sc} for a variety of incident intensities. The short circuit current density of the heterojunction is thermally activated, increasing with increasing temperature. The temperature dependence of the open circuit voltage is shown in Figure 7.51. V_{oc} generally increased with increasing temperature and started to saturate at temperatures T>200K.

The increase in V_{oc} and J_{sc} with temperature was manifested as an increase in conversion efficiency, $\eta\%$ with temperature, which again saturated as room temperature was reached shown in Figure 7.52. $\eta\%$ was more sensitive to the incident intensity at higher temperatures. The cell parameters as a function of temperature derived from this work are given in Appendix C.
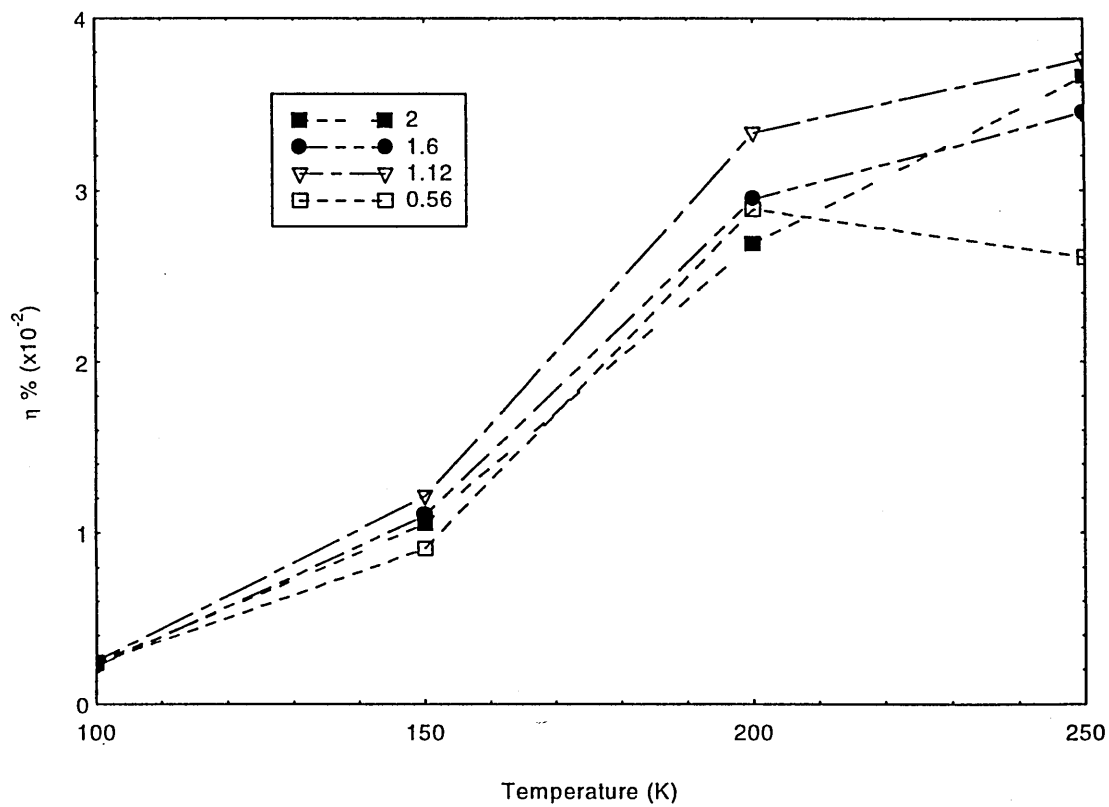
Figure 7.52. Dependence of $\eta\%$ with temperature for the Au/PbPc(100nm)/TiO$_2$(50nm)/InSnO$_2$ cell.
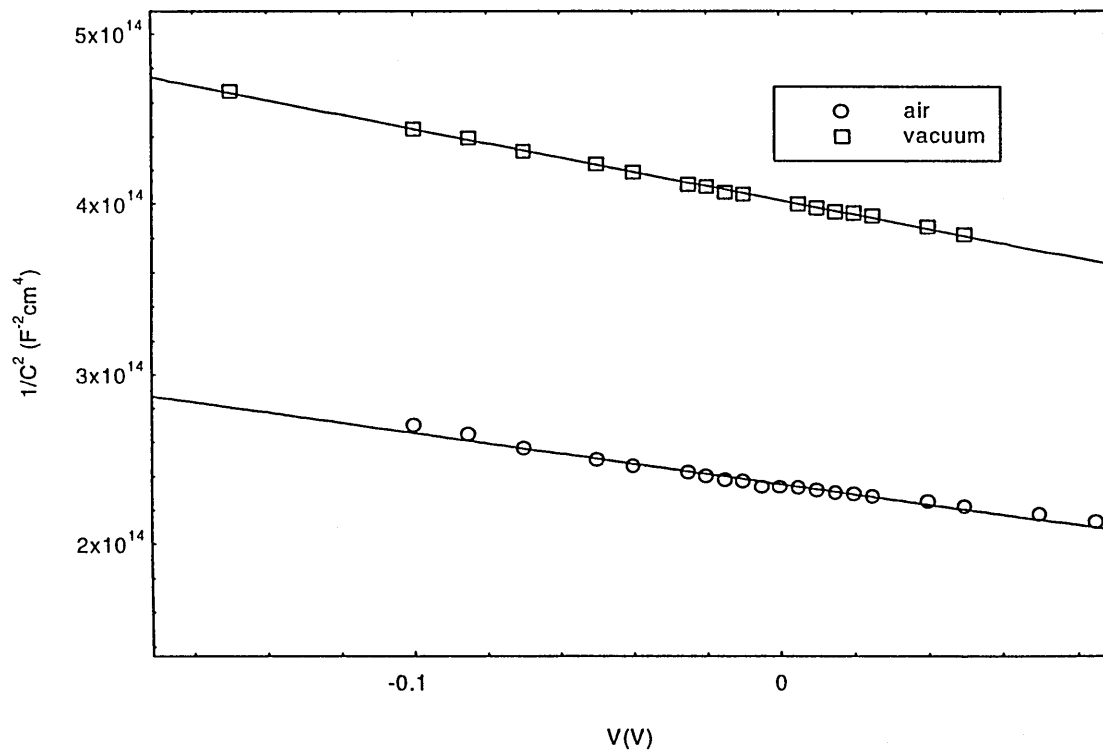
Figure. 7.53. C^{-2} Vs. V for a Au/PbPc(100nm)/TiO$_2$(50nm)/InSnO$_2$ heterojunction cell measured under darkness at room temperature.

7.5.4 C(V) Characteristics

Figure 7.53 displays the dark $1/C^2$ as a function of reverse applied bias at a fixed frequency of 500Hz for a $Au/PbPc(100nm)/TiO_2(50nm)/InSnO_2$ heterojunction cell. Measurements were made at room temperature and under both atmospheric and vacuum conditions as indicated. The $1/C^2$ against V curves were linear, indicating the presence of an electrically abrupt junction. Extrapolation of the curves to the voltage axis gave built in potentials of ϕ_{bp} of 0.95 V and 0.78 V under vacuum and atmospheric conditions respectively.

From the expression for an abrupt junction according to the Anderson model[1] and assuming an ionised donor concentration of N_d ~9×10^{18} cm^{-3} and permittivities of ε_1 ~ $1.77 \times 10^{-12} Fcm^{-1}$ (TiO_2) and ε_2~$3.16 \times 10^{-13} Fcm^{-1}$ (PbPc) as described in section 7.1, the ionised acceptor concentration N_a~ $5.24 \times 10^{19} cm^{-3}$ and $2.82 \times 10^{19} cm^{-3}$ under atmospheric and vacuum conditions respectively..

The depletion layer widths were calculated to be 11.8nm under atmospheric conditions and 12.4nm under vacuum (~10^{-3}torr) conditions. Under atmospheric conditions the penetration depths of the depletion layer were x_2~ 1.6nm and x_1~ 9.4nm into PbPc and TiO_2 respectively. Under vacuum the penetration depths were x_2~ 2.9nm and x_1~ 9.1nm into PbPc and TiO_2 respectively. In both cases $N_a > N_d$ and as such the depletion layer penetration distance was greatest into in the TiO_2 film.

REFERENCES

1. Anderson, R. L. *Solid State Elec.,* **5** (1962) 341.

2. Tang, H., Prasad, K., Sanjines, R., Schmid, P.E., and Levy, F. *J. Appl. Phys.* **75**(4) (1994) 2042-2047.

3. Yanagi, H., Kataura, H., and Ueda, Y. *J. Appl. Phys.* **75**(1) (1994) 568-576.

4. Gould, R. D. *Thin Solid Films* **125** (1985) 63-69.

5. Ahmad, A., and Collins, R. A. *Phys. Stat. Sol. (a)* **123** (1991) 201-211.

6. Missous, M., and Rhoderick, E. H. *Elec. Letts.* **22** (9) (1986) 477-478.

7. Lampert, M. A. *Rep. Prog. Phys.* **27** (1964) 329-367.

8. Helfrich, W. *Phys. Letts.* **16** (1966) 401.

9. Sze, S. M. *Physics of Semiconductor Devices.* Wiley, (1969).

10. Hovel, H. J. *Semiconductors and Semimetals, Solar Cells. Vol. 11.* Academic Press New York. (1975)

Chapter 8

Discussion of Experimental Results

8.1 TiO$_2$ via Sol-Gel Technology

The Sol stability was dependent on the procedure adopted for manufacture, the molar ratio of the metallo-organic precurser titanium isopropoxide (TIP):acetic acid and TIP concentration. Increasing the acid content resulted in Sols which were stable for longer periods of time. It is anticipated that the acid has an effect of slowing down the hydrolysis-condensation reaction by replacing the OR groups of the alkoxide precursor. The reaction results in a reduction in the gelation time of the Sol. These effects have been observed by Livage[1] on studies of similar titania Sol systems.

Many of the effects observed on stability are also similar to those of Yoldas[2] .The formation of clear solutions was dependent on the TIP:acetic acid molar ratio. However, according to Yoldas[2] for the most stable solutions too high or too low an acid:alkoxide ratio results in cloudiness. No upper limit for acid concentration was observed in the current studies which may suggest that further experimentation with the Sol-Gel parameters is required in order to optimise the stability.

8.1.1 Structural Studies

The heat treatment temperatures and times had influence on both the film surface quality, the crystalline structure and organic content of the films. It is believed that the three qualities are interlinked. Previous studies have shown that the crystallisation may correspond to the release of residual organics from the gel during heat treatment[2]. The observed transformation from an amorphous state obtained for unfired gels to a crystalline state of the anatase structure for gels heated to 500°C could be therefore be a consequence of a change in molecular separation caused by the removal of organic residuals observed in the infra red studies. Studies on titania gels[2] heated to 500°C have shown that when molecular spacing was 1 no rutile was formed however when the molecular spacing was 3 rutile forms appeared.

The pores visible in the unheated and low temperature films are attributed to removal of the solvent during the drying process. As the heat treatment temperature increases densification and crystallisation results, the pores collapse, and the film shrinks resulting in the observed cracking at the film edges.

Film thickness was found to be dependent on the withdrawal speed, increasing as the withdrawal speed increased. A similar dependence of withdrawal rate as a function of thickness has been found in a study of NASICON (Na^+ Super Ionic Conductor) thin films, prepared by the Sol-Gel method[3] and is consistent with theory proposed by Brinker[4] The effect has been explained as being due to the effect of viscous drag on the liquid meniscus[5].

It is suggested that the interaction effects can be attributed to three probable factors, which could produce the effects identified in these experiments. These factors being (i) the viscosity of the coating solution, (ii) the mechanism and kinetics of the reaction of the alkoxide precursor, and (iii) the surface interactions between the substrate and coating solution.

Referring to Table 6.2, the significant (positive) interaction effects between withdrawal speed with acid:TIP molar ratio [AB] and TIP concentration [AD] are most probably indicative of non-Newtonian[5] properties in the deposited film of the coating solution during dip coating, which appear to be exaggerated by the presence of either reaction modifying acetic acid, or the reaction precursor TIP at high concentrations. An increase in coating thickness would be predicted from an increase in the Sol viscosity during deposition. Other workers[6] have found evidence of non Newtonian behaviour during dip coating at withdrawal rates in excess of approximately 50 mm/min as used in these studies.

The interaction effects between the number of coatings with withdrawal speed [AC], acetic acid concentration [BC], and concentration of TIP [CD], and the three factor interaction between the number of coating layers with withdrawal speed and acetic acid concentration [ABC] can be attributed to a change in the surface interaction between the substrate and coating solution as these factors are varied. Previous work[5] has suggested that the thickness of the coating film produced during dip coating is determined by a number of factors related to surface effects including the viscous drag exerted on the liquid by the moving substrate. These effects are likely to be different between the coating liquid and a coated or uncoated substrate.

Previous studies[3] have also suggested that the thickness of the first coating layer in a multi layer coating is greater than that in subsequent coating layers. However, it can be deduced from the interactions identified in this work that such a phenomena is highly dependent upon the levels of other factors, and cannot be assumed to take place.

The significant negative interaction effect between the concentrations of the TIP precursor and acetic acid reaction modifier [BD] would appear to be indicative of a change in the kinetics, and perhaps mechanism of the hydrolysis and polycondensation reactions responsible for the gelation process. A reduction in film thickness would be expected if such an interaction resulted in a reduction in the reaction rate and/or solution viscosity. It is probable that the hydrolysis inhibiting reaction which occurs between the TIP and acetic acid[1] occurs faster and to a greater degree when the two reactants are present at a higher concentration.

8.1.2 Optical Studies

The computational technique of Ray and Hogarth[7] derived for non-crystalline materials was used to deduce δ (the nature of electronic transitions in the TiO_2) and E_o (the optical band gap). The results obtained using this technique were in good agreement with those derived from Tauc[8] plots. In the latter method the nature of electronic transitions must be assumed, and has therefore led to differing values of E_o for the same materials[7]. It appears from these studies that the computational technique was successful on thin films of anatase TiO_2 and it is anticipated therefore that the method can be extended to other

227

materials of this type. The results identified a dependence of the optical band gap E_0 and the nature of optical transitions on the number of coating layers (hence film thickness). The E_0 decreased as the thickness increased. This dependence is attributed to a quantum size effect[9] which could be either a result of the small size of crystalline grains in the films and/or the low film thickness itself, as observed in CdS films[9] and TiO_2 prepared via ion beam induced chemical vapor deposition (IBICVD)[10] (see section 2.5).

The value of the E_0 was ~3.4-3.35eV (where $\delta=2$ denoting an indirect allowed transition) for 1 coating layer and converged to E_0~3.2eV (where $\delta=3$ denoting an indirect forbidden transition) as the number of coating layers increased. The latter value for E_0 is in good agreement with Tang[11] as determined for anatase TiO_2 thin films. In contrast to these results, the transition was reported to be an indirect allowed transition. The former value for E_0 is in reasonable agreement with Leinen[10] on TiO_2 film prepared by IBICVD. However, a value of E_0 ~ 3.03eV an indirect gap for anatase TiO_2 thin films prepared via Sol-Gel has been reported[12]. Inaccuracies in the assumption of δ and quantum size effects due to small crystallites or the low film thicknesses used are believed to be to the reasons for the discrepancy.

The absorption coefficient (measured at a photon energy of 4eV) was between 0.623-$1.87 \times 10^5 cm^{-1}$, depending on the Sol parameters. Only the number of coating layers had a significant (negative) factorial effect on the absorption coefficient which was attributed to refractive index mismatch.

The values of the calculated absorption coefficient were comparable with H_2 reduced TiO_{2-x} films prepared by pulsed excimer laser ablation (PLA).[13] Pure TiO_2 has an absorption coefficient lower than those measured in these studies[13]. Reasons for the variance may be the scattering of light by surface and volume imperfections such as surface roughness or rough grain boundaries or due to a difference in the stoichiometry.

The calculated values of the refractive index n (shown in appendix A) of the TiO_2 anatase films in these studies are comparable with those reported in literature (e.g. 2.66 at 394nm compared to a reported value of 2.6 at 430nm).[10,13,14] The high value of n for the TiO_2 films (as a high as 2.7 in these studies) has previously been attributed to the high compactness of the films[10].

n was found to decrease with increasing wavelength (λ). This is similar to the dependence observed by Takahashi and Matsuoka[15] for anatase TiO_2 films prepared from a $Ti(O-I-PrOH)_4$-diethanolamine-H_2O-i-PrOH system. The $n(\lambda)$ dependence was well described by the single oscillator model.[16] The parameter E_d (the single oscillator strength) was lower than that reported for single crystal TiO_2 . E_d is a quantity that is related to the dielectric constant and to the chemical bonding. The difference in the value of E_d could be due to the polycrystalline nature of the film in comparison to the single crystal TiO_2 in which the strength of optical transitions is stronger. E_s the single oscillator energy was in good agreement with that reported by Wemple[16] for TiO_2.

The observed thickness independent n is in contrast to that reported by Leinen[10] on IBICVD TiO_2 films, in which n decreased slightly with increasing thickness and was attributed to the accumulation of defects and/or a small amounts of residual impurities as the layer grew. In contrast, Vorotilov[14] reported that for TiO_2 Sol-Gel derived films the n increases as the thickness (number of applications) increases, due to the larger crystallites in the thicker films, owing to their longer heat treatment time. The n(thickness) dependence stabilised as the thickness increased. In the films studied this threshold could therefore have been reached due to the long heat treatment times used (five hours) and as a consequence no measurable thickness dependence was observed.

8.1.3 Electrical Studies

The value of the conductivity measured for the anatase TiO_2 thin film deposited on $InSnO_2$ substrates was~4.26×10^{-6}S/cm. Single crystal anatase TiO_2 has a much higher reported conductivity of between 10-0.7S/cm which is likely to be a consequence of the higher charger carrier mobility due to the absence of imperfections such as grain boundaries. The measured conductivity is higher than that reported by Vorotilov[14] by several orders of magnitude ($\sim 1 \times 10^{-12}$S/cm) for Sol-Gel derived TiO_2 films deposited on silicon substrates. The higher conductivity is therefore presumably due to the effects of the base electrode used. In the current studies the high heat treatment temperature used would have resulted in diffusion of TiO_2 with the $InSnO_2$ resulting in a low resistance high quality ohmic contact as observed from J(V) characteristics, in contrast to the TiO_2/Si in which a relatively high interface trap density was observed.

The effects of heat treatment temperature indicated that a higher conductivity was measured for the unheated films. This is believed to have arisen from the contribution (to the conductivity) of residual organic material identified in the infra-red spectroscopy, and possibly also to the presence of adsorbed water in the pore structure of the gel. The reduction in conductivity as the heat treatment temperature increased is presumably due to the removal of the majority of these residual impurities.

As discussed in section 3.3.3 the total conductivity is the sum of both the extrinsic and intrinsic contribution. Due to the low temperatures used in these studies the observed conduction is believed to be extrinsic. Very low activation energies were observed, which suggests that nearly all electrons are free to contribute to conduction and indicates the possible presence of an impurity level. The low activation energy also suggests that conduction is likely to be through charge carrier hopping.

An activation energy 1.6 eV was observed by Konenkamp[17] over temperature range 434-322K and was believed to be intrinsic i.e. band to band conduction, however Ardakani[13] has observed low temperature activation energies in the range 0.008-.16 eV for hydrogen reduced non-stoichiometric TiO_{2-x} conduction was believed to be through charge carrier hopping involving either neutral centres or from singly ionised centres to free oxygen vacancies.

8.2 The Inorganic/Organic Heterostructure

8.2.1 Spectral Response

To spectrally sensitise TiO_2 into the visible region the sensitiser (Pc) must show appreciable absorption in the visible region. Both the Soret bands and Q-bands normally associated with MPcs were visible in all the film absorption spectra. The TiO_2 films were highly transparent over the visible wavelength range. Any wavelength dependence of J_{sc} observed is therefore anticipated to be a consequence of photocarrier excitation in the MPc and a subsequent charge separation and transfer mechanism at the MPc/TiO_2 interface.

For all devices studied the J_{sc} action spectra displayed a similar wavelength dependence as the absorbance spectra of the MPcs. The similarity of the absorption spectra to the action spectra indicated that sensitisation of the TiO_2 Sol-Gel layer with MPc dye molecules occurred resulting in the extension of the absorbance of TiO_2 into the visible region. $V_{oc}(\lambda)$ also displayed a good match to the absorption spectra studied in CuPc/TiO_2 and PbPc/TiO_2 cells.

An increase in J_{sc} was observed for those samples held under vacuum compared to atmospheric conditions in the ClAlPc/TiO_2 and PbPc/TiO_2 cells. The lower J_{sc} for these devices measured under atmospheric conditions could be a consequence of oxygen doping. O_2-electron acceptor impurities capture electrons generated through phototexcitation (e/o pairs). Therefore electrons are trapped by O_2 centres rather than transfer to the TiO_2 layer. This was further substantiated on observation of the effect on

quantum efficiency which increased under vacuum conditions for both cells. Also, under N_2 relatively little change was observed in both J_{sc} and Z for the CuPc cell in comparison to measurements made under atmospheric conditions. Therefore it is believed that evacuating the sample chamber and adding N_2 does not remove O_2 molecules from the MPc film as effectively as a continuous vacuum.

The effects of altering the base electrode from $InSnO_2$ to $F-SnO_2$ was assessed on the $CuPc/TiO_2$ device. Both J_{sc} and Z decreased at the higher wavelength range ~700nm, this may be caused by the observed lower transparency of the $F-SnO_2$ at this wavelength compared to the $InSnO_2$. At lower wavelengths ~345nm both J_{sc} and Z increased in the devices consisting of $F-SnO_2$ however, at this wavelength both substrates are of similar transparency.

Low quantum efficiencies <1% were observed in all devices comprising of 500nm thick organic layers. Several explanations are proposed to account for the low values of Z.
In heterojunction devices, low quantum efficiencies are often associated with the presence of recombination centres[18], which are likely to be present at the MPc/TiO_2 heterointerfaces. The recombination centres may be in the form of surface states at the TiO_2 surface, impurities in the MPc layer or grain boundaries within the TiO_2 or Mpc polycrystalline films. The low electrical conductivity of the TiO_2 and MPc films also causes a high series resistance (later studies on illuminated J(V)) characteristics show that the devices suffered from a high R_s). A reduction in the thickness of the organic layer, hence effective series resistance, resulted in a higher measured quantum efficiency in support of this claim.

The depression in J_{sc} and V_{oc} in the Soret bands region (wavelengths of strong absorption) are likely to be caused by attenuation of light reaching the heterojunction through the TiO$_2$ layer due to the onset of absorption in TiO$_2$ for $\lambda < \sim 320$nm. The TiO$_2$ being transparent to photon energies less than the band gap of 3.2eV.

In summary the spectral responses indicate that the Sol-Gel derived TiO$_2$ film can be sensitised to wavelengths outsides its intrinsic sensitivity by the MPc dyes under investigation.

8.2.2 Dark J(V) Characteristics

No blocking contact was formed at the TiO$_2$/InSnO$_2$ interface and MPc/Au contacts are known to exhibit ohmic behaviour[19]. The cell parameters are therefore determined by the MPc/TiO$_2$ contact and the resistivity of the constituent materials. All devices exhibited rectifying behaviour, although the rectification ratios were very low. It can therefore be assumed that a rectifying contact is formed between all the MPcs studied and TiO$_2$. This is encouraging since rectifying behaviour is required for charge separation.

The CuPc/TiO$_2$ devices had a significantly higher rectification ratio than the other devices studied. The reasons for this are unclear. Superior junction quality due to the planarity of the CuPc molecule in comparison to the PbPc and ClAlPc molecules, reduced pinhole formation resulting in a superior Au/MPc contact are believed to be contributing factors.

234

According to the theoretical models used, the dark characteristics of the devices can generally be divided into three working regimes. (i) A low forward/ reverse bias regime where V<3kT/e, (ii) an intermediate forward regime and (iii) a high forward regime.

(i) For reverse bias and low forward voltages where V<3kT/e V, the results are well represented by the Missous and Rhoderick[20] modified diode (equation (3.36)). Any departure from ideality of the devices was apparent and probably caused by generation /recombination within the depletion region. The calculated ideality factors for all devices studied were within the range 1<m<1.2. Factor values of around 1 indicate a predominance of the diffusion current within this regime. In most cases the diode quality factors were slightly higher than 1 indicating that although diffusion current dominates, recombination mechanisms may be present.

(ii) Generally, for all of the devices studied the standard diode equation (3.35) provided a good fit to observed forward J(V) characteristics. However the voltage ranges over which the characteristics were in agreement with the equation varied from device to device, presumably a consequence of differences in the MPc conductivities. In all devices the ideality factor m>2 over the higher bias ranges and for the ClAlPc(500nm)/TiO_2 and PbPc(100nm)/TiO_2 devices m>2 over the entire range studied.

This type of behaviour has been observed in IO heterojunctions of the form Ag/CuPc/p-Si and attributed to the presence of a high density of interface states in equilibrium with the inorganic layer. The states facilitate electron-hole recombination[21].

In the CuPc(500nm)/TiO$_2$ device m~2 indicating the predominance of recombination currents for low applied forward voltages and for the PbPc(500nm)/TiO$_2$ under vacuum m~1 in the low forward voltage region indicating the predominance of diffusion current. It is unknown why such variations in the value of m under low forward biases were observed, it is proposed that this is a result of space charge effects (see (iii) below) in the organic layer, which would cause m to be subject to errors. Within this regime the value of m must therefore be interpreted with some caution.

(iii) A common feature of the J(V) characteristics observed in all devices was a deviation from the standard diode equation as the forward applied bias increased. A non-linear dependence of this type has been observed in many MPcs and is caused by space charge effects in the organic layer[22]. Within this high forward voltage regime the behaviour of the IO heterojunctions is similar to that of a Schottky diode as the conduction in the organic materials is extrinsically space charge limited. It is expected that within this regime the electrical characteristics of the IO heterojunction are controlled by an exponential distribution of traps within the mobility gap of the organic materials.

From regions (i) and (ii) the saturation current densities J$_s$ were calculated. In all devices studied high values of J$_s$ were observed, which is evidence of the presence of a high density of defects at the TiO$_2$/MPc interfaces.

The temperature dependence of the dark J(V) characteristics were investigated for a PbPc/TiO$_2$ heterojunction. Both the ideality factor m and saturation current density J$_s$ were temperature dependent parameters regardless of the method used to calculate them. J$_s$ increased as the temperature increased and m decreased as the temperature increased.

The fact that in reverse bias the slopes of the lnI/[1-exp(-eV/kT)] against V plots were temperature independent indicates that over this temperature and voltage range the junction currents are controlled by recombination in the depletion region[23].

Also as the temperature decreased the saturation current density became less temperature dependent indicating that the tunnelling of carriers through the interface was the dominant current transport mechanism[24]. The junction current is therefore believed to be a composite of tunnelling and recombination currents.

8.2.3 Solar Cell Characteristics

Continuous exposure of the CuPc/TiO$_2$ devices to atmosphere resulted in a drop in the overall conversion efficiency, η. The η was also higher under vacuum for both the ClAlPc/TiO$_2$ and PbPc/TiO$_2$ cells than that measured under atmosphere. Exposure to atmosphere resulted in a decrease of the short circuit current density J$_{sc}$ and open circuit voltage, V$_{oc}$ which are among the parameters that determine the potential power output of the cell. As observed in the studies of spectral response, this dependence is presumably due to O$_2$ centres which capture electrons generated through photoexcitation of the dye layer. The magnitude of charge transfer is therefore reduced.

In all devices the J(V) characteristics were dominated by high series resistances R_s which seriously undermined the performance of the cells by reducing both the J_{sc} and FF fill factor. The series reistances obtained are expected to be a consequence of the low conductivity of the organic semiconductor, although the occurrence of pinholes may also contribute to a high R_s. In the CuPc/TiO$_2$ cells the R_s reduced after prolonged exposure to atmosphere which is likely to be due to the enhanced conductivity of the CuPc films from O$_2$ doping. However the reduction in R_s did not significantly affect the η which fell after prolonged atmospheric exposure. Hence, although R_s reduced, it did not counter effect the detrimental effects of electron hole recombination.

In both the CuPc/TiO$_2$ and PbPc/TiO$_2$ cells the R_{sh} decreased with increasing intensity. The R_s also decreased with increasing intensity as observed in the CuPc/TiO$_2$ cells. This can be attributed to photoconductive effects in the organic layer. The excess photogenerated carrier density becoming comparable or larger than the dark equilibrium carrier density, with a corresponding increase in conductivity, at higher intensities and therefore a correspondingly lower R_s.

The serious effects of the high R_s on the performance of the devices was further demonstrated when the organic layer film thickness was reduced. A 30 fold increase in η was observed in the PbPc(100nm)/TiO$_2$ cells compared to the PbPc(500nm)/TiO$_2$ cells which is further evidence of the low conductivity of the organic film contributing to the high series resistances. Illumination of the IO junction was directed through the TiO$_2$ face, hence losses through recombination effects within the organic layer are not expected to significantly contribute.

In the $PbPc/TiO_2$ cells the measured series resistances were less under illumination than those measured in darkness, again this could be a consequence of the photoconductive effects of the organic layer (increasing the conductivity of the film therefore lowering any series resistance caused by the film bulk). Similarly, the measured shunt resistances (R_{sh}) were less under illumination than those measured in darkness which would be explained if the levels of generation /recombination within the depletion region increased on illumination.

The R_s decreased when the film thickness decreased, ideally $R_{sh} \sim \infty$. It therefore appears that as the thickness of the organic film decreases the device becomes more prone to the effects of R_{sh} namely, diffusion along grain boundaries, or the formation of filamentary metallic bridges through pinholes and cracks in the films.

A logarithmic dependence of V_{oc} on light intensity is predicted by equation (3.38), and would be expected for a typical Schottky or p-n junction photovoltaic cell[23]. Such a dependence of the V_{oc} was observed in both the $PbPc/TiO_2$ and the $ClAlPc/TiO_2$ cells. The equation also predicts a linear dependence of J_{sc} on intensity (ϕ), (where $J_{sc} \propto \phi^y$). For the $PbPc(100nm)/TiO_2$ cells $y \sim 0.95$. $y \sim 1$ is expected in the absence of carrier recombination or when charge carriers recombine through monomolecular processes[25]. However a sub linear dependence was observed in the $ClAlPc/TiO_2$ cells. Values of y lower than 1 can be explained if the photocurrent is limited by space charge at high light intensities by the presence of both monomolecular and bimolecular processes or by a combination of deep and shallow traps[25].

It must be noted that the $J_{sc} \propto \phi$ dependence is expected when the series and shunt resistances are negligible[25]. Very high R_s and R_{sh} were observed in the $ClAlPc/TiO_2$

cells and hence a significant and another probable source of the sublinear J_s dependence on intensity.

R_s influences cell parameters at high intensities[23]. In the ClAlPc/TiO_2 cells, the very high R_s associated with the cells could be the cause of the reduction in $\eta\%$ observed at higher intensities. The effects of R_{sh} are known to dominate at low intensities[23], which would explain the lower V_{oc} and FF values at these intensities, however the value of R_s is relatively high and although FF and V_{oc} are very low a slight increase in $\eta\%$ is observed. It is therefore anticipated that the high series resistance is the dominating factor in explaining the poor performance of the cell rather than R_{sh}.

The peaks in the η (ϕ) dependence measurements in both PbPc/TiO_2 and ClAlPc/TiO_2 cells are therefore presumably due to the effects of R_s at high intensities and R_{sh} at low intensities.

The temperature dependencies of V_{oc} and J_{sc} were contradictory to that which would be expected for a typical Si or GaAs cell, in which the V_{oc} is expected to decrease as the temperature increases[23]. This is due to the strongly temperature dependent dark current increasing with increasing temperature. In conventional cells the dark current is made up of three current components J_{inj} (injected current), J_{rg} (recombination-generation current) and J_{tun} (tunnelling current)[23,24]. The first two are strongly temperature dependent increasing with increasing temperature, however the tunnelling current is not. Tunnelling dominates in heterojunctions such as Cu_2S-CdS[23] where the V_{oc} is constant with temperature.

Tunnelling is likely therefore be a pertinent conduction mechanism in the current IO heterojunctions, in partial agreement with the findings obtained from the dark J(V) characteristics.

In the PbPc/TiO$_2$ device both J$_{sc}$, V$_{oc}$ and η increased with increasing temperature and saturated as higher temperatures were reached. Temperature dependent measurements of conductivity in the PbPc samples (appendix D) indicated two different activation energies. The activation energy for temperatures <162K was very low. The J$_{sc}$ of the PbPc/TiO$_2$ cell saturates for higher temperatures and shows activated behaviour for low temperatures, therefore it is suggested that the J$_{sc}$ seems not to be restricted by the conductivity of PbPc film. Such an effect has been reported in a recent organic n-p cell comprising of a phthalocyanine/perylene heterojunction[26].

In organic cells degradation under strong illumination has been reported to be a major problem[27]. At room temperature no such degradation was observed in the cells. Studies of merocyanine/ZnO have also shown no degradation[27]. It is believed that the TiO$_2$ and the InSnO$_2$, F-SnO$_2$ electrodes act as filters to the UV content of the solar simulator.

The overall conversion efficiencies were relatively low in comparison with present day commercial inorganic photovoltaic cells[28]. They are comparable with a recently reported efficiency for ZnPc/TiO$_2$ heterojunction cell[29] with an $\eta\sim$ 0.01%. In these studies the highest $\eta\sim$ 0.046% for a PbPc(100nm)/TiO$_2$ cell.

Several explanations are proposed to account for the low efficiencies observed in the IO heterojunctions. The presence of defects at the TiO_2/MPc interfaces would be expected to result in a reduction of η as the defects would act as recombination centres for the photogenerated electron-hole pairs. These defects may take the form of surface states on the TiO_2 surface due to the lack of any surface treatment, similarly observed in the recent TiO_2/ZnPc cell[29]. Defects may also be introduced via grain boundaries and impurities on the surface and within the TiO_2 and MPc. The overall conversion efficiency is anticipated to be a function of the electrical resistance of the cell. The low electrical conductivity of the MPc films causes a high series resistance which lowers η. The non-ideal R_{sh} indicates the presence of pinholes and short circuits in the organic films which again undermines the devices efficiency.

8.2.4 C(V) Characteristics

The C(V) analysis on the PbPc/TiO_2 and the CuPc/TiO_2 cells allowed calculation of the built in potentials ϕ_{bp}. These were greater than the highest measured V_{oc} of the cells, which is expected since the V_{oc} cannot physically be greater than the built in potential of the heterojunction[23]. The calculated acceptor concentrations N_a of the MPc films varied between 2.82×10^{19}-$6.8 \times 10^{19} cm^{-3}$, which is in close agreement with the reported values of the ionised acceptor concentrations of the MPcs[30].

For all the devices the C^{-2}(V) characteristics were linear and indicates that the MPc/TiO_2 junctions formed were electrically abrupt. Since the calculated acceptor concentrations $N_a > N_d$ (the donor concentration in the MPc) it is expected that the penetration distance

(x_2 and x_1 into the p-type and n-type material respectively) of the depletion layer will be greater into the TiO_2 (n-type material). Calculated values of x_2 were all less than x_1 indicating that this was indeed the case.

In the $PbPc/TiO_2$ films the calculated penetration distance of the depletion layer into the TiO_2 was greater under atmospheric conditions than under vacuum presumably a consequence of the increased hole concentration in the PcPc film due to O_2 molecules. PbPc is known to be highly sensitive to O_2 which increases the free carrier concentration[31].

Using derived parameters and available reported parameters an energy band diagram for the IO ($TiO_2/PbPc$) heterojunction is proposed, shown in Figure 8.1.
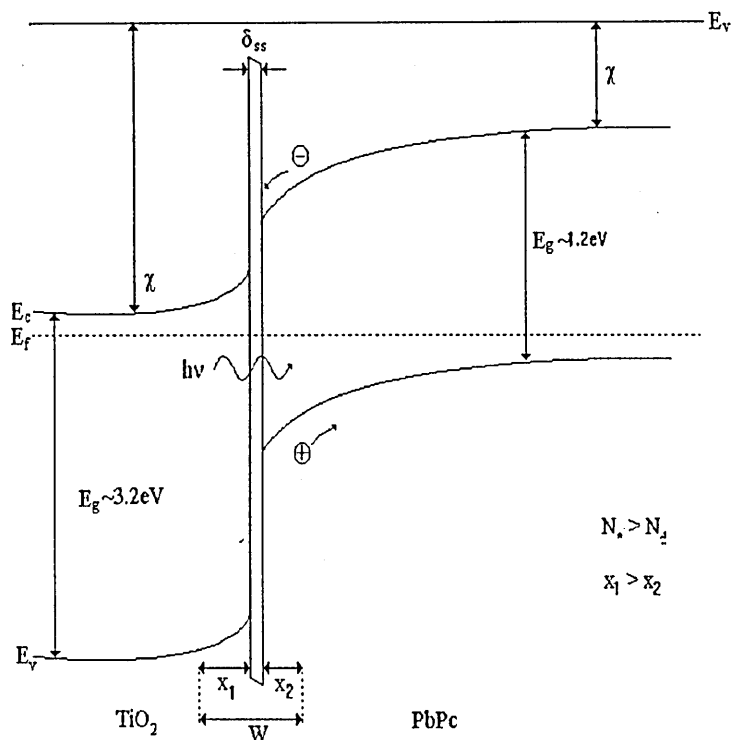
Figure 8.1. Proposed energy band diagram for the dye sensitised IO Heterojunction. x=penetration depth of the depletion layer width, where $x_1>x_2$, δ_{ss}=interface states, W=depletion layer width, χ=electron affinity. $\chi(TiO_2)> \chi(MPc)$ according to Takada[32]. E_g (PbPc) from Schmeißer[33].$E_g(TiO_2)$ as derived in these studies.

REFERENCES

1. Livage, J. *Mat. Res. Soc. Symp. Proc.* **73** (1986) 717-724.

2. Yoldas, B. E. *J. Mat. Sci.* **21** (1986) 1087-1092.

3. Huang, Y. L., Caneiro, A., Attari, M., and Fabry, P. *Thin Solid Films.***196** (1991) 283-294.

4. Brinker, C. J., Hurd, A. J., Schunk, P. R., Frye, G. C., and Ashley, C. S., *J. Non-Cryst-Solids*, **147-148** (1992) 424-436.

5. Brinker, C. J., and Scherer, G. W. *Sol-Gel Science*, Academic Press, New York 1990.

6. Strawbridge, I., and James, P. F. *J. Non. Cryst. Solids.* **86** (1986) 381-393.

7. Ray, A. K., and Hogarth, C. A. *J. Phys. D. Appl. Phys.* **23** (1990) 458-459.

8. Tauc, J. *The Optical Properties of Solids,* Ed. F. Abeles, North-Holland Publ. Co., Amsterdam, 1970.

9. Chuu, D. S., and Dai, C. M. *Phys. Rev. B* **45**(20) (1992) 805-809

10. Leinen, D., Espinós, J. P., and Gonzàlez-Elipe, A. R. *J. Vac. Sci. Technol. A.* **12**(5) (1994) 2728-2732.

11. Tang, H., Prasad, K., Sanjilnès, R., Schmid, P. E., and Lévy, F. *J. Appl. Phys.* **75**(4) (1994) 2042-2047.

12. Yoko, T., Yuasa, A., Kamiya, K., and Sakka, S. *J. Electrochem. Soc.* **138**(8) (1991) 2279-2285.

13. Ardakani, H. K. *Thin Solid Films.* **248** (1994) 234-239.

14. Vorotilov, K. A. *Thin Solid Films.* **207** (1992) 180-184.

15. Takahashi, Y., and Matsuoka, Y. *J. Mat. Sci.* **23** (1988) 2259-2266.

16. Wemple, S. H., and DiDomenico, Jr., M., *Phys Rev B.* **3** (4) (1971) 1338-1351.

17. Könenkamp, R., and Henninger, R. *Appl. Phys. A* **58** (1994) 87-90.

18. Sravini, C., Reddy, K. T. R., Hussain, O., and Reddy, P. J. *Thin Solid Films*. **253** (1994) 339-343.

19. Boudjema, B., Guillard, G., Gamoudi, M., Maitrot, M., Andre, J. J., Martin, M., and Simon, J. *J. Appl. Phys*. **56** (8) (1984) 2323.

24. Sze, S. M. Physics of Semiconductor Devices. Wiley, 1969.

20. Missous, M., and Rhoderick, E. H., *Elec. Letts*. **22** (9) (1986) 477-478.

21. Antohe, S., Tomozeiu, N., and Gogonea, S. *Phys. Stat. Sol. (a)* **125** (1991) 397-408.

22. Antohe, S. *Rev. Roum. Phys*. **37**(3) (1992) 309-313.

23. Hovel, H. J. *Semiconductors and Semimetals, Solar Cells. Vol. 11*. Academic Press New York. (1975)

25. Yanagi, H., Kataura, H., and Ueda, Y. *J. Appl. Phys*. **75**(1) (1994) 568-576.

26. GÜnster, S, Siebentritt, S., and Meissner, D.*Mol. Crys. Liq. Cryst*. **229** (1993)111-116.

27. Kudo, K., and Moriizumi, T. *Jap. J. Appl. Phys*. **19**(11) (1980) L683-L685.

28. Green, M. A. and Emery, K. *Progress in Photovoltaics: Research. and Applications*. **2** (1994) 27-34.

29. Kajihara, K., Tanaka, K., Hirao, K., and Soga, N.*Jpn. J. Appl. Phys*. **35**(1996) 6110.

30. Simon, J., and Andre, J. J. *Molecular Semiconductors*, Springer, 1983

31. Ahmad, A. and Collins, R. A. *Thin Solid Films*. **217** (1992) 75-82.

32. Takada, J., Awaji, H., Koshioka, M., Nakajima, A., and Nevin, W. A. *Appl. Phys. Letts*. **61** (1992) 2186.

33. Schneisser, D., Rager, A., Thonke, K., Pilkuhn, M., Frohlich, D., Gauglitz, G., Schafer, M., and Oeilkrug, D. *Synthetic Metals,* **41-43** (1991) 1457-1463.

Chapter

Conclusions and Suggestions for Further Work

The main emphasis of this work was put on obtaining a working dye sensitised photovoltaic (PV) cell from TiO_2 produced by Sol-Gel techniques which promises low cost manufacturing. The work was divided into two main research areas (i) development and investigations of Sol-Gel derived TiO_2 for use in the PV IO heterojunction and (ii) investigations of the spectral, dark and phototvoltaic properties of the IO heterojunction cells.

As a result of the trials on preparations procedures and conditions and experiments carried out on dip coating and heat treatment processes, a robust, chemically and thermally stable TiO_2 film which was largely free from cracks and other surface defects was formed onto a conducting glass support. The films had strong adherence to the substrates following heat treatment.

The factorial investigations have confirmed the effect of previously documented factors such as withdrawal speed, alkoxide concentration and number of coatings on the properties of alkoxide derived Sol-Gel films. However, the results have also shown that these factors undergo significant interaction with particular effects on the thickness obtained during dip coating, with corresponding effects on thickness related properties

such as optical absorption and electrical properties of the coatings. The effects are explained by three main areas (i) the viscosity of the coating solution, (ii) the mechanism and kinetics of the reaction of the alkoxide precursor, and (iii) the surface interactions between the substrate and coating solution.

The presence of these interactions may explain the limited scope of existing theoretical models developed to predict and explain the behaviour of such materials, which has hitherto resulted in new systems being developed by a largely empirical process. An improved understanding of their causes and effects may allow the future development of more flexible predictive models for the behaviour of Sol-Gel systems.

The studies identified that the computational technique of Ray and Hogarth is in good agreement with Tauc in determining E_o and δ the optical band gap and the nature of electronic transitions respectively, the former method having the advantage that δ need not be assumed. The E_o varied from 3.4-3.35eV where $\delta=2$ indicting an indirect allowed transition in 1 layer thick films to E_o ~3.2eV where $\delta=3$ indicating indirect forbidden transition as the number of coating layers increased.

The film refractive index n was in the range 2.73-1.81 and wavelength dependent. Good correlation between the experimental values and the single oscillator model was observed. The conductivity of the films determined from a $Au/TiO_2/InSnO_2$ structure was 4.26×10^{-6}S/cm. Higher conductivities were observed in unheated films due to residual impurities and absorbed water within the pore structure.

Over the temperature range 100-250K low activation energies were observed and indicated that charge carrier hopping is the most likely conduction mechanism in the films.

The spectral response, dark and illuminated J(V) and dark C(V) properties of Au/MPc/TiO$_2$/InSnO$_2$ or F-SnO$_2$ IO heterojunction diodes (where MPc= copper phthalocyanine , chloroaluminium phthalocyanine or lead phthalocyanine) have been determined. Analysis of the results leads to the following conclusions.

The correlation between the short circuit current density of the cell and the absorption spectrum of the MPc films suggests that the major part of the incident light effectively contributes to the photocarrier generation because of the wide band gap of TiO$_2$ and that excited MPc molecules are responsible for photocarrier generation in these devices. All of the organic dyes studied can be successfully used to sensitise Sol-Gel derived TiO$_2$ into the visible region. The low quantum efficiencies are anticipated to be a consequence of the presence of recombination centres at the TiO$_2$/MPc heterointerfaces and the high series resistances of the organic layers. A reduction of the organic layer thickness increased the quantum efficiency.

The MPc/TiO$_2$ junction produces a rectifying contact. Capacitance/voltage measurements confirm that the junction is abrupt. The dark J(V) characteristics were divided into three regimes.

(i) The reverse bias regime in which the device acts as a p-n heterojunction, the ideality factors were 1<m<1.2 and indicated that although diffusion current dominates recombination mechanisms may be present. (ii) The intermediate forward voltage

regime. Within this regime, generally the derived values of m>2 and therefore the presence of a high density of interface states in equilibrium with the inorganic layer is expected to exist. The development of space charge limited currents in the organic films gave rise to variations and potential errors in m. Temperature dependence measurements of $PbPc/TiO_2$ heterojunctions show that the junction currents are a composite of tunnelling and recombination. (iii) High forward regime. All devices deviate from the standard diode equation (3.35) as a consequence of space charge effects in the organic layer, the ideality factors m>>2.

Photovoltaic effects were observed in all the devices studied. The characteristics are highly influenced by changes in ambient conditions, the thickness of organic layers and variations in incident intensity. Prolonged exposure to atmosphere and the high series resistances due to the low conductivity of the organic layers, reduces the overall conversion efficiency. The $V_{oc}(\phi)$ and $J_{sc}(\phi)$ are logarithmically and directly proportional to light intensity respectively. At high intensities the conversion efficiency is limited by space charge and very high R_s, while at low intensities by R_{sh}. The presence of tunnelling current was further supported by the observed V_{oc} / temperature dependence.

It is anticipated that electron-hole pairs are created within the phthalocyanine on application of a light source, however, because of the higher electron affinity of TiO_2 the electrons are injected into the TiO_2 semiconductor, the ionised dye molecule is reduced by electron injection from the top electrode. Therefore in comparison with conventional PV devices the photoeffect (or production of photogenerated carriers) does not take place inside the semiconductor TiO_2 but in the sensitising dye on its surface.

The future potential of the IO heterojunction cell, particularly in competing with commercial Si devices, lies in the improvement of the overall conversion efficiency. The best performance characteristic in these studies was 0.05% for a $Au/PbPc/TiO_2/InSnO_2$ cell compared to ~10-12% for commercial Si cells, hence substantial improvements are necessary. However, the inherent advantages of the successful development of such cells are highly attractive. In comparison to commercial Si the manufacturing technologies are relatively simple, in addition only small quantities of active materials are required to fabricate the thin film cells. This results in dramatically reduced costs. The bulk of the material required to fabricate IO devices is likely to comprise conventional glass, to which the active layers are added by evaporation techniques. The most expensive component of the devices is likely to be the evaporated Au electrode. However, the total thickness of this layer is only of the order of 10-50nm, and thus the high costs are of relatively limited significance.

In summary the TiO_2/MPc heterojunction cell offers an alternative approach for PV devices. The overwhelming advantages are the low cost materials and manufacturing technologies. However, optimisation of these devices is now required. For achieving higher efficiencies the following routes are suggested.

The use of dyes with broader ranges in absorption therefore utilising more of the solar spectrum, higher current densities should be obtained.

The minimisation of losses through recombination via defects in the form of surface, and bulk imperfections. by the use of well purified materials and surface treatment of the inorganic films.

An in depth assessment of the effects of film thickness, in particular the organic layer as a route to reducing the series resistance's induced by it.

Increasing the conductivity of the inorganic layer. For example by the introduction of dopants into the Sol during the manufacturing process.

Further analysis of the temperature dependence of dark and illuminated J(V) characteristics needs to be carried out for a greater understanding of the junction transport phenomena.

Further investigations into the effects of Sol-Gel parameters on the device performance are required. In particular emphasis should be placed on a detailed quantitative assessment of the effects on efficiency of the porosity of the TiO_2 film. In these studies a large fraction of the MPc molecules had no direct contact with the TiO_2 film, therefore electron transfer from these molecules into the conduction band of TiO_2 can occur only with difficulty or not at all. An increase in the direct contact of MPc molecules with the TiO_2 film is required to increase the quantum efficiency of these devices. Therefore direct measurements of the light harvesting efficiency as a function of the TiO_2 porosity would be of great benefit in the cell optimisation process.

Alternative constructional options include the formation of a TiO_2/phthalocyanine matrix, in which the dye is embedded within the TiO_2 forming a novel optical material with a very high interfacial area and hence potential light harvesting capabilities. Unfortunately, little information on the effectiveness of introducing dye molecules into Sol-gel networks exists. An additional option is the formation of a multilayer device consisting of a wide band gap inorganic transporting material such as a TiO_2 layer in conjunction with multilayers of thin dye layers. The dyes would be sensitive to complementary regions of the solar spectrum and an electron affinity gradient between the layers would ensure an effective charge transfer.

APPENDIX A : SWANEPOEL PROCEDURE

The tables contained within this appendix refer to section 6.6.3 and 6.7.4. They contain values of T_M, T_m, the refractive indicies, n_s, n_1, n_2, derived thicknesses, d_1, d_2, and the values of m_o, and m as a function of wavelength (λ). The average values determined for thickness d_{1av} and the second more accurate estimate d_{2av} are also shown.

All are for TiO_2 Sol-Gel films prepared from a molar ratio of Acetic acid:TIP of 4.16:1 and concentration of TIP in ethanol 12.6%., the films were annealed to 500°C for 5 hours.

The accuracy to which n and d can be determined depends on the accuracy to which λ, T_M, and T_m can be measured. The scale used for λ yields an accuracy of +/- 5nm and the maximum accuracy with which T_M, and T_m could be determined was +/- 5% (+/- 0.005). This yields an overall thickness accuracy of +/- 2%.

The sample references indicate the withdrawal rate, denoted 'A' and 'B' for 100mm/min and 250 mm/min. respectively and the number of coating layers denoted 5,6,7 or 8. Repeat measurements are also shown.

Sample	λ (nm)	T_M	T_m	n_s	n_1	d_1 (nm)	m_o	m	d_2 (nm)	n_2
A5	358	0.816	0.496	1.522	2.799	147	2.61	2.5	160	2.73
	397	0.877	0.627	1.481	2.342	186	1.97	2	170	2.43
	487	0.972	0.727	1.447	2.156	-	1.48	1.5	169	2.23
	610	0.993	0.806	1.422	1.955	-	1.07	1	156	1.86
						d_{1av}=167			d_{2av}=164	
A5 Repeat	370	0.867	0.557	1.511	2.613	172	2.6	2.5	177	2.63
	415	0.917	0.657	1.473	2.303	196	2.04	2	180	2.36
	510	0.972	0.737	1.440	2.122	-	1.53	1.5	180	2.17
	645	0.977	0.802	1.423	1.938	-	1.11	1	166	1.83
						d_{1av}=184			d_{2av}=176	
B5	394	0.906	0.638	1.486	2.728	200	4.73	4.5	325	2.66
	430	0.917	0.697	1.465	2.17	430	3.45	3.5	347	2.26
	487	0.917	0.697	1.447	2.153	395	3.02	3	339	2.19
	570	0.935	0.682	1.43	2.213	-	2.66	2.5	322	2.14
	715	0.968	0.681	1.418	2.255	-	2.16	2	317	2.15
						d_{1av}=342			d_{2av}=330	

Sample	λ (nm)	T_M	T_m	n_s	n_1	d_1 (nm)	m_o	m	d_2 (nm)	n_2
B5	350	0.607	0.447	1.546	2.584	385	5.17	5	339	2.54
	395	0.932	0.637	1.485	2.403	298	4.26	4.5	370	2.58
Repeat	488	0.948	0.716	1.447	2.149	366	3.08	3	341	2.12
	710	0.971	0.718	1.421	2.156	-	2.13	2	329	2.06
						d_{1av}=350			d_{2av}=345	
A6	360	0.812	0.577	1.522	2.446	280	4.2	4	294	2.39
	383	0.886	0.698	1.495	2.136	338	3.45	3.5	314	2.22
	433	0.987	0.737	1.466	2.17	291	3.1	3	299	2.15
	500	0.988	0.776	1.447	2.048	325	2.53	2.5	305	2.07
	605	0.971	0.778	1.425	1.994	-	2.04	2	303	2.01
	785	0.967	0.767	1.414	2.007	-	1.58	1.5	293	1.95
						d_{1av}=309			d_{2av}=302	

Sample	λ (nm)	T_M	T_m	n_s	n_1	d_1 (nm)	m_o	m	d_2 (nm)	n_2
A6	388	0.962	0.707	1.493	2.242	236	2.84	3	260	2.28
	460	0.967	0.722	1.453	2.168	255	2.32	2.5	265	2.55
Repeat	560	0.952	0.747	1.43	2.051	-	1.8	2	273	2.196
	715	0.948	0.771	1.418	1.966	-	1.35	1.5	273	2.103
						$d_{1av}=246$			$d_{2av}=268$	
B6	409	0.787	0.551	1.473	2.453	242	4.4	4.5	375	2.51
	496	0.921	0.767	1.444	1.948	491	2.88	3	382	2.03
	666	0.976	0.802	1.424	1.937	-	2.13	2	345	1.81
						$d_{1av}=367$			$d_{2av}=367$	
B6	385	0.816	0.558	1.496	2.504	267	4.92	5	384	2.62
Repeat	414	0.847	0.627	1.475	2.281	323	4.17	4	363	2.25
	457	0.892	0.697	1.457	2.116	430	3.5	3.5	378	2.18
	505	0.936	0.758	1.44	2	490	2.99	3	379	2.06
	580	0.978	0.776	1.424	2.011	-	2.62	2.5	361	1.97
	675	0.982	0.787	1.42	1.984	-	2.22	2	340	1.84
						$d_{1av}=378$			$d_{2av}=367$	

Sample	λ (nm)	T_M	T_m	n_s	n_1	d_1 (nm)	m_o	m	d_2 (nm)	n_2
A7	350	0.642	0.482	1.546	2.49	409	5.04	5	351	2.53
	395	0.867	0.627	1.485	2.328	350	4.17	4	339	2.29
	498	0.958	0.696	1.446	2.223	304	3.16	3	336	2.16
	705	0.968	0.776	1.418	1.988	-	1.996	2	355	2.046
						d_{1av}=354			d_{2av}=345	
A7 Repeat	368	0.787	0.517	1.503	2.631	-	4.747	4.5	315	2.58
	400	0.856	0.588	1.476	2.441	-	4.05	4	328	2.5
	463	0.962	0.697	1.453	2.233	283	3.2	3	311	2.17
	530	0.968	0.786	1.447	1.987	380	2.49	2.5	333	2.07
	640	0.972	0.792	1.422	1.955	-	2.02	2	327	1.997
	830	0.972	0.767	1.418	2.019	-	1.6	1.5	308	1.94
						d_{1av}=332			d_{2av}=320	

Sample	λ (nm)	T_M	T_m	n_s	n_1	d_1 (nm)	m_o	m	d_2 (nm)	n_2
B7	375	0.717	0.507	1.5	2.522	327	5.8	6	446	2.642
	425	0.883	0.667	1.472	2.208	469	4.48	4.5	433	2.246
	495	0.877	0.707	1.446	2.044	497	3.56	3.5	424	2.034
	670	0.947	0.727	1.422	2.092	-	2.69	2.5	400	1.967
						d_{1av}=431			d_{2av}=426	
B7 Repeat	374	0.627	0.467	1.504	2.487	437	5.88	6	451	2.47
	422	0.872	0.627	1.47	2.323	464	4.87	5	454	2.321
	495	0.888	0.668	1.446	2.192	425	3.91	4	452	2.178
	665	0.956	0.701	1.422	2.163	-	2.88	3	461	2.195
						d_{1av}=442			d_{2av}=455	
A8	375	0.777	0.547	1.5	2.476	327	5.02	5	379	2.35
	395	0.857	0.647	1.485	2.239	351	4.31	4.5	397	2.22
	437	0.966	0.708	1.465	2.218	346	3.86	4	394	2.19
	483	0.975	0.767	1.446	2.05	422	3.25	3.5	412	2.11
	552	0.98	0.782	1.432	2.005	456	2.76	3	413	2.07
	645	0.982	0.792	1.423	1.974	-	2.33	2.5	408	2.02
	780	0.986	0.792	1.419	1.977	-	1.93	2	395	1.95
						d_{1av}=380			d_{2av}=399	

Sample	λ (nm)	T_M	T_m	n_s	n_1	d_1 (nm)	m_o	m	d_2 (nm)	n_2
A8 Repeat	366	0.737	0.547	1.506	2.39	375	4.98	5	383	2.33
	385	0.848	0.646	1.496	2.235	361	4.42	4.5	388	2.21
	425	0.956	0.708	1.472	2.209	332	3.96	4	385	2.17
	468	0.967	0.757	1.452	2.069	391	3.37	3.5	396	2.09
	535	0.967	0.787	1.439	1.975	448	2.81	3	406	2.05
	620	0.982	0.802	1.424	1.948	-	2.39	2.5	398	1.98
	755	0.988	0.806	1.419	1.944	-	1.96	2	388	1.93
						$d_{1av}=381$			$d_{2av}=392$	
B8	397	0.742	0.527	1.48	2.467	342	6.29	6.5	523	2.51
	427	0.832	0.602	1.469	2.337	403	5.54	5.5	502	2.28
	453	0.852	0.662	1.459	2.153	622	4.81	5	526	2.19
	492	0.863	0.686	1.445	2.082	676	4.28	4.5	532	2.15
	533	0.918	0.711	1.44	2.105	488	4	4	506	2.07
	595	0.968	0.746	1.427	2.078	506	3.53	3.5	501	2.02
	670	0.967	0.787	1.422	1.96	-	2.96	3	513	1.95
						$d_{1av}=506$			$d_{2av}=515$	

Sample	λ (nm)	T_M	T_m	n_s	n_1	d_1 (nm)	m_o	m	d_2 (nm)	n_2
	380	0.646	0.468	1.502	2.538	402	6.67	6.5	487	2.48
B8	397	0.727	0.527	1.48	2.431	477	5.84	6	490	2.39
Repeat	426	0.828	0.606	1.471	2.316	420	5.43	5.5	506	2.35
	453	0.859	0.624	1.459	2.299	435	4.92	5	493	2.28
	485	0.868	0.696	1.446	2.06	591	4.12	4	471	1.95
	532	0.917	0.717	1.443	2.088	497	3.92	4	510	2.14
	595	0.967	0.765	1.427	2.024	571	3.39	3.5	514	2.09
	670	0.966	0.788	1.422	1.955	-	2.91	3	514	2.02
	767	0.957	0.787	1.417	1.937	-	2.52	2.5	495	1.93
						$d_{1av}=485$			$d_{2av}=498$	

APPENDIX B: ANOVAS AND TABLES DERIVED FROM YATES ANALYSIS

1. Overall Coating Thickness
   Table 1. Yates Analysis
   Table 2. ANOVA

2. Average Coating Layer Thickness
   Table 3. Yates Analysis
   Table 4. ANOVA

3. Measured Absorption at 4eV
   Table 5. Yates Analysis
   Table 6. ANOVA

4. Calculated Absorption Coefficient ($10^5 cm^{-1}$)
   Table 7. Yates Analysis
   Table 8. ANOVA

Factorial Experiment.
Yates Analysis

Results for: Overall Coating Thickness

a = withdrawal rate, b = Acetic Acid :T.I.P., c = No. of Coatings, d = Conc. of T.I.P.

Treatment	First Replicate	Second Replicate	Combined Total	(1)	(2)	(3)	(4)		Mean factorial effect ((col.4)/2^(k-1))	degrees of freedom	(effect) Sum of squares ((col.4)^2/(R*(2^k)))	(effect) mean squares	Square of first replicate values	Square of second replicate values
1	0.0700	0.0800	0.1500	0.2900	0.5400	2.0100	5.1000	= T					0.0049	0.0064
a	0.0700	0.0700	0.1400	0.2500	1.4700	3.0900	0.7800	= [A]	0.0488	1	0.0190	0.0190	0.0049	0.0049
b	0.0700	0.0500	0.1200	0.5600	0.7000	0.1500	0.1000	= [B]	0.0062	1	0.0003	0.0003	0.0049	0.0025
ab	0.0700	0.0600	0.1300	0.9100	2.3900	0.6300	0.4200	= [AB]	0.0263	1	0.0055	0.0055	0.0049	0.0036
c	0.1400	0.1400	0.2800	0.3900	0.0000	0.3100	2.6200	= [C]	0.1638	1	0.2145	0.2145	0.0196	0.0196
ac	0.1500	0.1300	0.2800	0.3100	0.1500	-0.2100	0.6600	= [AC]	0.0413	1	0.0136	0.0136	0.0225	0.0169
bc	0.2000	0.1800	0.3800	1.2600	0.0600	0.1700	0.3400	= [BC]	0.0213	1	0.0036	0.0036	0.0400	0.0324
abc	0.2900	0.2400	0.5300	1.1300	0.5700	0.2500	0.3800	= [ABC]	0.0238	1	0.0045	0.0045	0.0841	0.0576
d	0.0900	0.0900	0.1800	-0.0100	-0.0400	0.9300	1.0800	= [D]	0.0675	1	0.0365	0.0365	0.0081	0.0081
ad	0.1000	0.1100	0.2100	0.0100	0.3500	1.6900	0.4800	= [AD]	0.0300	1	0.0072	0.0072	0.0100	0.0121
bd	0.0700	0.0700	0.1400	0.0000	-0.0800	0.1500	-0.5200	= [BD]	-0.0325	1	0.0085	0.0085	0.0049	0.0049
abd	0.1000	0.0700	0.1700	0.1500	-0.1300	0.5100	0.0800	[ABD]	0.0050	1	0.0002	0.0002	0.0100	0.0049
cd	0.2700	0.2800	0.5500	0.0300	0.0200	0.3900	0.7600	= [CD]	0.0480	1	0.0181	0.0181	0.0729	0.0784
acd	0.3600	0.3500	0.7100	0.0300	0.1500	-0.0500	0.3600	= [ACD]	0.0225	1	0.0041	0.0041	0.1296	0.1225
bcd	0.1800	0.1800	0.3600	0.1600	0.0000	0.1300	-0.4400	= [BCD]	-0.0275	1	0.0061	0.0061	0.0324	0.0324
abcd	0.3800	0.3900	0.7700	0.4100	0.2500	0.2500	0.1200	[ABCD]	0.0075	1	0.0005	0.0005	0.1444	0.1521
						Total (T) 5.1000				Total Effect S.S.=	0.3420		0.5981	0.5593

no. of treatments (t) =   16 <<<<<<<< ENTER VALUE
no of replicates (r) =   2 <<<<<<<< ENTER VALUE
no of measurements (N) = r x t =   32
Correction Factor (CF) = (T)^2/N =   0.8128
No of Factors (k) i.e 2^k design =   4 <<<<<<< ENTER VALUE
Calculated sums of squares of individual data values (I.S.S.) =   1.1574
TOTAL SUMS OF SQUARES (I.S.S. - CF)=   0.3446
CALCULATED RESIDUAL SUM OF SQUARES = TOTAL S.S. - TOTAL EFFECT S.S. =   0.0026

Total number of degrees of freedom (txr)-1) =   31
Degrees of freedom for all treatments (t-1) =   15
degrees of freedom for residual t((r-1)) =   16

Table 1

Analysis of variance of data: Overall Coating Thickness

SOURCE OF VARIATION	degrees of freedom.	sum of squares	mean square	(Pooled error estimate) MEAN SQUARE/ ERROR MEAN SQUARE (for f test (5,1) comparison)	Significance	(Residual error estimate) MEAN SQUARE/ ERROR MEAN SQUARE (for f test (16,1) comparison).	Significance
Withdrawal rate (A)	1	0.0190	0.0190	6.2285	*	117.0000	***
Acetic acid:TIP (B)	1	0.0003	0.0003	0.1024	N/S	1.9231	N/S
No. of Coatings (C)	1	0.2145	0.2145	70.2744	***	########	***
Conc. of T.I.P. solution.	1	0.0365	0.0365	11.9410	**	224.3077	***
Interactions: (2nd order)							
AB	1	0.0055	0.0055	1.8059	N/S	33.9231	***
AC	1	0.0136	0.0136	4.4595	*	83.7692	***
AD	1	0.0072	0.0072	2.3587	N/S	44.3077	***
BC	1	0.0036	0.0036	1.1835	N/S	22.2308	***
BD	1	0.0085	0.0085	2.7682	N/S	52.0000	***
CD	1	0.0181	0.0181	5.9132	*	111.0769	***
(3rd order)							
ABC	1	0.0045	0.0045	1.4783	—	27.7692	***
ABD	1	0.0002	0.0002	0.0655	—	1.2308	N/S
ACD	1	0.0041	0.0041	1.3268	—	24.9231	***
BCD	1	0.0061	0.0061	1.9820	—	37.2308	***
(4th order)							
ABCD	1	0.0005	0.0005	0.1474	—	2.7692	N/S
Error terms:							
Residual	16	0.0026	0.0002	----			
(pooled 3rd and 4th order terms)	5	0.0153	0.0031	----			

F test values:

	(5 & 1 degrees of freedom)	(16 & 1 degrees of freedom)
f > 1%	16.3000	8.5300
f > 5%	6.6100	4.4900
f > 10%	4.0600 estimate	3.000

(5 & 1 degrees of freedom)
Indicated as *** in results.
Indicated as ** in results.
Indicated as * in results.

(16 & 1 degrees of freedom)
Indicated as *** in results.
Indicated as ** in results.
Indicated as * in results.

Table 2

Factorial Experiment.
Yates Analysis

Results for: Average Coating Layer Thickness

a = withdrawal rate, b = Acetic Acid :T.I.P., c = No. of Coatings, d = Conc. of T.I.P.

Treatment	First Replicate	Second Replicate	Combined Total	(1)	(2)	(3)	(4)		Mean factorial effect ((col.4)/2^(k-1))	degrees of freedom	(effect) Sum of squares {((col.4)^2/(R*(2^k)))}	(effect) mean squares	Square of first replicate values	Square of second replicate values
1	0.0500	0.0600	0.1100	0.2100	0.3800	0.7075	1.8050	= T					0.0025	0.0036
a	0.0500	0.0500	0.1000	0.1700	0.3275	1.0975	0.2400	= [A]	0.0150	1	0.0018	0.0018	0.0025	0.0025
b	0.0500	0.0300	0.0800	0.1200	0.5400	0.0375	-0.0650	= [B]	-0.0041	1	0.0001	0.0001	0.0025	0.0009
ab	0.0500	0.0400	0.0900	0.2075	0.5575	0.2025	0.1200	= [AB]	0.0075	1	0.0005	0.0005	0.0025	0.0016
c	0.0300	0.0300	0.0600	0.3100	0.0000	0.0475	-0.0350	= [C]	-0.0022	1	0.0000	0.0000	0.0009	0.0009
ac	0.0325	0.0275	0.0600	0.2300	0.0375	-0.1125	0.1200	= [AC]	0.0075	1	0.0005	0.0005	0.0011	0.0008
bc	0.0450	0.0400	0.0850	0.2950	0.0600	0.0575	0.1750	= [BC]	0.0109	1	0.0010	0.0010	0.0020	0.0016
abc	0.0675	0.0550	0.1225	0.2625	0.1425	0.0625	0.0800	= [ABC]	0.0050	1	0.0002	0.0002	0.0046	0.0030
d	0.0700	0.0700	0.1400	-0.0100	-0.0400	-0.0525	0.3900	= [D]	0.0244	1	0.0048	0.0048	0.0049	0.0049
ad	0.0800	0.0900	0.1700	0.0100	0.0875	0.0175	0.1650	= [AD]	0.0103	1	0.0009	0.0009	0.0064	0.0081
bd	0.0500	0.0500	0.1000	0.0000	-0.0800	0.0375	-0.1600	= [BD]	-0.0100	1	0.0008	0.0008	0.0025	0.0025
abd	0.0800	0.0500	0.1300	0.0375	-0.0325	0.0825	0.0050	= [ABD]	0.0003	1	0.0000	0.0000	0.0064	0.0025
cd	0.0625	0.0650	0.1275	0.0300	0.0200	0.1275	0.0700	= [CD]	0.0044	1	0.0002	0.0002	0.0039	0.0042
acd	0.0850	0.0825	0.1675	0.0300	0.0375	0.0475	0.0450	= [ACD]	0.0028	1	0.0001	0.0001	0.0072	0.0068
bcd	0.0400	0.0400	0.0800	0.0400	0.0000	0.0175	-0.0800	= [BCD]	-0.0050	1	0.0002	0.0002	0.0016	0.0016
abcd	0.0900	0.0925	0.1825	0.1025	0.0625	0.0625	0.0450	[ABCD]	0.0028	1	0.0001	0.0001	0.0081	0.0086
			Total (T) 1.8050					Total Effect S.S.=			0.0109		0.0596	0.0541

no. of treatments (t) = 16 <<<<<<<< ENTER VALUE
no of replicates (r) = 2 <<<<<<<<< ENTER VALUE
no of measurements (N) = r x t = 32
Correction Factor (CF) = (T)^2/N = 0.1018
No of Factors (k) i.e 2^k design 4 <<<<<<<< ENTER VALUE
Calculated sums of squares of individual data values (I.S.S.) = 0.1136
TOTAL SUMS OF SQUARES (I.S.S. - CF)= 0.0118
CALCULATED RESIDUAL SUM OF SQUARES = TOTAL S.S. - TOTAL EFFECT S.S. = 0.0009

Total number of degrees of freedom ((t x r)-1) = 31
Degrees of freedom for all treatments (t-1) = 15
degrees of freedom for residual (t(r-1)) = 16

Table 3

Analysis of variance of data: Average Coating Layer Thickness

SOURCE OF VARIATION	degrees of freedom.	sum of squares	mean square	(Pooled error estimate) MEAN SQUARE/ ERROR MEAN SQUARE (for f test (5,1) comparison)	Significance	(Residual error estimate) MEAN SQUARE/ ERROR MEAN SQUARE (for f test (16,1) comparison).	Significance
Withdrawal rate (A)	1	0.0018	0.0018	17.0667	***	31.5616	***
Acetic acid:TIP (B)	1	0.0001	0.0001	1.2519	N/S	2.3151	N/S
No. of Coatings (C)	1	0.0000	0.0000	0.3630	N/S	0.6712	N/S
Conc. of T.I.P. solution.	1	0.0048	0.0048	45.0667	***	83.3425	***
Interactions:							
(2nd order)							
AB	1	0.0005	0.0005	4.2667	*	7.8904	**
AC	1	0.0005	0.0005	4.2667	*	7.8904	**
AD	1	0.0009	0.0009	8.0667	**	14.9178	***
BC	1	0.0010	0.0010	9.0741	**	16.7808	***
BD	1	0.0008	0.0008	7.5852	**	14.0274	***
CD	1	0.0002	0.0002	1.4519	N/S	2.6849	N/S
(3rd order)							
ABC	1	0.0002	0.0002	1.8963	—	3.5068	N/S
ABD	1	0.0000	0.0000	0.0074	—	0.0137	N/S
ACD	1	0.0001	0.0001	0.6000	—	1.1096	N/S
BCD	1	0.0002	0.0002	1.8963	—	3.5068	N/S
(4th order)							
ABCD	1	0.0001	0.0001	0.6000	—	1.1096	N/S
Error terms:							
Residual	16	0.0009	0.0001	----			
(pooled 3rd and 4th order terms)	5	0.0005	0.0001	----			

F test values:

(5 & 1 degrees of freedom)
f > 1%   16.3000   Indicated as *** in results.
f > 5%   6.6100   Indicated as ** in results.
f > 10%   4.0600   Indicated as * in results.

(16 & 1 degrees of freedom)
f > 1%   8.5300   Indicated as *** in results.
f > 5%   4.4900   Indicated as ** in results.
f > 10%   3.000   estimate   Indicated as * in results.

Table 4

Factorial Experiment.
Yates Analysis

Results for: Measured Absorption at 4eV

a = withdrawal speed, b = Acetic Acid :T.I.P., c = No. of Coatings, d = Conc. of T.I.P.

treatment	First Replicate	Second Replicate	combined total	(1)	(2)	(3)	(4)		Mean factorial effect {(col.4)/ 2^(k-1)}	degrees of freedom	(effect) Sum of squares {(col.4)^2/ (R*(2^k))}	(effect) mean squares	Square of first replicate values	Square of second replicate values
1	0.578	0.542	1.120	2.334	4.490	13.844	38.009	= T					0.334	0.294
a	0.599	0.615	1.214	2.156	9.354	24.165	8.513	= [A]	0.532	1	2.265	2.265	0.359	0.378
b	0.521	0.547	1.068	4.910	5.895	2.200	-2.237	= [B]	-0.140	1	0.156	0.156	0.271	0.299
ab	0.546	0.542	1.088	4.444	18.270	6.313	-1.217	= [AB]	-0.076	1	0.046	0.046	0.298	0.294
c	0.900	0.900	1.800	3.089	0.114	-0.644	17.239	= [C]	1.077	1	9.287	9.287	0.810	0.810
ac	1.540	1.570	3.110	2.806	2.086	-1.593	5.159	= [AC]	0.322	1	0.832	0.832	2.372	2.465
bc	0.921	0.913	1.834	9.790	1.563	-0.608	-1.315	= [BC]	-0.082	1	0.054	0.054	0.848	0.834
abc	1.310	1.300	2.610	8.480	4.750	-0.609	-0.151	[ABC]	-0.009	1	0.001	0.001	1.716	1.690
d	0.531	0.508	1.039	0.094	-0.178	4.864	10.321	= [D]	0.645	1	3.329	3.329	0.282	0.258
ad	1.110	0.940	2.050	0.020	-0.466	12.375	4.113	= [AD]	0.257	1	0.529	0.529	1.232	0.884
bd	0.584	0.543	1.127	1.310	-0.283	1.972	-0.949	= [BD]	-0.059	1	0.028	0.028	0.341	0.295
abd	0.732	0.947	1.679	0.776	-1.310	3.187	-0.001	[ABD]	0.000	1	0.000	0.000	0.536	0.897
cd	1.980	1.690	3.670	1.011	-0.074	-0.288	7.511	= [CD]	0.469	1	1.763	1.763	3.920	2.856
acd	3.300	2.820	6.120	0.552	-0.534	-1.027	1.215	[ACD]	0.076	1	0.046	0.046	10.890	7.952
bcd	1.510	1.580	3.090	2.450	-0.459	-0.460	-0.739	[BCD]	-0.046	1	0.017	0.017	2.280	2.496
abcd	2.560	2.830	5.390	2.300	-0.150	0.309	0.769	[ABCD]	0.048	1	0.018	0.018	6.554	8.009
			Total (T) 38.009								Total Effect S.S. = 18.371		33.043	30.711

no. of treatments (t) =   16 <<<<<<<< ENTER VALUE
no of replicates (r) =   2 <<<<<<<< ENTER VALUE
no of measurements (N) = r x t =   32
Correction Factor (CF) = (T)^2/N =   45.146
No of Factors (k) i.e 2^k design   4 <<<<<<<< ENTER VALUE
Calculated sums of squares of individual data values (I.S.S) =   63.754
TOTAL SUMS OF SQUARES (I.S.S.- CF)=   18.608
CALCULATED RESIDUAL SUM OF SQUARES = TOTAL S.S. - TOTAL EFFECT S.S. =   0.236
Total number of degrees of freedom ((txr)-1) =   31
Degrees of freedom for all treatments (t-1) =   15
degrees of freedom for residual (t(r-1)) =   16

Table 5

Analysis of variance of data

SOURCE OF VARIATION	degrees of freedom.	sum of squares	mean square	(Pooled error estimate) MEAN SQUARE/ ERROR MEAN SQUARE (for f test (5,1) comparison)	Significance	(Residual error estimate) MEAN SQUARE/ ERROR MEAN SQUARE (for f test (16,1) comparison.	Significance
Withdrawal rate (A)	1	2.265	2.265	137.438	***	153.234	***
Acetic acid:TIP (B)	1	0.156	0.156	9.490	**	10.581	***
No. of Coatings (C)	1	9.287	9.287	563.592	***	628.370	***
Conc. of T.I.P. solution.	1	3.329	3.329	202.015	***	225.234	***
Interactions: (2nd order)							
AB	1	0.046	0.046	2.809	N/S	3.132	*
AC	1	0.832	0.832	50.474	***	56.276	***
AD	1	0.529	0.529	32.082	***	35.769	***
BC	1	0.054	0.054	3.279	N/S	3.656	*
BD	1	0.028	0.028	1.708	N/S	1.904	N/S
CD	1	1.763	1.763	106.988	***	119.285	***
(3rd order)							
ABC	1	0.001	0.001	0.043	—	0.048	N/S
ABD	1	0.000	0.000	0.000	—	0.000	N/S
ACD	1	0.046	0.046	2.800	—	3.121	*
BCD	1	0.017	0.017	1.036	—	1.155	N/S
(4th order)							
ABCD	1	0.018	0.018	1.121	—	1.250	N/S
Error terms:							
Residual	16	0.236	0.015	-----			
(pooled 3rd and 4th order terms)	5	0.082	0.016	-----			

F test values:

(5 & 1 degrees of freedom)		(16 & 1 degrees of freedom)	
f > 1%	16.300	f > 1%	8.530
f > 5%	6.610	f > 5%	4.490
f > 10%	4.060	f > 10%	3.0???

Indicated as *** in results.
Indicated as ** in results.
Indicated as * in results.

Table 6

Factorial Experiment.
Yates Analysis

Results for: Calculated Absorption Coefficient ($10^5 cm^{-1}$)

a = withdrawal speed, b = Acetic Acid :T.I.P., c = No. of Coatings, d = Conc. of T.I.P.

treatment	First Replicate	Second Replicate	combined total	(1)	(2)	(3)	(4)		Mean factorial effect $\{(col.4)/2^{(k-1)}\}$	degrees of freedom	(effect) Sum of squares $\{(col.4)^2/(R*(2^k))\}$	(effect) mean squares	Square of first replicate values	Square of second replicate values
1	1.180	1.165	2.345	5.195	11.915	19.195	37.475	= T					1.392	1.357
a	1.220	1.630	2.850	6.720	7.280	18.280	2.855	= [A]	0.178	1	0.255	0.255	1.488	2.657
b	1.060	2.680	3.740	4.780	10.595	1.045	1.035	= [B]	0.065	1	0.033	0.033	1.124	7.182
ab	1.115	1.865	2.980	2.500	7.685	1.810	-3.745	= [AB]	-0.234	1	0.438	0.438	1.243	3.478
c	0.820	0.915	1.735	4.490	-0.255	-0.755	-7.545	= [C]	-0.472	1	1.779	1.779	0.672	0.837
ac	1.300	1.745	3.045	6.105	1.300	1.790	-0.445	= [AC]	-0.028	1	0.006	0.006	1.690	3.045
bc	0.570	0.685	1.255	3.755	1.905	-2.585	-5.245	= [BC]	-0.328	1	0.860	0.860	0.325	0.469
abc	0.545	0.700	1.245	3.930	-0.095	-1.160	-0.825	[ABC]	-0.052	1	0.021	0.021	0.297	0.490
d	0.800	0.920	1.720	0.505	1.525	-4.635	-0.915	= [D]	-0.057	1	0.026	0.026	0.640	0.846
ad	1.475	1.295	2.770	-0.760	-2.280	-2.910	0.765	= [AD]	0.048	1	0.018	0.018	2.176	1.677
bd	1.190	1.435	2.625	1.310	1.615	1.555	2.545	= [BD]	0.159	1	0.202	0.202	1.416	2.059
abd	0.975	2.505	3.480	-0.010	0.175	-2.000	1.425	[ABD]	0.089	1	0.063	0.063	0.951	6.275
cd	0.890	0.770	1.660	1.050	-1.265	-3.805	1.725	= [CD]	0.108	1	0.093	0.093	0.792	0.593
acd	1.095	1.000	2.095	0.855	-1.320	-1.440	-3.555	[ACD]	-0.222	1	0.395	0.395	1.199	1.000
bcd	1.045	1.185	2.230	0.435	-0.195	-0.055	2.365	[BCD]	0.148	1	0.175	0.175	1.092	1.404
abcd	0.805	0.895	1.700	-0.530	-0.965	-0.770	-0.715	[ABCD]	-0.045	1	0.016	0.016	0.648	0.801
			Total (T) 37.475								Total Effect S.S. = 4.382		17.145	34.172

no. of treatments (t) = 16 <<<<<<< ENTER VALUE
no of replicates (r) = 2 <<<<<<< ENTER VALUE
no of measurements (N) = r x t = 32
Correction Factor (CF) = (T)^2/N = 43.887
No of Factors (K) i.e 2^k design 4 <<<<<<< ENTER VALUE
Calculated sums of squares of individual data values (I.S.S.) = 51.318
TOTAL SUMS OF SQUARES (I.S.S.- CF)= 7.431
CALCULATED RESIDUAL SUM OF SQUARES = TOTAL S.S. - TOTAL EFFECT S.S. = 3.049
Total number of degrees of freedom ((txr)-1) = 31
Degrees of freedom for all treatments (t-1) = 15
degrees of freedom for residual (t(r-1)) = 16

Table 7

Analysis of variance of data

SOURCE OF VARIATION	degrees of freedom.	sum of squares	mean square	(Pooled error estimate) MEAN SQUARE/ ERROR MEAN SQUARE (for f test (5,1) comparison)	Significance	(Residual error estimate) MEAN SQUARE/ ERROR MEAN SQUARE (for f test (16,1) comparison.	Significance
Withdrawal rate (A)	1	0.255	0.255	1.900	N/S	1.337	N/S
Acetic acid:TIP (B)	1	0.033	0.033	0.250	N/S	0.176	N/S
No. of Coatings (C)	1	1.779	1.779	13.267	**	9.335	***
Conc. of T.I.P. solution.	1	0.026	0.026	0.195	N/S	0.137	N/S
Interactions:							
(2nd order)							
AB	1	0.438	0.438	3.269	N/S	2.300	N/S
AC	1	0.006	0.006	0.046	N/S	0.032	N/S
AD	1	0.018	0.018	0.136	N/S	0.096	N/S
BC	1	0.860	0.860	6.411	*	4.511	**
BD	1	0.202	0.202	1.510	N/S	1.062	N/S
CD	1	0.093	0.093	0.693	N/S	0.488	N/S
(3rd order)							
ABC	1	0.021	0.021	0.159	—	0.112	N/S
ABD	1	0.063	0.063	0.473	—	0.333	N/S
ACD	1	0.395	0.395	2.945	—	2.072	N/S
BCD	1	0.175	0.175	1.304	—	0.917	N/S
(4th order)							
ABCD	1	0.016	0.016	0.119	—	0.084	N/S
Error terms:							
Residual	16	3.049	0.191	-----			
(pooled 3rd and 4th order terms)	5	0.670	0.134	-----			

F test values:

(5 & 1 degrees of freedom)
f > 1 %   16.300   Indicated as *** in results.
f > 5 %   6.610   Indicated as ** in results.
f > 10 %   4.060   Indicated as * in results.

F test values
(16 & 1 degrees of freedom)
f > 1 %   8.530   Indicated as *** in results.
f > 5 %   4.490   Indicated as ** in results.
f > 10 %   3.0???   Indicated as * in results.

Table 8

APPENDIX C: IO HETEROJUNCTION PARAMETERS

1. Spectral Response Characteristics

2. Solar Cell Characteristics

3. Temperature Dependent Characteristics for $Au/PcPc/TiO_2/InSnO_2$ cell.

Organic layer and ~thickness	Base electrode	Ambient	λ (nm) maxima	J_{sc} ($\mu A/cm^2$)	Z % max
ClAlPc(500nm)	InSnO$_2$	Air	380	0.027	0.28
"	"	Vacuum	"	0.029	0.3
"	"	Air	700	0.038	0.21
"	F-SnO$_2$	Vacuum	"	0.133	0.74
"	"	"	"	0.087	0.48
"	"	"	345	0.07	0.79
CuPc(500nm)	InSnO$_2$	Air	350	0.039	0.43
"	"	N$_2$	"	0.031	0.34
"	"	Air	590	0.043	0.28
"	"	N$_2$	"	0.034	0.22
"	"	Air	700	0.036	0.2
"	"	N$_2$	"	0.027	0.15
PbPc(500nm)	"	Air	360	0.031	0.42
"	"	"	680	0.072	0.41
PbPc(100nm)	"	"	665	0.067	0.4
"	"	"	335	0.059	0.68
"	"	Vacuum	375	0.14	1.45
"	"	"	680	0.363	2.07

Summary of results obtained for J_{sc} and Z% for the IO heterojunctions from spectral response measurements.

Dye and Thickness (nm)	Substrate	Ambient	Light Intensity mW/cm^2	J_{sc} x 10^{-7} (A/cm^2)	V_{oc} (v)	FF	$\eta\%$ (x 10^{-2})
ClAlPc(500)	F-SnO$_2$	Vacuum	0.2	0.48	0.248	0.15	0.09
"	"	"	0.16	0.43	0.238	0.155	0.099
"	InSnO$_2$	"	1.6	3.58	0.492	0.129	0.142
"	"	"	1.12	3.64	0.479	0.304	0.473
"	"	"	0.56	2.19	0.45	0.098	0.172
"	"	"	0.16	1.82	0.447	0.079	0.402
"	F-SnO$_2$	Air	0.8	2.13	0.375	0.21	0.21
"	"	"	0.2	0.477	0.204	0.152	0.074
"	InSnO$_2$	"	2	2.87	0.495	0.189	0.134
"	"	"	1.6	2.34	0.477	0.177	0.123
"	"	"	1.12	2.19	0.468	0.165	0.151

Summary of the solar cell parameters J_{sc}, V_{oc}, FF and the overall conversion efficiencies ($\eta\%$), (at room temperature) for the Au/MPc/TiO$_2$/InSnO$_2$ or F-SnO$_2$ heterojunction cells prepared in this work. Where MPc = CuPc, PbPc or ClAlPc film thickness indicated. TiO$_2$ (~50nm) prepared according to code 'B' in table 5.3, using Sol-Gel technology. Ambient conditions as indicated in table.

Dye and Thickness (nm)	Substrate	Ambient	Light Intensity mW/cm²	J_{sc} x 10^{-7} (A/cm²)	V_{oc} (V)	FF	$\eta\%$ (x 10^{-2})
ClAlPc(500)	InSnO$_2$	Air	0.64	1.04	0.42	0.129	0.088
"	"	"	0.56	0.82	0.4	0.145	0.085
"	"	"	0.16	0.338	0.348	0.147	0.11
CuPc(500)	"	Vacuum	60.6	120	0.024	0.24	0.011
"	"	"	2.4	2.09	0.111	0.198	0.019
"	"	"	0.56	0.452	0.058	0.291	0.014
"	"	Air	2.4	6.35	0.109	0.217	0.063
"	"	Air (1Day)	"	4.44	0.116	0.233	0.05
"	"	Air (2 Days)	"	4.12	0.09	0.246	0.038
PbPc(100)	InSnO$_2$	Vacuum	0.16	8.4	0.16	0.233	2
"	"	"	0.56	26.7	0.242	0.233	2.7
"	"	"	1.12	53.3	0.283	0.339	4.6

Dye and Thickness (nm)	Substrate	Ambient	Light Intensity mW/cm^2	J_{sc} x 10^{-7} (A/cm^2)	V_{oc} (v)	FF	$\eta\%$ (x 10^{-2})
PbPc(100nm)	InSnO$_2$	Vacuum	1.6	73.3	0.301	0.232	3.2
"	"	"	2	92.3	0.328	0.239	3.6
"(500nm)	"	"	0.16	0.4	0.128	0.147	0.05
"	"	"	0.56	2.78	0.192	0.133	0.13
"	"	"	1.12	4.99	0.228	0.138	0.14
"	"	"	1.6	8.44	0.261	0.14	0.19
"	"	"	2	12	0.296	0.175	0.31
"	"	Air	0.8	1.54	0.16	0.129	0.04
"	"	"	1.04	3.3	0.193	0.137	0.08
"	"	"	1.52	4.67	0.2	0.162	0.1
"	"	"	2	5.11	0.2	0.14	0.07
"	"	"	2.88	5.33	0.2	0.11	0.04

Temperature (K)	Intensity (mW/cm^2)	Voc (mV)	Isc (x10^{-8}A)	FF	η% (x10^{-2})
100	0.16	80	0.797	0.2	0.266
"	0.56	145	1.147	0.24	0.238
"	1.12	175	1.91	0.252	0.251
"	1.6	194	2.19	0.248	0.22
"	2	218	3.21	0.206	0.24
150	0.16	110	1.29	0.217	0.642
"	0.56	184	3.84	0.216	0.908
"	1.12	241	7.06	0.238	1.21
"	1.6	256	7.97	0.259	1.1
"	2	269	9.1	0.257	1.05
200	0.16	254	2	0.208	2.2
"	0.56	336	6.88	0.21	2.89
"	1.12	404	11.2	0.247	3.33
"	1.6	434	12.7	0.257	2.95
"	2	458	14	0.252	2.69
250	0.56	320	6.64	0.206	2.61
"	1.12	404	13.2	0.237	3.76
"	1.6	410	16.5	0.245	3.45
"	2	410	20	0.268	3.66

Summary of results obtained for V_{oc}, I_{sc}, FF and η% of a Au/PbPc(100nm)/TiO$_2$(50nm)/InSnO$_2$ heterojunction cell as a function of temperature. Device active area 0.07cm^2 measurements made under vacuum.

APPENDIX D: PUBLICATIONS AND CONFERENCES ATTENDED

1. The Role and Interactions of the Process Parameters on The Nature of Alkoxide Derived Sol-Gel Films. Proceedings of AMPT'95, *Advances in Materials and Processing Technologies* p. 1268 Vol (3), 1995. (Accepted for publication in *J. Mat. Proc. Tech*; in press)

2. Synthesis and Characterisation of a Novel Semiconducting N-Alkylpyridinium Benzimidazolate Betaine-TCNQ Charge Transfer Complex. Allen, D. W., Hawkrigg, J., Tracey, S. M., Ray, A. K., and Hassan, A. *Synthetic Metals*, (Accepted ; in press).

3. Sol-Gel Derived TiO_2 / Lead Phthalocyanine Photovoltaic Cells. Tracey, S. M., Hodgson, S. N. B. Ray, A. K. *J. Sol-Gel Science and Technology*, (Accepted ; in press).

4. Electrical properties of a novel TCNQ adduct. *International Conference on Molecular Electronics and Biocomputing*, Goa, India, September 25-30, 1994. (presentation)

5. The Role and Interactions of the Process Parameters on the Nature of Alkoxide Derived Sol-Gel Films. *AMPT'95 Advances in Materials and Processing Technologies*, Dublin, Ireland August 8-12, 1995. (presentation)

6. Spectral Sensitisation of Sol-Gel Derived Titanium Dioxide films by Nickel Phthalocyanine. *First International Workshop on Materials for Optoelectronics*, Sheffield, August 22-23, 1995. (presentation)

THE ROLE AND INTERACTIONS OF THE PROCESS PARAMETERS ON THE NATURE OF ALKOXIDE DERIVED SOL-GEL FILMS

S.M. Tacey*, S.N.B. Hodgson**, A.K. Ray*, and Z. Ghassemlooy*

*Sheffield Hallam University, School of Engineering and Information Technology, UK
**University of Humberside, School of Engineering, UK

ABSTRACT

Dip-coated TiO_2 sol-gel films have been used as a representative system to investigate the effects of, and interactions between, the principle parameters for the sol-gel process. The studies have been carried out on various aspects of the optical, structural and electrical nature of the films, using the statistical analysis technique, factorial experimental design (FED) where appropriate. The work has identified the existence of highly significant interactions between process parameters such as withdrawal rate, sol concentration and the number of coating layers. Appropriate models are proposed in order to explain the observed effects.

1. INTRODUCTION.

The sol-gel method offers many advantages over other methods of producing inorganic thin films. For example, the low processing temperature; the possibility to change the sol composition and therefore produce a change in film microstructure, and low processing cost compared to some competitive processes such as C.V.D. In addition, the problems of producing good stoichiometric ratio of elements and molecular homogeneity are overcome, [1]. Many inorganic thin films have been produced using this technique and have found applications in a wide variety of areas including antireflective coatings, gas sensors, magnetic core materials, electrical and optoelectronic devices, [2-6].

It is recognised that process parameters have a major influence on the properties of sol-gel products. Parameters such as heat treatment conditions, sol reactivity and viscosity, oxide ratio, and the number of coatings have been shown in some cases to drastically alter the electrical, optical and structural properties of the films, [7,8]. However, the models developed to explain and predict the behaviour of such systems have tended to characterise the role of individual factors in the process, and remain of limited general applicability. Consequently the development of novel systems has tended to occur on a largely empirical basis. Little published work exists on the role and nature of interactions between the process parameters to allow a more general understanding of the role of the process parameters to be developed.

Factorial experimental design (FED) is a useful, highly efficient statistical technique for assessing and predicting the effect of both individual factors (i.e. process parameters), and any interaction between factors that may exist, [9]. Originally developed by Fisher in 1926 [10], it is a technique that offers a number of advantages over the traditional 'one-factor-at-a-time' approach, in which the effect of changing any one variable is assessed independently of the others. For example, for n factors the design requires n times fewer measurements than the 'one-factor-at-a-time' approach to acquire the same information. Using a 'one-factor-at-a-time' approach there exists the possibility of

drawing misleading conclusions in systems which undergo interaction, these can be effectively avoided through the use of FED.

Our investigations have been conducted on Titanium dioxide films obtained through hydrolysis of Titanium Isopropoxide (TIP). This material is a popular choice for use in many electronic and optoelectronic devices, due to its high dielectric constant, chemical stability, high refractive index, and low sensitivity to temperature and frequency, [11]. As a consequence, this material has attracted considerable interest, [8, 12 , 13].

It is anticipated that the findings presented in this paper will be applicable to a wide variety of similar alkoxide systems, and that elucidation of the nature of interactions between the process parameters will lead to a greater understanding of their role.

2. EXPERIMENTAL METHODOLOGY.

2.1. Production of TiO_2 films.

The TiO_2 thin films were prepared through the room temperature hydrolysis of the metal-organic precursor, Titanium(IV) Isopropoxide $Ti[OCH(CH_3)_2]_4$ (97% pure) supplied by Aldrich Chemicals. This was performed in the presence of (99.5%) pure glacial acetic acid $CH_3 \cdot COOH$, which has the effect of controlling the rate and extent of the hydrolysis of the TIP, [14]. The acetic acid was first added to (99.7-100%) anhydrous ethanol (50ml) and allowed to mix for 5 minutes after which the precursor material was added with the solution continuously stirred for a further 2 minutes. Dip coating was then immediately carried out.

A linear dipping mechanism supplied by Nima Technology was used to deposit the films onto appropriate substrates under atmospheric conditions. All samples were dried in air for 24 hours at room temperature then heat treated in air at temperature of 500°C (unless specified otherwise) for 5 hours. For the multiple coated samples the heat treatment process was repeated after each subsequent deposition. The solution was dip coated onto chemically and ultrasonically cleaned glass substrates at a dip withdrawal speed of 100 or 250 mm/minute.

2.2. Infra red studies.

Infra red studies were carried out on residues of the sol mixture in the wavenumber range 500 to 4000 cm^{-1}. These studies were necessary in order to identify the presence of any organic residue, water or solvent left after heat treatment. Analysis was performed using an ATI Mattson Genesis Series FTIR spectrometer on pressed KBr discs containing 1% by mass of the powdered sample.

2.3. X-Ray diffraction.

In order to determine the effect of the process route and heat treatment conditions on the structure of the sol-gel product X-ray diffraction studies were performed on residues of the sol mixture subjected to identical heat treatment to the coating films. These experiments were carried out using a Philips PW1710 diffractometer with monochromated Cu radiation at a scan speed of 0.01 degree (2θ) per second.

2.4. Conductivity measurements

The effect of the heat treatment conditions on the electrical conductivity of the TiO_2 sol gel films was determined using specially prepared films which were dip coated, as a single layer onto a glass slide preprinted with platinum interdigital electrodes. A dip withdrawal speed of 250 mm/minute was used.

Each of the 15 electrodes were 186μ wide and 60μ apart, and overlapped by 3.125mm providing approximately 252 squares of surface electrode (N). The intrinsic conductivity of the films applied to this electrode could then be estimated from the equation, [15];

$$\left(\sigma = \frac{S}{t}\frac{1}{N}\right)$$

(1)

Where σ is the intrinsic conductivity (S/cm), S the measured conductance, t the film thickness (cm) and N is the number of squares in the electrode. A Keithley 617 programmable electrometer measured the current as a function of applied DC voltage in the range ±40V. Conductance (S) values were determined from the slope of I/V plots. All measurements were performed in an Oxford Instruments Cryostat under a vacuum of ~ 0.1torr. The measurements were performed on slides coated under the following conditions: Mole ratio of acetic acid to TIP = 4:1 and TIP concentration = 6.3 mls in 50 ml ethanol.

2.5. Application of Factorial experimental design to the present investigations.

In these investigations each factor or process parameter was represented by two levels (a high and a low) giving a 2^n design, where n was the number of factors studied. A systematic tabular method derived by Yates [16] has been used to calculate the total effects for each treatment combination (or particular combination of factor levels). These effects were then used to produce an ANOVA (analysis of variance) in which, the significance of effects and interactions were assessed against the f-distribution. In order to carry out the statistical analysis effectively an estimation of the experimental error was required, which was achieved by replicating the experiments.

For the factorial design the factors investigated were (a) the effect of dip withdrawal speed, (b) the effect of the relative mole ratio of acetic acid: TIP, (c) the effect of the number of coating layers applied, and (d) the effect of the concentration of TIP precursor used. In the latter case, the concentration of acetic acid was varied proportionally to maintain the respective mole ratio of acetic acid to TIP. Standard notation has been used in these experiments where the upper case letter e.g. [A] denotes the calculated effect of a factor or interaction (e.g. [AB]) and the lower case letter e.g. [a,b,c,d] indicates that the sample was prepared with that factor at a high level.

2.5.1. Thickness measurements.

A planar surfometer (Surfcom 300) was used to measure the film thickness to an accuracy of approximately ±0.01μm. Thickness measurements were carried out by measuring the step height of the coating film relative to the substrate, at a fixed distance (2mm) from the top edge of the coating. For each coated sample a total of 4 thickness measurements were made (2 on each side of the sample). The process parameters investigated as factors and their respective levels are listed in table 1.

Table.1. Notation used and process parameters investigated during factorial experiments.

Effect	Factor	High Level	Low Level
[A]	Withdrawal speed	250 mm/min	100 mm/min
[B]	Mole ratio of acetic acid:TIP	4.1:1	3.1:1
[C]	No of coating layers	4	1
[D]	Concentration of TIP in ethanol. (acetic acid increased proportionally)	6.3ml TIP 50 ml ethanol	3.15ml TIP 50 ml ethanol

2.5.2. Absorption coefficient.

An ATI Unicam (UV2-100) UV/VIS spectrophotometer was used to determine the absorption spectra of the films in a wavelength range of 300-800nm. Both the total absorption and absorption coefficient (α) of the films were studied, where the absorption of the films is defined as the ratio of $\ln(I_0/I)$ where I_0 and I are the initial and transmitted light intensity respectively, and the absorption coefficient is the ratio of absorption to the film thickness. The absorption behaviour was wavelength dependent, and a standard photon energy of 4eV, which was within the absorption band edge, was therefore used in these calculations. The process parameters investigated were as listed in table 1.

3. RESULTS AND DISCUSSION.

3.1. The dip coating process.

The dip coating and heat treatment processes resulted in all cases in a robust, chemically and thermally stable transparent TiO_2 film which was free from cracks and other surface defects. No evidence of precipitation or crystallisation could be identified either visually, or by optical or electron microscopy.

The stability of the coating solutions was found to be dependant upon the respective concentrations of acetic acid and TIP used. For sols containing less than 4 moles of acetic acid per mole of TIP, the sols became cloudy after a period of approximately 1 hour and underwent gelation in approximately 2 hours. Sols prepared with more than 4 moles of acetic acid per mole of TIP were found to remain stable and clear for at least 24 hours.

3.2. Infra red absorption measurements.

The results of the infra red absorption measurements carried out on the variously heat treated gels showed the expected reduction in the absorption peaks due to residual organic groups, as heat treatment temperature was increased, Fig.1. In particular, a reduction was observed in the intensity of the two absorption peaks at approximately 1500 cm^{-1}, which have been attributed to bridging acetate groups, [12], from the reaction modifying acetic acid.

The results show that, even at the highest heat treatment temperature used (500°C) there remained a small, but significant absorption from these organic groups, showing that these had not been completely eliminated. It is suggested that these impurities may have been effectively eliminated at lower temperatures for the (submicron thickness) coating films compared to the bulk gels used in this study, but this could not be determined due to problems of substrate absorption. Future work is planned using silicon substrates to confirm this.
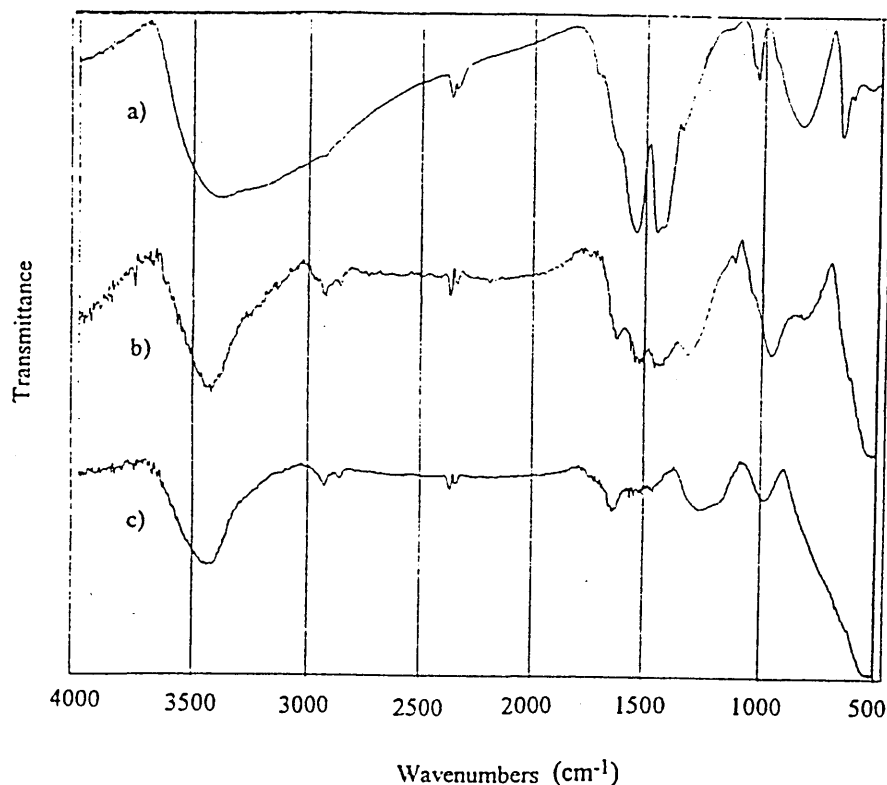
Figure.1. Infra Red absorption spectra for variously heat treated TiO_2 gels.
    a) unheated, b) 350°C c) 500°C

3.3. X-Ray diffraction measurements.

The results of the X-Ray diffraction studies carried out on bulk gel samples showed that the structure of the gel product varied according to the heat treatment conditions used. For the unfired gels, the X-Ray diffraction patterns obtained were in all cases indicative of an amorphous structure. In gels heat treated to a temperature of 350° C the structure was predominantly amorphous although there was evidence of crystallisation beginning to take place. At a temperature of 500°C diffraction peaks characteristic of the anatase crystal structure were obtained indicating that crystallisation had occurred. Presumably the crystal size was too small to be determined by microscopy. Other studies, [14], have identified crystallisation in titanium ethoxide derived TiO_2 gels heat treated to temperatures as low as 150°C with the temperature stability being found to be a function of the alkoxide precursor used and the dilution of the alkoxide precursor. It has been suggested, [14], that the onset of crystallisation may correspond to the release of residual organics from the gel during heat treatment.

3.4. Electrical conductivity.

The results of the experimental determination of the effect of heat treatment conditions on the electrical conductivity of sol-gel derived TiO_2 films are shown in Fig.2. The results show that there was an apparent decrease in conductivity in films heat treated at 200°-350°C compared to the non-heat treated films. The greater conductivity of the unheated films most probably arises from the contribution (to the conductivity) of residual organic material identified in the infra-red spectroscopy, and possibly also due

to the presence of adsorbed water in the pore structure of the gel. These would be expected to be removed during heat treatment. The diminishing reduction in the conductivity of the film is presumably due to removal of the majority of these residual impurities. It was not possible to determine the effect of heat treatment temperatures in excess of 350°C in this study due to degradation of the metal electrodes at heat treatment temperatures in excess of this. Further studies are planned using I.T.O coated glass substrates as electrodes to investigate the effect of higher heat treatment temperatures. The change in electrical behaviour also correlated broadly with the onset of crystallisation in the specimens, and it is possible that this crystallisation may be either the cause of the change in behaviour, or may arise from the same phenomena (the removal of residual organics).
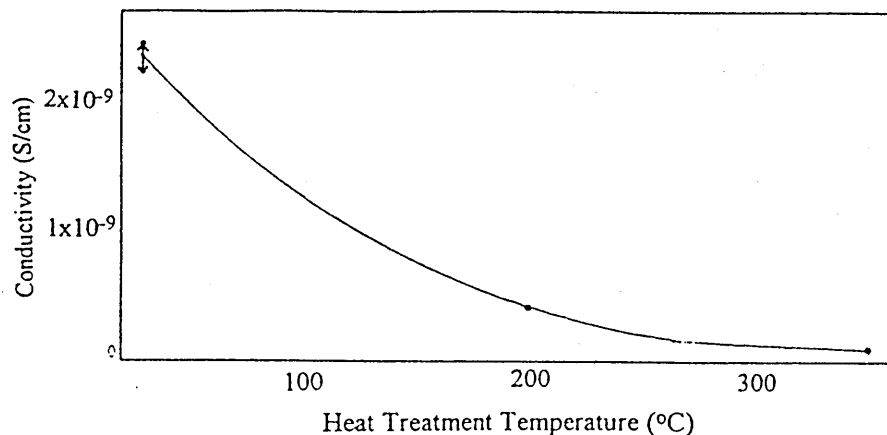
Figure 2 - The effect of heat treatment on the conductivity of TiO_2 film.

3.5. Factorial experiments.

3.5.1. Film thickness determinations.

The results of the thickness determinations carried out on the coated glass substrates indicated that this was generally consistent across the coatings, with total film thicknesses in the range 0.03 to 0.37 μm being produced according to the process parameters used. However, in all cases there was evidence of a small region of considerably greater thickness (approximately 1 μm) close to the top edge of the coated region, and some evidence of a slight and gradual reduction in coating thickness towards the bottom of the dip coated substrate. This latter point was extremely difficult to confirm due to variations in the flatness of the substrate at this scale.

The results of the factorial experiments and the associated analyses of variance for the effect of withdrawal speed, acetic acid : TIP mole ratio, number of coatings applied, and the concentration of TIP on both the total coating thickness, and the individual coating layer thickness are shown in table 2.

3.5.1.1. Interpretation of calculated main effects.

The calculated main effects for a factorial experiment represent the effect of each factor, averaged over all levels and combinations of the other factors. Thus in systems in which considerable multi-factor interaction occurs, the calculated main effects are of limited significance, since the effect of each factor is dependent upon the levels of the other factors present, and should be interpreted with some caution.

The calculated main effects of the dipping speed, ([A] in table 2) indicates an increase in both total film and coating layer thickness as the dipping speed is increased. This is consistent with theory

Table 2:
Results of factorial experiment
for coating and coating layer thickness.

Overall coating thickness				Average coating layer thickness			
Treatment	Mean Measured Coating Thickness (um)	Mean factorial Effect (um)	Significance	Treatment	Mean coating layer thickness (um)	Mean factorial Effect (um)	Significance
1	0.055			1	0.055		
a	0.050	[A] = 0.049	***	a	0.050	[A] = 0.015	***
b	0.040	[B] = 0.006	N/S	b	0.040	[B] = -0.004	N/S
c	0.120	[C] = 0.164	***	c	0.030	[C] = -0.002	N/S
d	0.070	[D] = 0.068	***	d	0.070	[D] = 0.390	***
Two Factor Interactions				Two Factor Interactions			
ab	0.045	[AB] = 0.026	***	ab	0.045	[AB] = 0.008	**
ac	0.120	[AC] = 0.041	***	ac	0.030	[AC] = 0.008	**
ad	0.085	[AD] = 0.030	***	ad	0.085	[AD] = 0.010	***
bc	0.170	[BC] = 0.021	***	bc	0.043	[BC] = 0.011	***
bd	0.050	[BD] = -0.033	***	bd	0.050	[BD] = -0.160	***
cd	0.260	[CD] = 0.048	***	cd	0.064	[CD] = 0.004	N/S
Three Factor Interactions				Three Factor Interactions			
abc	0.245	[ABC] = 0.024	***	abc	0.061	[ABC] = 0.005	N/S
abd	0.065	[ABD] = 0.005	N/S	abd	0.065	[ABD] = 0.000	N/S
acd	0.335	[ACD] = 0.023	***	acd	0.084	[ACD] = 0.003	N/S
bcd	0.160	[BCD] = -0.028	***	bcd	0.040	[BCD] = -0.005	N/S
Four Factor Interactions				Four Factor Interactions			
abcd	0.365	[ABCD] = 0.007	N/S	abcd	0.091	[ABCD] = 0.003	N/S

KEY: a,b,c,d, ab = treatment includes specified factor at high level
[A],[B],[C],[D],[ABC] = calculated mean effect of that factor or interaction
A = effect of withdrawal rate,   B = effect of acetic acid:TIP mole ratio
C = effect of number of coatings, D = effect of T.I.P. concentration
*** = Significant at f<1% level   ** Significant at f<5% level
* = Significant at f<10% level,   N/S = Not significant

Table 3:
Results of factorial experiment for
optical absorption and absorption coefficient, (10^{5}cm^{-1}).

Measured absorption at 4eV				Calculated absorption coefficient at 4eV			
Treatment	Mean absorbance	Mean factorial effect	Significance	Treatment	Mean calculated absorption coefficient	Mean factorial effect	Significance
1	0.56			1	1.175		
a	0.607	[A] = 0.532	***	a	1.425	[A] = 0.178	N/S
b	0.804	[B] = -0.140	***	b	1.870	[B] = 0.065	N/S
c	0.900	[C] = 1.077	***	c	0.868	[C] = -0.472	***
d	0.520	[D] = 0.645	***	d	0.860	[D] = -0.057	N/S
Two Factor Interactions				Two Factor Interactions			
ab	0.544	[AB] = -0.076	*	ab	1.490	[AB] = -0.234	N/S
ac	1.555	[AC] = 0.322	***	ac	1.523	[AC] = -0.028	N/S
ad	1.025	[AD] = 0.257	***	ad	1.390	[AD] = 0.048	N/S
bc	0.917	[BC] = -0.082	*	bc	0.628	[BC] = -0.328	**
bd	0.564	[BD] = -0.059	N/S	bd	1.343	[BD] = 0.159	N/S
cd	1.835	[CD] = 0.469	***	cd	0.830	[CD] = 0.108	N/S
Three Factor Interactions				Three Factor Interactions			
abc	1.305	[ABC] = -0.009	N/S	abc	0.623	[ABC] = -0.052	N/S
abd	0.840	[ABD] = 0.000	N/S	abd	1.740	[ABD] = 0.089	N/S
acd	3.060	[ACD] = 0.076	*	acd	1.048	[ACD] = -0.222	N/S
bcd	1.545	[BCD] = -0.046	N/S	bcd	1.112	[BCD] = 0.148	N/S
Four Factor Interactions				Four Factor Interactions			
abcd	2.695	[ABCD] = 0.048	N/S	abcd	0.850	[ABCD] = -0.045	N/S

KEY: a,b,c,d, ab = treatment includes specified factor(s) at high level
[A], [B],[C],[D], [ABC] =Calculated mean effect of that factor, or interaction.
A = effect of withdrawal speed   B = effect of acetic acid:TIP mole ratio.
C = effect of number of coatings, D = effect of T.I.P. concentration
*** = Significant at f<1% level   ** Significant at f<5% level
* = Significant at f<10% level,   N/S = Not significant

proposed by other workers, [17], and has been explained as being due to the effect of viscous drag on the liquid meniscus, [1].

No significant effect could be identified for the acetic acid: TIP mole ratio [B] in the thickness factorial experiments. This was somewhat unexpected since, as discussed in section 3.1, the level of acid present resulted in a change in the reactivity (and gelation times) of the alkoxide precursor, and might therefore be expected to result in a change in the viscosity of the coating solution. This discrepancy may be due to the short time elapsed between alkoxide addition and the dip coating process, resulting in relatively small differences between the progress of the relative reactions of the sols containing different levels of acid addition. However, it is also possible that the presence of such an effect may be masked by the large interaction effects involving this factor.

The total thickness of the coating showed the expected increase as the number of coating layers [C] was increased from 1 to 4 (by an average of 0.16 μm averaged over all levels and combinations of the other factors). However, the calculated factorial effect of the number of coatings, on the thickness of the individual coating layers was not found to be significantly large. significant interaction effects were found involving this factor, and these are discussed in more detail in subsequent sections.

The calculated main effects of TIP concentration [D] in the factorial experiments showed an increase in both total coating thickness and individual layer thickness with an increase in the concentration of the TIP as might be intuitively expected. However, the magnitude of the calculated factorial effect for this factor has little practical significance due the presence of numerous interactions involving this factor. The effect of changing TIP concentration on the coating thickness depends upon a number of other factors.

3.5.1.2. Interaction effects.

The results of the factorial experiments for both total coating and individual coating layer thickness indicated the presence of numerous interaction effects. A number of significant two and three factor interaction effects could be identified in the experiment for the overall coating layer thickness which appear to be not significant in the experiment for the individual coating layer thickness. However, this apparent discrepancy is most probably due to the increased sensitivity of the former experiment in detecting what are in all cases relatively small effects relative to the error in the thickness determinations.

It is suggested that the interaction effects can be attributed to three probable factors, which could produce the effects identified in these experiments. These factors being (i) the viscosity of the coating solution, (ii) the mechanism and kinetics of the reaction of the alkoxide precursor, and (iii) the surface interactions between the substrate and coating solution.

The significant (positive) interaction effects between withdrawal speed with acid: TIP molar ratio [AB] and TIP concentration [AD] are most probably indicative of non-Newtonian properties in the deposited film of the coating solution during dip coating, which appear to be exaggerated by the presence of either reaction modifying acetic acid, or the reaction precursor TIP at high concentrations. An increase in coating thickness would be predicted from an increase in the sol viscosity during deposition. Other workers, [18], have found evidence of non-Newtonian behaviour during dip coating at withdrawal speeds in excess of approximately 50 mm per minute as used in this study.

The interaction effects between the number of coatings with withdrawal speed [AC], acetic acid concentration [BC], and concentration of TIP [CD], and the three factor interaction between the number of coating layers with withdrawal speed and acetic acid concentration [ABC] can be attributed to a change in the surface interaction between the substrate and coating solution as these factors are varied. Previous work, [1], has suggested that the thickness of the coating film produced during dip coating is determined by a number of factors related to surface effects including the viscous drag exerted on the liquid by the moving substrate. These effects are likely to be different between the coating liquid and a coated or uncoated substrate.

Previous studies, [19], have suggested that the thickness of the first coating layer in a multi-layer coating is greater than that in subsequent coating layers. However, it can be deduced from the interactions identified in this work, that such a phenomena is highly dependent upon the levels of other factors, and cannot be assumed to take place.

The significant negative interaction effect between the concentrations of the TIP precursor and acetic acid reaction modifier [BD] would appear to be indicative of a change in the kinetics, and perhaps mechanism of the hydrolysis and polycondensation reactions responsible for the gelation process. A reduction in film thickness would be expected if such an interaction resulted in a reduction in the reaction rate and/or solution viscosity. It is probable that the hydrolysis inhibiting reaction which occurs between the TIP and acetic acid, [12], occurs faster and to a greater degree when the two reactants are present at a higher concentration.

3.5.2. Optical absorption experiments.

The results of the measured optical absorption and calculated optical absorption coefficient values for the sol-gel derived films together with the calculated factorial effects and associated analyses of variance are shown in table 3.

The results of experiments for optical absorption indicate the presence of large numbers of apparent effects of interactions. However, when these effects are converted to absorption coefficient, to incorporate the effect of film thickness, the majority of these are eliminated, indicating that these changes in optical absorption can be attributed to the variation in film thickness associated with changes in the process parameters. The remaining effects, which were significant in both optical absorption and absorption coefficient experiments indicate effects which cannot be attributed solely to changes in film thickness and which must arise due to changes in the behaviour of the coating films themselves.

The most significant effects in both experiments were associated with the effect of the number of coating layers applied, which was also the largest factor affecting the thickness of the coating. The calculated main effects of the number of coating layers [C] showed the expected increase in overall optical absorption as the number of coating layers, and hence coating thickness increased (manifested as a positive factorial effect). However, once the effects of coating thickness are taken into account (i.e. in the absorption coefficient), the calculated effect of this factor was found to change from a positive to a negative effect (-0.472).

One possible explanation of this phenomena is that a large contribution to the apparent optical absorption may be due to reflectance at the coating/substrate interface due to refractive index mismatch. This effect will occur only for the initial coating layer (since subsequent layers will have identical refractive index to the first layer), and thus subsequent coating layers will have a smaller effect on absorption and apparent absorption coefficient than the first. This would be manifested as a negative factorial effect for the number of coatings in the absorption coefficient experiment.

4. CONCLUSIONS.

The results of this study have confirmed the effect of previously documented factors such as withdrawal speed, alkoxide concentration and number of coatings on the properties of alkoxide derived sol-gel films. However, the results have also shown that these factors undergo significant interaction with particular effects on the thickness obtained during dip coating, with corresponding effects on thickness related properties such as optical absorption and electrical properties of the coatings.

The presence of these interactions may explain the limited scope of existing theoretical models developed to predict and explain the behaviour of such materials, which has hitherto resulted in new systems being developed by a largely empirical process. An improved understanding of their causes and effects may allow the future development of more flexible predictive models for the behaviour of sol-gel systems.

REFERENCES

[1]   C.F. Brinker and G.W. Scherer, *Sol-Gel Science, The Physics and Chemistry of Sol-Gel Processing*, Academic Press, London, 1990.

[2]   H. Dislich, " Glassy and Crystalline Systems from Gels: Chemical Basis and Technical Application," *Journal of Non-Crystalline Solids*, Vol. 57, 1983, pp. 371-388.

[3]   V. Raman, O.P. Bahl and V.K. Parashar, "Sol-Gel doped with analytical reagent for nitrate/nitrogen dioxide," *Journal of Materials Science Letters*, Vol. 13, 1994, pp. 579-581.

[4]   K. Tanaka, T. Yoko, M. Atarashi and K. Kamiya, "Preparation of Fe_3O_4 thin film by the sol-gel method and its magnetic properties," *Journal of Materials Science Letters*, Vol. 8, 1989, pp. 83-85.

[5]   A. Patel, N.M. Shorrocks, and R.W. Whatmore, "Preparation and Properties of $PbTiO_3$ and $Pb(Sc_{0.5}Ta_{0.5})O_3$ Thin Films by Sol-Gel Processing," *IEEE Transactions on Ultrasonics, Ferroelectrics, and Frequency Control*, Vol. 38, No. 6, 1991, pp. 672-676.

[6]   J.I. Zink and B.S.Dunn, "Photonic Materials by the Sol-Gel Process," *The Centennial Memorial Issue of The Ceramic Society of Japan*, Vol. 99, No. 10, 1991, pp. 878-893.

[7]   K.A. Vorotilov, E.V. Orlova and V.I. Petrovsky, "Sol-Gel TiO_2 Films on Silicon Substrates," *Thin Solid Films*, Vol. 207, 1992, pp. 180-184.

[8]   T. Yoko, A. Tuasa, K. Kamiya and S. Sakka, "Sol-Gel-Derived TiO_2 Film Semiconductor Electrode for Photocleavage of water," *Journal of the Electrochemical Society*, Vol. 138, No. 8, Aug 1991, pp. 2279-2284.

[9]   D.C. Montgomery, *Design and Analysis of Experiments*, John Wiley & Sons, New York, 2nd ed. 1984.

[10]   R.A. Fisher, "The Arrangement of Field Experiments," *Journal of the Ministry of Agriculture*, Vol. 33, 1926, pp. 503-513.

[11]   F.A. Grant, "Properties of Rutile (Titanium Dioxide)," *Reviews of Modern Physics*, Vol. 31, No. 3, July 1959, pp. 646-673.

[12]   J. Livage, "Synthesis, Structure and Applications of TiO_2 Gels," *Materials Research Society Symp. Proceedings*, Vol. 73, 1986, pp. 717-724.

[13]   M. Anast, A. Jamting, J.M. Bell and B. Ben-Nissan, "Surface Morphology examination of Sol-Gel deposited TiO_2 films," *Thin Solid Films*, Vol. 253, 1994, pp. 303-307.

[14]   B.E. Yoldas, "Hydrolysis of Titanium Alkoxides and effects of Hydrolytic Polycondensation Parameters," *Journal of Materials Science*, Vol. 21, 1986, pp. 1087-1092.

[15]   F.W. Kutzler, W.R. Barger, A.W. Snow and H. Wohltjen, "An Investigation of Conductivity in Metal-Substituted Phthalocyanine Langmuir-Blodgett Films," *Thin Solid Films*, Vol 155, 1987, pp. 1-16.

[16]   F.Yates, "The Design and Analysis of Factorial Experiments," *Imperial Bureau of Soil Science, Technical Communications*, No. 35, 1937.

[17]   C.J. Brinker, A.J. Hurd, P.R. Schunk, G.C. Frye and C.S. Ashley, "Review of Sol-Gel Thin Film Formation," *Journal of Non Crystalline Solids*, Vol. 147 and 148, 1992, pp. 424-436.

[18]   I. Strawbridge and P.F. James, "The factors affecting the thickness of sol-gel derived silica coatings prepared by dipping," *Journal of Non Crystalline Solids*, Vol. 86, 1986, pp. 381

[19]   Y.L. Huang, A. Caneiro, M. Attari and P. Fabry, "Preparation of Nasicon Thin Films by Dip-Coating on Si/SiO_2 Wafers and Corresponding C-V measurements," *Thin Solid Films*, Vol. 196, 1991, pp. 283-294.
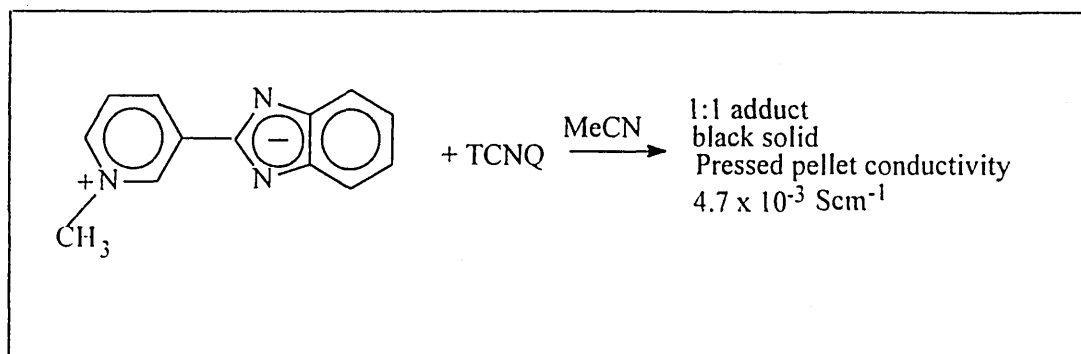
Synthesis and Characterisation of a Novel Semiconducting N- Alkylpyridinium Benzimidazolate Betaine-TCNQ Charge-Transfer Complex

David W Allen*, Jacqueline Hawkrigg*, Sandra M.Tracey**, Asim.K.Ray**, and Aseel Hassan**

*Division of Chemistry and Materials Research Institute

** School of Engineering

Sheffield Hallam University, Sheffield S1 1WB

+ TCNQ $\xrightarrow{\text{MeCN}}$ 1:1 adduct
black solid
Pressed pellet conductivity
4.7×10^{-3} Scm^{-1}

Synthesis and Characterisation of a Novel Semiconducting N- Alkylpyridinium Benzimidazolate Betaine-TCNQ Charge-Transfer Complex

David W Allen*, Jacqueline Hawkrigg*, Sandra M.Tracey**, Asim.K.Ray**, and Aseel Hassan**
*Division of Chemistry and Materials Research Institute
** School of Engineering
Sheffield Hallam University, Sheffield S1 1WB

ABSTRACT

A three stage synthesis of the 2-(1-methylpyridinium-3-yl) benzimidazolate betaine is described. The reaction of the betaine with an equimolar proportion of tetracyanoquinodimethane (TCNQ) in the presence of acetonitrile results in the formation of a novel semiconducting black microcrystalline adduct. Microanalysis of the material indicates a betaine/TCNQ ratio of 1:1. J(V) characteristics have revealed that conduction in this adduct is ohmic over the range studied, with room temperature conductivity being 4.7×10^{-3} S/cm. The ohmic activation energy was 51meV. Hopping is believed to be the dominant conduction mechanism.

1.0 INTRODUCTION

Charge-transfer complexes of donor molecules with the electron acceptor tetracyanoquinodimethane (TCNQ) have been studied extensively over the past thirty years. A great variety of such complexes has now been characterised, with electrical conductivities spanning the whole range from insulator to semi-conductor to organic metal. As part of this development, there have been extensive studies of the interactions of TCNQ with nitrogen heterocycles, and their related quaternary salts derived from iodoalkanes[1]. Interest in this area continues[2]. We have recently developed synthetic routes to a range of phosphonioaryl benzimidazolate betaines, e.g. (1),[3] and are interested in comparing their properties with those of the related N-alkylpyridinium systems (2), the chemistry of which has been developed by Alcalde et al[4]. Such dipolar systems have considerable potential as materials that may exhibit phenomena such as molecular rectification, solvato-chromism, halochromism, non-linear optical and other properties that can form the basis of sensing techniques[5-7] . In this paper, we describe the synthesis and DC electrical characterisation of a TCNQ

adduct of the pyridinium betaine (5), a black solid which exhibits a significant level of semiconductivity at room temperature.
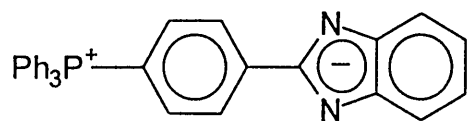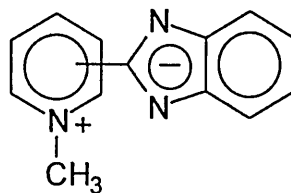

(1)   (2)

RESULTS AND DISCUSSION

The synthetic proceedure used to prepare the betaine/TCNQ adduct is outlined in scheme 1. The 3-pyridylazole(3) starting material was prepared as previously described by Alcalde *et al*[8]. Conversion of the pyridylazole into the corresponding N-alkylated salt(4) was carried out using methyl iodide under standard conditions[9]. Treatment of the salt with an equimolar proportion of sodium hydroxide in ethanol gave the stable betaine(5). Reaction of the betaine(5) with an equimolar proportion of TCNQ in acetonitrile resulted in the formation of a black microcrystalline 1:1 adduct.
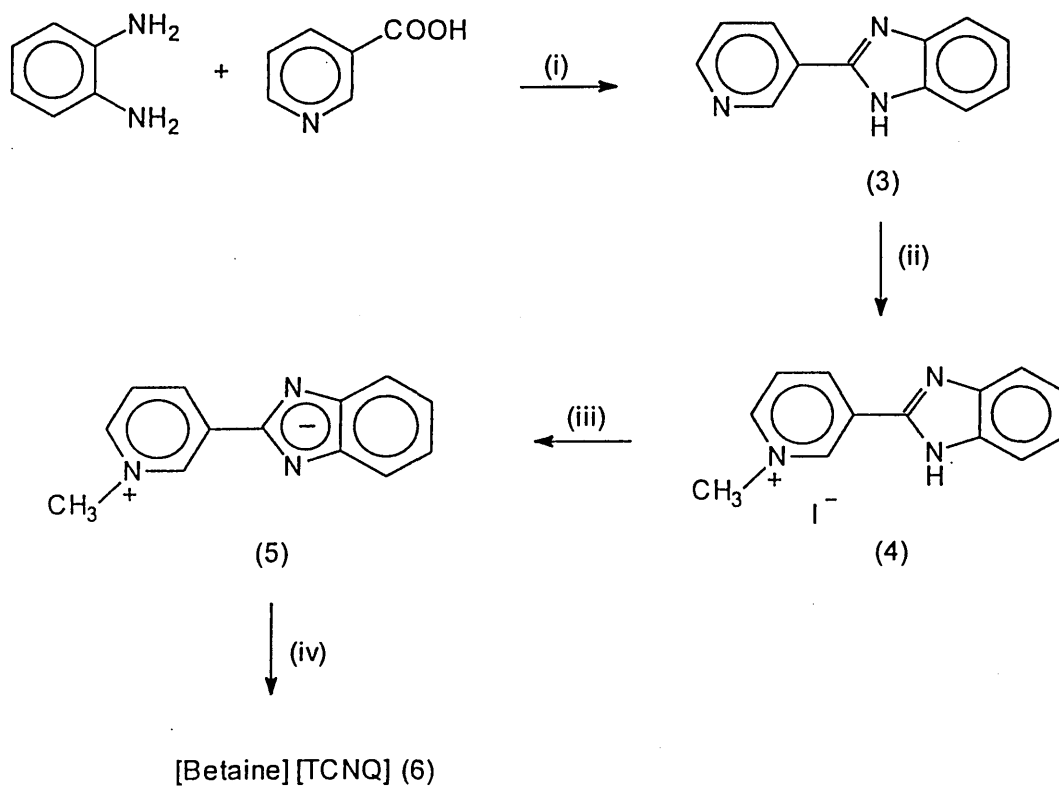
Scheme 1. Reagents and percentage yields: (i) PPA, (81%); (ii) methyl iodide(69%); (iii) 1M sodium hydroxide(95%); (iv) TCNQ (68%).

The infrared spectrum of the adduct exhibited $C \equiv N$ stretching vibrations at 2194 and 2174 cm^{-1}, consistent with a significant degree of charge transfer from the betaine to TCNQ. For comparison, neutral TCNQ[10] exhibits v $(C \equiv N)$ at 2234 cm^{-1}, whereas the TCNQ-radical anion[11] has the related absorption at 2186 cm^{-1}.

The adduct was soluble in both acetonitrile and DMF, to give green solutions, the uv-visible spectrum of which showed significant absorption in the region 700-900 nm, consistent with the presence of the TCNQ radical anion. Thin layer chromatography studies indicated that the adduct dissociated to reform the betaine and TCNQ.

The DC conductivity (σ) of a compressed pellet of the material has been measured at room temperature and was found to be 4.7×10^{-3} S/cm, well within the semiconducting range. The room temperature $J(V)$ characteristic was linear, with a gradient of 0.99 ± 0.01, and reproducible for both polarities, (Fig.1.). An estimation of the carrier concentration (n) may be obtained from:

$$J = ne\mu_n \left(\frac{V}{d} \right) \qquad (1)$$

where J is the measured current density for an applied potential V, A is the active electrode area, d is the pellet thickness, e is the elementary charge and μ_n. is the carrier mobility. Using a value of $\mu_n = 6.49 \times 10^{-6} \mathrm{cm^2 V^{-1} S^{-1}}$ determined for Ag-TCNQ, which has a similar room temperature conductivity[12], the carrier concentration is estimated to be n = $4.52 \times 10^{21} \mathrm{cm^{-3}}$.

Temperature dependence of the conductivity was measured in order to determine the type of conduction process which prevails in this material. Figure 1 shows a typical plot of the natural logarithm of conductivity as a function of inverse temperature in the range 80-300K. The curve shows a linear dependence of ln(σ) on temperature which indicates the presence of one type of conduction regime within the range of study. This temperature dependence was found to obey the following relation which is observed for many organic semiconductors:

$$\sigma = \sigma_o \exp\left[-\frac{\Delta E}{kT} \right] \qquad (2)$$

where ΔE is the activation energy, k is the Boltzman constant, T is the absolute temperature and σ_o is a constant (pre-exponential factor). Using equation (2) a value of 51meV was derived from the slope of Fig.2. This low activation energy may suggest

that the charge transport is limited by grain boundaries which could be caused during the pellet preparation[13]. It may also indicate that band conduction is not likely to be responsible for charge transport, and that hopping of charge carriers via trapping sites, which could be in the form of grain boundaries, is the most likely conduction mechanism. Similar results have been found for other TCNQ adducts prepared as thin films[9]. A trap to trap transition is a form of low field hopping where a carrier is excited from a lattice trap[14]. The probability of a carrier hopping is affected by the energy barrier of the trap which in turn is controlled by the activation energy. The carrier migrates between molecules until it falls into another trapping site.

For comparison, we have also investigated the reaction of the pyridium salt (4) (the precursor of the betaine (5)) with, respectively, lithium TCNQ$^-$, and neutral TCNQ. Reactions of this type have been commonly empoloyed by others for the synthesis of TCNQ charge transfer systems. However, in the above cases, neither system gave well-defined products which showed any resemblance to the black crystalline adduct of the betaine (5) with TCNQ. The reaction of the salt (4) with lithium TCNQ$^-$ in DMF gave a dark brown amorphous solid, of composition approximating to a 1:1 complex of the pyridinium cation with the TCNQ$^-$ anion. Infrared studies revealed v (C$\equiv$N) at 2177 and 2141 cm^{-1}. The room temperature conductivity of a compressed pellet was 1.13 x 10^{-5} Scm^{-1}. The related reaction of the salt (4) with neutral TCNQ also gave a dark brown amorphous solid, of poorly defined composition, which exhibited v (C$\equiv$N) at 2202, 2170 and 2158 cm^{-1}, and a room temperature conductivity of 1.38 x 10^{-7} Scm^{-1}. Neither of these materials, therefore, resembles the initial adduct of the betaine (5) with TCNQ, which appears to be a well-defined semiconducting charge-transfer adduct. As yet, we have been unable to grow single crystals of the adduct which are suitable for X-ray diffraction studies, and so the solid state structure remains unknown.

5

EXPERIMENTAL

^{1}H nmr studies were carried out using a Brüker AC 250 FTNMR spectrometer. Mass spectra were recorded on a VG Micromass 7070F instrument using the FAB technique. Infrared spectra were recorded as a KBr disc or mull using a Phillips PU9706 spectrometer. UV-Vis spectra were recorded on a Unicam UV-Vis spectrometer. Silica cells were used with a 1cm path length. Acetonitrile was used as the solvent unless otherwise stated.

2-(3'-Pyridyl)-1H-benzimidazole (3)

Prepared essentially as described by Alcalde[8] by condensation of pyridine-3-carboxylic acid with *o*-phenylenediamine suspended in polyphosphoric acid, and heated in an oil bath at 170-200°C for four hours. The reaction mixture was cooled and poured into ice-water and the resulting solution neutralised to pH 8 with aqueous ammonia. The precipitated solid was then recrystallised from a methanol-water solvent (70:30 v/v), to give pale cream crystals (81%), m.p. 242-243°C. (Found: C,73.70;H,4.65; N,21.50. Calc. for $C_{12}H_9N_3$,C,73.85; H,4.65; N,21.50%). m/z 195(M$^+$).

1-Methyl-3-(2-benzimidazolyl)pyridinium Iodide (4)

To a solution of the pyridylbenzimidazole (7.27g, 35.8 mmol.) in anhydrous acetone was added, dropwise, a solution of iodomethane (5g, 35.2 mmol.) in anhydrous acetone, and the resulting solution heated under reflux for three hours. On cooling, the pale yellow solid was collected by filtration and recrystallised from ethanol-water (70:30), to give pale yellow crystals, (5.95g, 48%), mp 222-223°C. (Found: C,46.40; H,3.55; N,12.40. $C_{13}H_{12}N_3I$ requires C,46.30;H,3.60; N,12.45%).

δ^1H(CD$_3$OD):4.6(3H,s,CH$_3$); 7.35(m,2ArH); 7.75(m,2ArH); 8.25(t,1H,pyridine ring); 9.0(1H,d,pyridine ring); 9.10(1H,d,pyridine ring), and 9.6(s,1H,pyridine ring)ppm λ_{max} (CH$_3$CN) 318 nm.

2-(1-methylpyridinium-3-yl) benzimidazolate (5)

To a solution of the above salt (3g, 14 mmol) in ethanol was added dropwise an aqueous solution of sodium hydroxide (1 mol dm^{-3}, 14 cm^3). A yellow crystalline solid precipitated out almost instantaneously, and was collected by filtration and washed repeatedly with aqueous ethanol to give the *betaine*, (2.78g, 95%). m.p. 205°C (from ethanol-water 70:30 v/v). (Found: C,63.35;H,6.20;N,16.8. C$_{13}$H$_{11}$N$_3$. 2H$_2$O requires 63.65;H,6.10;N,17.15%). FABMS:m/z 210 (M$^+$+1). λ_{max} (CH$_3$CN):345 nm. δ^1H(CD$_3$OD): 4.25(s,3H,CH$_3$); 7.05(m,2ArH);7.55(m,2ArH); 7.85(t,1H,pyridine ring); 8.4(d,1H,pyridine ring); 8.95(d,1H,pyridine ring), and 9.15(s,1H,pyridine ring)ppm.

Betaine-TCNQ Adduct

The adduct was prepared by heating together betaine (5) with TCNQ (1) in equimolar quantities in acetonitrile under reflux for several hours. On cooling the dark brown solution deposited a black microcrystalline solid (68%). Attempts to prepare crystals suitable for x-ray diffraction, using the slow diffusion technique, have been unsuccessful to date. m.p.above 260°C decomp. (Found: C, 71.47; H, 3.46. N, 24.39. C$_{25}$H$_{15}$N$_7$.MeCN requires: C, 71.35; H, 3.99; N, 24.65%). i.r. (KBr): 2194, 2174 (CN) cm^{-1}. FABMS m/z 210 (M$^+$+1, betaine component).

For comparison purposes the following adducts were prepared:-

(Pyridinium iodide salt) (4) (LiTCNQ) adduct

The adduct was prepared by heating together the salt (4) with LiTCNQ in equimolar quantities in DMF under reflux for several hours. The mixture was evaporated and the residue triturated with water resulting in a crude dark brown solid (54%). (Found: C, 68.60; H, 4.09. N, 21.09%). i.r. max (KBr): 2177, 2141 (CN) cm^{-1}.

(Pyridinium iodide salt(4)) (TCNQ) adduct

The adduct was prepared by heating together compound (4) with TCNQ in equimolar quantities in DMF under reflux for several hours. The mixture was evaporated and the residue triturated with ether resulting in a crude dark brown solid (68%). Found: C, 56.01; H, 3.52. N, 17.06%. υ max (KBr): 2202, 2170, 2158 (CN) cm^{-1}.

DC conductivity studies

For the electrical measurements, the 0.425mm thick TCNQ-adduct pressed powder pellets were sandwiched between two vacuum evaporated gold electrodes. The electrode active area was ≈25mm^2. Cu wires were attached to the electrodes using silver conducting paint. Measurements were taken with the devices placed in an Oxford Instruments Liquid Nitrogen Cryostat and to prevent the formation of ice particles on the sample surface they were held under a Nitrogen gas atmosphere. The temperature range studied was 80K to 300K; this was monitored via an ITC4 proportional / integral / derivative temperature controller and determined by a thermocouple positioned close to the samples inside the cryostat. The circulating current I_c, was measured as a function of the steady state voltage applied to the pellet, from 0V to 1V in steps of 0.1V, using a Keithley 617 programmable electrometer.

REFERENCES

1   G J Ashwell, *Phys Status Solidi b* 1978, *86*, 705: J B Torrance,*Acc. Chem. Res.*, 1979, *12*, 79 and refs therein; R M Metzger, N E Heimer, and G J Ashwell, *Mol. Cryst., Liq. Cryst.*, 1984, *107*, 133.

2   A M Grainger, *Synthetic Metals*, 1994, *66*, 291.

3   D W Allen and P Benke, *Phosphorus, Sulfur, Silicon, Related Elem.*, 1994, *86*, 259; *J Chem Soc Perkin Trans 1*, 1995, 2789.

4   E Alcalde, *Advances in Heterocyclic Chemistry*, 1994, *60*, 197, and refs therein.

5   R M Metzger, *Advances in Chem. Series*, 1994, *240*, 81, and refs therein.

6   C Reichardt, *Chem. Soc. Reviews*, 1992, 147; *Chem. Revs.*, 1994, *94*, 2319.

7   A S Martin, J R Sambles, and G J Ashwell, *Phys. Rev. Lett.*, 1993, *70*, 218

8   E Alcalde, I Dinares, L Perez-garcia and T Roca, Synthesis, 1992, 395.

9   A E Tschitschibabin and E D Ossetronan, *Chem. Ber,* 1925, 58, 1708.

10   R Bozio, I Zanon, A Girlando, and C Pecile, *J. Chem. Soc., Faraday Trans. 2*, 1978, *74*, 235.

11   A Girlando, and C Pecile, *Spectrochim Acta*, Part A, 1973, *29*, 1859.

12   G Zhongze, W Yu, and L Juzheng, *Mat. Sci. Eng.*, 1993, *B20*, 298.

13   G Kossmehl, D Kabbeck-Kupijai, *Syn. Metals,* 1993, 53, 347.

14   A K Jonscher, *J. Vac. Sci. Tech.*, 1971, *8*, 135.

Figure. 1. Current Density / Voltage characteristics for the TCNQ adduct at room temperature.
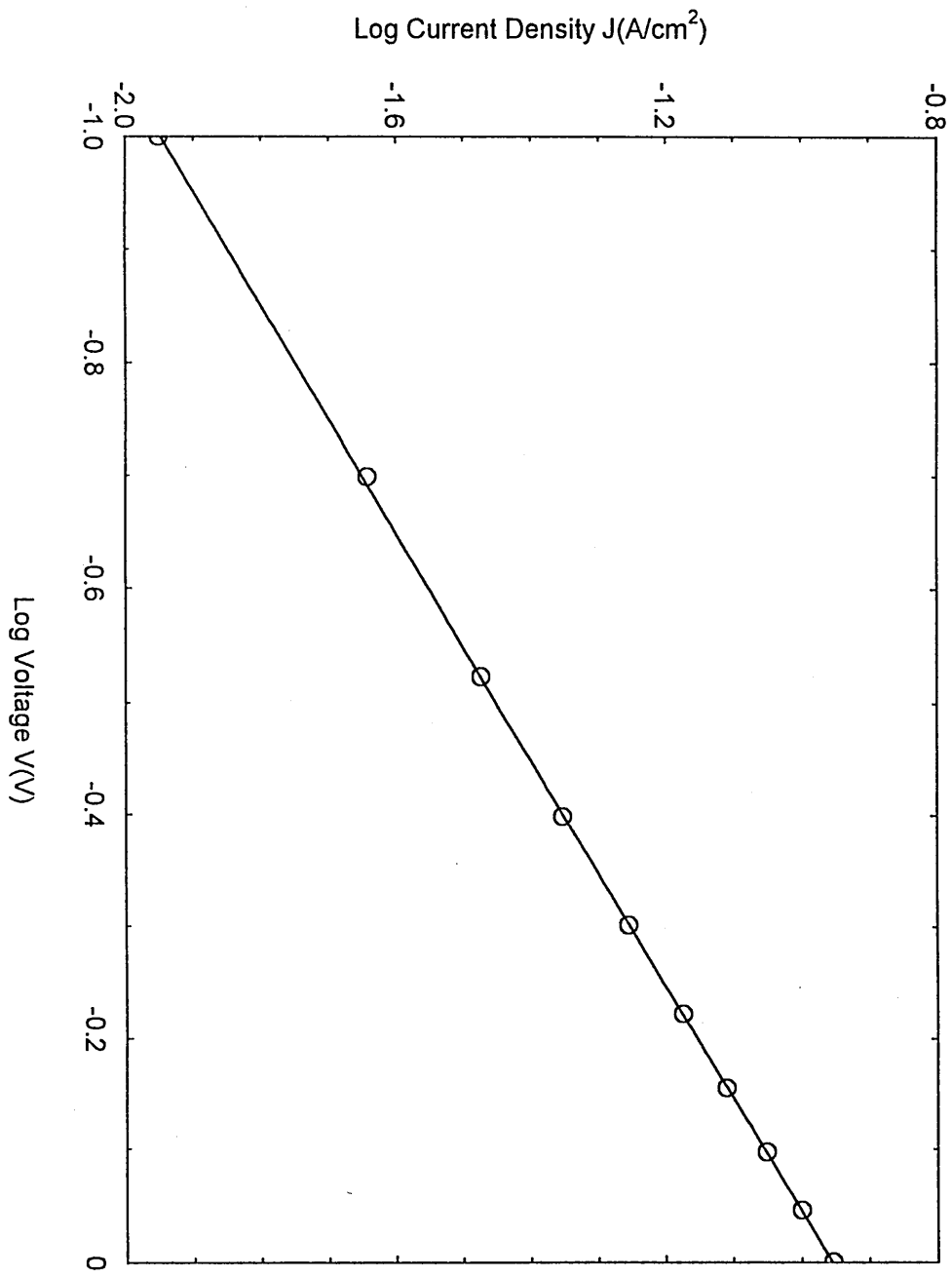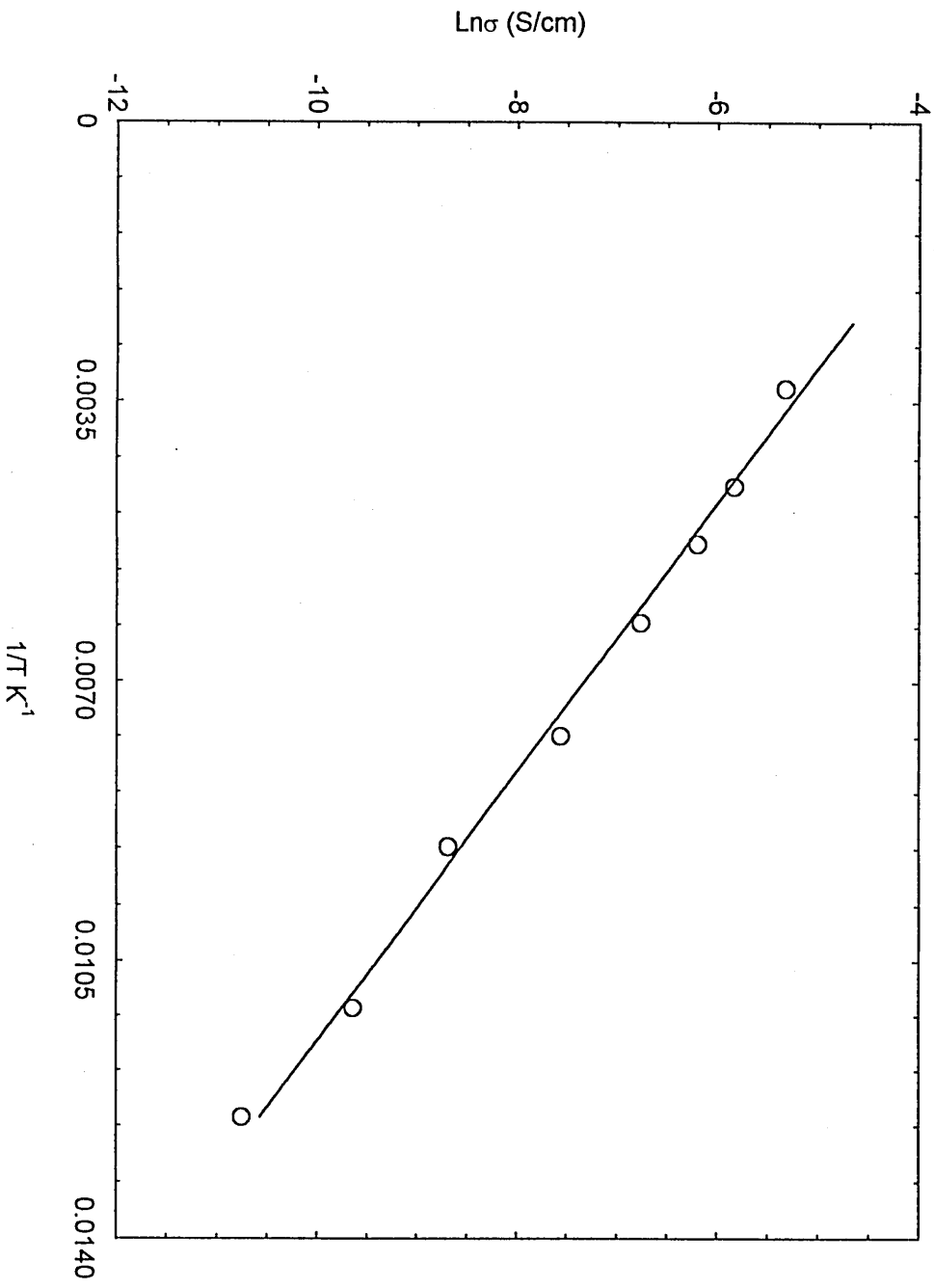
SOL-GEL DERIVED TiO$_2$ / LEAD PHTHALOCYANINE PHOTOVOLTAIC CELLS

S. M. Tracey[ab], S.N.B.Hodgson[a], A. K. Ray[b]

"University of Humberside and Lincolnshire, School of Engineering and Information Technology.
[b]Sheffield Hallam University, School of Engineering Information Technology.

Abstract

Transparent TiO$_2$ films were deposited onto a base electrode comprising an InSnO$_2$ glass substrate using the (alkoxide) Sol-Gel technique. Lead Phthalocyanine was subsequently vacuum sublimed onto the TiO$_2$ surface. The resulting InSnO$_2$/TiO$_2$/PbPc/Au heterojunction cell was investigated for its illuminated current density/voltage, and spectral characteristics. The ideality factor (m) and saturation current (J_o) were determined from $J(V)$ measurements. Photoelectrical measurements were conducted under both simulated AM2 solar radiation and within a wavelength range of 300-900nm. This allowed calculation of V_{oc}, J_{sc}, FF, Z and the overall conversion efficiency, $\eta\%$. Typical photovoltaic characteristics were obtained indicating the devices potential for solar cell applications, however efficiency improvements are required.

1. Introduction

The principle drawbacks of conventional Si-Based cells are the high material and manufacturing costs. Consequently, a number of alternative material and device structures have been considered, including both organic [1] and hybrid organic/inorganic systems, [2]. The main aims of these investigations are to improve overall conversion efficiency while also reducing production costs. Research has shown that organic dyes can be successfully used to spectrally sensitise wide band gap metal oxide semiconductors, resulting in a low cost photoelectrochemical cell, [3]. Such devices incorporate a liquid electrolyte and there are significant concerns regarding their long term stability. Consequently there is considerable interest in the development of solid state inorganic/organic heterostructures as low cost photovoltaic devices. This paper describes the development and results obtained from such a cell, which is in the form; Au/Lead Phthalocyanine (PbPc) /TiO$_2$/InSnO$_2$.

PbPc and TiO$_2$ can be considered to be p-type and n-type semiconductors respectively. Therefore the contact formed between the PbPc and TiO$_2$ will produce an inorganic/organic (IO) p-n heterojunction. The nature of the charge transfer and transport mechanisms in IO heterojunctions of this type remains the subject of some debate with a direct electron transfer mechanism being the most favoured to explain the observed photovoltaic behaviour. Within the heterostructures the organic layer absorbs light, generating excitons which diffuse to the heterointerface and dissociate. Electrons transfer to the TiO$_2$ layer which provides electron transport, and the holes remain within the organic layer and are transported therein. [4] The electrical current is supported only by majority charges. Therefore such devices drastically differ from conventional p-n semiconductor devices in which the electrical current is supported by minority carriers [5]. and would be anticipated to be less sensitive to surface and bulk defects obviating the need for the supertechnology and costs associated with most semiconductor device manufacture.

The fabrication of such devices entails the need to manufacture thin films of the organic and inorganic components. The fabrication of the inorganic layer in particular requires a relatively low cost, low temperature process capable of providing an optically transparent, electrically semiconducting, mechanically and chemically stable thin film, with good electronic contact with the substrate electrode. The Sol-Gel process is thus ideally suited for this application.

Titanium dioxide is an n-type semiconductor, easily formed by the Sol-Gel method and has the advantage of both chemical and thermal stability. Added to this it possess economical and environmental advantages of over some of the more prominent PV materials such as CdS, Si and GaAs. Lead Phthalocyanine, (PbPc) belongs to a class of organic materials that have over the years received considerable attention [6] this is mainly due to their semiconductive properties. Added to this they are abundant, stable and relatively cheap. However, attempts to produce substituted Phthalocyanine solar cells have consistently shown low overall conversion efficiencies and in most cases this has been attributed to their low quantum efficiency and/or low charge carrier mobility [6]. They are however good photogenerators of free charge carriers.

2. Experimental Procedures
2.1 Device Fabrication

The device comprised a sandwich structure of an In-SnO$_2$ glass electrode and substrate, transparent Sol-Gel derived TiO$_2$, PbPc dye and Au counter electrode. The complete device structure is shown in the inset of figure 1.

Optically transparent TiO$_2$ films were deposited onto ultrasonically cleaned InSnO$_2$ glass substrates by dip coating at a withdrawal rate of 250mm/min.. The dip coating solution consisted of 12.6 volume % of Titanium Isopropoxide (TIP) in ethanol, stabilised with glacial acetic acid additions in a molar ratio 4.16:1 TIP:ACID

The entire procedure was carried out under atmospheric conditions. The films were left to dry in air for 24 hours then heated under atmospheric conditions to 500°C for 5 hours. X-ray diffraction analysis carried out on residues of the Sol mixture revealed that for gels heated to 500°C anatase is the predominant physical structure. The thickness of the TiO$_2$ films were measured using a planar surfometer and estimated to be in the order of 50nm. Films of Lead Phthalocyanine (PbPc) were prepared by vacuum sublimation. The TiO$_2$ coated substrates were held at room temperature and under a vacuum of ~10^{-5} mbar during the sublimation process. A deposition rate of 1-10A/sec was used. The final film thickness was in the order of 500nm, determined by a quartz crystal monitor in situ. Electrical connections were provided by evaporation of Au contacts onto the PbPc surface.

2.2 Photoelectrical Measurements

The performance of the cell was assessed using both the wavelength dependent short circuit phototcurrent density J$_{sc}$, and the illuminated current-density/voltage, $J(V)$ characteristics under simulated solar radiation.

Comparison of the PbPc absorption spectra with the, $J_{sc}(\lambda)$ action spectra allowed calculation of the quantum efficiency (Z) defined as the ratio of photocurrent collected at each wavelength to the number of photons incident on the surface at that wavelength according to the following equation;

$$Z = \frac{Rhc}{e\lambda} \qquad (1)$$

Where R is the device responsivity given by (J_{sc}/ϕ), ϕ is the incident intensity level in W/m^2, h is Planck's constant, c the speed of light, λ the wavelength of the incident monochromatic radiation and e the electronic charge. Comparison of the PbPc absorption spectra with the J_{sc} action spectra is also a direct indication of the ability of the dye to spectrally sensitise the TiO_2 to wavelength regions outside its intrinsic sensitivity.

The illumination for wavelength dependent measurements was provided by a Spex 1681 0.22m spectrometer in conjunction with a SPEX 1682A broad band radiation source. A 1683L tungsten/halogen incandescent lamp provided illumination over the wavelength range 300-900nm. The V_{oc} and J_{sc} of the cell were measured as a function of wavelength (λ) in this range. The monochromator intensity level (ϕ) was found to be in the order of 32 $\mu W/cm^2$. A UV/Vis Unicam spectrometer was used to provide optical absorption spectra of the PbPc and TiO_2 films for comparison with the action spectra.

Illuminated $J(V)$ characteristics were used to determine the performance of the cell under white light conditions. The following photovoltaic cell parameters were obtained; Open circuit voltage (V_{oc}), ;Short circuit current density (J_{sc}),; The fill factor (FF) or the fraction of the product of J_{sc} and V_{oc} available as power output given by;

$$FF = \frac{V_{mp}J_{mp}}{V_{oc}J_{sc}} \qquad (2)$$

where V_{mp} and J_{mp} represent the voltage and current at the maximum power point respectively[ref] $\eta\%$, the overall conversion efficiency may then be calculated according to;

$$\eta = \frac{V_{oc}J_{sc}FF}{P_{in}} \qquad (3)$$

where P_{in} is the power of the incident intensity (W/m^2).

Illuminated $J(V)$ measurements were performed under atmospheric conditions, using an electrometer. In all measurements the polarity of the forward voltages was positive at the Au electrode. For all illuminated $J(V)$ measurements, irradiation of the $TiO_2/PbPc$ junction was directed through the $InSnO_2/TiO_2$ face. An Applied Physics, model 9500 solar simulator provided AM2 radiation at an intensity level of $1.52mW/cm^2$.

3. Results and discussion
3.1 Action spectra

To demonstrate photosensitisation of the TiO_2 photocurrent action spectra were obtained over the range of visible light. Figure 1 displays the $J_{sc}(\lambda)$ action spectra obtained for the PbPc/TiO_2 cell in comparison with both the PbPc and TiO_2 absorption spectra. The PbPc film exhibits appreciable absorption in the 320-500nm and ~580-900nm ranges, typical of that observed in sublimed thin films of the material [7]. The TiO_2 films were highly transparent over the visible wavelength range.

Good agreement between the absorption spectra of the PbPc film and the spectral dependence of J_{sc} was observed for most of the visible region. Anomalies were observed

for wavelengths below ~400nm. Most probably due to a combination of optical absorption effects in TiO_2 and the $InSnO_2$ glass substrate. The similarity of the absorption spectra to the action spectra indicates that sensitisation of the TiO_2 Sol-Gel layer with PbPc dye molecules occurred resulting in the extension of the absorbance of TiO_2 into the visible region. The observed wavelength dependence of J_{sc} must therefore be a consequence of photocarrier excitation in the PbPc and a subsequent transfer mechanism to the TiO_2 film.

The calculated quantum efficiencies (Z) at PbPc absorption maxima were Z~0.42% at the lower maxima ~360nm and Z~ 0.41% at the higher maxima ~680nm, the corresponding J_{sc} were $0.031 \mu A/cm^2$ and $0.072 \mu A/cm^2$ respectively. This is an interesting observation, since a lower measured J_{sc} at 360nm did not give rise to a lower value of Z in fact little difference in Z was observed. Two possible arguments are proposed to account for this effect, firstly the increase in absorption of the PbPc film may contribute to a higher density of excitons within the organic layer. Alternatively the onset of absorption in the TiO_2 film at these wavelengths may result in increase charge carrier generation. This is in agreement with recent studies on $ZnPc/TiO_2$ cells which have shown that UV absorption in TiO_2 results in an increase in carrier density and conductivity of the TiO_2 film and that the UV absorbed in the space charge layer of the TiO_2 contributes to the photovoltaic effect [8]. It is anticipated therefore that both of these mechanisms results in the observed $Z(\lambda)$ dependence.

The quantum efficiencies obtained for this device were low. However such efficiencies are not atypical of similar devices, the low efficiency having been previously attributed to recombination centres at the heterojunction interface, [8], which may be present at the TiO_2 surface. The TiO_2 film was not treated in any way and as a consequence surface states could be present which can act as recombination centres. Impurities in the PbPc layer or grain boundaries within the TiO_2 or PbPc, polycrystalline films would also act as trapping sites for charge carriers.
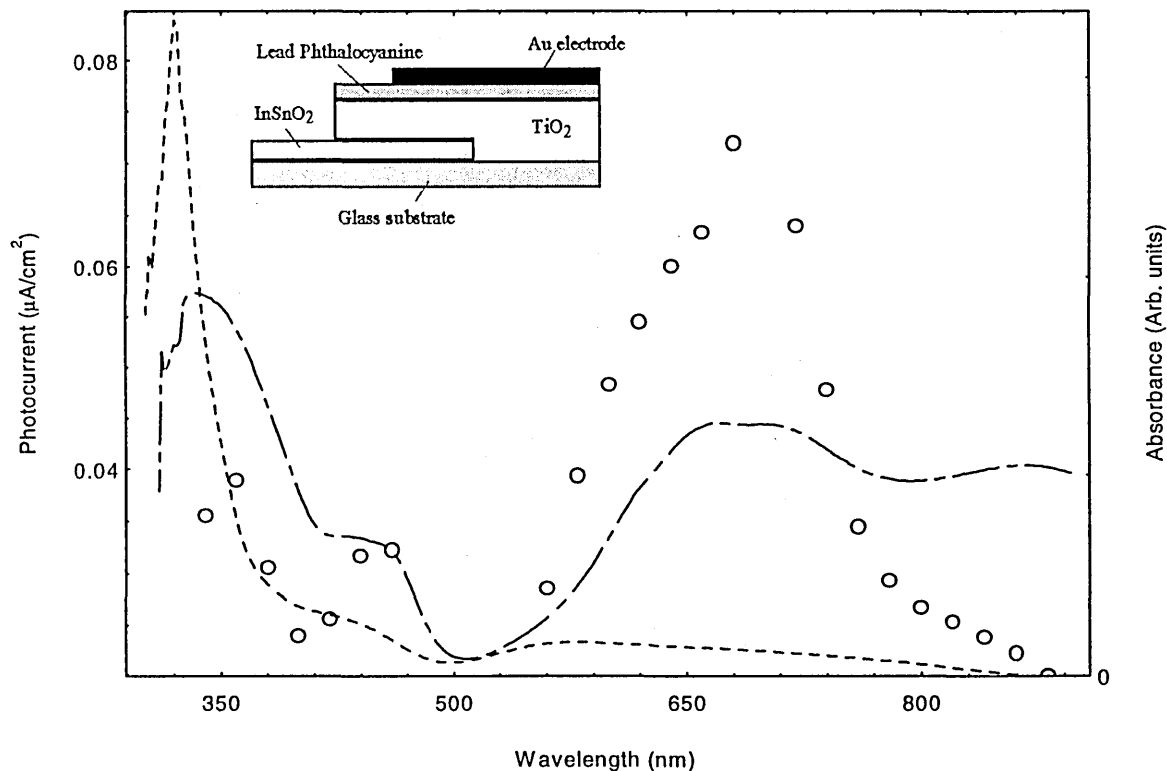

Fig. 1. Photocurrent density action spectra (O) of a $Au/PbPc(500nm)/TiO_2(50nm)/InSnO_2$ cell. Absorbance of TiO_2 and PbPc film given by (---) and (— — — —) respectively. Device schematic shown in inset.

3.2 Illuminated J(V) characteristics

From the illuminated characteristics under simulated AM2 radiation, the following values were obtained for typical solar cell parameters. V_{oc} = 200mV, J_{sc}=4.67x10^{-7}A/cm^2, and FF (fill factor) = 0.162. These values corresponded to an overall power conversion efficiency of $\eta\%$ ~ 0.001%, according to equation 3.

The relatively low values obtained for the conversion efficiency can be attributed both to interfacial and bulk effects as follows:

The presence of defects at the TiO$_2$/PbPc interface would be expected to result in a reduction of the power conversion efficiency as explained in the previous section. In addition the overall conversion efficiency would be anticipated to be a function of the electrical resistance of the cell. The low electrical conductivity of the PbPc films would be expected to cause a high series resistance. This was confirmed from measurements of the series resistance (R_s) which under illuminated conditions was found to be R_s~ 57.5kΩ/cm^2. Such a high R_s indicates the disadvantage of the low conductivity of the organic semiconductor.

4. Conclusions

A low cost photovoltaic cell based on a p-PbPc/n-TiO$_2$ thin film heterojunction has been successfully produced utilising the Sol-Gel technique.

The results indicate that a Sol-gel derived TiO$_2$ film can be sensitised to wavelengths outsides its intrinsic sensitivity. The observed response is anticipated to be a consequence of light absorption in the dye layer and the separation of photoexcited carriers at the PbPc/TiO$_2$ heterointerface.

The high series resistance caused by the organic layer is believed to be responsible for the low conversion efficiency of the cell and efficiency improvements are required. Preliminary investigations on devices incorporating thinner and/or more conductive organic layers are currently on going, and are yielding encouraging results with conversion efficiencies of at least an order of magnitude higher than this reported.

REFERENCES

[1] H. Yanagi, M. Imamura, and M. Ashida, Journal of Applied Physics **75** (4) 2061 (1994).
[2] S. Antohe, Revue Roumanie de Phys **37** (3) 309 (1992).
[3] B. O'Regan, and M. Grätzel, Nature **353** 737 (1991).
[4] Y, Shen, L. Wang, Z. Lu, Y. Wei, Q. Zhou, H. Mao, and H. Xu, Thin Solid Films. **257** 144 (1995).
[5] M. S. Tyagi, *Introduction to Semiconductor Materials and Devices* (John Wiley & Sons, 1991) p. 340.
[6] J. Simon and J. J. Andre, *Molecular Semiconductors* (Springer, 1983), p. 73.
[7] D. Schmeißer, A. Rager, K. Thonke, M. Pilkuhn, D. Fr öhlich, G. Gauglitz, M. Schäfer, and D.
     Oelkrug, Synthetic Metals **41-43**, 1457 (1991).
[8] K. Kajihara, K. Tanaka, Kk. Hirao, and N. Soga, Japanese Journal of Physics **35** 6110 (1996).